The XENON100 Dark Matter Experiment: Design, Construction, Calibration and 2010 Search Results with Improved Measurement of the Scintillation Response of Liquid Xenon to Low-Energy Nuclear Recoils

Guillaume Plante

Submitted in partial fulfillment of the
requirements for the degree of
Doctor of Philosophy
in the Graduate School of Arts and Sciences

COLUMBIA UNIVERSITY

2012

ABSTRACT

The XENON100 Dark Matter Experiment: Design, Construction, Calibration and
2010 Search Results with Improved Measurement of the Scintillation Response of
Liquid Xenon to Low-Energy Nuclear Recoils

Guillaume Plante

An impressive array of astrophysical observations suggest that 83% of the matter in the universe is in a form of non-luminous, cold, collisionless, non-baryonic dark matter. Several extensions of the Standard Model of particle physics aimed at solving the hierarchy problem predict stable weakly interacting massive particles (WIMPs) that could naturally have the right cosmological relic abundance today to compose most of the dark matter if their interactions with normal matter are on the order of a weak scale cross section. These candidates also have the added benefit that their properties and interaction rates can be computed in a well defined particle physics model.

A considerable experimental effort is currently under way to uncover the nature of dark matter. One method of detecting WIMP dark matter is to look for its interactions in terrestrial detectors where it is expected to scatter off nuclei. In 2007, the XENON10 experiment took the lead over the most sensitive direct detection dark matter search in operation, the CDMS II experiment, by probing spin-independent WIMP-nucleon interaction cross sections down to $\sigma_{\chi N} \sim 5 \times 10^{-44}\,\mathrm{cm}^2$ at $30\,\mathrm{GeV}/c^2$.

Liquefied noble gas detectors are now among the technologies at the forefront of direct detection experiments. Liquid xenon (LXe), in particular, is a well suited target for WIMP direct detection. It is easily scalable to larger target masses, allows discrimination between nuclear recoils and electronic recoils, and has an excellent stopping power to shield against external backgrounds. A particle losing energy in LXe creates both ionization electrons and scintillation light. In a dual-phase LXe time projection chamber (TPC) the ionization electrons are drifted and extracted into the gas phase where they are accelerated to amplify the charge signal into a proportional scintillation signal. These two signals allow the three-dimensional localization of events with millimeter precision and the ability to fiducialize the target volume, yielding an inner core with a very low background. Additionally, the ratio of ionization and scintillation can be used to discriminate between nuclear recoils, from

neutrons or WIMPs, and electronic recoils, from γ or β backgrounds. In these detectors, the energy scale is based on the scintillation signal of nuclear recoils and consequently the precise knowledge of the scintillation efficiency of nuclear recoils in LXe is of prime importance.

Inspired by the success of the XENON10 experiment, the XENON collaboration designed and built a new, ten times larger, with a one hundred times lower background, LXe TPC to search for dark matter. It is currently the most sensitive direct detection experiment in operation. In order to shed light on the response of LXe to low energy nuclear recoils a new single phase detector designed specifically for the measurement of the scintillation efficiency of nuclear recoils was also built. In 2011, the XENON100 dark matter results from 100 live days set the most stringent limit on the spin-independent WIMP-nucleon interaction cross section over a wide range of masses, down to $\sigma_{\chi N} \sim 7 \times 10^{-45}\,\mathrm{cm}^2$ at $50\,\mathrm{GeV}/c^2$, almost an order of magnitude improvement over XENON10 in less than four years.

This thesis describes the research conducted in the context of the XENON100 dark matter search experiment. I describe the initial simulation results and ideas that influenced the design of the XENON100 detector, the construction and assembly steps that lead into its concrete realization, the detector and its subsystems, a subset of the calibration results of the detector, and finally dark matter exclusion limits. I also describe in detail the new improved measurement of the important quantity for the interpretation of results from LXe dark matter searches, the scintillation efficiency of low-energy nuclear recoils in LXe.

Contents

List of Figures

List of Tables

ACKNOWLEDGMENTS

First I thank my advisor, Elena Aprile, for transmitting to me her enthusiasm about liquid Xe detectors and their use in the field of direct dark matter detection. Her passion and dedication to the XENON project, her pragmatic and direct approach to problem solving, and her high expectations have all contributed greatly to my motivation to excel.

I thank Karl Giboni, under whose guidance I learned so much of what cannot be learned in textbooks about the construction and operation of liquid Xe detectors. I am grateful for having had the chance of participating in the design and construction stages of the XENON100 detector, an invaluable experience during which I could learn first hand about the intricacies of Xe dual-phase time projection chambers.

Over the years in the XENON group at Columbia I have met and enjoyed working with many postdoctoral researchers, Masaki Yamashita, Roberto Santorelli, Maria Elena Monzani, Kaixuan Ni, Antonio Melgarejo Fernandez, Rafael Lang, Ranny Budnik, and fellow graduate students, Bin Choi, Kyungeun Lim, Luke Goetzke, Hugo Contreras. Some of you have introduced me to research, some of you have thought me new techniques, and to some of you I have looked for guidance. Sometimes you have challenged my assumptions about a problem and sometimes you helped me reach a deeper level of understanding. All of you, I know, have helped me become a scientist, and for that I am grateful.

The success of the XENON100 experiment is due to the dedicated, persistent, and hard working group of scientists that make up the collaboration, my thanks to all, none of my work would have been possible without you. I feel priviledged to have been part of this grand endeavour. To the small group of collegues with whom I had the pleasure of working in close contact with during 2008 and 2009 at LNGS, Alfredo Ferella, Marc Schumann, Eirini Tziaferi, Yuan Mei, Luis Coelho, Alexander Kish, Ethan Brown, Emilija Pantic, Peter Shagin, Joao Cardoso, Antonio Ribeiro, you all made my time there a period I will never forget.

I also thank my collegues from the XENON10 collaboration, with whom I have learned much of the skill of data analysis. I could not have asked for a better environment to acquire this knowledge than my stay at LNGS in summer 2006 during the commissioning of XENON10.

I am deeply grateful to Adel F. Antippa, whose trust in my abilities inspired me to pursue the Ph.D. in physics, without his initial encouragement I might not have chosen this path.

Finally, I thank my friends and family, who have supported and encouraged me along the way. I am especially thankful to all of you for having kept the relationship alive in moments where I had a harder time reconciling work and life. Mina, جونم, I will forever be grateful for your patience during my time abroad, I am immensely happy that in the end this experience made our bond stronger. Your belief in me has always been an inspiration, thank you.

Chapter 1

Dark Matter

In the last decades, an impressive amount of independent observations have lead us to believe that the energy density of our universe is dominated by two components whose exact nature we have not yet understood. One is a new, collisionless type of matter, dark matter, whose interactions with normal matter we observe only through the gravitational force. The second is an almost perfectly uniform component called dark energy, of which we know even less, except that it is responsible for the acceleration of the expansion of the universe. These two components form 96% of the energy density of the universe, relegating what we originally thought of as the main constituents to a mere 4% of the total.

The essential ingredients to construct a cosmological model are: Einstein's equations, which describe the geometry of the universe through its energy content, a metric, which encapsulates the symmetries of spacetime, and equations of state, which describe the properties of the matter and energy contained in the universe. Assuming that the universe is homogeneous and isotropic, which is observed at scales of ~100 Mpc in galaxy surveys, leads to a specific form for the metric

$$ds^2 = -c^2dt^2 + a^2(t)\left(\frac{dr^2}{1-kr^2} + r^2d\Omega^2\right) \tag{1.1}$$

where $a(t)$ is the scale factor, and k is a constant that describes the spatial curvature of the universe and can take values of -1, 0, or 1. Einstein's equations can be solved with this metric with one component giving the Friedmann equation

$$\left(\frac{\dot{a}}{a}\right)^2 + \frac{k}{a^2} = \frac{8\pi G_N}{3}\rho_{\rm tot} \tag{1.2}$$

where G_N is Newton's constant and $\rho_{\rm tot}$ is the total average energy density of the universe. The expansion rate of the universe is characterized by the Hubble parameter, $H(t) = \dot{a}(t)/a(t)$, which at the present epoch is called the Hubble parameter, $H_0 = 73 \pm 3\,{\rm km\,s^{-1}\,Mpc^{-1}}$. It is customary to rewrite the Friedmann equation in terms of the density parameter, Ω, as

$$\Omega - 1 = \frac{k}{H^2 a^2} \tag{1.3}$$

where

$$\Omega = \frac{8\pi G_N}{3H^2}\rho_{\rm tot} = \frac{\rho_{\rm tot}}{\rho_c} \tag{1.4}$$

and where the last equality defines the critical density, $\rho_c = 3H^2/8\pi G_N$. In this form, it is clear why the ρ_c is called the critical density, that is, when $\rho_{\rm tot} = \rho_c$ the universe is flat ($k = 0$). The energy density of a component i (matter, radiation, vacuum energy) is also expressed in terms of the critical density with

$$\Omega_i = \frac{\rho_i}{\rho_c}, \tag{1.5}$$

with the total energy density of the universe given by $\Omega = \sum \Omega_i$. Cosmological-scale measurements, like those of anisotropies in the cosmic microwave background (CMB) (Komatsu *et al.*, 2011), large scale structure, and supernova surveys, favor the "cosmological concordance" model, ΛCDM: a flat universe $\Omega \sim 1$, with a baryon density $\Omega_b \sim 0.04$, a non-baryonic dark matter density $\Omega_c \sim 0.23$, and a dark energy density $\Omega_\Lambda \sim 0.73$. In the next section we will look at some of the evidence at different scales for the existence of dark matter.

1.1 Evidence for the Existence of Dark Matter

An extensive amount of cosmological and astrophysical observations point to the presence of dark matter in our universe, and this at many different scales. We will not present here an exhaustive survey of all these observations but rather present some of the most compelling evidence for the existence of dark matter at different scales.

1.1.1 Galactic Rotation Curves

The galactic rotation curves of spiral galaxies are probably the most convincing piece of evidence for the existence of dark matter at the galactic scale (Sofue and Rubin, 2001). The orbital velocity as a function of radius can be obtained from the measurement of the redshift of the 21 cm hyperfine transition line of hydrogen (Begeman *et al.*, 1991). Clouds of neutral hydrogen extend far beyond the galactic disk and thus allow the measurement of the orbital velocity much further out than the stars. From a measurement of the rotational velocity of stars and gas as a function of radius r one can compute the mass $M(r)$ of the galaxy enclosed within that radius. In Newtonian mechanics, since $v(r) = \sqrt{GM(r)/r}$, one would expect that at a radius beyond the extent of the stellar disk the rotational velocity should go as $v(r) \propto r^{-1/2}$. Instead, rotation curves exhibit a flat behavior that extends far beyond the stellar disk. A typical galactic rotation curve, from the spiral galaxy NGC6503 is shown in Fig. 1.1 (left, points) along with a picture of NGC6503 (right). The expected contribution to the rotational velocity from the luminous mass (disk) and the interstellar gas (gas) by themselves cannot explain the observed rotation curve but the assumption of the presence of a dark halo with $M(r) \propto r$ can account for the observed behavior.

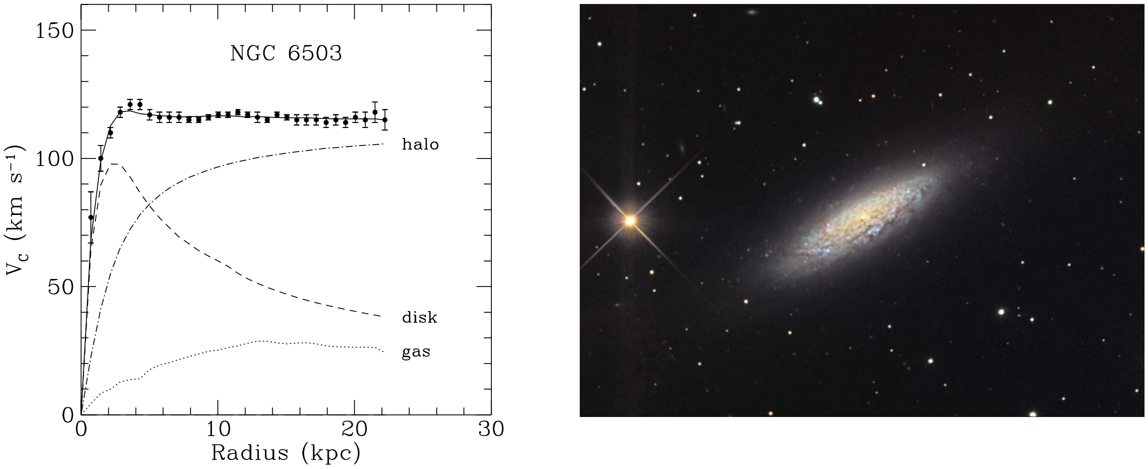

Figure 1.1: Measured rotation curve (left) along with the mass contributions as a function of radius, for the visible component (dashed), the gas component (dotted), and the dark halo (dash dotted). Picture of the NGC6503 spiral galaxy (right). Figure (left) from Begeman *et al.* (1991). Image credit (right): Adam Block/NOAO/AURA/NSF.

Measurements of galactic rotation curves are additionally very important for the problem of estimating the local dark matter density in the Milky Way, a typical spiral galaxy. This parameter is required for the prediction interaction rates in direct detection experiments.

1.1.2 Galaxy Clusters

Early analysis of galaxy clusters using the virial theorem revealed that there is more matter than what can be inferred from the stellar component (Zwicky, 1933), as a matter of fact this was also of the earliest predictions for the existence of dark matter. Later it was discovered that these massive structures contain large quantities of hot x-ray emitting plasma. The plasma is heated to high temperature by the gravitational potential well of the cluster and emits bremsstrahlung x-rays. As the x-ray emission is proportional to the plasma density squared, the mass of this component can be estimated with an x-ray satellite like the Chandra X-ray Observatory. The total mass required to explain the dynamics of clusters is much higher (by $\gtrsim 5$) than the sum of the stellar and the baryonic intracluster plasma components. The remainder is attributed to a dark matter.

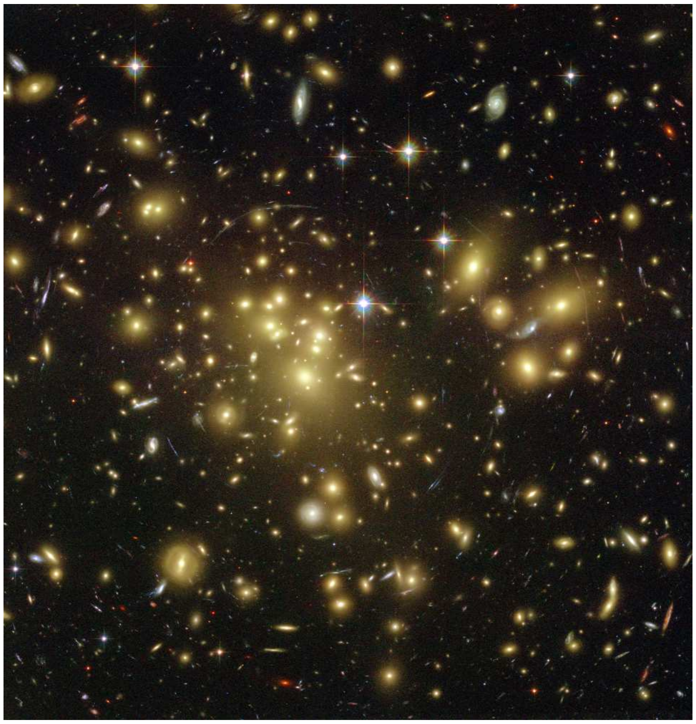

Figure 1.2: Hubble Space Telescope Advanced Camera for Surveys image of the lensing cluster Abell 1689. Image credit: NASA, N. Benitez, T. Broadhurst, H. Ford, M. Clampin, G. Hartig, G. Illingworth, the ACS Science Team and ESA.

Gravitational lensing occurs when a massive foreground object bends light from distant objects behind it, distorting their images and sometimes creating multiple images of the same structure. The strength of the lensing depends on the mass of the lens, the massive foreground object, and the distances between observer, lens, and background objects. These positions can be computed when the redshift of the lens and the distant objects are known. Gravitational lensing can thus provides and independent measurement of the total mass of a cluster. Fig. 1.2 shows a picture of one of the largest galaxy clusters observed, Abell 1689, acting as a gravitational lens. Many arcs and multiple images of distant galaxies are visible.

One of the most visually striking pieces of evidence towards the existence and nature of dark matter is at the galaxy cluster scale, from the gravitational lensing results on the "Bullet cluster" 1E 0657-56 (Clowe *et al.*, 2006) and the cluster MACS J0025.4-1222 (Bradač *et al.*, 2008) (Fig. 1.3). The hot baryon distribution (pink), as measured from its x-ray signature by Chandra, is clearly separated from the mass distribution inferred from weak and strong gravitational lensing (blue), whereas the visible cluster galaxy population follows the lensing mass. This separation results from the recent merger of both clusters. The hot gas components interact with one another during the merger while the collisonless nature of dark matter implies that both dark matter distributions pass through each other with minimal interactions. Alternative explanations, especially those that rely on the mass distribution being centered on the baryon distribution, have a hard time explaining these observations as simply as the decoupling of the intracluster plasma component from the collisionless dark matter component.

1.1.3 Cosmic Microwave Background

The most precise measurements of the abundance of dark matter in our universe and stringent constraints on its baryonic content come from measurements of the cosmic microwave background (CMB). Much has happened since the accidental discovery (Dicke *et al.*, 1965; Penzias and Wilson, 1965) of the predicted left over radiation from the Big Bang. We now know that it follows with extreme precision the black body spectrum at a temperature of 2.725 K, and that anisotropies are at the level of $10\,\mu$K. Fig. 1.4 shows the Wilkinson Microwave Anisotropy Probe (WMAP) 7-year map of the microwave sky. The image reveals the primordial fluctuations that eventually lead to the gravitational growth of structures like galaxies.

These temperature fluctuations are usually expanded in terms of spherical harmonics Y_{lm} with coefficients a_{lm}. With Gaussian temperature fluctuations, what is consistent

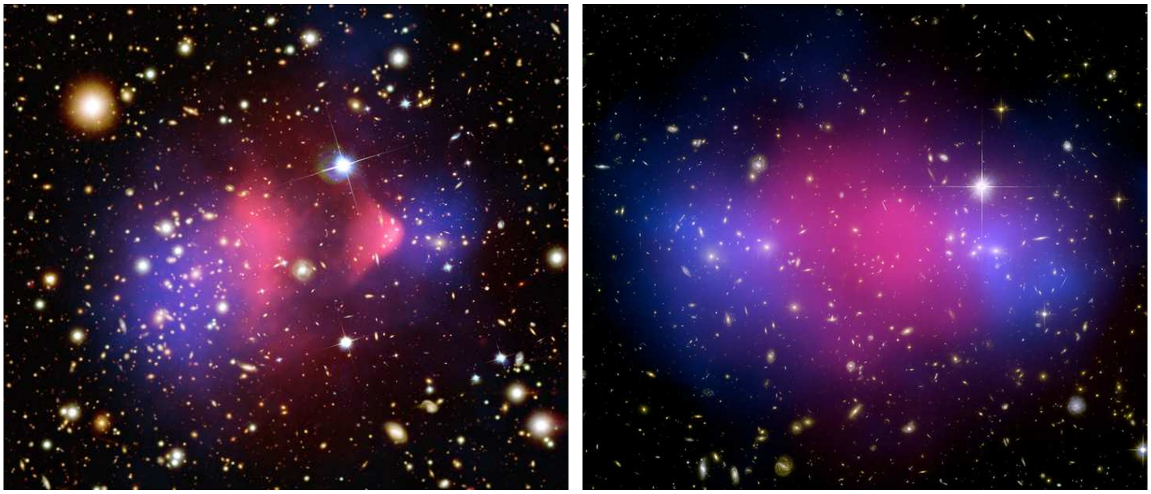

Figure 1.3: Mass distributions from gravitational lensing (blue) and x-ray emissivity maps (pink) composited on optical images of 1E 0657-56 and MACS J0025.4-1222 showing a clear separation between the distribution of hot baryons and the mass responsible for the lensing after the cluster collision. Image credit (left): X-ray (NASA/CXC/CfA/M.Markevitch et al.); Optical: (NASA/STScI; Magellan/U.Arizona/D.Clowe et al.); Lensing Map: (NASA/STScI; ESO WFI; Magellan/U. Arizona/D. Clowe et al.). Image credit (right): X-ray (NASA/CXC/Stanford/S. Allen); Optical/Lensing (NASA/STScI/UC Santa Barbara/M. Bradac)

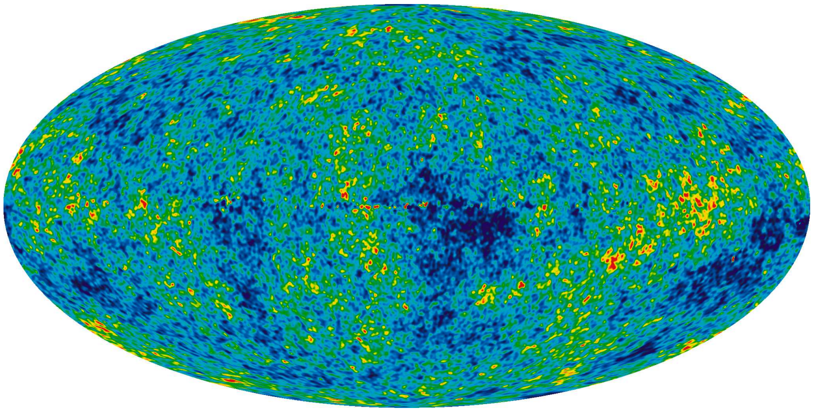

Figure 1.4: WMAP 7-year map of the microwave sky that reveals the primordial temperature fluctuations responsible formation of large-scale structure. The temperature range of the image is ±200 μK. Image credit: NASA / WMAP Science Team.

with current measurements (Larson *et al.*, 2011), the variance of the spherical harmonic coefficients $C_l = \langle |a_{lm}|^2 \rangle$ essentially encodes all the information present in the temperature field. Fig. 1.5 shows the 7-year WMAP angular power spectrum of the temperature map.

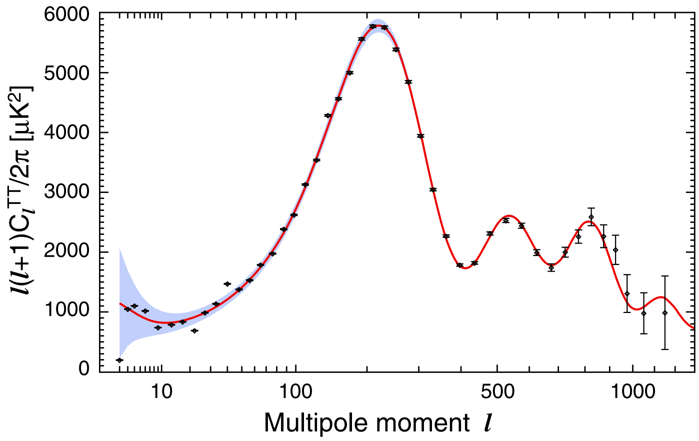

Figure 1.5: The 7-year temperature angular power spectrum from WMAP. The solid curve is the best fit ΛCDM model to the WMAP data. Figure from Larson *et al.* (2011).

The angular power spectrum of the CMB depends on parameters like the physical baryon density, $\Omega_b h^2$, the physical cold dark matter density, $\Omega_c h^2$, and the dark energy density Ω_Λ. The measurement of the temperature anisotropies thus provides constraints on the cosmological parameters. From WMAP data alone, the abundance of baryons, the abundance of cold dark matter, and the dark energy density, to list only three parameters, are obtained as $\Omega_b h^2 = 0.02258^{+0.00057}_{-0.00056}$, $\Omega_c h^2 = 0.1109 \pm 0.0056$, $\Omega_\Lambda = 0.734 \pm 0.029$. It is remarkable that CMB measurements are able to place such tight constraints on the parameters of the standard model of cosmology. No compelling signs for deviations from the ΛCDM model are present.

1.2 Dark Matter Candidates

As we discussed in the previous section, there is convincing evidence for the existence of non-baryonic dark matter at astrophysical scales that range from the galactic to the cosmological scale. The question then becomes of whether any of the known particles could make up the bulk of this cold, dark, collisionless matter or if only new hypothetical particles can satisfy all the constraints. The list of constraints include that dark matter must not, or have only extremely weak, interactions with photons. Otherwise we would see it absorbing some of the light from distant objects such as quasars. Interactions with baryons must also be very weak, otherwise we would observe similar dark matter and baryon disks in galaxies. Furthermore, self-interactions of dark matter particles should be small, otherwise we could not observe dislocated dark matter and intracluster plasma mass distributions such as in the case of the Bullet cluster. The only particles from the Standard Model of particle physics that would meet these constraints are neutrinos. However, CMB anisotropy measurements (Dunkley *et al.*, 2009) combined with large-scale structure data suggest that the physical neutrino density is constrained to $\Omega_\nu h^2 < 0.0067$ (95% c.l.) and thus clearly not abundant enough to compose a significant fraction of the dark matter.

Among the wealth of hypothetical candidate particles that could make up dark matter, perhaps two emerge as well motivated from particle physics, weakly interacting massive particles (WIMPs) and axions. WIMPs or axions constituting a large fraction of the dark matter in the universe would be in itself a more appealing solution as these particles were introduced to solve problems related to the Standard Model of particle physics and not the dark matter problem specifically. In this section we shall briefly present the two candidates.

1.2.1 Axions

Axions are pseudoscalars that are introduced in the Peccei-Quinn mechanism as a solution to the strong CP problem (Peccei and Quinn, 1977). The question of "Why is the Θ parameter of the QCD CP violating term of the Standard Model Lagrangian so close to zero ($< 10^{-9}$)?" constitutes what is called the strong CP problem. By introducing a new spontaneously broken global symmetry to the Standard Model Lagrangian this parameter comes out naturally to be extremely small ($\Theta \sim 10^{-15}$) (Weinberg, 1978; Wilczek, 1978). The axion is the pseudo-Goldstone boson associated with the spontaneously broken Peccei-Quinn symmetry and thus acquires a small mass. Axions could have been produced in cosmologically interesting amounts, for example non-thermally at the QCD phase transition, at which time the background axion field is displaced from the minimum of its effective potential and oscillates around it (Asztalos *et al.*, 2006).

The Axion Dark Matter Experiment (ADMX) (Asztalos *et al.*, 2010; Duffy *et al.*, 2006) searches for axions with a tunable microwave resonant cavity with a large axial magnetic field. Axions would be detected through their conversion into microwave photons in the magnetic field of the cavity and the small amount of power they transfer to it. As it stands now, it seems that the dark matter axion will either be discovered soon or be ruled out completely.

1.2.2 Weakly Interacting Massive Particles

Several extensions of the Standard Model of particle physics aimed at solving the hierarchy problem predict stable WIMPs that could naturally have the right cosmological relic abundance today to compose most of the dark matter, if their interactions with normal matter are on the order of a weak scale cross section. These candidates also have the added benefit that their properties and interaction rates can be computed in a well defined particle physics model. WIMPs in thermal equilibrium in the early universe were being produced from and annihilated into Standard Model particles at equal rates. As the universe expanded and cooled down, came a point where its temperature dropped below the WIMP mass and the WIMP density started to decrease faster than that of Standard Model particles since the WIMP production reactions no longer occurred. However, at some point the WIMP density became so small that the annihilation interactions were not likely anymore, and the density then only decreased with the expansion, leaving a WIMP relic density that could be making up the bulk of dark matter. An order of magnitude estimate for the relic density is (Jungman *et al.*, 1996)

$$\Omega_\chi h^2 \sim \frac{3 \times 10^{-27}\,\mathrm{cm}^3\,\mathrm{s}^{-1}}{\langle \sigma v \rangle} \tag{1.6}$$

where $\langle \sigma v \rangle$ is the thermal average of the total annihilation cross section of the particle multiplied by velocity. We see that a weak scale cross section for those hypothetical particles would naturally give the approximately correct relic density.

1.3 Direct Detection

If most of the dark matter energy density of the universe is due to WIMPs, and galactic WIMPs are responsible for the observed behavior of rotation curves of spiral galaxies, then presumably our own galaxy is filled with WIMPs. It should thus be possible to detect them. If WIMPs could annihilate into Standard Model particles in the early universe, then they should also be able to be produced in accelerators, or indirectly detected, through their annihilation products, or directly detected, through their interactions with normal matter. For the remainder of the chapter we shall focus on the direct detection of WIMPs. First, on the calculation of their expected interaction rates and the energy spectrum of recoils they would produce, and finally on the detection strategies employed by direct detection experiments.

1.3.1 Interaction Rates and Recoil Spectra

WIMPs are expected to interact primarily with atomic nuclei, and since they are non-relativistic, the most likely interaction is elastic scattering. In this section we use the results of Jungman *et al.* (1996) and those of Lewin and Smith (1996) where needed. If the Earth is moving through the galactic halo a large number of WIMPs are expected to pass through any terrestrial detector. The rate of interactions per unit mass of the detection medium should go as $R \approx n_\chi \sigma \left\langle v \right\rangle / m_N$, where n_χ is the local WIMP number density, σ its elastic scattering cross section on normal matter, $\langle v \rangle$ the average WIMP velocity with respect to the target, and m_N the nucleus mass of the target. Defining m_χ as the mass of the WIMP particles and ρ_0 as the local WIMP energy density,

$$R \approx \frac{\rho_0 \sigma \langle v \rangle}{m_\chi m_N}. \tag{1.7}$$

The differential rate per unit energy transfered, per unit mass, for an energy Q transfered to the target nucleus can be written as

$$\frac{dR}{dQ} = \frac{\rho_0 \sigma_0}{\pi^{1/2} v_0 m_\chi m_r^2} F^2(Q)\, T(Q) \tag{1.8}$$

where σ_0 is the zero-momentum transfer cross section and $F(Q)$ is a form factor correction due to the finite size of the nucleus, which depends on the energy transfered and on the nuclear radius, $T(Q)$ is a WIMP velocity dependent factor, m_r is the WIMP-nucleus reduced mass $m_r = m_\chi m_N / \left(m_\chi + m_N\right)$ and v_0 is the circular velocity of the Sun around the galactic center. The WIMP velocity factor is given by

$$T(Q) = \frac{\pi^{1/2}}{2k} v_0 \int d\Omega \int_{v_{\rm min}}^{v_{\rm esc}} v f(\mathbf{v}, \mathbf{v}_E)\, d^3 v \tag{1.9}$$

where $f(\mathbf{v}, \mathbf{v}_E)$ is the WIMP velocity distribution, with $\mathbf{v}$ the WIMP velocity relative to the target and $\mathbf{v}_E$ the Earth velocity in the rest frame of the galaxy, $v_{\rm min} = \sqrt{Q m_N / \left(2 m_r^2\right)}$ is the minimum WIMP velocity that can produce a recoil of energy Q, $v_{\rm esc}$ is the galactic

WIMP escape velocity, and k a normalization factor

$$k = \int d\Omega \int_{v_{\min}}^{v_{\rm esc}} f(\mathbf{v}, \mathbf{v}_E)\, d^3v. \tag{1.10}$$

Assuming a WIMP Maxwellian halo,

$$f(\mathbf{v}, \mathbf{v}_E) = \exp\left[-\frac{(\mathbf{v}+\mathbf{v}_E)^2}{v_0^2}\right] \tag{1.11}$$

one obtains the normalization factor k as

$$k = \left(\pi v_o^2\right)^{3/2}\left[\mathrm{erf}\left(\frac{v_{\rm esc}}{v_0}\right) - \frac{2}{\pi^{1/2}}\frac{v_{\rm esc}}{v_0}\exp\left(-\frac{v_{\rm esc}^2}{v_0^2}\right)\right] \tag{1.12}$$

and a WIMP velocity factor of

$$T(Q) = \frac{1}{k}\left\{\frac{\pi^{1/2}}{4}\frac{v_{\rm esc}}{v_0}\left[\mathrm{erf}\left(\frac{v_{\min}+v_E}{v_0}\right) - \mathrm{erf}\left(\frac{v_{\min}-v_E}{v_0}\right)\right] - \exp\left(-\frac{v_{\rm esc}^2}{v_0^2}\right)\right\}. \tag{1.13}$$

The Earth's velocity is parametrized as

$$v_e = v_0\left[1.05 + 0.07\cos\left(\frac{t-t_p}{1\,\mathrm{yr}}\right)\right] \tag{1.14}$$

with the phase t_p on June 2nd. This variation in the Earth's velocity due to its motion around the Sun induces an annual modulation in the rate. The WIMP-nucleus interaction is the sum of a scalar interaction and a spin interaction. For spin-independent interactions the analytic Helm form factor is convenient

$$F(Q) = 3\frac{j_1(qr_n)}{qr_n}e^{-(qs)^2/2} \tag{1.15}$$

with $q = \sqrt{2m_N Q}$ the momentum transfer, $j_1(qr_n)$ the spherical Bessel function of the first kind, $s \sim 0.9\,\mathrm{fm}$, and r_n the nuclear radius, which can approximated by

$$r_n = \sqrt{\left(1.23A^{1/3} - 0.6\right)^2 + \tfrac{7}{3}\left[\pi^2 \cdot 0.52^2 - 5 \cdot 0.9^2\right]}\,\mathrm{fm}. \tag{1.16}$$

The expected differential recoil spectra from WIMP-nucleon spin-independent scattering rate on xenon, argon, germanium and silicon is shown in Fig. 1.6.

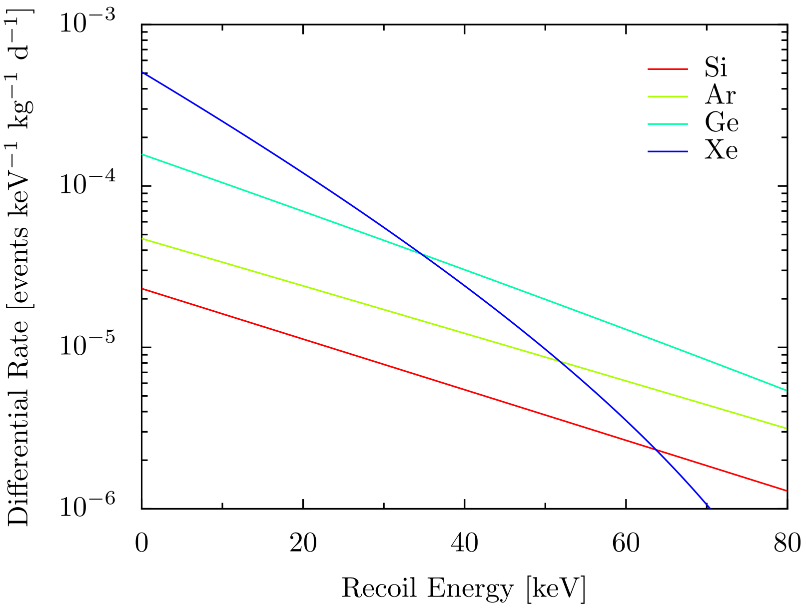

Figure 1.6: Expected differential recoil spectra from WIMP-nucleon scattering in different target materials, for a WIMP mass $m_\chi = 100\,\text{GeV}$, and a WIMP-nucleon spin-independent cross section of $\sigma_{\chi N} = 1 \times 10^{-44}\,\text{cm}^2$.

1.3.2 Detection Strategies

From the properties of WIMPs and the expected interaction rates in normal matter it is possible to identify the characteristics required of an instrument aiming at the detection of the scattering of WIMPs in its target volume. The detector should have a very low threshold (~10 keV) for the detection of nuclear recoils, as the expected exponential spectrum of recoil energies translates into a large sensitivity increase with reduced thresholds. Given the extremely low interaction rates expected, the detector should have a very low radioactive background, especially at low energies. If the detector is capable of discriminating between nuclear recoils and electronic recoils this will constitute a clear advantage since the most predominant background, electronic recoils from γ rays and β decays, will be rejected. Fast neutrons, which can produce low energy nuclear recoils, are then the ultimate background remaining. Finally, if the detector can measure an expected feature of WIMP interactions with normal matter, such as the annual modulation of the rate, the anisotropy of the nuclear recoil directions, or the rate dependence on the target material, then this will also constitute a clearer signature.

In general, when depositing energy in a material, particle interactions can produce three types of elementary excitations, ionization, phonons, and, in certain materials, scintillation photons. Detectors can be based on the measurement of the energy of nuclear recoils from a single excitation channel, like Ge diodes, which use the ionization channel, or scintillators coupled with photomultiplier tubes (PMTs), which use the scintillation channel. Most detectors that can differentiate nuclear recoils from electronic recoils do so by the simultaneous measurement of two excitation channels. The basis for discrimination usually arises from the fact that slow nuclear recoils are in general not as efficient as fast electrons in producing ionization.

Fig. 1.7 shows representatives of past and present WIMP direct detection experiments from each of the six possible classes of single-channel and dual-channel excitations measured. In the next sections we briefly describe the operation and recent results of experiments belonging to some of these classes. We will focus on the different detection strategies instead of trying to cover the large number of experiments aiming at detecting dark matter interactions.

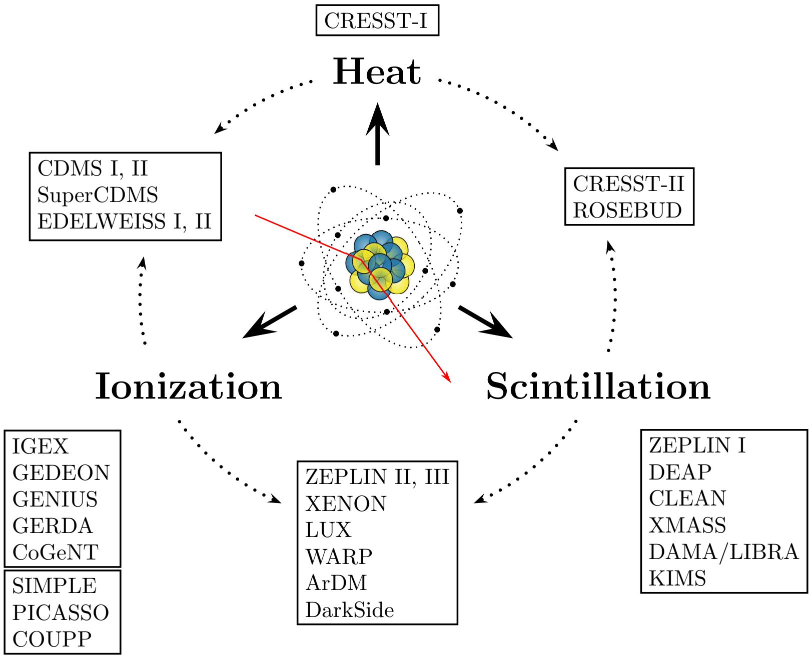

Figure 1.7: Past and present WIMP direct detection experiments classified according to the excitation channels measured.

1.3.3 Annual Modulation Signature

As mentioned earlier, one possible signature of the scattering of WIMPs in terrestrial detectors is an annual modulation of the WIMP-induced nuclear recoil rate. The DAMA/LIBRA experiment, a successor of the DAMA/NaI experiment, uses 232.8 kg of radiopure thallium-doped sodium iodide scintillators to search for such an annual modulation. In fact, the DAMA collaboration had reported the observation of an annual modulation signature and the DAMA/LIBRA experiment confirmed the result (Bernabei *et al.*, 2008). Fig. 1.8 shows the combined DAMA/NaI and DAMA/LIBRA modulation signal. This signal, however, has proven to be incompatible with null results from other experiments in the context of standard WIMP models (Aalseth *et al.*, 2008; Ahmed *et al.*, 2009; Angle *et al.*, 2008a; Behnke *et al.*, 2008; Lee *et al.*, 2007). There is still no satisfactory explanation for these conflicting experimental results but one element is clear, the possibility of backgrounds producing an annual modulation signature is not negligible.

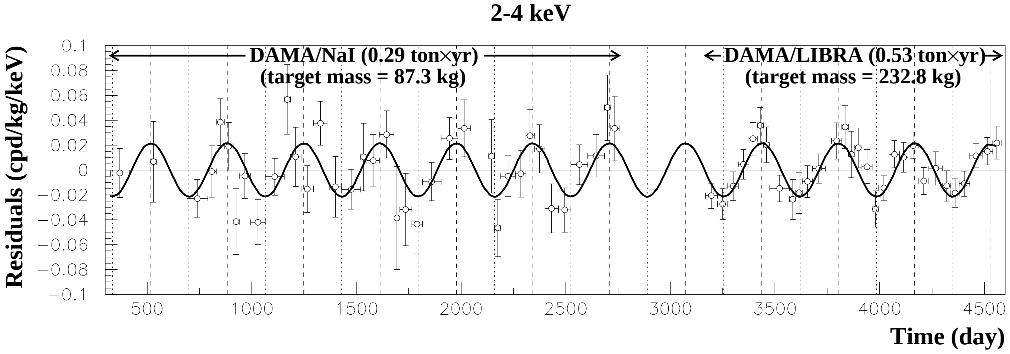

Figure 1.8: Annual modulation signature measured by the DAMA/NaI and DAMA/LIBRA experiments. Residual of the rate of single hit interactions in the 2-4 keV (points) along with a cosinusoidal function with a period of 1 year and a phase of 152.5 d, with the best-fit modulation amplitude of $0.0215 \pm 0.0026\,\mathrm{counts\,keV^{-1}\,kg^{-1}\,d^{-1}}$. Figure from Bernabei *et al.* (2008).

1.3.4 Cryogenic Detectors

Cryogenic detectors employ a variety of target materials and read-outs to measure precisely the recoil energy and, in the case of dual excitation channel detectors, to discriminate nuclear recoils from electronic recoils.

Ionization Phonon Detectors

Ionization phonon detectors measure both electronic excitations and thermal excitations induced by recoiling particles. CDMS uses an array of 30 high-purity Ge (HPGe) and Si cylindrical detectors with single crystal masses of 250 g and 100 g, respectively. Four athermal phonon sensors are used to measure the recoil energy and position of events within the crystal. The ionization signal is measured with two concentric charge electrodes. The outer ring is used to reject events that occur near the edge of the crystal. The ratio of ionization to recoil energy allows event-by-event rejection of electronic recoils to up to one in 10^4. However, events occurring near the surface of the crystal can be misidentified as nuclear recoils due to incomplete charge collection. The rise-time of phonon pulses is used to reject such events, resulting in a rejection better than 10^6 (Ahmed *et al.*, 2009). Fig. 1.9 shows a calibration with a ^{252}Cf neutron source. The upper band is due to electronic recoils from γ rays while the lower band is from neutron-induced nuclear recoils. Other experiments which belong to this class of detectors are the EIDELWEISS (Armengaud *et al.*, 2011), and the future SuperCDMS (Akerib *et al.*, 2006b) experiment. With their excellent energy resolution and electronic recoil discrimination, ionization phonon detectors have for a long time set the most stringent limits on WIMP-nucleon interactions (Akerib *et al.*, 2004, 2006a). Recently, an alternative class of detectors, liquid noble gas detectors, with their very low backgrounds and large target masses, has come to the forefront of direct dark matter detection.

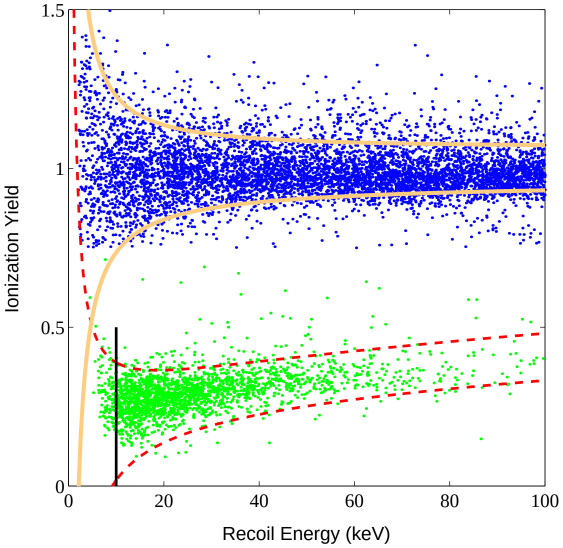

Figure 1.9: Ionization yield as a function of recoil energy for calibration data with a ^{252}Cf neutron source showing the discrimination power of the CDMS detector. The upper band is due to electronic recoils from γ rays while the lower band is from neutron-induced nuclear recoils. Figure from Akerib *et al.* (2004).

Scintillation Phonon Detectors

The CRESST II (Angloher *et al.*, 2009; Bravin *et al.*, 2000) and ROSEBUD (Cebrián *et al.*, 2001) experiments use an ingenious technique to measure the scintillation signal from crystals at cryogenic temperatures, $CaWO_4$ in the case of CRESST II, where conventional techniques such as PMTs cannot be used. The scintillation signal is read by a separate phonon sensor attached to a thin Si or Ge wafer. The target material is enclosed in a reflective film to increase the light collection efficiency of the light detector. Scintillation phonon detectors measure the recoil energy with the phonon signal and use the light yield to distinguish the recoiling particles. However, the discrimination power is strongly affected by the statistical fluctuations in the number of emitted scintillation photons. The efficient rejection of surface backgrounds is currently not possible with such detectors.

Ionization Detectors

Single-channel excitation ionization detectors are also used in the search for dark matter, abandoning the capability to discriminate nuclear recoils from electronic recoils but achieving ultra-low sub-keV energy thresholds. The CoGeNT collaboration, using a 475 g Ge crystal specially equipped with a point-like electrode (p-type point-contact HPGe) and loise-noise FET that results in very good energy resolution and ultra-low energy threshold (~0.4 keV), have recently observed a signal that could be interpreted as the scattering of low-mass WIMPs (Aalseth *et al.*, 2011a) in their detector, and later an annual modulation signature (Aalseth *et al.*, 2011b). Whether this is due to an unknown background or truly attributable to recoils from low-mass WIMPs is not clear. This detector technology has a surface background rejection capability but its power starts to reach its limits at these low energies ($\lesssim 2\,\mathrm{keV}$).

1.3.5 Liquid Noble Gas Detectors

Liquid noble gas detectors employ a different strategy for background reduction, the self-shielding of the target material. Large homogeneous volumes can be instrumented with PMTs to measure the scintillation excitation, of LXe or liquid argon (LAr) for example, and, in the case of ionization scintillation detectors, an electric field is applied across the volume to additionally measure the ionization. The ratio of ionization to scintillation can then be used to discriminate between electronic recoils and nuclear recoils. The high atomic number and the large density, especially of LXe, make the inner volume of these targets virtually free of electromagnetic backgrounds. The ability to reconstruct the position of events within the target volume is crucial to the background reduction through self-shielding.

Ionization Scintillation Dual-Phase Detectors

Dual-phase ionization scintillation liquid noble gas detectors measure both the prompt scintillation light, emitted as a particle recoils in the liquid target, and the ionization electrons produced, via the proportional scintillation light emitted as they are accelerated in the gas phase. These detectors are often called time projection chambers (TPCs) in an analogy with traditional gas TPCs since they can measure the 3D position of interactions within their volume. Fig. 1.10 depicts the measurement principle of a dual-phase xenon detector.

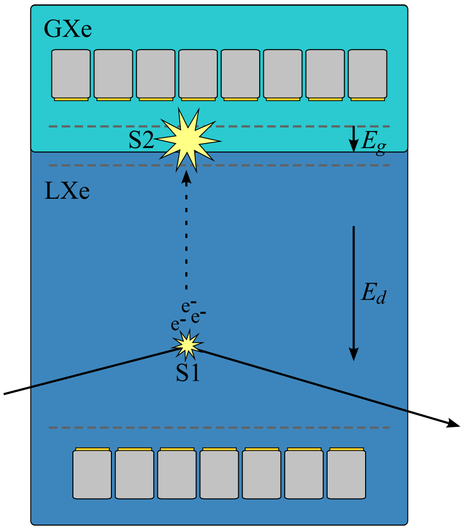

Figure 1.10: Measurement principle of a dual-phase xenon ionization scintillation detector.

When a particle interacts within the LXe active volume both scintillation photons and ionization electrons are created at the interaction site. The applied electric field, E_d, drifts the ionization electrons to the surface of the liquid and a stronger electric field, E_g, extracts the electrons into the gas phase. Scintillation photons are emitted as the electrons are accelerated in this high field region, with a total number proportional to the number of ionization electrons. Two arrays of PMTs, one immersed in the liquid and one above the liquid level, are used to detect both the prompt scintillation signal, called the S1 signal, and the proportional scintillation signal, called the S2 signal. The time difference between the S1 and the S2 signal is used to measure the depth coordinate while the distribution of the S2 signal on PMTs of the top array provides a way to reconstruct the xy position in the transverse plane. As mentioned earlier, this 3D localization of interactions results in an excellent background rejection capability, as most external backgrounds will generally interact in the outer layers of the target volume. The second background reduction strategy is the discrimination of nuclear recoils from electronic recoils through the ratio of the ionization signal to the scintillation signal, with a discrimination power at the ~99.5% level at low energies.

The XENON10 experiment was the first liquid noble gas detector to reach and surpass the sensitivity of the CDMS experiment at the time (Angle *et al.*, 2008a). The considerable background reduction from the self-shielding of LXe, the low energy threshold, and the appreciable discrimination down to low recoil energies all contributed to the impressive result. The successful operation of the XENON10 detector has lead to a rapid increase in scale and to the next phase of the program, the XENON100 detector, with a 62 kg target mass. The design and the construction of the XENON100 detector is the subject of Chap. 3, the calibration described in Chap. 4, and the results from a 100 live days run are presented in Chap. 6. Other LXe based dual-phase detectors include the ZEPLIN II and ZEPLIN III detectors, which obtained competitive results (Alner *et al.*, 2007; Lebedenko *et al.*, 2009b), and the LUX detector (McKinsey *et al.*, 2010), a 300 kg LXe TPC, currently being deployed at the surface facility of the future Deep Underground Science and Engineering Laboratory (DUSEL) at the Homestake mine, in South Dakota.

Dual-phase LAr ionization scintillation detectors have an additional discrimination tool at their disposal. The primary scintillation signal of LAr allows pulse shape discrimination (PSD) techniques to distinguish electronic recoils from nuclear recoils down to nuclear recoil energies of ~50 keV with a rejection power of ~10^6 (Lippincott *et al.*, 2008). This additional discrimination power is required however to suppress the large background (~1 Bq/kg) due to ^{39}Ar, a β emitter, present in atmospheric Ar. So far, the only LAr detector having set a competitive WIMP-nucleon scattering cross section limit (Benetti *et al.*, 2008) is a 2.3 l (3.2 kg) detector operated by the WArP collaboration. The next generation experiment, with an active volume of 100 l (140 kg), is in the commissioning phase. The ArDM (Laffranchi *et al.*, 2007) and the DarkSide (Alton *et al.*, 2011) experiments are two additional experiments that use LAr dual-phase TPCs. The main distinguishing features of the ArDm experiment is the use of large electron multipliers (LEM) plates for the amplification of the ionization signal in the gas phase and the generation of the high-voltage required for the drift field via a Greinacher voltage doubler circuit in the LAr volume. The DarkSide-50 detector, with a 50 kg active target, is currently in the construction stage and will employ Ar from underground sources, shielded from cosmogenic activity and hence depleted in the ^{39}Ar isotope, low-background photodetectors, and a boron-loaded scintillator active veto.

Single-Phase Detectors

Single-phase detectors push the self-shielding background discrimination capability of condensed noble gases to achieve extremely low event rates by building very large volume detectors. The XMASS800 detector (Abe *et al.*, 2008), currently in operation at the Kamioka mine, has a spherical geometry surrounded by photodetectors, and contains 800 kg of LXe. The event localization relies solely on the distribution of the LXe scintillation light on the PMTs. The DEAP (Boulay and Hime, 2006) and CLEAN (Horowitz *et al.*, 2003) experiments are two other experiments which will employ large single-phase LAr and liquid neon targets, respectively. The LAr PSD capability is expected to provide a large enough reduction of the electronic recoil backgrounds.

1.3.6 Superheated Liquid Detectors

Another category of WIMP detectors, superheated liquid detectors, employs a very different strategy than the self-shielding of liquid noble gas detectors to suppress backgrounds: the threshold of bubble nucleation to reject energy deposits with low ionizing density. The operating pressure and temperature of such detectors can be set so that they are completely insensitive to electronic recoils. The bubbles created by nuclear recoils can be detected optically or acoustically. The PICASSO (Archambault *et al.*, 2009), SIMPLE (Girard *et al.*, 2005), and COUPP (Behnke *et al.*, 2008) experiments are based on this background rejection principle.

1.3.7 Directional Detectors

Directional WIMP detectors belong in a separate category as they would probably provide the most convincing evidence that the detected particles constitute the galactic dark matter, considering the difficulty for a terrestrial background to reproduce this signature. The basic assumption of the directional signature is that our sun has a finite orbital velocity with respect to the WIMP velocity distribution in the galactic halo. This means that a directional detector in the solar system would experience a WIMP "wind" from the direction of our motion in the galaxy (Spergel, 1988). Nuclear recoils induced should preferentially point to particles coming from that direction and show a strong diurnal asymmetry due to the Earth rotation. Given the difficulties in measuring the orientation of WIMP-induced nuclear recoil tracks with $\lesssim 100\,\text{nm}$ range in solids or liquids, the detector technology employed is that of low pressure ($\lesssim 100\,\text{Torr}$) gas TPCs. The extremely challenging problem of building a sizable target mass detector with 3D directional sensitivity to low-energy nuclear recoil tracks has meant that directional detection experiments have remained mostly in the research and development phase so far, although great progress has been achieved in the last decade. The DRIFT (Alner *et al.*, 2005), NEWAGE (Nishimura *et al.*, 2009), MIMAC (Moulin *et al.*, 2005), and DMTPC (Battat *et al.*, 2010) experiments are the main current directional detection experiments.

Chapter 2

Liquid Xenon as Detection Medium

In this chapter we will present the properties of LXe related to the detection of radiation, more specifically the properties related to the conversion of the energy absorbed into signal carriers that can be measured. We will also discuss the properties of LXe that make it a well suited medium for the detection of rare events and the concepts needed to detect nuclear recoils and discriminate them from backgrounds in large scale LXe TPCs.

In Sec. 2.1 the physical properties of LXe and those related to the detection of radiation are listed while in Sec. 2.2 the interactions and energy loss of different types of ionizing radiation are discussed. Sec. 2.3 and 2.4 discuss the scintillation and ionization signals of LXe, and Sec. 2.5 lists the different energy scale definitions employed to characterize interactions in LXe detectors that measure both of those signals.

2.1 Properties

Xenon is the heaviest non-radioactive element of the noble gases and is present in concentrations of ~0.1 ppm in the Earth's atmosphere. Xenon is obtained as a byproduct of the liquefaction of air and its separation into oxygen and nitrogen. The resulting liquid oxygen mixture contains both krypton and xenon, which can be extracted from it by fractional distillation. The last stage is the extraction of xenon from the krypton/xenon mixture by distillation. Xenon costs about 1000$/kg, much more than other noble gases, due to its rarity.

Nine[1] stable isotopes of Xe exist in nature. This makes Xe the element with the second largest number of stable isotopes, tin is the first with ten stable isotopes. Xe also does not have any long-lived radioisotopes, the longest-lived being ^{127}Xe with a half-life of 36.3 d. This makes Xe an attractive detection medium for rare searches since it has essentially no intrinsic radioactivity from naturally occurring Xe isotopes. Of the nine stable isotopes, two have non-zero nuclear spins, ^{129}Xe and ^{131}Xe, and can thus be used to probe spin-dependent interactions of dark matter particles.

One of the most important characteristics of a material for the detection of radiation is its capacity to transform the energy absorbed into measurable signals. In this respect LXe is also a very attractive material as both scintillation photons and ionization electrons are produced in response to ionizing radiation. LXe is a very efficient scintillator with a yield of ~45×10^3 photons/MeV for relativistic electrons and is also transparent to its own scintillation light, due the mechanism responsible for the scintillation process (Sec. 2.3). The high mobility of ionization electrons in LXe also means that charge signals can be drifted through the homogeneous volume under an external electric field and measured.

Tab. 2.1 lists some physical properties of Xe and Tab. 2.3 some properties of LXe related to particle detection.

Table 2.1: Physical properties of xenon.

Property	Value
Atomic number, Z	54
Molar mass	$131.29\,\mathrm{g\,mol^{-1}}$
Isotopic abundances	^{124}Xe (0.095%), ^{126}Xe (0.089%), ^{128}Xe (1.91%) ^{129}Xe (26.4%), ^{130}Xe (4.07%), ^{131}Xe (21.2%) ^{132}Xe (26.9%), ^{134}Xe (10.4%), ^{136}Xe (8.86%)
Gas density (273 K, 1 atm)	$5.8971\,\mathrm{g\,L^{-1}}$
Liquid density (165.05 K, 1 atm)	$3.057\,\mathrm{g\,cm^{-3}}$
Melting point, (1 atm)	161.4 K
Boiling point, (1 atm)	163.05 K
Triple point	161.31 K, 0.805 atm, $3.08\,\mathrm{g\,cm^{-3}}$
Critical point	289.74 K, 57.65 atm, $1.155\,\mathrm{g\,cm^{-3}}$
Latent heat of fusion	$17.29\,\mathrm{kJ\,kg^{-1}}$

---

[1] Strictly speaking, this is not entirely true with the recent observation of the two-neutrino double-beta decay of ^{136}Xe (Ackerman *et al.*, 2011). However, with a half-life 10^{21} yr this is an extremely rare process.

Table 2.2: Physical properties of xenon (continued).

Property	Value
Thermal properties	
Heat conductivity (gas, 273 K, 1 atm), λ	$5.192\,\mathrm{mW\,m^{-1}\,K^{-1}}$
Heat conductivity (liquid, 178 K), λ	$71.1\,\mathrm{mW\,m^{-1}\,K^{-1}}$
Electrical properties	
Relative permittivity (gas), ϵ_r	1.00
Relative permittivity (liquid), ϵ_r	1.96[a]
Dielectric strength	$\gtrsim 400\,\mathrm{kV\,cm^{-1}}$[b]
Optical properties	
Refractive index (178 nm)	1.69[c]
Rayleigh scattering length (178 nm), $\lambda_{\mathrm{Rayleigh}}$	29 cm[d]

[a] Schmidt (2002)
[b] Jones and Kunhardt (1995)
[c] Solovov *et al.* (2004)
[d] Ishida *et al.* (1997)

Table 2.3: Table of properties of liquid xenon related to particle detection.

Property	Value
Avg. energy per electron-ion pair, W_{i}	15.6 eV[a]
Avg. energy per scintillation photon, W_{ph} (max)	13.8 eV[b]
Ratio of excitons to ionization $N_{\mathrm{ex}}/N_{\mathrm{i}}$	0.06[a]
Scintillation properties	
Scintillation wavelength, λ_s	178 nm[c]
Excimer singlet lifetime, τ_1	2.2 ns[d]
Excimer triplet lifetime, τ_3	27 ns[d]

[a] Takahashi *et al.* (1975)
[b] Doke *et al.* (2002)
[c] Jortner *et al.* (1965)
[c] Kubota *et al.* (1978b)

2.2 Energy Loss

As mentioned earlier, one of the most important characteristics of a material for the detection of radiation is its capacity to transform the energy absorbed into measurable signals, but also its ability to stop incident radiation. Interactions in general depend on the type of incident particle. Charged particles interact with matter through collisions with atomic electrons or with nuclei, mediated by electrostatic forces. In these interactions, charged particles ionize and excite Xe atoms, creating a track of free electrons and ionized atoms. At high velocities, energy loss can also occur through bremsstrahlung, however, its contribution is not significant at the energies we are interested in ($< 1\,\mathrm{MeV}$). Inelastic collisions with atomic electrons, which produce excitation and ionization, both included under the name of electronic excitation, are the dominant mechanism for energy loss of electrons and α particles in LXe. Non-relativistic heavy charged particles, such as a recoiling nuclei, in addition, loose a substantial amount of energy through elastic collisions with atomic nuclei. In LXe, since the measurable signals come from electronic excitation this leads to a quenching of the signal (nuclear quenching).

In the track, excited atoms, or "excitons", rapidly form excited dimers, or "excimers", which subsequently decay and emit scintillation photons. Unless an electric field is applied, ionization electrons will recombine and also form excimers which eventually leads to the production of scintillation photons (see Sec. 2.3). Scintillation photons are thus produced both from direct excitation and from ionization. Strong evidence for this comes from the observation that a higher electric field reduces the scintillation signal, by reducing the fraction of electrons that recombine (Kubota *et al.*, 1978b). Even without the application of an external electric field some electrons might escape recombination in a timescale useful for the collection of signals if they thermalize too far from their parent ion (Doke *et al.*, 1988).

The efficiency of the conversion of absorbed energy into measurable signals is often characterized by the average energy required to produce an electron-ion pair, the W-value, W_{i}, and the average energy required to produce a scintillation photon, W_{ph}. For LXe W_{i} is 15.6 eV. The value of W_{i} is larger than the ionization energy of Xe because of other mechanisms by which the particle loses energy which do not produce ionization, excitation for example, as we mentioned before. If one assumes that recombination is complete and that one exciton produces one scintillation photon and that one recombined electron-ion pair produces one scintillation photon, then W_{ph} can be written as

$$W_{\mathrm{ph}} = E/\left(N_{\mathrm{i}} + N_{\mathrm{ex}}\right) = W_{\mathrm{i}}/\left(1 + N_{\mathrm{ex}}/N_{\mathrm{i}}\right) \tag{2.1}$$

where N_{i} and N_{ex} are the number of electron-ion pairs and excitons, respectively, produced by a recoil of energy E, and where we have used the definition $W_{\mathrm{i}} = E/N_{\mathrm{i}}$. The ratio of excitons to electron-ion pairs in LXe is estimated to be $N_{\mathrm{ex}}/N_{\mathrm{i}} \approx 0.06$ from a calculation based on oscillator strengths of solid Xe obtained from absorption spectra (Takahashi *et al.*, 1975). A higher bound of 0.20 on $N_{\mathrm{ex}}/N_{\mathrm{i}}$ was obtained by Doke *et al.* (2002) which lead them to estimate the W_{ph} value that leads to the maximum scintillation yield in LXe as $W_{\mathrm{ph}}(\mathrm{max}) = 13.8 \pm 0.9\,\mathrm{eV}$.

2.2.1 Electronic Stopping Power

As the measurable signals in Xe come from electronic excitation one quantity of interest is the stopping power of LXe from electronic interactions. Fig. 2.1 shows the electronic stopping power of Xe for electrons, α particles, and nuclear recoils in Xe. Since the stopping power for electrons increases with decreasing energy below 1 MeV the tracks of electronic recoils will tend to exhibit a higher ionization and excitation density near the end of the track. In contrast, nuclear recoils will tend to exhibit a higher ionization and excitation density at the beginning of the track. At the energies of interest for dark matter searches, nuclear recoils have a higher ionization density than electronic recoils. As the recombination probability is expected to increase with ionization density one then expects that nuclear recoils should suffer less reduction of their scintillation signal as the electric field is increased than electronic recoils, something that is indeed observed (Sec. 2.4.3).

The large stopping power of LXe, partly due to its high density, is a valuable quality for a detection medium. It means that particles can be stopped efficiently and that an inner volume with a very low interaction rate can be obtained in the center of the target. This is often referred to as the self-shielding property of LXe targets since the detection medium itself can act as a shield from external radiation. This inner volume is usually called a fiducial volume since it is a volume that will exclude most of the background interactions. Electronic recoils at the energies relevant for dark matter searches ($< 100\,\mathrm{keV}$) have tracks

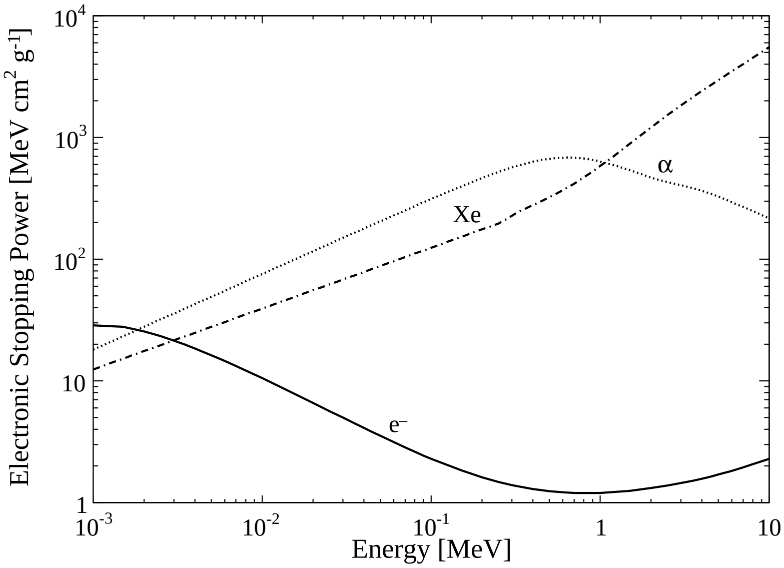

Figure 2.1: Electronic stopping power for electrons (Berger *et al.*, 2005b), for alpha particles (Berger *et al.*, 2005a), and for nuclear recoils (Ziegler, 2011) in Xe.

that spread over less than ~10 μm and can thus be considered essentially point like. External α and β emitters thus do not contribute to the background rate inside the fiducial volume. External γ ray emitters however will contribute, as we will see in the next section.

2.2.2 X-ray and γ Interactions

X-rays and γ rays interact with matter through photoelectric absorption, Compton scattering, or pair production. In these three processes energetic electrons (and positrons in the case of pair production) are produced and will lose energy through electronic excitation and produce excitons and electron-ion pairs. In the case of Compton scattering the scattered γ ray can continue its path and produce other energetic electrons via subsequent interactions.

Fig. 2.2 shows the total, photoelectric absorption, Compton scattering, and pair production γ ray mass attenuation coefficients in Xe, as a function of energy. The right axis indicates the attenuation length in LXe, using a density of $2.86\,\mathrm{g\,cm^{-3}}$. Below 300 keV the dominant interaction is photoelectric absorption while above it is Compton scattering. The attenuation length at 300 keV is ~2 cm and ~6 cm at 1 MeV. From this we can deduce that the main external background producing electronic recoils in the energy region of interest for dark matter searches will come mainly from low-energy single Compton scatters. Most external low-energy γ rays are absorbed in the outer layers of the detection medium and do

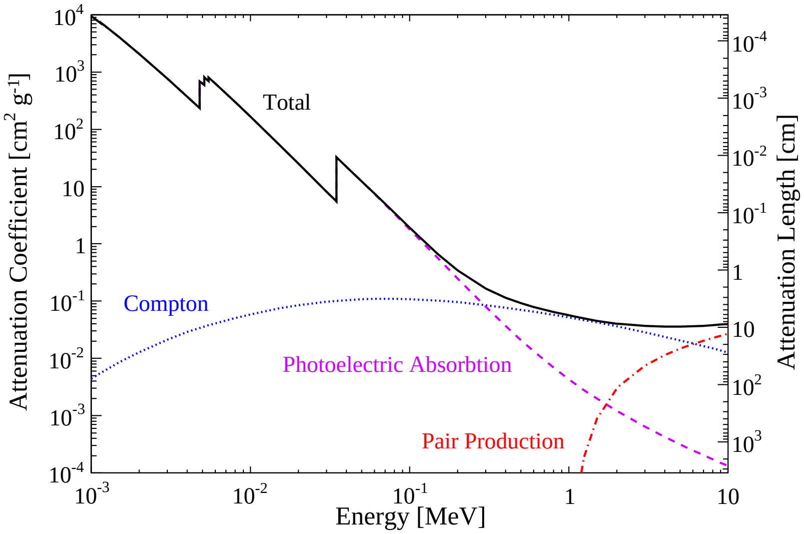

Figure 2.2: Total (solid black), photoelectric absorption (dashed violet), Compton scattering (dotted blue), and pair production (dash-dotted red) γ ray mass attenuation coefficients in Xe, as a function of energy. The right axis indicates the attenuation length in LXe, using a density of 2.86 g cm^{-3}. Data from the XCOM database (Berger *et al.*, 2010).

not reach the fiducial volume.

2.2.3 Neutron Interactions

Neutron interactions in LXe vary depending on the neutron energy. Fast neutrons interact primarily through elastic scattering with Xe nuclei and therefore produce nuclear recoils. At MeV energies inelastic interactions start to play a role. The most likely inelastic interactions are reactions of the type $^{A}\mathrm{Xe}(n,n')^{A}\mathrm{Xe}$ which leave the nucleus in an excited state that decays with the emission of a γ ray, usually a short time afterwards ($\lesssim$ 1 ns). In some instances, ^{129}Xe and ^{131}Xe, the excited state is so long-lived that it is called a metastable state and decays can be observed several days after the neutron irradiation. At neutron energies of 100 keV and lower, interactions consist of elastic scattering and radiative capture, $^{A}\mathrm{Xe}(n,\gamma)^{A+1}\mathrm{Xe}$. At these energies, most elastic scatters will not produce nuclear recoils that can be measured. Tab. 2.4 lists the most likely inelastic interactions with production of low-energy γ rays. Fig. 2.3 shows the neutron total elastic scattering, total inelastic scattering and radiative capture cross sections on Xe as a function of energy.

Neutron interactions that produce low-energy γ rays are useful to calibrate large volume LXe detectors. Since low-energy γ rays cannot penetrate the volume (a good thing since

Table 2.4: Table of the most likely inelastic interactions with production of low-energy γ rays for neutrons on Xe. Data from the ENDF/B-VII.0 database (Chadwick *et al.*, 2006).

Reaction	Cross Section[a] (barns)	Decay Half Life	γ Energy (keV)
$^{129}\mathrm{Xe}(n,n')^{129}\mathrm{Xe}$	0.28	0.97 ns	39.58
$^{131}\mathrm{Xe}(n,n')^{131}\mathrm{Xe}$	0.15	0.48 ns	80.19
$^{129}\mathrm{Xe}(n,n')^{129m}\mathrm{Xe}$	0.011	8.88 d	236.14
$^{131}\mathrm{Xe}(n,n')^{131m}\mathrm{Xe}$	0.054	11.84 d	163.93

[a] Cross section at 1 MeV.

it means the background from external sources is low) and since higher energy γ rays will usually interact at multiple locations and much more near the surface of the volume, neutrons can penetrate deeper and allow a more uniform γ source distribution.

Neutron inelastic interactions do not constitute a background for a dark matter search as the γ ray accompanying the nuclear recoil very likely pushes the energy of the event far from the region of interest. Neutron elastic interactions, however, constitute an irreducible background and precautions must be taken to reduce their occurrence as much as possible. The neutron elastic scattering mean free path ranges from ~13 cm at 100 keV up to ~20 cm at 10 MeV. Fortunately, fast neutrons are thus likely to scatter multiple times in larger scale detectors and hence be rejected as a background. At the current scale of LXe detectors (~30 cm) the single to multiple ratio is such that the rejection efficiency has not yet reach an extremely useful level. Consequently, detector materials have to be chosen such that their neutron production rates, through (α, n) reactions or spontaneous fission, yield much less than one neutron interaction in the energy range of interest during a dark matter search.

2.3 Scintillation Signal

As mentioned earlier, a recoiling particle in LXe will create a track of excited Xe atoms or “free” excitons, Xe*, and electron-ion pairs, Xe$^+ + e^-$. The scintillation signal is produced after the creation of the excitons and the electron-ion pairs. Excitons can form excited molecular states, Xe$_2^*$, called excimers by colliding with neighbouring Xe atoms. Ionized

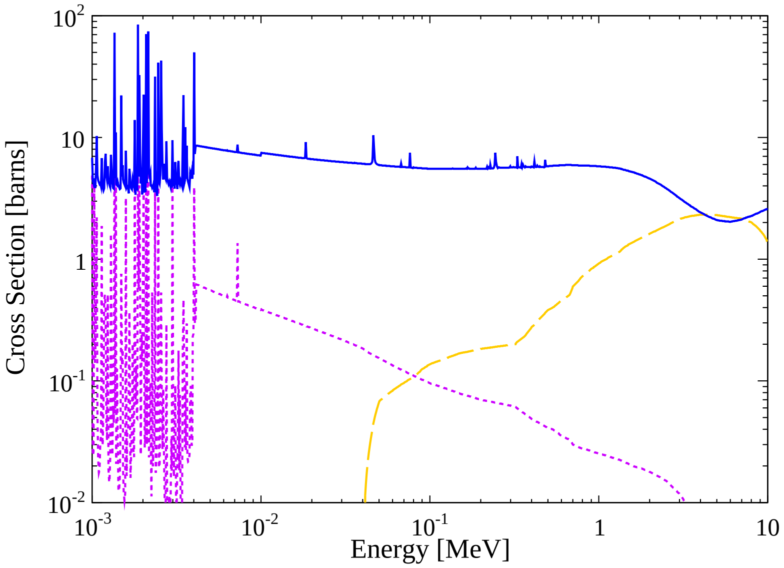

Figure 2.3: Neutron total elastic scattering (solid blue), total inelastic scattering (long dashed orange), and radiative capture (dashed violet) cross sections on Xe (Chadwick *et al.*, 2006).

atoms can also form excimers through the processes

$$\mathrm{Xe}^+ + \mathrm{Xe} \to \mathrm{Xe}_2^+, \tag{2.2}$$

$$\mathrm{Xe}_2^+ + e^- \to \mathrm{Xe}^{**} + \mathrm{Xe}, \tag{2.3}$$

$$\mathrm{Xe}^{**} \to \mathrm{Xe}^* + \mathrm{heat}, \tag{2.4}$$

$$\mathrm{Xe}^* + \mathrm{Xe} \to \mathrm{Xe}_2^*. \tag{2.5}$$

The excimers subsequently decay to the dissociative ground state and produce scintillation light

$$\mathrm{Xe}_2^* \to 2\mathrm{Xe} + h\nu. \tag{2.6}$$

The spectrum of LXe scintillation photons is in the vacuum ultraviolet range, centered at a wavelength of 178 nm, which corresponds to an energy of 7 eV, and with a width of 13 nm (Jortner *et al.*, 1965). The scintillation light has two components from the decay of the singlet and triplet states of the excimers. For relativistic electrons with an applied electric field, the singlet and triplet states have decay times of 2.2 and 27 ns (Kubota *et al.*, 1978a), respectively. This makes Xe one of the fastest scintillators. With no electric field applied the recombination time dominates and a single decay time of 45 ns is observed (Hitachi *et al.*, 1983). For α particles the decay times are 4.2 and 22 ns for the singlet and triplet states, respectively. The decay times depend only weekly on the ionization density but the ratio of singlet to triplet states is higher at higher ionization density.

In GXe, scintillation comes almost exclusively from direct excitation because the collision process that leads to recombination (Eq. 2.4) is not very likely. As mentioned earlier, in LXe the application of an external field reduces the scintillation signal as a large fraction of it comes from recombination. Even at zero field, however, some electrons do not recombine (in a timescale practical for their detection) and this is thought to be the explanation for the reduce light yield (see Sec. 2.3.1) at low values of linear energy transfer (LET), closely related to the electronic stopping power.

At high ionization densities an additional mechanism could play a role for the quenching of the scintillation light, as is observed for α particles for example. Since the scintillation decay times do not depend on ionization density, this suggests that the quenching occurs before the creation of the excitons (Hitachi, 2005). Hitachi proposed the “bi-excitonic” quenching mechanism

$$\mathrm{Xe}^* + \mathrm{Xe}^* \rightarrow \mathrm{Xe}_2^{**} \rightarrow \mathrm{Xe} + \mathrm{Xe}^+ + e^- \tag{2.7}$$

where two excitons collide and produce an electron-ion pair. The electron may later recombine and lead to the production of one scintillation photon. Two excitons, which would normally produce one scintillation photon each, end up producing only one. Since excitons need to collide into each other for this quenching to occur, this mechanism can only apply to very high LET tracks, such as α particles, fission fragments, and nuclear recoils. Fig. 2.4 shows schematically the processes we have discussed in this section.

2.3.1 Absolute Light Yield

As one realizes, there are many effects playing a role in the production and the potential reduction in the number of scintillation photons created by different types of ionizing radiation in LXe. An electric field can reduce the scintillation yield by reducing the recombination fraction, low ionization density tracks, such as those of electronic recoils, can have a reduced scintillation yield due to escape electrons, nuclear quenching reduces the scintillation yield of nuclear recoils through energy lost to atomic motion (Sec. 2.3.2), and high excitation density tracks can suffer electronic quenching via biexcitonic quenching for

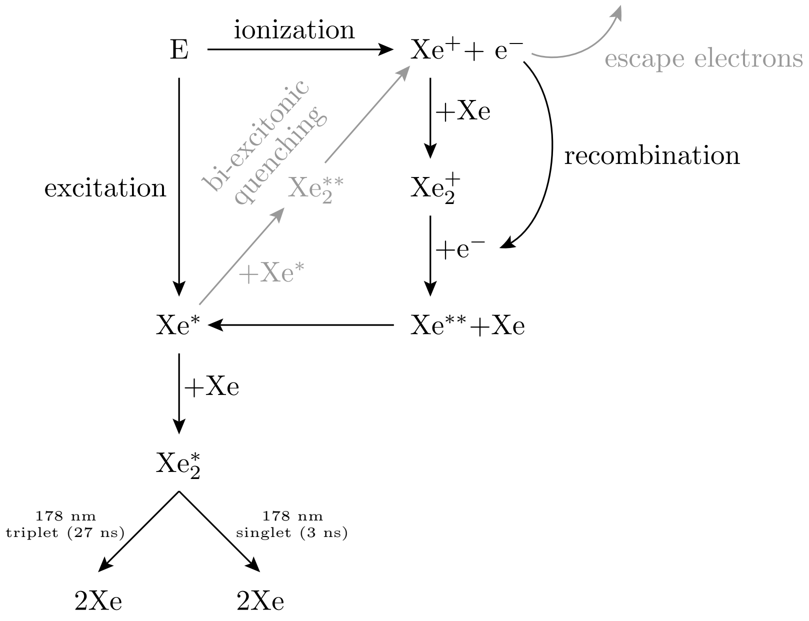

Figure 2.4: Scintillation mechanism in LXe (black) and different processes that can lead to the quenching of scintillation light (gray), as discussed in the text.

example.

Fig. 2.5 shows the LET dependence of the scintillation yield in LXe for various types of particles. At high LET a flat top response is observed for relativistic heavy ions (solid circles). At lower LET values, relativistic electrons (solid square) and electronic recoils from γ rays (open squares) are interpreted to have a reduced scintillation yield due to incomplete recombination (escape electrons) while the reduced scintillation yield of α particles, at higher LET, is attributed to biexcitonic quenching (Hitachi, 2005). From the simultaneous measurement of ionization and scintillation for 1 MeV electrons (solid square) and assuming full recombination and no biexcitonic quenching for relativistic heavy ions the maximum scintillation yield in LXe, or the average energy required to produce a scintillation photon, is estimated as $W_{\mathrm{ph}}(\mathrm{max}) = 13.8\,\mathrm{eV}$ (Doke *et al.*, 2002).

2.3.2 Lindhard Factor

As mentioned earlier, in contrast with recoiling electrons, which lose almost all of their energy through electronic excitation, recoiling nuclei transfer only a part of their energy to electronic excitation and the rest is lost to atomic motion. Lindhard calculated the total electronic energy loss in a nuclear recoil (Lindhard *et al.*, 1963). The Lindhard factor,

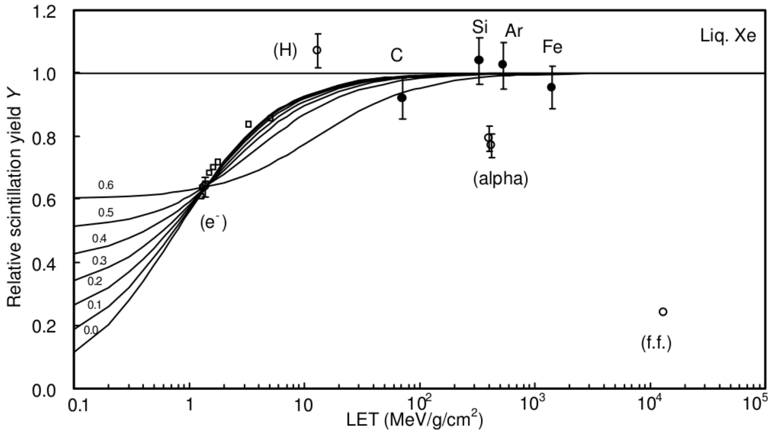

Figure 2.5: LET dependence of the scintillation yield for various types of particles in LXe. Relativistic heavy ions (solid circles) at high LET have a scintillation yield independent of LET and assumed to be the maximum scintillation yield in LXe. Relativistic electrons (solid square) and electronic recoils from γ rays (open squares) are interpreted to have a reduced scintillation yield due to the effect of escape electrons. The reduced scintillation yield of α particles is attributed to biexcitonic quenching (Hitachi, 2005). Figure from Doke *et al.* (2002).

$\mathcal{L}$, defined as the fraction of the recoil energy lost to electronic excitation is parametrized as (Lewin and Smith, 1996)

$$\mathcal{L} = \frac{kg(\epsilon)}{1 + kg(\epsilon)} \tag{2.8}$$

where

$$\epsilon = 11.5 E_r(\text{keV})\, Z^{-7/3}, \quad k = 0.133 Z^{2/3} A^{1/2}, \quad \text{and} \quad g(\epsilon) = 3\epsilon^{0.15} + 0.7\epsilon^{0.6} + \epsilon, \tag{2.9}$$

and provides an accurate prediction of the nuclear quenching of ionization signals in semiconductors (Chasman *et al.*, 1968; Jones and Kraner, 1975; Messous *et al.*, 1995). In LXe, nuclear quenching alone cannot explain the observed scintillation yield at low energies (Aprile *et al.*, 2005), but reasonable agreement can be obtained when electronic quenching is considered (Hitachi, 2005; Mei *et al.*, 2008). Recently, it has been suggested that if both the scintillation and ionization signals are included, the Lindhard prediction is compatible with the observed quenching (Sorensen and Dahl, 2011). The lower scintillation yield observed is attributed to a change in the fraction of energy that ultimately goes into ionization instead of scintillation. Experimenters usually do not measure the Lindhard factor directly but rather the relative scintillation efficiency of nuclear recoils, $\mathcal{L}_{\text{eff}}$, the subject of the next section.

2.3.3 Relative Scintillation Efficiency of Nuclear Recoils

As we previously discussed, the scintillation yield, defined as the number of photons produced per unit energy, depends on both the type of particle and the energy deposited. For historical reasons, the scintillation signal is most commonly used to measure the energy of a particle in LXe dark matter detectors. Since a precise measurement of the absolute scintillation yield is rather difficult, the relative scintillation efficiency of nuclear recoils, $\mathcal{L}_{\text{eff}}$, is the quantity that is used to convert the scintillation signals to nuclear recoil energies. $\mathcal{L}_{\text{eff}}$, an energy dependent quantity, is defined as the ratio of the scintillation yield of nuclear recoils to that of electronic recoils from photoabsorbed 122 keV γ rays from a ^{57}Co source, at zero electric field

$$\mathcal{L}_{\text{eff}}\left(E_{\text{nr}}\right) = \frac{L_{y,\text{nr}}\left(E_{\text{nr}}\right)}{L_{y,\text{er}}\left(E_{\text{er}} = 122\,\text{keV}\right)}, \tag{2.10}$$

where the subscripts "nr" and "er" refer to nuclear and electronic recoils. The 122 keV γ ray energy is used simply for convenience because ^{57}Co is a common calibration source.

Two methods have been used to measure $\mathcal{L}_{\text{eff}}$ at different energies, an indirect method with the full spectrum comparison of the simulated response to the measured response from the irradiation with a neutron source, and a direct method with monoenergetic neutron fixed-angle scatters. Indirect measurements (Horn *et al.*, 2011; Lebedenko *et al.*, 2009b; Sorensen *et al.*, 2009) infer the energy dependence of $\mathcal{L}_{\text{eff}}$ by comparing experimental data obtained with a neutron source and a Monte Carlo simulation of the expected nuclear recoil energy spectrum. By proceeding in this way, however, any neglected factors are absorbed in the energy dependence of $\mathcal{L}_{\text{eff}}$. Such factors can include uncertainties in the energy spectrum of the neutron source, efficiency losses near threshold, energy dependence of selection cuts, etc, and are typically difficult to measure precisely. Direct measurements (Akimov *et al.*, 2002; Aprile *et al.*, 2005, 2009; Arneodo *et al.*, 2000; Bernabei *et al.*, 2001; Chepel *et al.*, 2006; Manzur *et al.*, 2010) are performed by recording fixed-angle elastic scatters of monoenergetic neutrons tagged by organic liquid scintillator detectors. Direct measurements are typically less affected by systematic uncertainties and can provide a more accurate measurement of $\mathcal{L}_{\text{eff}}$. The recoil energy of the Xe nucleus is then entirely fixed by kinematics and, when

$M_{\mathrm{Xe}} \gg m_n$ and $E_n \ll m_n c^2$, is approximately given by

$$E_r \approx 2E_n \frac{m_n M_{\mathrm{Xe}}}{(m_n + M_{\mathrm{Xe}})^2} (1 - \cos\theta) \tag{2.11}$$

where E_n is the energy of the incoming neutron, m_n and M_{Xe} are the masses of the neutron and Xe nucleus, respectively, and θ is the scattering angle. The spread in measured recoil energies in direct measurements mostly comes from the energy spread of the neutron source and the angular acceptance of the LXe and neutron detectors due to their finite sizes. Fig. 2.6 shows a compilation of the measurements of $\mathcal{L}_{\mathrm{eff}}$, prior to 2011. There is considerable spread and disagreement in the different measurements, a sign that some unaccounted for systematic effects are probably present in some of the measurements. The measurement of $\mathcal{L}_{\mathrm{eff}}$ is the subject of Chap. 5.

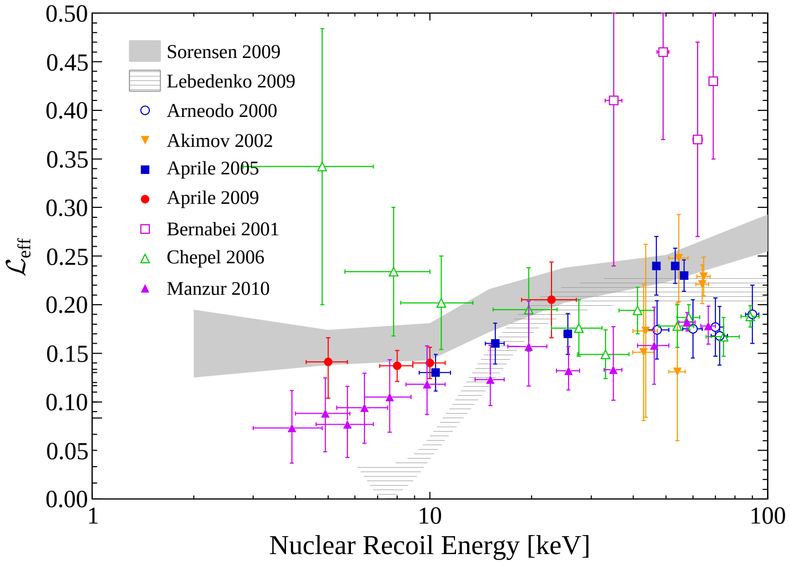

Figure 2.6: Measurements of the relative scintillation efficiency of nuclear recoils in LXe, prior to 2011.

Since dual-phase LXe detectors operate with an external electric field applied, the scintillation signal is quenched due to a reduction in the fraction of electrons that recombine. This is also an effect that depends on both the type of recoiling particle and the energy deposited, although the energy dependence appears very mild for nuclear recoils (Manzur *et al.*, 2010). The effect is incorporated in the reconstruction of the energy through the use of the field quenching factors of electronic and nuclear recoils, $S_{\mathrm{er}}(E)$ and $S_{\mathrm{nr}}(E)$, respectively, where E here refers to the electric field (see Sec. 2.5).

2.3.4 Absorption, Reflection, and Scattering

We now turn to processes that can affect the collection of the produced scintillation light in a LXe detector. LXe itself is transparent to its own scintillation light, as the absorption band of the free exciton is at a higher energy than the scintillation light energy (Schwenter *et al.*, 1985). However, even minuscule amounts of impurities can absorb a large fraction of the scintillation photons. Water is the most serious due to its high absorption cross section at 7 eV but oxygen can also contribute with an absorption cross section roughly a factor of ten lower. The effect of absorption is usually modelled with an exponential attenuation coefficient λ_{abs} for the scintillation light. The Rayleigh scattering length in LXe is also an important factor in the collection of scintillation light, especially for large volume detectors, because it increases the distance a photon has to travel before it reaches a photosensor, increasing the probability that it gets absorbed along the way. The Rayleigh scattering length was to be $\lambda_{\mathrm{Rayleigh}} = 29\,\mathrm{cm}$ in LXe (Ishida *et al.*, 1997).

The index of refraction of LXe being higher than that of GXe (see Tab. 2.1), the majority of the scintillation photons emitted below the liquid level, the direct scintillation light of dual-phase LXe detectors for example, will undergo total internal reflection at the liquid-gas interface. The inner surface of LXe detectors is often made of VUV reflecting materials that are employed to increase the scintillation light collection efficiency of the photosensor arrays. The most widely used material is PTFE for its high VUV reflectivity. Measurements of the reflectivity of PTFE for Xe scintillation light have ranged from 60% (Barabanov *et al.*, 1987) to values as large as 95% (Yamashita *et al.*, 2004). It has recently been measured accurately at the LXe scintillation wavelength and for different types of PTFE, with values ranging from 47% to 66%, but there are indications that when immersed in LXe its reflectivity could be considerably larger (Silva *et al.*, 2010).

2.4 Ionization Signal

In the previous section we have discussed the production of scintillation photons in LXe and the many processes which can play a role in the reduction of the measured scintillation signal. We now turn to the complementary signal, the ionization signal. LXe has an electronic band structure with a band gap between the valence band and the conduction band (Steinberger and Asaf, 1973) and the large gap energy of 9.28 eV makes LXe a very good insulator. The average energy required to produce an electron-ion pair, as mentioned earlier, is 15.6 eV, which makes LXe the liquefied noble gas with the largest ionization yield. In LXe, electrons from the valence band excited to the conduction band by ionizing radiation can be drifted over long distances. To measure the ionization signal, electrons need to be prevented to undergo recombination by applying an external electric, and drifted through the medium without loss due to attachment to impurities. These different processes are described in the following sections.

2.4.1 Electron Drift Velocity

At low values of the electric field, the drift velocity, v_d, is proportional to the applied electric field. The proportionality constant is called the electron mobility, μ. At larger field strengths the drift velocity reaches a maximum value and flattens out. In the Cohen-Lekner theory (Cohen and Lekner, 1967; Lekner, 1967) the larger drift velocity in LXe at lower fields and the saturation are understood (Atrazhev *et al.*, 2005) as being due to elastic scattering of electrons on spatially correlated Xe atoms (structure density effect) and whose closer interatomic distance weakens the polarization interaction (polarization density effect). Another theory is that inelastic electron interactions with Xe atoms are responsible for the saturation of the drift velocity (Gordon *et al.*, 1994) in which case the scintillation light produced by drifting electrons under high fields should be observable. Fig. 2.7 shows the variation of the electron drift velocity in LXe and GXe as a function of reduced electric field.

Ions drift at much smaller velocities than electrons in LXe. The mobility of negatively charged molecular oxygen for example has been measured at 165 K and gives $\sim 0.7 \times 10^{-3}\,\mathrm{cm^2\,V^{-1}\,s^{-1}}$ (Hilt *et al.*, 1994).

2.4.2 Electron Attachment

When conduction electrons drift in LXe and collide with electronegative impurities they can attach to these impurities. The ions formed then drift at much slower speeds than electrons and the charge signal is reduced. In fact, the attachment of electrons to impurities in LXe can be considered one of the most important factors that affect the performance of large scale LXe detectors that measure the ionization signal of recoiling particles. The average time a conduction electron stays free before attachment to an electronegative impurity is

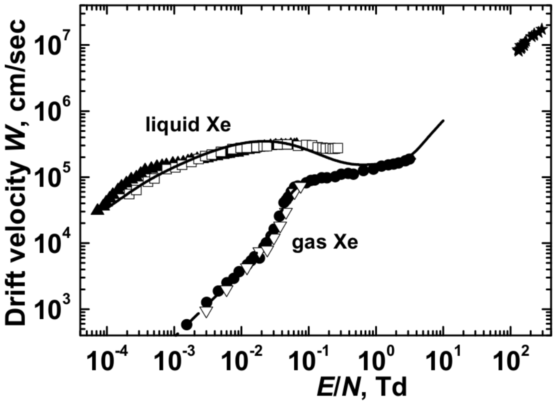

Figure 2.7: Electron drift velocity in LXe and GXe as a function of reduced electric field for several measurements (Gushchin *et al.*, 1982; Huang and Freeman, 1978; Pack *et al.*, 1992; Wagner *et al.*, 1967), as well as a calculation (Atrazhev *et al.*, 2005). Figure from Atrazhev *et al.* (2005).

called the electron lifetime, τ_e. Assuming a uniform distribution of impurities, the number of electrons surviving after drifting a distance z in a LXe detector, $N_e(z)$, from an initial number of electrons $N_{0,e}$, is given by

$$N_e(z) = N_{0,e} \exp\left(-\frac{z}{v_d \tau_e}\right). \tag{2.12}$$

The most common impurity responsible for electron attachment in LXe is O_2. The electron lifetime depends on the concentration of the different electronegative impurities, n_i, and the rate constant for electron attachment to the different impurities, k_i, through $\tau_e = (\sum k_i n_i)^{-1}$. Since the exponential attenuation of the charge signal with drift distance is easy to measure in LXe TPCs and since in most circumstances O_2 dominates, the concentration of impurities is often calculated from the electron lifetime and quoted in oxygen-equivalent units, $n_{O_2-\text{eq.}} = \tau_e / k_{O_2}$.

Since the probability of capture by impurities is a function of the electron energy the applied electric has an effect on the rate constants for electron attachment. For O_2, the attachment rate constant decreases with increased electric field. The rate constants of electron attachment to SF_6, N_20, and O_2 impurities in LXe are shown in Fig. 2.8 as a function of the applied electric field.

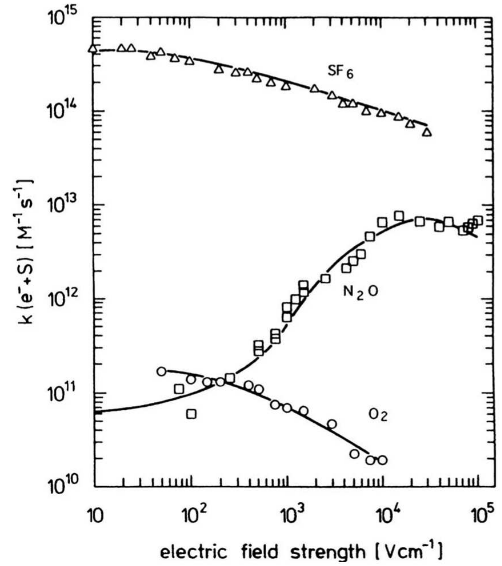

Figure 2.8: Electric field dependence of the rate constants of electron attachment to different solutes in LXe. Figure from Bakale *et al.* (1976).

2.4.3 Recombination

As discussed previously, the application of an electric field reduces the scintillation signal from recoiling particles in LXe, most dramatically the scintillation signal of electronic recoils. This is accompanied by an increase in the charge signal as electrons that did not recombine and produce scintillation are measured in the charge signal. The electric field dependence of the scintillation and ionization yield in LXe was first observed by Kubota *et al.* (1978b) and in fact provided strong evidence for recombination luminescence in LXe. Tracks with different ionization densities are affected differently by an external electric field. In higher ionization density tracks like those of α particles or nuclear recoils, more electrons can still recombine even in the presence of a strong electric field compared to electron recoil tracks with lower ionization density. It is this effect which is at the basis of the electronic and nuclear recoil discrimination capability of LXe (Sec. 2.4.4). Fig. 2.9 shows the Aprile *et al.* (2006b) measurement of the relative ionization and scintillation yields for nuclear recoils as a function of applied electric field.

The anti-correlation between ionization and scintillation fluctuations, that is, that on an event by event basis, a smaller amount of ionization is *always* accompanied by a larger amount of scintillation was first observed by Conti *et al.* (2003). The anti-correlation of ionization and scintillation fluctuations can be used to greatly improve on the achievable

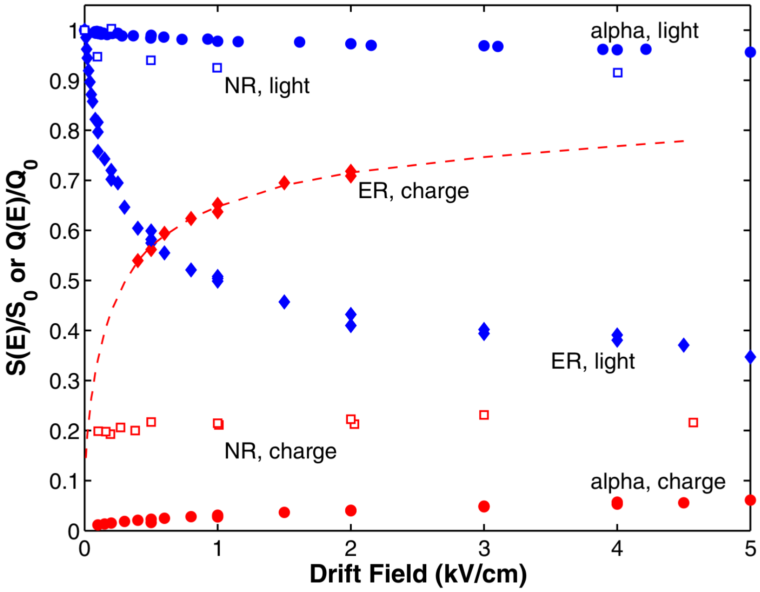

Figure 2.9: Field dependence of relative ionization and scintillation yields of α particles, electronic recoils (ER), and nuclear recoils (NR) in LXe. Figure from Aprile *et al.* (2006b).

resolution in either of the channels alone (Aprile *et al.*, 2007).

2.4.4 Discrimination

Recoiling particles in LXe have different track structures due to their different ionization densities. High ionization density tracks should suffer less quenching of their scintillation signal from the application of an external field. This effect can be used to distinguish recoiling particles. The ability to discriminate nuclear recoils from electronic recoils at low energies and based on their difference in the ratio of ionization to scintillation was first measured in Aprile *et al.* (2006b). In LXe dual-phase detectors, the charge signal is amplified in the gas phase and the ratio of the proportional scintillation signal to the direct scintillation signal is used as a discriminant. Fig. 2.10 shows the response of the XENON10 detector to low energy electronic recoils from a ^{137}Cs γ source and neutron-induced elastic nuclear recoils from an AmBe source. The separation between the two bands allows to reject electronic recoil events at the ~99.5% level while keeping 50% acceptance on nuclear recoils. Surprisingly, the rejection power increases as the electronic recoil energy decreases and the band is observed to become narrower.

We should note that the microscopic explanation for the origin of discrimination in LXe is

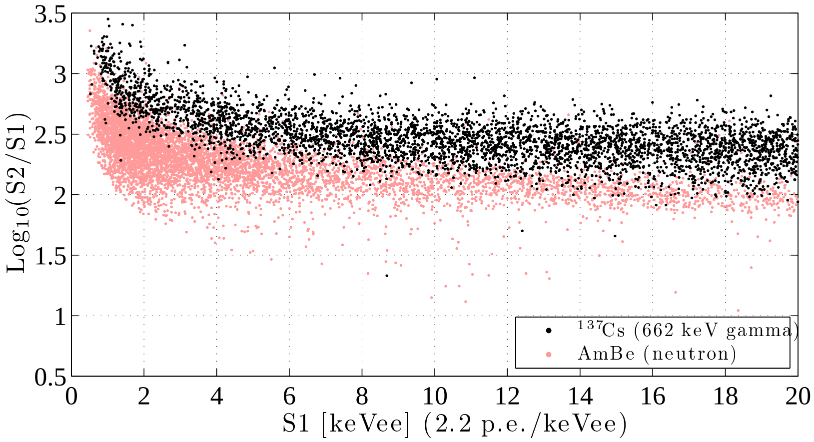

Figure 2.10: Response of the XENON10 detector to low energy electronic recoils from a ^{137}Cs γ source and neutron-induced elastic nuclear recoils from an AmBe source. Figure from Aprile *et al.* (2011b).

not entirely clear. The recombination model in (Dahl, 2009) correctly reproduces the energy and electric field dependence of the electronic and nuclear recoil band centroids (mean recombination) but recombination fluctuations associated with variations in track structure can only account for about half the measured variance of the bands. The interpretation of the results of the model may also give a hint that at recoil energies of WIMP searches the discrimination could come from a different ratio of excitons to electron-ion pairs for nuclear recoils rather than purely from the higher stopping power for nuclear recoils. In any case, practically it is possible for LXe dual-phase detectors to measure directly their response to both types of recoils and claim the presence of a WIMP signal without the detailed understanding of the origin of discrimination.

2.4.5 Electron Emission

Under certain conditions it is possible to extract ionization electrons from the liquid phase into the gas phase. Since the dielectric constant of LXe is larger than that of GXe, electrons in the liquid phase near the interface experience a repulsive image potential. By the application of a sufficiently high electric field it is possible to "heat" the electrons such that their average kinetic energy exceeds the potential barrier. Electrons with a momentum projection perpendicular to the interface that exceeds the potential barrier are then readily extracted into the gas phase. This is the mechanism that allows the ionization electrons in LXe dual-phase TPCs to be amplified in the gas phase through electroluminescence.

2.4.6 Electroluminescence

In GXe, under the effect of a high electric field, drifting electrons can acquire enough energy between collisions with Xe atoms to excite the atoms and produce scintillation light. This effect is called electroluminescence, or proportional scintillation, as the scintillation produced will be proportional to the number of electrons drifting. The photon yield per unit length per electron dN_{ph}/dx is empirically determined as (Belogurov *et al.*, 1995)

$$\frac{dN_{\mathrm{ph}}}{dx} = \alpha \left(\frac{E_g}{p} - \beta \right) p \tag{2.13}$$

with $\alpha = 70\,\mathrm{photons\,kV^{-1}}$ and $\beta = 1\,\mathrm{kV\,cm^{-1}\,atm^{-1}}$, where E_g is the electric field in the gas and p the pressure. This process, coupled with the extraction of electrons from the liquid phase provides an extremely efficient way of amplifying the ionization signal of LXe TPCs and even leads to the detection of single electron signals (Edwards *et al.*, 2008).

2.5 Energy Scales

As presented in this chapter, LXe is extremely attractive as a detection medium for ionizing radiation. The ionization and scintillation signals created by recoiling particles can be used to determine their energy and to some extent their type. Since one is interested to ascribe an energy to signals created in a detector, this naturally leads to the question of energy scales and calibration. In this section we present the different scales used in LXe detectors, their motivations, and sometimes their shortcomings.

Throughout the text we will reserve the use of “keV” for known energies, when discussing Monte Carlo simulations for example, and not reconstructed energies. The three main energy scales used are presented below.

2.5.1 Electronic-Recoil Equivalent Energy

The electronic-recoil equivalent energy scale is the name given to the energy scale where a γ ray calibration source is used to obtain the conversion between energy and the detector response, usually measured in photoelectrons, for the scintillation signal, or electrons, for the charge signal. This is common practice even for a detector which is meant to measure nuclear recoil energies, as the calibration in electron-equivalent energies will allow easier identification of lines from radioisotope decays in background spectra for example. Reconstructed energies with such a scale will have units of "keV$_{\mathrm{ee}}$", keV electron-equivalent. If the scintillation signal alone or the ionization signal alone is used to define the scale it will in general not be linear over large range of energies, mostly because the fraction of electrons that recombine changes with energy. Consequently, implicitly attached to the unit of keV$_{\mathrm{ee}}$ is the energy at which the calibration was performed.

2.5.2 Electronic-Recoil Combined Energy Scale

Since fluctuations in ionization and scintillation are anti-correlated, one can construct a linear energy scale in which those recombination fluctuations are cancelled by adding the two signals with appropriate factors, an idea suggested in (Seguinot *et al.*, 1992). This electronic recoil energy scale is called the combined energy scale and several γ sources are usually used to construct it, hence units of keV$_{\mathrm{ee}}$ are also used for energies reconstructed with it. The combined energy scale is used for the comparison of background spectra with Monte Carlo expectations since the improved resolution greatly helps in the separation of lines from radioisotope decays.

2.5.3 Nuclear-Recoil Equivalent Energy

In dual-phase LXe TPCs that are searching for nuclear recoils from dark matter particles the energy scale is most often based on the scintillation of nuclear recoils in LXe. Explicitly, the recoil energy E_{nr} is computed from the direct scintillation signal, $\mathsf{S1}$, as

$$E_{\mathrm{nr}} = \frac{\mathsf{S1}}{L_y} \frac{1}{\mathcal{L}_{\mathrm{eff}}} \frac{S_{\mathrm{er}}}{S_{\mathrm{nr}}} \tag{2.14}$$

where $L_y = L_{y,\mathrm{er}}\,(E_{\mathrm{er}} = 122\,\mathrm{keV})$ is the light yield of photoabsorbed 122 keV γ rays, $\mathcal{L}_{\mathrm{eff}}$ is the relative scintillation efficiency of nuclear recoils in LXe, and S_{er} and S_{nr} are the scintillation light field quenching factors for electronic and nuclear recoils, respectively. The unit "keV$_{\mathrm{nr}}$" is employed for energies reconstructed with the nuclear recoil equivalent energy scale.

Chapter 3

The XENON100 Experiment

After the successful demonstration of the performance of the XENON10 detector in the search of WIMP dark matter (Angle *et al.*, 2008a,b), the next step was clear: build a larger scale LXe detector with a lower background level, using the same principle of operation and reusing many of the design features of the XENON10 detector. A design goal of a factor ten increase in target mass and a reduction of the low-energy γ background level by a factor of one hundred was set.

In Sec. 3.1 we discuss the early design decisions and simulations that helped shape the XENON100 detector into its final form. Sec. 3.2 describes the construction and assembly phase while Sec. 3.3 presents a detailed description of the XENON100 detector and its subsystems. Finally, Sec. 3.4 describes the computing infrastructure deployed to support data taking operations.

3.1 Design

In general, the γ background within a radiopure LXe fiducial volume can always be made smaller by increasing the LXe volume around it. In practice, however, the approach of increasing the volume alone is not adequate due to other constraints: the need for a low energy threshold, hence high photosensor coverage, implies an increase in complexity and costs. The approach taken must be multiple-fold: selection of radiopure materials for detector construction, minimization of contamination of materials in the assembly process, and use of background rejection techniques.

An extensive materials radioactivity screening campaign was undertaken to find radiopure materials suitable for the construction of the detector (stainless steel, PTFE, copper) and to measure the intrinsic radioactivity of several commercial components used in the assembly (PMTs, PMT bases, cables). The acceptable limit for the radioactivity depends on the mass of the material or component and its proximity to the target volume, and this limit can only be adequately determined through extensive simulations. The description of the facilities used for the measurements and results are presented in Aprile *et al.* (2011d).

To further reduce the contribution to the γ background from detector components, one can proceed by shielding the target volume from some components. In the design phase, three components were identified early on as potential candidates: the pulse tube refrigerator (PTR) system, used to maintain the operating temperature, the electrical feedthroughs for both PMT signals and PMT high voltage, and the cryostat vessel. In the XENON10 detector the PTR was mounted directly on top of the chamber vessel (see Aprile *et al.*, 2011b, Fig. 2). Additionally the large amount of steel around the target volume was known as a background source. Moving the PTR system, composed of the PTR coldhead, the motor-valve, and the buffer tank, outside of the passive shield surrounding the detector would allow to eliminate its contribution to the radioactivity in the immediate vicinity of the detector. It would also reduce the uncertainty on the predicted low-energy γ background since measuring the intrinsic radioactivity of such a large commercially procured apparatus is not easily achievable.

Specifically, the remote cooling of the LXe volume has been implemented by extending the vacuum cryostat outside the passive shield. The PTR, mounted on top of a "cooling tower", is coupled to the inner volume of the cryostat through a copper cold finger. The GXe that condenses on the cold finger and drips is collected with a funnel and flows back to the detector vessel by gravity. The cryogenic system of the XENON100 detector is described in details in Sec. 3.3.5. The same concept was applied to the ceramic electrical feedthroughs. However, since this extended volume would not contain any cold GXe flow, only the inner volume was extended outside the passive shield. Excessive heat losses can be avoided by passing the tubes of the inner volume through cold jackets. This design has the added advantage that electrical connections to the detector, now outside the passive shield, can easily be undone without the opening the shield door. A technical drawing of the final design with the detector inside the shield is shown Fig. 3.12 of Sec. 3.1.4.

Working on the data from the XENON10 experiment, especially on events that did not meet the analysis requirements, gave invaluable insights into likely physical causes for certain classes of events and also ideas on how to avoid some peculiarities present in that prototype detector. The so-called "anomalous leakage events" (Angle *et al.*, 2008a), identified as multiple-scatter events with one scatter in a charge-insensitive region, mostly below the cathode, and a second scatter in the sensitive LXe volume, for example, were a particular concern and efforts were made to minimize as much as possible their occurrence. This resulted in two main design choices. First, to keep the distance between the cathode and the bottom PMT array as small as possible and to reduce the volume of charge insensitive regions around the bottom PMT array. Second, it spawned the idea of using an active LXe veto to tag some of these events. The reasoning was the following. Only high energy γ rays are likely to travel distances of several centimeters and deposit energies, via Compton scattering, of only a few kiloelectron volts. Furthermore, with such a small energy deposited the trajectory of the γ ray is approximately a straight line. For such event topologies, one would expect the z distribution of energy deposits within the sensitive volume to decrease with increasing distance from the cathode. That is, events with a γ ray traversing the full drift distance should be suppressed compared to those with the γ ray traversing a shorter distance. Hence γ rays responsible for anomalous leakage events from additional scatters in charge insensitive regions should escape the sensitive region on the side or on the bottom. Having an additional instrumented LXe volume below the bottom PMT array and surrounding the sensitive volume should thus help reducing the rate of such events.

As it turns out, the LXe veto volume idea would be adopted in the design also because of other practical reasons. Since the total event rate scales with the external surface of the LXe volume, then an increase by a factor ten in mass implies a factor of about five increase in event rate. In practice, however, the only relevant information in a LXe volume where the background rate is high is if energy was deposited or not, as this volume would be fiducialized away to reach the desired γ background level in the central part of the target. By making the external part of the volume optically separated from the target volume, instrumenting it, and operating it as an active veto, it should be possible to achieve a very good γ background rejection. Furthermore, this should be possible even with a relatively high energy threshold (~100 keV) if the veto volume thickness is substantial (~3 cm). This can be seen in Fig. 3.1 where the fraction of γ rays which deposit energies above a given threshold in slabs of LXe of different thicknesses is shown for different γ-ray energies. The efficiency at which γ rays can be tagged does not substantially vary with thresholds below a few hundred kiloelectron volts. Instrumenting the full volume instead of segmenting it into a target volume and an active veto would most likely require more PMTs without providing a significant advantage in terms of background reduction, especially considering that adding photosensors would increase the background level. That is, the photosensor density required to operate a LXe volume as a veto with an energy threshold of ~100 keV should be less than what is required for the target volume.

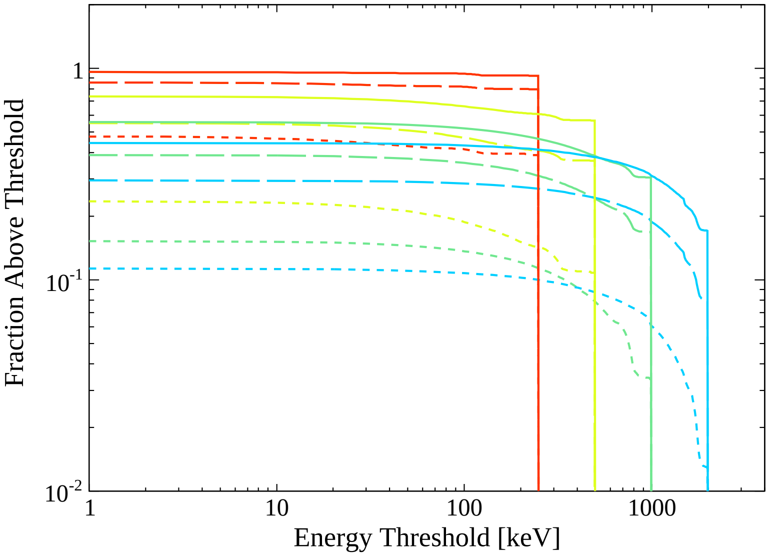

Figure 3.1: Fraction of γ rays that deposit an energy above threshold for LXe thicknesses of 1 cm (short dashed lines), 3 cm (long dashed lines), and 5 cm (solid lines), for γ-ray energies of 250 keV (red), 500 keV (yellow), 1 MeV (green), and 2 MeV (cyan), as a function of the energy threshold.

Reducing the total event rate inside the sensitive volume with a veto volume has other advantages, one specific example is the reduction in the data volume created. For the XENON10 experiment, the raw data acquired for each trigger consisted of 88 waveforms of 16350 14 bit samples (2 B/sample) for a total of 2.7 MB per event. This would have lead to alarming data volumes and consequently provisions were made to reduce the raw data size on the data acquisition (DAQ) computer. Specifically, additional programs were created to set to zero samples of the waveform that consisted only of baseline noise, and to subsequently compress losslessly the modified waveforms. However, this solution did not remove the main bottleneck to high data taking rates, namely the VME transfer speed between the DAQ computer and the VME crate. This solution also left the DAQ computer with cpu intensive tasks running constantly. For a detector with an order of magnitude increase in mass, and which would certainly require more photosensor channels, the data volume problem would certainly be exacerbated.

An initial proposal for the XENON100 DAQ system considered the possibility of using charge-to-digital converters (QDCs) and time-to-digital converters (TDCs) instead of digitizing PMT signals with flash ADCs. This would have led to a large reduction in data volume but the versatility of the FADC approach was preferred. The FADC approach allows a detailed time analysis of triggered events, a valuable tool in the understanding of background events. The solution adopted to reduce the event size was to implement a data reduction algorithm on the field programmable gate array (FPGA) of the FADCs. The company manufacturing the FADCs chosen for the experiment, CAEN Technologies (CAEN), accepted to modify their firmware to include our specification for a baseline suppression algorithm. The algorithm implemented is described in Sec. 3.3.10. This data reduction before the transfer to the DAQ computer would allow faster data taking rates, still limited by the VME transfer speed but now mostly given by the average duration of the S2 signal. That is, most of the samples kept in a waveform would be those of the S2 signal. An added benefit of using a veto volume in conjunction with the on-board baseline suppression algorithm is that veto PMT signals would require almost no space to be stored, as they would only be comprised of fast direct scintillation light S1 signals and no long S2 signals.

Another area where it was thought improvement over XENON10 was possible was the position reconstruction performance near the edge of the sensitive volume. With a distance of ~1.7 cm between the proportional scintillation amplification region and the top PMT array, most of the S2 signal in XENON10 was concentrated into up to 4 top array PMTs. If the top PMT array coverage does not extend significantly beyond the radius of the sensitive volume, then events closer to the edge have a significant fraction of their S2 signal which comes from reflections of the proportional scintillation signal instead of a line-of-sight signal. Since the distribution of the S2 signal on the top PMT array is used to reconstructed the (x, y) position of events this can lead to degraded performance near the edge of the sensitive volume. The design choice for XENON100 was thus made to have the top PMT array extend by one PMT width beyond the radius of the sensitive volume. Furthermore, since the radial coordinate is usually more important than the azimuthal one for fiducialization purposes, a concentric PMT rings arrangement was chosen for the top array. Lastly, the mesh frame inner diameter was chosen to extend beyond that of the sensitive volume to prevent additional reflections of the proportional scintillation signal. As in the XENON10 design, the liquid level will be maintained at a fixed height with a cylinder closed on top, similar to a diving bell. Having the bell, which houses the top PMT array, larger than the sensitive volume by one full PMT width, naturally gave the space for a LXe veto that laterally surrounds the sensitive volume. Since most of the direct scintillation light is detected by the bottom PMT array, the closely packed square grid arrangement of XENON10 was kept for the XENON100 bottom array. The photosensor coverage was increased by reducing the inter-PMT distance.

3.1.1 Initial Simulations

As a first step in the estimation of the performance of a generic LXe detector with the characteristics described earlier, GEANT4 (Agostinelli *et al.*, 2003) Monte Carlo simulations were performed to calculate the low-energy γ background contribution of the PMT arrays (including bases) and the cryostat for different inner detector configurations. Previous simulations, in the case of XENON10 for example, have shown that the largest contribution to the γ background rate at low energies is from the PMTs and the cryostat vessel, provided that the contribution from impurities in the LXe is negligible. Including only the radioactivity from those components should thus provide an adequate estimate.

The expected γ background was obtained by simulating the decay of all radioactive isotopes present in each material, in this case only the stainless steel cryostat vessel, the PMT bases and the PMTs. The activities assumed for this initial simulation and the quantity of each component are listed in Tab. 3.1. Each decay chain was simulated using the `G4RadioactiveDecay` class of the GEANT4 package, itself based on the evaluated nuclear structure data file (ENSDF) (Tuli, 2001). The `G4VPrimaryGenerator` derived class that creates initial particles is used to generate the desired isotopes uniformly within the volumes of each material. For long decay chains the secular equilibrium approximation was assumed to hold. Another approximation was made, specifically that each daughter decay in a chain would trigger as a separate event in the real detector. With an event length of ~300 μs this holds for all decay products in the ^{232}Th chain except the "fast" $^{212}\mathrm{Bi} \overset{\beta}{\to} {}^{212}\mathrm{Po} \overset{\alpha}{\to} {}^{208}\mathrm{Pb}$ delayed coincidence, due to the ^{212}Po mean life of 432 ns. Similarly it holds for all decay products of the ^{238}U chain except the "slow" $^{214}\mathrm{Bi} \overset{\beta}{\to} {}^{214}\mathrm{Po} \overset{\alpha}{\to} {}^{210}\mathrm{Pb}$ delayed coincidence, due to the ^{214}Po mean life of 236.6 μs. In any case, the low-energy background should not be affected by this simulation approximation as both of those decays are at much higher energies. This approximation was implemented by a custom `G4UserStackingAction` that postpones the decay of any daughters of the current primary particle to the next simulated event.

Table 3.1: Radionuclide activities assumed for the initial simulation and the quantity of each component in the baseline configuration simulation.

Component	Unit	Quantity	^{238}U	^{232}Th	^{40}K	^{60}Co
PMTs	mBq/PMT	251	0.17	0.20	10	0.56
PMT Bases	mBq/base	251	0.16	0.10	<0.16	<0.01
Stainless Steel	mBq/kg	55 kg	<4.4	8.9	<31	12

The information recorded in the simulation includes the energy, position, time, type of particle, and physical process responsible for each energy deposit in the LXe sensitive volume. For each event some of the expected detector responses were applied to convert the detailed information into variables closer to the measured quantities. Specifically, the measured XENON10 double scatter `S2` peak resolution of 3 mm was used to convolve the list of simulated energy deposits. That is, a detector with a similar `S2` signal width as XENON10 can only resolve double scatter events with 100% efficiency if the inter-scatter distance is larger than 3 mm. No spatial dependence of the scintillation response or the charge response was assumed for the sensitive volume or the veto volume.

Simulations for three different configurations were performed to examine the effect of different sources of radioactivity on the low-energy γ background. The first configuration, the *baseline* configuration, has a cylindrical LXe target volume with 15.2 cm (6 in) radius and 30.5 cm (12 in) drift length, defined by a PTFE cylinder with a 1.3 cm thick wall. The target volume PMTs are positioned to cover maximally the surface available (for simplicity), 131 PMTs in the top array, 84 PMTs in the bottom array. The veto volume has a cylindrical shell shape that covers the side of the target volume and is instrumented by 36 PMTs, placed in a circular arrangement at the bottom of the volume. The outer surface of the veto volume is covered by a 6.4 mm thick PTFE lining. The cryostat is a double-wall vacuum insulated stainless steel cylinder with a flange at the top, allowing this large mass to be far away from the target volume. The vacuum insulation thickness is 2.5 cm. In the baseline configuration the bell is made out of copper and has a radius of 202 mm and a thickness of 1 mm. The *thick bell* configuration is the same as the baseline configuration except that the thickness of the top of the bell is increased by an additional amount which varied from 1 mm to 10 mm. In the *lowered bases* configuration the PMT bases of the bottom PMT array are lowered by 1 cm or 3 cm with respect to the baseline configuration. Fig. 3.2 shows the geometry of the baseline configuration.

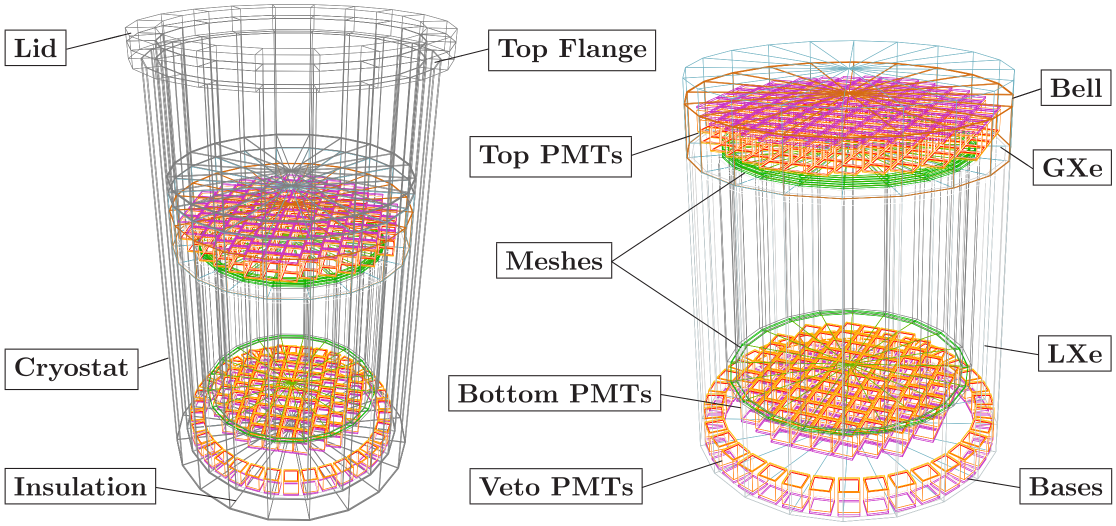

Figure 3.2: Detector geometry used for the baseline configuration simulation of the expected low-energy electronic recoil background. The main components included in the simulation are the double-wall vacuum insulated stainless steel cryostat, the PTFE cylinder separating the target volume and the veto volume, the top, bottom, and veto PMT arrays, the PMT bases, the bell, and, most importantly the LXe and GXe volumes.

The main results of the simulation are shown in Figs. 3.3, 3.4, 3.5, and 3.6. Fig. 3.3 (left) shows the total electronic recoil background differential rate expected in the sensitive volume. The sensitive volume is understood as the charge sensitive part of the target volume, that is, the LXe volume above the cathode and within the PTFE cylinder separating the target volume and the veto volume. This rate includes events with multiple interactions within the sensitive volume. The integral of the differential spectrum gives the total event rate and can be used to estimate the trigger rate of the hypothetical detector. This assumes the use of a S2-based trigger, as was used for the XENON10 detector (Aprile *et al.*, 2011b), since the region below the cathode does not produce S2 signals but would produce S1 signals that could be triggered on with a S1-based trigger. The value obtained for the total event rate with this detector configuration is 428 events $\mathrm{kg}^{-1}\,\mathrm{d}^{-1}$, which corresponds to a trigger rate of 0.33 Hz. The main contribution at low energies ($< 100\,\text{keV}$) comes from decays of ^{60}Co, most likely from the cryostat, which has a higher total activity for that isotope than the PMT arrays. This is closely followed by the contributions of the ^{232}Th chain, of ^{40}K decays, and of the ^{238}U chain.

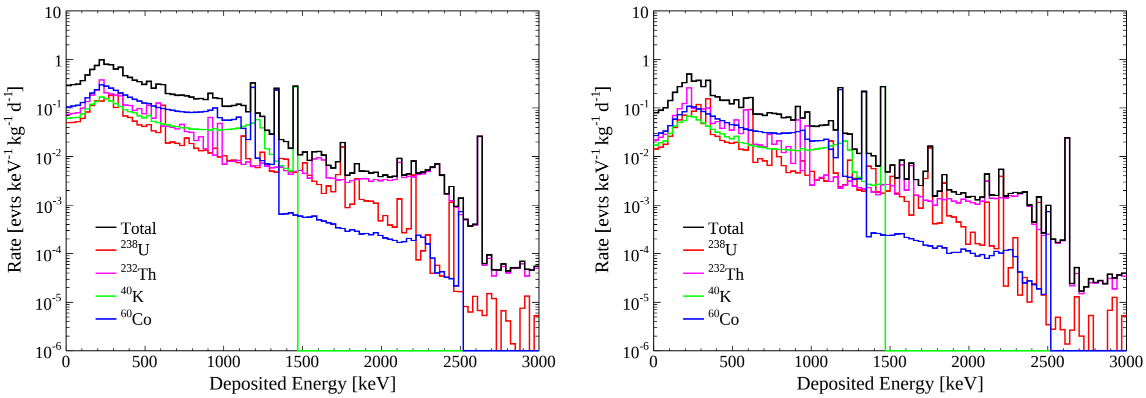

Figure 3.3: Predicted total background differential rate in the sensitive volume (left) and differential single scatter rate (right) in the sensitive volume with individual contributions from different radioisotopes.

Fig. 3.3 (right) shows the total electronic recoil background differential single scatter rate in the sensitive volume, that is, requiring that events deposit energy only at a single position within the volume. As mentioned earlier, the inter-scatter distance at which the detector is assumed to be able to resolve two energy deposits with 100% efficiency is 3 mm in the z direction. This means that a γ ray that is photoabsorbed or a γ ray that Compton scatters and is photoabsorbed less than 3 mm away in the z direction from the Compton interaction point would both be registered as single scatter interactions. Since the ionization electrons from two energy deposits at the same drift time but separated in the xy plane produce an overlapping S2 signal in the time coordinate, the double scatter resolving power in this case has to come from the S2 signal distribution on the top PMT array. Intuitively, the capability to distinguish a distribution with two superimposed signals from one with a single signal is likely quite limited compared to the capability in the z direction, especially considering that the PMTs provide $2.5\,\text{cm} \times 2.5\,\text{cm}$ “pixels”. Multiple scatters in the same z slice are thus all approximated as single scatter events. At low energies, the differential rate is reduced by a factor of $\sim$3 by selecting only single scatter events. As we will see shortly, the main reduction in the low-energy rate will come from the fiducialization of the sensitive volume and requiring that no interactions occur in the veto volume.

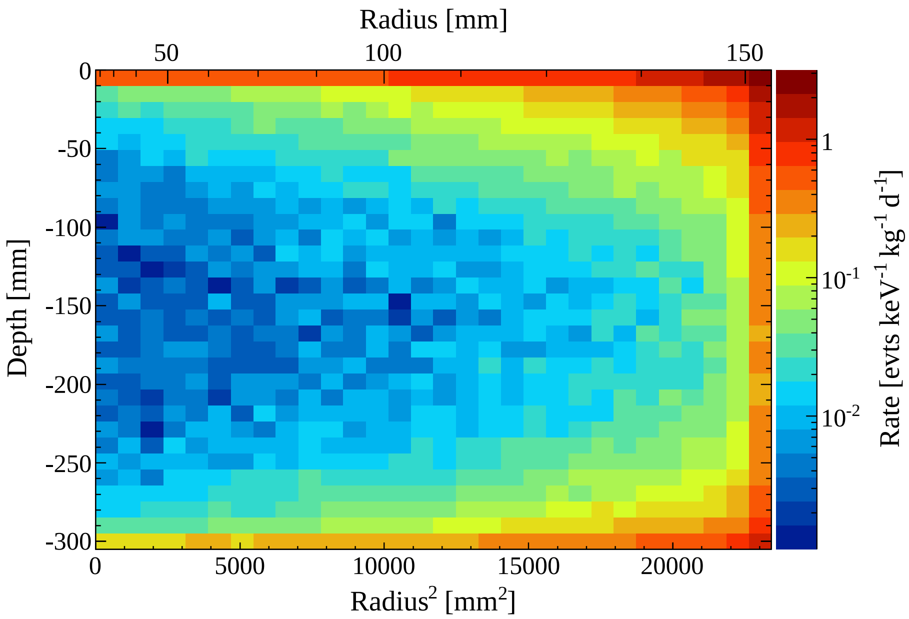

Figure 3.4: Predicted γ background average low-energy (0-100 keV) differential single scatter rate as a function of radius squared and depth due to the intrinsic radioactivity of the PMTs, PMT bases and cryostat.

To profit from the background reduction power of fiducialization one needs of course to know the precision at which the position of events within the sensitive volume can be inferred from the S2 signal. For the results of this simulation we assumed that the position reconstruction resolution in the xy plane is ~1 mm, the same value as that inferred for the XENON10 detector (Aprile *et al.*, 2011b). The position resolution in the z direction is taken the same but is typically better than that in the xy plane since it is based on the time measurement of the S2 signal within the digitized waveform. If the actual position reconstruction resolution is worse than the value assumed here, the background rate estimate would be worsened by a factor that depends on the slope of the rate as a function of position. Fig. 3.4 shows the average low-energy (0-100 keV) γ background differential single scatter rate as a function of radial position squared and depth in the sensitive volume. This is probably the most dramatic visual demonstration of the effect of fiducialization. At $r^2 = 0$, from the liquid level ($z = 0$) to a depth of 50 mm the rate drops by about 2 orders of magnitude. The rate in the top layers is larger than in the bottom layers because the bottom PMT array is shielded by an additional layer of 12.5 mm of LXe whereas the top PMT array lies in GXe. The part of the cryostat above the sensitive volume also increases the rate in the top layers.

The next step in estimating the γ background contribution is evaluating the performance of the veto volume in conjunction with fiducial volume cuts. In some sense, requiring that no energy be deposited in the veto volume would the same as a radial fiducial volume cut in those outer layers of the LXe if the activity of the PTFE cylinder was negligible. As shown in Fig. 3.1 the energy requirement for the veto might not need to be extremely low to be effective. Both those effects mean that it is interesting to look at the reduction in the γ background single scatter rate as a function of both the fiducial volume cut and the veto energy threshold. Fig. 3.5 shows the results of such an analysis. The average low-energy (0-100 keV) γ background differential single scatter rate as a function of the veto energy threshold is shown for different optimal fiducial volumes. The optimal fiducial volume is defined as the cylindrical fiducial volume with the lowest rate obtainable for a given LXe mass. In practice the algorithm proceeds by calculating the total rate in the outermost top, bottom, and side layers of the initial fiducial volume and cuts away the layer with highest rate, until a volume with the desired mass is obtained. The thicknesses of the layers used were 2.5 mm along r and 5 mm along z but the result is rather insensitive as long as the thicknesses are smaller than ~1 cm. Obviously this only results in an optimal *cylindrical* fiducial volume but it nevertheless partially solves the problem of how to vary the fiducial mass in a semi-continuous manner to explore the background reduction performance. The truly optimal fiducial volume would be one that follows the contours of equal rate in Fig. 3.4.

Fig. 3.5 shows that most of the reduction in rate from the veto cut is obtained as the energy threshold is reduced from 1 MeV to 100 keV, after which point the improvement is not as substantial. As a good benchmark value for the veto energy threshold one can thus take 100 keV. For a fixed veto threshold of 100 keV, the rate initially drops very rapidly from the maximum mass of ~65 kg until a fiducial mass of 60 kg, then continues to drop but with a slowly decreasing slope. This means that in the absence of any uniform electronic recoil background in the LXe, such as decays of ^{85}Kr for example, one should compute the maximum exposure (mass × live time) without background leaking into the WIMP signal region for each fiducial mass. We will reserve this calculation for the next iteration in the design and limit ourselves here to the benchmark case of a 50 kg fiducial mass, which seems to strike a good balance between background reduction and fiducial mass size. The top, bottom and radial cuts of the optimal cylindrical fiducial volume are respectively, 40 mm, 20 mm, and 5 mm.

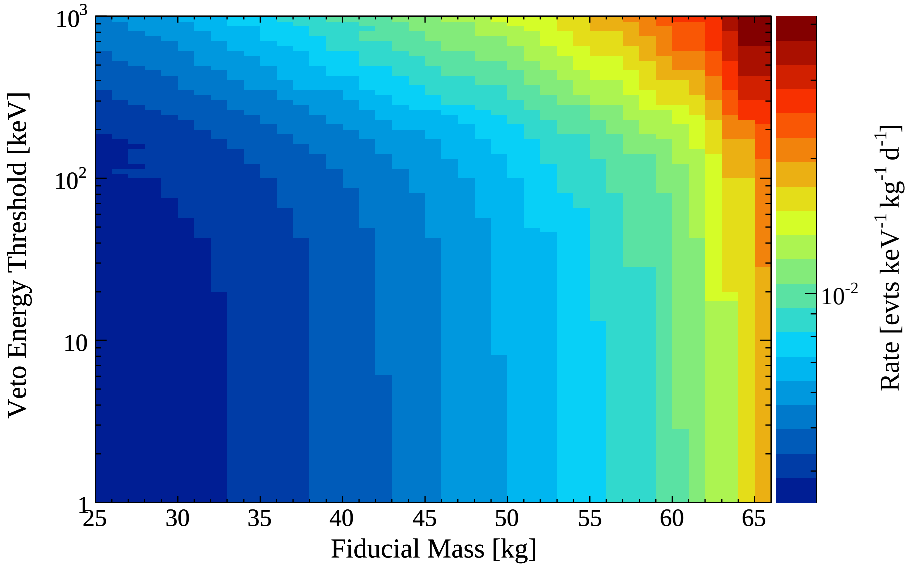

Figure 3.5: Predicted γ background average low-energy (0-100 keV) differential single scatter rate as a function of the active veto energy threshold for different optimal fiducial volumes (see text).

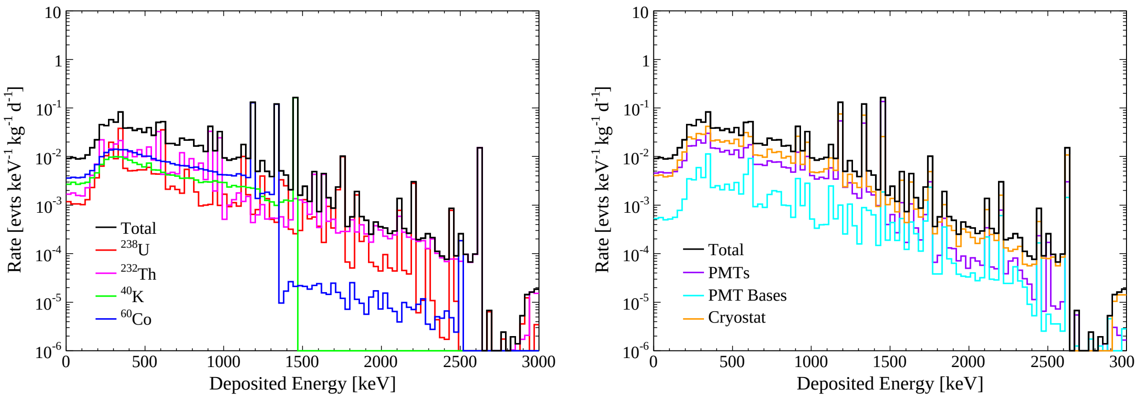

Figure 3.6: Predicted total γ background low-energy differential single scatter rate in the benchmark 50 kg fiducial volume with a veto energy threshold of 100 keV, with individual contributions from different radioisotopes (left), and contributions from different components (right).

The predicted γ background differential single scatter rate in this benchmark 50 kg fiducial volume and with a veto energy threshold of 100 keV is shown in Fig. 3.6 (left). The total predicted rate at low energies is $9.2 \pm 0.1\,\mathrm{events\,keV^{-1}\,kg^{-1}\,d^{-1}}$, where the uncertainty accounts only for the statistical uncertainty of the simulation. Obviously as the radioactivity of many of the materials that would make up the hypothetical detector are only upper limits this number constitutes an upper limit to the rate. The values assumed for the radioactivity of the materials (Tab. 3.1) should also be considered as indicative. Nevertheless, it is possible to draw some interesting conclusions from these results. Decays of the ^{60}Co isotope are the largest contribution to the rate, followed by those of ^{40}K. This is to be expected as these two isotopes emit high energy γ rays, 1.17 MeV and 1.33 MeV for ^{60}Co, 1.46 MeV for ^{40}K, which are much more likely to Compton scatter, deposit a small amount of energy, and escape the fiducial volume than lower energy γ rays are. The features in their spectra are also easy to recognize, a full absorption peak at the γ energies emitted, a relatively flat Compton scatter continuum from the low energies to the Compton edge (easily recognizable at 1.24 MeV in the ^{40}K spectrum for example), and a prominent “backscatter” peak at ~250 keV. The backscatter peak is due γ rays that scatter at large angles in materials near the LXe sensitive volume, for which the scattered γ ray has an energy which tends to $m_e/2$ as $E_\gamma \to \infty$ (Knoll, 2000).

Fig. 3.6 (right) shows the rate contribution from the different components of the simulated geometry. With the activities assumed, the PMTs and the cryostat contribute about equally to the rate in the fiducial volume while the PMT bases have a contribution of ~10% of that of the PMT arrays. The contribution of the PMT bases is thus negligible. The initial motivation to include them as a source in the simulation was due to an initial measurement of their intrinsic radioactivity, much higher than the subsequent measurement listed in Tab. 3.1. This was also the motivation for the simulation of additional detector configurations where the bottom PMT bases are lowered to increase the amount of LXe between the bases and the fiducial volume.

Tab. 3.2 lists the contributions to the predicted average low-energy differential single scatter rate in the benchmark 50 kg fiducial volume with a veto threshold of 100 keV (active veto column). To see the effect of instrumenting the veto volume and using it in anti-coincidence, the predicted rate is also calculated without the veto cut and without the radioactivity contribution of the veto PMTs (passive veto column). The reduction obtained

Table 3.2: Predicted total γ background low-energy differential single scatter rate in the benchmark 50 kg fiducial volume with a veto energy threshold of 100 keV (active veto) for different components, along with a comparison of the expected rate in the case where the veto volume is not instrumented with PMTs (passive veto), for the different configurations simulated (baseline, lowered bases, and thick bell). Errors only account for the statistical uncertainty of the simulation.

Component	Design	Rate (events $\mathrm{keV^{-1}\,kg^{-1}\,d^{-1}}$)	
		Passive Veto	Active Veto
PMTs	baseline	8.85 ± 0.06	4.65 ± 0.05
PMT Bases	baseline	1.16 ± 0.01	0.52 ± 0.01
	lowered bases, 1 cm	1.05 ± 0.01	0.47 ± 0.01
	lowered bases, 3 cm	0.89 ± 0.01	0.39 ± 0.01
Cryostat	baseline	10.65 ± 0.14	4.01 ± 0.09
	thick bell, 1 mm	10.39 ± 0.14	3.97 ± 0.08
	thick bell, 3 mm	10.16 ± 0.14	3.85 ± 0.08
	thick bell, 10 mm	9.70 ± 0.14	3.66 ± 0.08
Total	baseline	20.66 ± 0.16	9.19 ± 0.10

in the total rate from a passive to an active veto volume is sizeable, slightly more than a factor of two.

The results for the simulations of the alternate configurations are also listed in Tab. 3.2. In the active veto case, a reduction of 25% of the PMT base contribution could be achieved by lowering the bases by 3 cm from their position in the baseline configuration. Additionally, by making the top surface of the bell thicker the contribution of the cryostat could be reduced by as much as 9%.

The conclusions from this initial round of simulations was that the active veto idea was worth pursuing. With the knowledge that the PMT bases intrinsic radioactivity might not be as problematic as originally thought, the idea of moving them further away from the sensitive volume was abandoned. Also, since the reduction in the γ background contribution from the cryostat could not be substantially reduced by thickening the bell, the decision was made to use a stainless steel construction, easier to build and lighter for the desired strength of the structure.

3.1.2 4π Active Veto

Following the results of the background simulation described in Sec. 3.1.1 a new round of simulations was performed to estimate the effect of using an instrumented LXe veto volume above the bell as well. Another ring of PMTs was added to the simulation geometry above the bell and the LXe volume was made to extend above these top veto PMTs. A different LXe level can be maintained inside the bell at the correct height for the proportional scintillation signal and also maintained outside the bell at a different level if one can have a pressure difference between the GXe volume inside and outside the bell. That result can be achieved by using the purified GXe from the recirculation system, with the recirculation pump providing the pressure difference. This new *veto above bell* configuration has 100 top array PMTs, 31 top veto PMTs, 84 bottom PMTs, and 36 bottom veto PMTs. The estimate of the amount of LXe required such that the level is above the top veto PMTs is 135 kg. Fig. 3.7 shows the updated detector geometry used for the simulation.

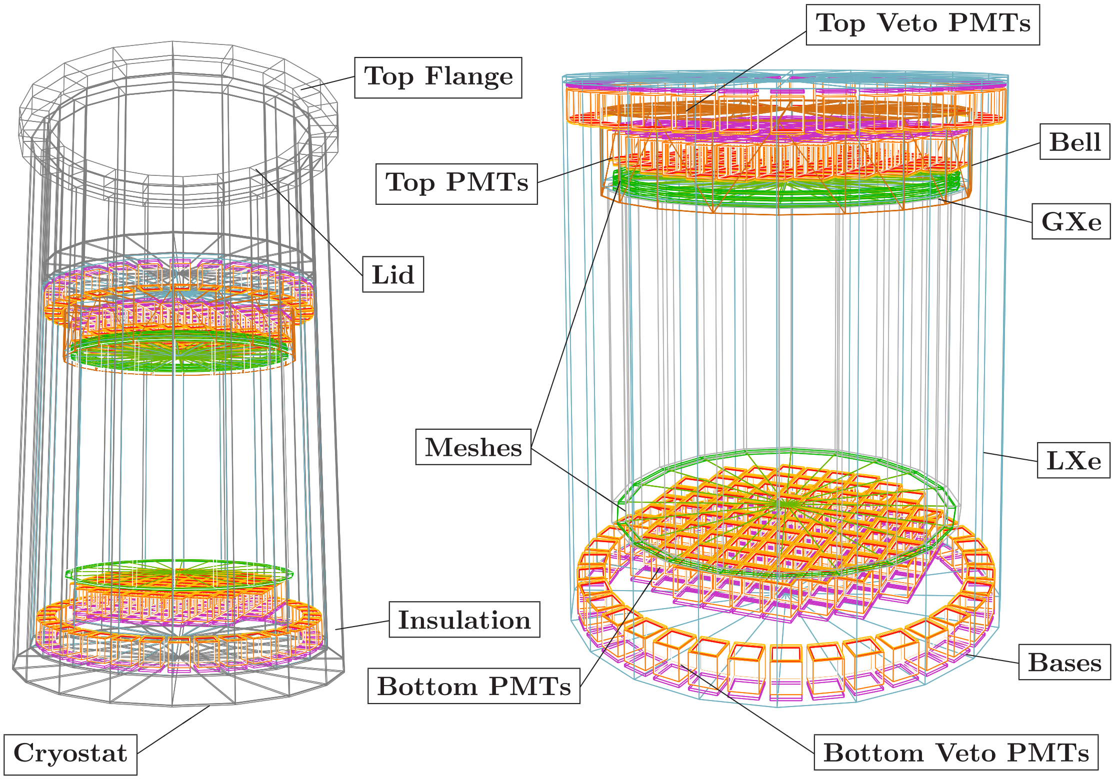

Figure 3.7: Detector geometry used for the *veto above bell* configuration simulation of the expected low-energy electronic recoil background. The new components included in the simulation are the top veto PMT array, and the LXe volume extending above it.

In addition to the cryostat, PMTs, and PMT bases contributions, two new sources were included in the simulation: the stainless steel frames holding the anode, top, bottom, and cathode meshes, collectively called the *mesh frames* contribution, and the polyethylene that constitutes the innermost layer of the passive shield. As part of the extensive materials radioactivity screening campaign for the XENON100 experiment mentioned earlier (Aprile *et al.*, 2011d), the radiopurity of the polyethylene used for the construction of the XENON10 passive shield (Aprile *et al.*, 2011b), inside which the XENON100 detector was planned to be installed, was reassessed. The new activities measured at the time of the design of XENON100 from a sample of the shield door were 6.5/5.8/13/1.7 mBq/kg for ^{238}U/^{232}Th/^{40}K/^{60}Co respectively, and all upper limits. The large mass of polyethylene could make this component a rather sizeable contribution to the electronic recoil background. The mesh frames were added as a new source due to their proximity to the fiducial volume and potentially larger impact on the γ background. The activity assumed at the time for the mesh frames was 2.7/1.5/12/13 mBq/kg in ^{238}U/^{232}Th/^{40}K/^{60}Co, respectively, with a total mass of 500 g for the four mesh frames.

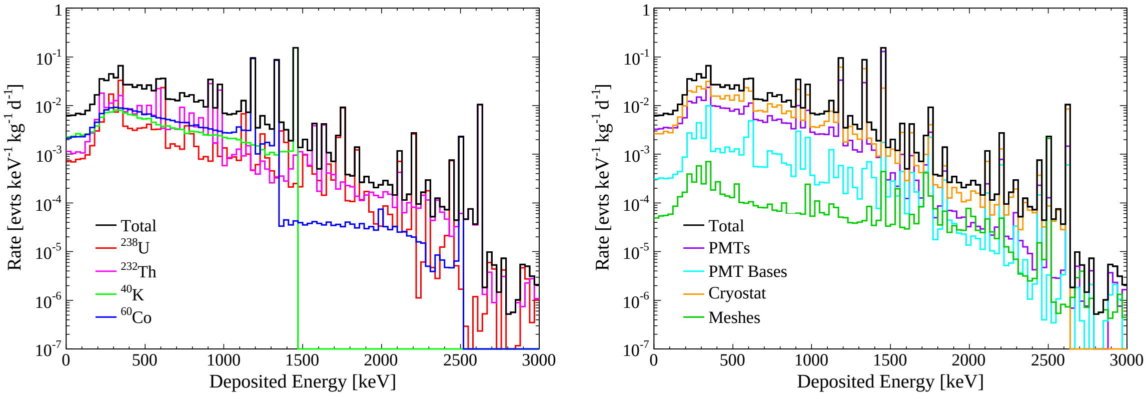

Figure 3.8: Predicted total γ background low-energy differential single scatter rate for the *veto above bell* configuration in the benchmark 50 kg fiducial volume with a veto energy threshold of 100 keV, with individual contributions from different radioisotopes (left), and contributions from different components (right). Note that the contribution from the shield polyethylene is not included (see text).

Fig. 3.8 shows the results of the simulation. In Fig. 3.8 (left) the predicted γ background differential single scatter rate for the same benchmark 50 kg fiducial volume as used in Sec. 3.1.1 and with a veto energy threshold of 100 keV shows a sizeable improvement with the addition of the veto volume above the bell, with a rate of about 6 events keV^{-1} kg^{-1} d^{-1}. From Fig. 3.8 (right) the PMTs and the cryostat still dominate, the new piece of information was that the mesh frames contribution is negligible with the assumed activity.

The contribution of the shield polyethylene was not included in Fig. 3.8 but is listed in Tab. 3.3 along with the contribution of all simulated components, for both an active and passive veto volume. From Tab. 3.3 one immediately concludes that if the activity assumed for the polyethylene is correct then its contribution to the γ background is large, as much as the rest of the components. Since the screening results were all upper limits to the activity, testing lower values would necessarily have required longer counting times with larger samples. At the time the decision was made to add a layer of oxygen-free high-conductivity (OFHC) copper of 5 cm thickness to the cavity of the passive shield to reduce the potential contribution of the polyethylene to the γ background. Estimating the copper attenuation with $e^{-\mu\rho\ell}$, where μ is the copper total mass attenuation coefficient for 1 MeV γ rays $\mu_{\text{copper}} = 5.717 \times 10^{-2}\,\text{cm}^2\,\text{g}^{-1}$, ρ is the copper density $\rho_{\text{copper}} = 8.94\,\text{g}\,\text{cm}^{-3}$, and ℓ is the copper thickness, we obtain that this thickness of copper should reduce the polyethylene contribution by a factor of $\gtrsim 10$, making it sub-dominant compared to the PMTs and cryostat contributions. Subsequent counting measurements have resulted in lower upper limits by a factor of ~40 for ^{238}U, ^{232}Th, and ^{60}Co but in a detection for ^{40}K at the mBq/kg level (Aprile *et al.*, 2011d).

Table 3.3: Predicted total γ background low-energy differential single scatter rate in the benchmark 50 kg fiducial volume with a veto energy threshold of 100 keV (active veto) for different components, along with a comparison of the expected rate in the case where the veto volume is not instrumented with PMTs (passive veto), for the *veto above bell* configuration. Errors only account for the statistical uncertainty of the simulation. Note that the contribution from the shield polyethylene is not included in the total (see text).

Component	Design	Rate (events $\text{keV}^{-1}\,\text{kg}^{-1}\,\text{d}^{-1}$)	
		Passive Veto	Active Veto
Total	baseline	20.66 ± 0.16	9.19 ± 0.10
PMTs	veto above bell	7.43 ± 0.05	3.41 ± 0.04
PMT Bases	veto above bell	0.96 ± 0.01	0.32 ± 0.01
Mesh Frames	veto above bell	0.13 ± 0.00	0.05 ± 0.00
Cryostat	veto above bell	9.89 ± 0.14	2.74 ± 0.07
Shield Polyethylene	veto above bell	17.42 ± 0.69	6.13 ± 0.41
Total	veto above bell	18.40 ± 0.15	6.52 ± 0.08

The predicted background reduction from the addition of the veto volume above the bell is substantial. Assuming that the shield polyethylene contribution becomes negligible with the addition of the OFHC copper layer, the predicted low-energy differential single scatter rate in the fiducial volume chosen drops to $6.52 \pm 0.10\,\text{events}\,\text{keV}^{-1}\,\text{kg}^{-1}\,\text{d}^{-1}$ from $9.19 \pm 0.08\,\text{events}\,\text{keV}^{-1}\,\text{kg}^{-1}\,\text{d}^{-1}$ for the baseline configuration. The reduction from the cryostat contribution is the largest at 32% while that of the PMT contribution is at 27%.

As was the case for the baseline configuration the advantage of instrumenting the veto volume with PMTs is clear when the veto volume extends above the bell, with almost a factor three improvement in the electronic recoil rate background rate at low energies.

3.1.3 Initial Sensitivity Projection

The results of the second round of simulations for the predicted low-energy electronic recoil single scatter rate in the benchmark 50 kg fiducial volume and a 100 keV veto threshold can be used to make a projection on the sensitivity of such a detector. Several additional assumptions about the detector performance have to be made to perform the computation but one can make educated guesses from the performance of the XENON10 detector to estimate many of those.

The energy range for the XENON10 dark matter search (Angle *et al.*, 2008a) was from 4.5 keV to 26.9 keV nuclear-recoil equivalent energy, based on a constant $\mathcal{L}_{\mathrm{eff}}$ of 0.19. Assuming a total light detection efficiency which is ×1.5 lower than what was achieved with XENON10 then a reasonable lower energy threshold could bet set at 7.5 keV nuclear-recoil energy. A similar reduction in light detection efficiency can be obtained from light propagation simulations for a detector with the dimensions of the baseline detector compared to the dimensions of the XENON10 detector using a LXe scintillation light absorption length of $\lambda_{\mathrm{abs}} = 100\,\mathrm{cm}$, a Rayleigh scattering length $\lambda_{\mathrm{Rayleigh}} = 30\,\mathrm{cm}$, and a PTFE reflectivity $\varrho_{\mathrm{PTFE}} = 0.95$ (Sec. 2.1 and Sec. 2.3.4). From the XENON10 electronic recoil light yield at 122 keV of $L_y = 3.0\,\mathrm{pe/keV}$ one would then expect a light yield of $2\,\mathrm{pe/keV}$. Consequently, using the most recent measurement of $\mathcal{L}_{\mathrm{eff}}$ available at the time (Aprile *et al.*, 2009) and the scintillation light field quenching at the design drift field of $E_d = 1\,\mathrm{kV/cm}$ (Fig. 2.9), the threshold estimate corresponds to, via Eq. 2.14, $\mathsf{S1}_l = 0.1370 \cdot 7.5\,\mathrm{keV} \cdot 2\,\mathrm{pe/keV} \cdot 0.92/0.65 \approx 3\,\mathrm{pe}$.

The sensitivity was calculated using the expressions of Sec. 1.3.1 for the expected WIMP interaction rate. The energy range assumed was from 7.5 keV to 30 keV. The electronic recoil discrimination assumed was 99.5% at a nuclear-recoil acceptance of 50%, a value supported by the XENON10 measurement (Angle *et al.*, 2008a). The electronic recoil background rate assumed was that in the 50 kg benchmark fiducial volume with a veto energy threshold of 100 keV, which leads to an expected number of background events of about one in a 90 live days run. The 90% confidence upper limit was calculated using

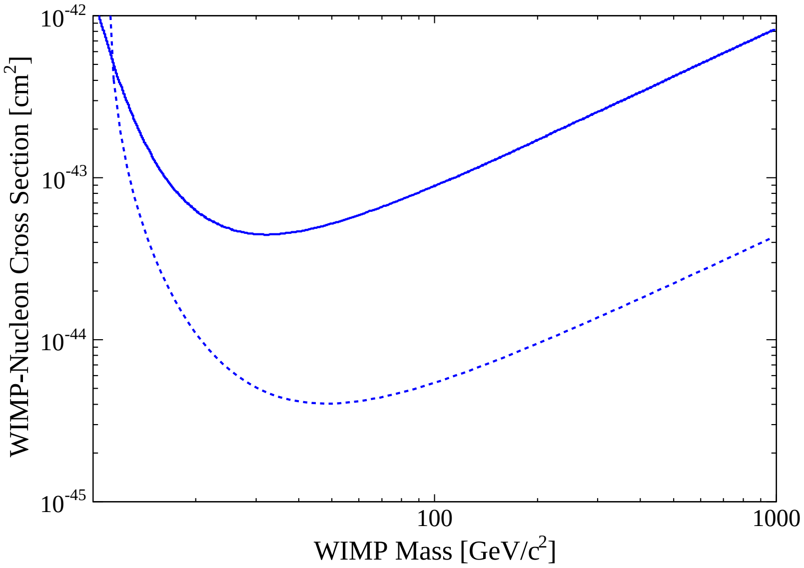

Figure 3.9: Projected sensitivity for the spin-independent WIMP-nucleon scattering cross section as a function of WIMP mass for the benchmark 50 kg fiducial volume and a veto threshold of 100 keV. See text for other assumptions.

Feldman-Cousins statistics (Feldman and Cousins, 1998) and an observed number of events given by rounding the expected number of events to the nearest integer. Fig. 3.9 shows the projected sensitivity for the spin-independent WIMP-nucleon scattering cross section as a function of WIMP mass for a 90 live days run, compared to the limit obtained for the XENON10 58.6 live days run (Angle *et al.*, 2008a), based on the assumption of an isothermal WIMP halo with $v_0 = 230\,\mathrm{km/s}$, density $0.3\,\mathrm{GeV\,c^{-2}\,cm^{-3}}$, and $v_{\mathrm{esc}} = 600\,\mathrm{km/s}$ (Lewin and Smith, 1996). Here the finite resolution of the S1 signal near threshold was not taken into account for the calculation of the limit. Since the expected WIMP recoil spectrum is a decreasing exponential, one would expect more recoils below the energy threshold (the energy that corresponds to the S1 threshold) to have a S1 signal that fluctuates above the S1 threshold than recoils above threshold whose S1 signal fluctuates below the S1 threshold (Sec. 4.6). This effect leads to a gain in sensitivity when the mean expected recoil energy is below threshold but was not taken into account here.

It is interesting to explore the potential sensitivity increase as a function of fiducial mass. The equivalent of Fig. 3.5 but for the *veto above bell* configuration gives the optimized expected electronic recoil background differential rate as a function fiducial mass. This information can then be used to predict the rate as a function of fiducial mass and thus

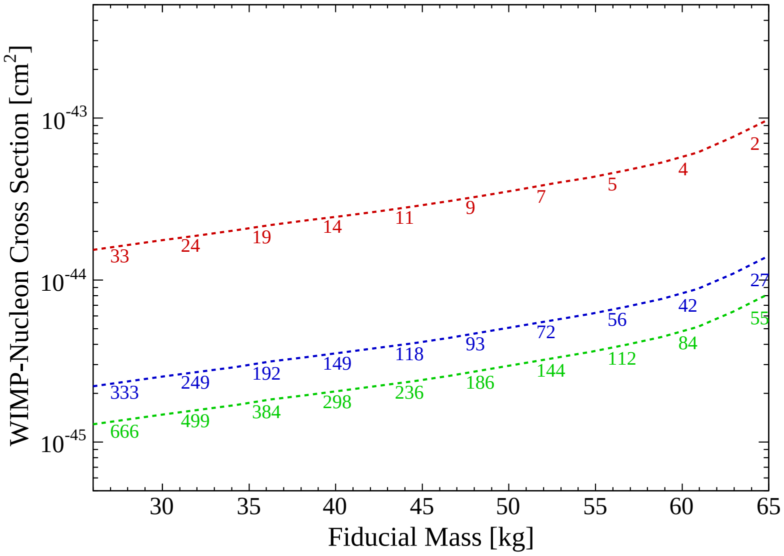

Figure 3.10: Projected sensitivity for the spin-independent WIMP-nucleon scattering cross section at a WIMP mass of 50 GeV/c^2 for the *veto above bell* configuration as a function of fiducial mass and for 0.1 (red dashed), 1 (blue dashed), and 2 (green dashed) expected background events. The numbers indicate the number of days before the expected number of background events is reached. See text for other assumptions.

the number of electronic recoil background events. The live time of a run with an expected 0.1, 1, or 2 electronic recoil events leaking in the signal region can be computed for each fiducial mass, with the assumption that the 99.5% rejection power does not depend on the size of the fiducial volume. It is then straightforward to compute the sensitivity using the same assumptions as earlier for each fiducial mass. Fig. 3.10 shows the result of such a computation. The upper limit is calculated using Feldman-Cousin statistics and assuming that the number of observed events is equal to the number of expected events. Under the assumptions taken, we see that this design can probe down to spin-independent WIMP-nucleon scattering cross sections of 10^{-46} cm^2 in the time frame of a year of data taking.

3.1.4 Final Design

The initial simulations showed the potential and the sensitivity of a LXe detector at the 100 kg scale with the basic characteristics chosen. The defining elements that the final design of the XENON100 detector would include are: the use of a bell to stabilize and set the LXe level between the meshes of the proportional amplification region, an extra ring of PMTs beyond the radius of the sensitive volume to improve the performance of the position reconstruction near the edge, a 4π active LXe veto volume instrumented with PMTs, and, as an additional step in the pursuit of background reduction, a novel cryogenics design with the pulse tube refrigerator (PTR) located far from the detector and outside its shielded cavity, along with PMT signal and high-voltage feedthroughs. The PTR would be housed in an extension of the vacuum cryostat outside the shield in a "cooling tower". All of the equipment required for the diverse operation modes of the detector, pressure sensors, turbo molecular pumps, diaphragm vacuum pumps, vacuum gauges, would then also be attached to the cryostat volume outside the passive shield, eliminating their contribution to the background. To enable a rapid deployment of the experiment the decision was made to design the XENON100 cryostat such that it would fit in the existing XENON10 passive shield, which had been designed with the next generation detector in mind (Sorensen, 2008). As mentioned earlier the cavity of the passive shield would later be upgraded with a 5 cm layer of OFHC copper to reduce the background contribution from the shield polyethylene.

Fig. 3.11 shows a technical drawing of the final detector design approved for construction while Fig. 3.12 shows the detector in the passive shield with the cooling tower and feedthroughs outside the passive shield.

The cylindrical target volume has a radius of 15.3 cm and a height of 30.6 cm. It is optically separated from the veto volume by 24 6.4 mm thick PTFE panels held by two copper rings, one on top and one the bottom. The PTFE panels are slotted into one another to preserve the optical separation at LXe temperature, a temperature at which the PTFE thermal contraction is substantial (PTFE has a linear thermal expansion coefficient of $\sim 1.2 \times 10^{-4}\,\mathrm{K}^{-1}$). Since the panels are held by copper rings this also prevents the deformation of the assembly due to the different thermal expansion coefficients of PTFE and copper. The TPC volume thus contracts vertically with the PTFE thermal expansion coefficient and horizontally with that of copper. The TPC volume is closed on the bottom by a cathode mesh and on top by a grounded mesh (bottom mesh). Copper wire field shaping rings hold the PTFE panels in a rigid structure and ensure a uniform drift field. The liquid level is kept at a fixed and precise height by a stainless steel diving bell, to which the top copper ring of the TPC is attached. The bell thus supports the weight of the entire inner structure of the detector. The structure is reinforced by additional PTFE rods in the veto volume. An anode mesh, 5 mm above the bottom mesh, and another grounded mesh, the top mesh, 5 mm above the anode, are all secured in place by a PTFE

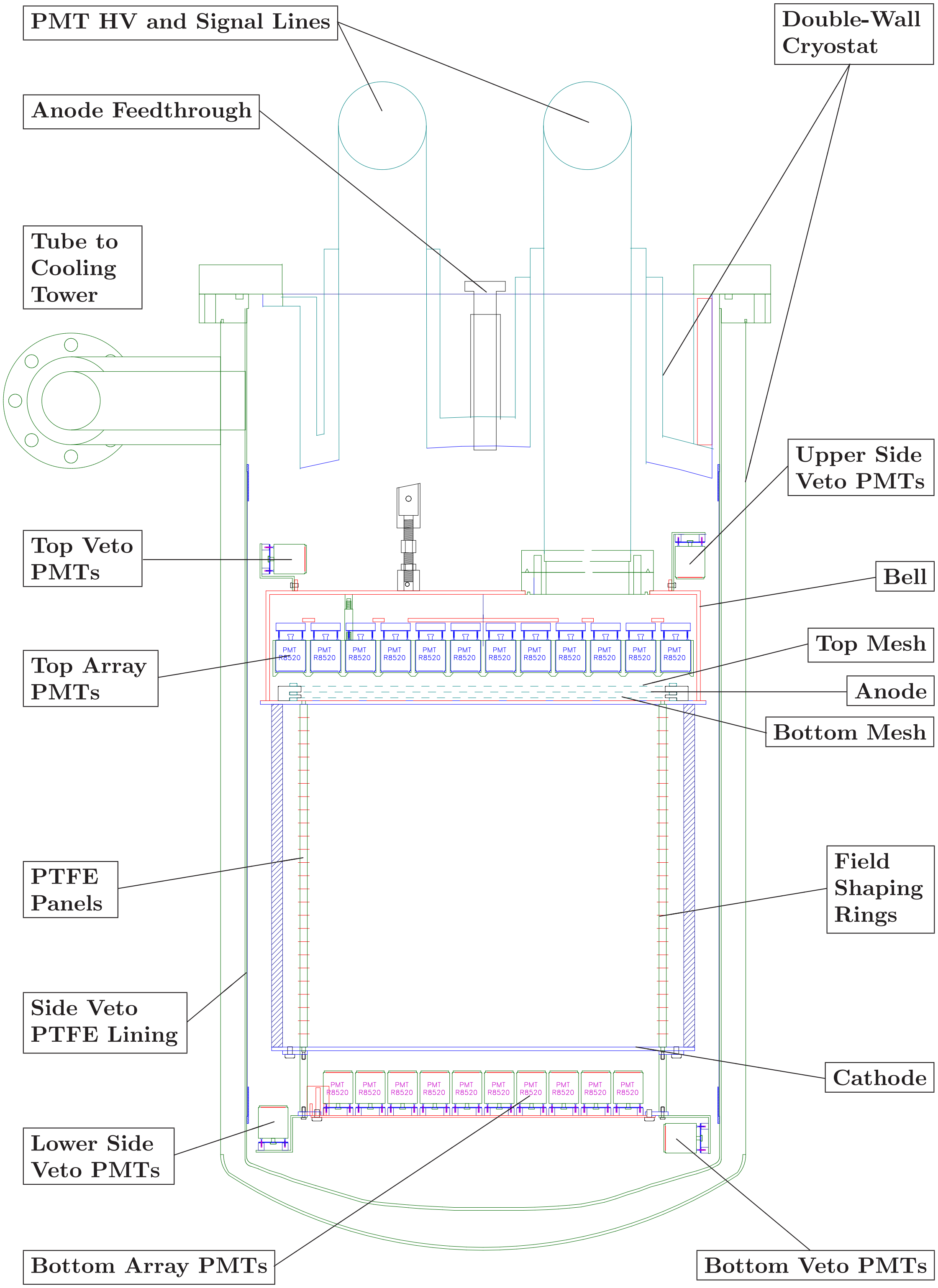

Figure 3.11: Technical drawing of the XENON100 detector. Drawing by Dr. K. Giboni.

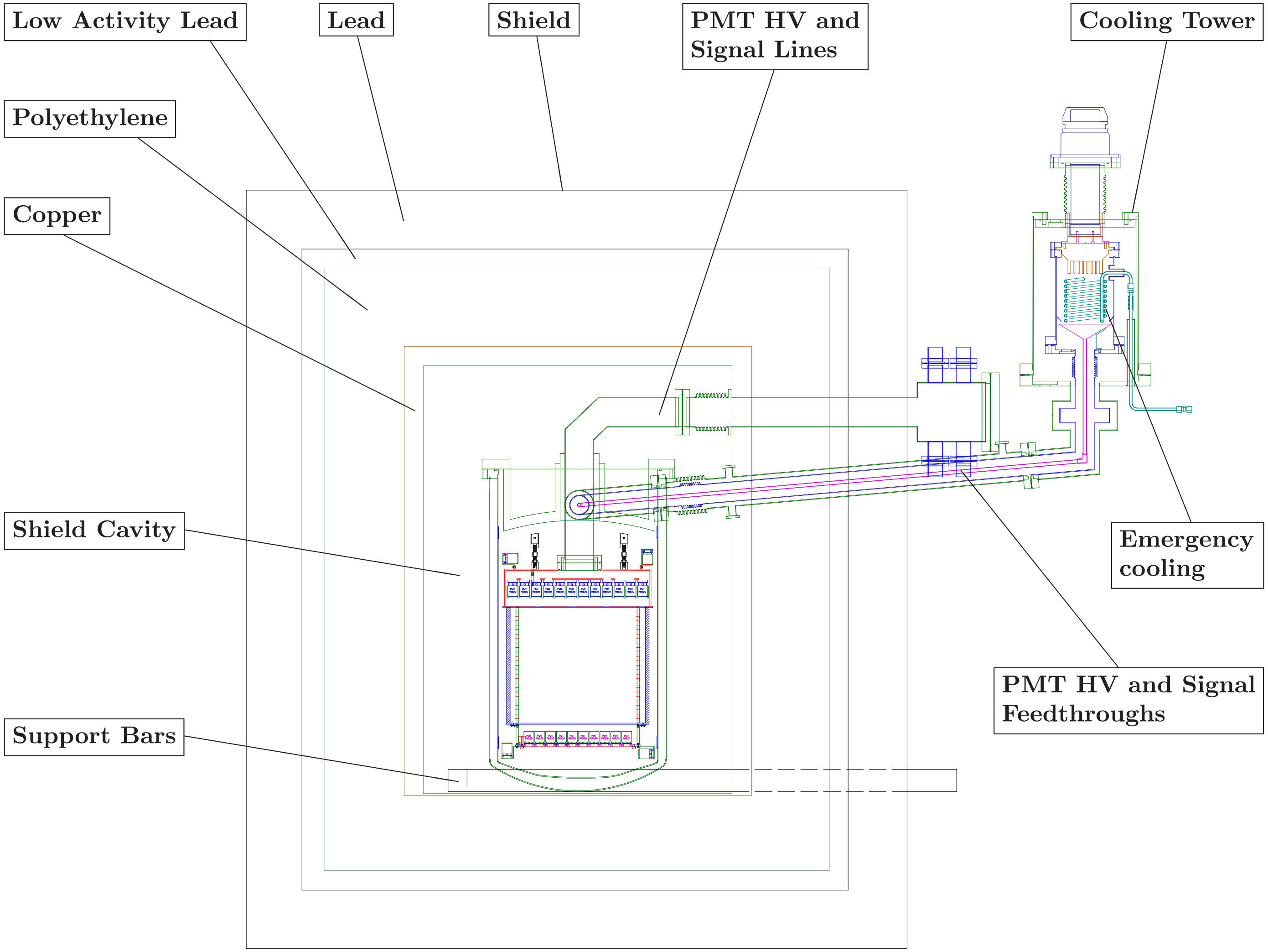

Figure 3.12: Technical drawing of the XENON100 detector inside the passive shield.

holding arrangement. The liquid level is kept between the bottom mesh and the anode. Custom made low-radioactivity high-voltage feedthroughs are used to bias the cathode and the anode, providing the drift field in the TPC and the proportional amplification field in the GXe.

Two PMT arrays, one in the GXe, above the TPC, and one in the LXe, below the cathode, composed respectively of 98 and 80 PMTs, detect the direct and proportional scintillation light of interactions in the TPC volume. The PMTs of the top array are inserted in individual compartments in a large PTFE structure which holds them in place, the top array PMT holder. The top array PMT holder itself is attached to the bell with four screws into threaded posts welded inside the bell. The bottom array PMTs are attached to a copper plate using their Cirlex® base. Three screws hold in place each base and short PTFE tubes keep the base at a fixed distance from the bottom array copper plate. The PTFE tubes are slightly compressible and thus permit the alignment of each PMT by applying the appropriate amount of force on each screw. Since the PMT base employs a grounded-anode scheme (Sec. 3.3.2) and since the PMT bodies are each biased with a different negative voltage to obtain a small dispersion in the PMT gains, it is important to keep the PMT bodies from touching each other. An arrangement of shorter PTFE panels, also held by two copper rings, is fixed to the bottom copper ring of the TPC and holds the bottom array copper plate. The veto volume is instrumented with 64 PMTs separated into two rings, one above the bell and one below the TPC, of alternating horizontally and vertically mounted PMTs. The PMTs are mounted on L-shaped or S-shaped copper pieces, themselves fixed to the bell in the case of the top veto ring PMTs or fixed to the bottom PTFE panels assembly in the case of the bottom veto ring PMTs. The exterior surface of the veto volume is lined by a thin PTFE sheet to improve its light collection efficiency.

The PMT high-voltage and signal cables, as well as other instrumentation cabling, travel along two stainless steel pipes which extend outside the passive shield. As mentioned earlier, with this configuration the ceramic electrical feedthroughs, which usually cannot easily be found with a low radioactivity level, will have a negligible contribution to the background. In Fig. 3.11, the pipe on the left carries the cables from the bottom array PMTs and the veto PMTs while the pipe on the right carries those of the top array PMTs.

The cryostat is a double-wall vacuum insulated stainless steel vessel. The cryostat extends outside the passive shield and connects to the cooling tower. The PTR is mounted on top of the cooling tower, fixed to a copper piece that seals off the inside volume from the insulation vacuum and acts as a cold finger. The bottom of the cooling tower is connected to the main cryostat with a vacuum insulated pipe at a height above the liquid level. GXe condenses on the cold finger and LXe droplets are collected by a funnel at the base of the cooling tower. LXe flows back into the main cryostat through a smaller pipe at the center of the insulated pipe. The insulated pipe is inclined by 5° with respect to the horizontal to allow gravity to drive the liquid flow. By remotely cooling the GXe in this manner, the total mass of steel within the shield cavity can be reduced drastically. Aluminized mylar superinsulation films are used to reduce the radiative heat transfer from the outside wall of the cryostat to the inside wall at LXe temperature, both for the main cryostat and the cooling tower.

An exhaustive description of the XENON100 detector and its subsystems is given in Sec. 3.3. In the next section we will describe the construction of the detector and present many of the details of the steps involved in the assembly and the metamorphosis of the design into its concrete realization.

3.2 Construction

The machining of the parts of the XENON100 detector was done mostly at the machine shop of the Laboratori Nazionali del Gran Sasso (LNGS), with the exception of the cooling tower which was machined and assembled at Columbia University before being shipped to LNGS. Some other components such as the PTFE top array PMT holder and TPC panels, mesh frames and meshes, LXe level meters, were fabricated at other collaborating institutions and sent to LNGS. The construction, assembly and initial tests of the detector took place in the external laboratory buildings at LNGS.

In the following sections all major assembly steps from the cooling tower assembly, to the completed inner detector structure, to the installation underground, are described. Sec. 3.2.1 discusses the cooling tower assembly, Sec. 3.2.2 the cryostat, Sec. 3.2.3 the TPC, Sec. 3.2.4 the PMT arrays, Sec. 3.2.5 the high-voltage connections, Sec. 3.2.7 the installation underground, and Secs. 3.2.8-3.2.11 the first through the fourth opening of the detector cryostat for the upgrade of specific components.

3.2.1 Cooling Tower Assembly

The cooling tower allows the remote cooling of the detector through the liquefaction of Xe on the cold finger and the subsequent evaporation of LXe drops on other surfaces. By creating a predefined path where LXe can flow from the cooling tower to the main detector cryostat, with sufficient thermal insulation from the outside environment, the LXe will progressively cool down the flow path to LXe temperature by several condensation-evaporation cycles. Once the path is at an appropriate temperature and the LXe flow can reach the main detector vessel this process continues with the cooling of the main cryostat and the inner detector structure.

Fig. 3.13 (left) shows a technical drawing of the cooling tower. The outer vessel (dark green) is closed on the bottom by a ConFlat® (CF) flange and on the top by a flange with a Viton® fluoroelastomer o-ring. A stainless steel bellow between the PTR flange and the cooling tower top flange allows for the difference in thermal contraction of the inner vessel and the PTR with respect to the outer vessel. The inner vessel (dark blue) is closed on top and bottom by CF flanges. The top flange of the inner vessel holds the cold finger (orange) in place and is sealed with a custom-made pure aluminium ring that sits in a “v” groove in the flange. The aluminium ring is deformed when the flange is first tightened. The lower part of the cold finger is comb-shaped to maximize the contact surface between the cold finger and the GXe.

The funnel collects LXe droplets and forces the LXe to flow toward the main vessel in a stainless steel pipe (pink) held in the center of the vacuum insulated double-wall pipe with PTFE spacers. The relatively low heat conductivity of PTFE means not much heat leaks from the spacers to the center pipe. The poor heat conductivity of GXe also helps in keeping the heat influx from the inner wall to the center pipe low and ensuring that the LXe flow can reach the main vessel. The inner vessel of the cooling tower is also surrounded by multiple layers of aluminized mylar film superinsulation to reduce the radiative heat transfer from the outside vessel wall to the inside vessel.

The PTR cold head is connected to the cold finger through a cylindrical copper cup (pink) onto which are glued resistive heaters. The temperatures above and below the heater are measured with 4-wire Pt-100 temperature sensors. The temperature of the cold finger can thus be adjusted by controlling the power output of the heaters. A stainless steel tubing coil (turquoise) below the cold finger and whose input and output reach outside of the cooling tower can be used to flow liquid nitrogen and replace the primary cooling system in the case of an emergency.

Two electrical vacuum feedthroughs, on the bottom of the outer and inner vessels, allow instrumentation cables to reach the interior volume. The bottom temperature sensor (see Sec. 3.3.4) was initially connected via these feedthroughs. They were intended for sensors that stay inside the cooling tower or the bottom of the main vessel. Two additional electrical feedthroughs on the top flange of the outer vessel (only one shown) are used to apply current to the heaters and to connect the PTR coldhead and cold finger temperature sensors.

Fig. 3.13 (right) shows the assembled cooling tower during the installation of the PTR cooling system components. The superinsulation is covering the inner vessel. An aluminium frame supports the cooling tower and allows it to rest on a horizontal surface. The PTR motor-valve and buffer tank are also mounted on this aluminium frame. The insulation vacuum pumping port can be seen on the bottom right of the cooling tower bottom flange. A host of required equipment is connected to the main detector vessel volume through the cooling tower. A Bourdon pressure gauge, a pressure transducer for use during positive pressure operations, a safety burst disc, and a vacuum pressure gauge for use during pump down operations, are all connected to the cooling tower inner GXe volume.

Fig. 3.14 (left) shows a picture of the cooling tower funnel and bottom flanges of the inner and outer vessels. The initial bottom temperature sensor cables can be seen running in the pipe to the main detector vessel. The cooling tower pumping port as well as the connections to the emergency cooling coil are visible. Fig. 3.14 (right) presents a close view of the PTR coldhead, heater cup and cold finger coupling. Two of the four resistors can be seen in the center of the picture. On the right, the coldhead (top) and cold finger (bottom) temperature sensor cables can be seen along with their connection to the feedthrough. The heater connection feedthrough is not visible in this picture.

3.2.2 Cryostat Assembly

The cryostat was machined and assembled in November and December 2007. Fig. 3.15 shows a picture of the completed main cryostat. The cryostat wall, the two top pipes and the cover were all formed out of 1.5 mm 316Ti stainless steel. The curved bottom was formed and the top flange machined out of 2.5 mm and 25 mm 316Ti stainless steel,

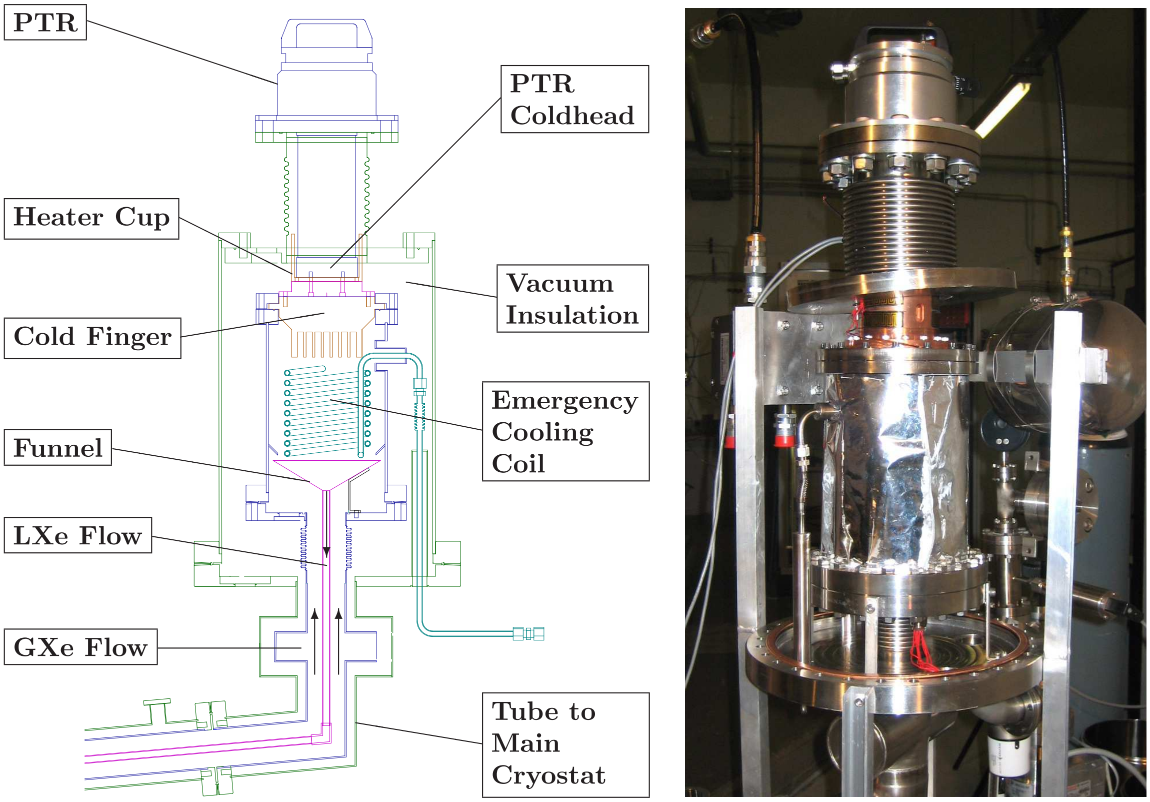

Figure 3.13: Technical drawing of the XENON100 cooling tower (left) and picture of the cooling tower during the installation of the components of the PTR cooling system (right). The motor-valve and the buffer tank are mounted on the frame that supports the cooling tower. The Bourdon pressure gauge, the pressure transducer, the safety burst disc, and the vacuum pressure gauge (used during pump down operations) of the detector inner vessel are connected to the bottom of the cooling tower.

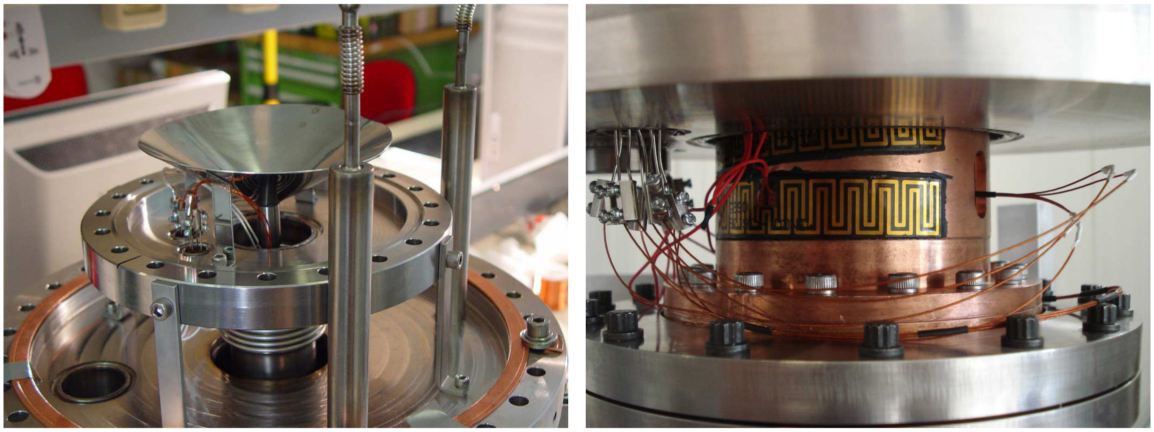

Figure 3.14: Funnel and bottom flange of the inner vessel of the cooling tower (left) and the PTR, heater cup, cold finger coupling at the top of the cooling tower (right). The GXe that condenses on the combed structure of the cold finger (see Fig. 3.13, left) drips in the funnel and flows back to the detector vessel in a stainless steel pipe in the center of the double-wall vacuum insulated pipe that connects the cooling tower to the main cryostat. Resistive heaters are glued to the cylindrical copper cup between the PTR coldhead and the cooling tower cold finger to regulate the temperature of the cold finger. The coldhead and cold finger 4-wire Pt-100 temperature sensors are connected to the electrical feedthrough on the top flange.

respectively. The steel used was selected for its low radioactivity (Aprile *et al.*, 2011d).

The bottom part of the cryostat rests on three leveling mounts. The two mounts in the back of Fig. 3.15 (left) are equipped with couplings that allow the leveling of the cryostat from outside the passive shield. The bottom part of the cryostat will be installed permanently in the passive shield along with the cooling tower and the double-wall pipe connecting them. When completed, the inner detector structure will be attached to the bottom of the bell. The weight of the bell and the future structure below is held by the cryostat lid via the pipe attached to the bell and two additional supports. The supports connect the lid to the bell with left-right handed screws to enable the leveling of the bell with respect to the cryostat lid. The pipe on the left will carry cables from the bottom array and veto PMTs to the feedthroughs while the pipe on the right will carry those of the top array PMTs. The pipe on the right and the bell constitute a separate GXe volume with higher pressure than the GXe outside of the bell.

Fig. 3.16 (left) shows the inside of the cryostat after the veto PTFE lining has been installed. Welded steel holders maintain the PTFE lining in place. The double-wall pipe connecting the cooling tower and the cryostat can be seen on the top part of the cryostat

Figure 3.15: The completed main cryostat vessel (left) during a lowering test of the cryostat lid with the diving bell attached, using a Y-shaped lifting apparatus (right). The bottom part of the cryostat rests on three leveling mounts. The four vertical rods align the top and bottom part of the cryostat during a lowering operation. When assembled, the inner detector structure will be attached to the bottom of the bell. The PMT HV and signal cables will run from the PMT arrays to the feedthroughs at the end of the two pipes on top. From left to right: the author, A. Ferella (University of Zurich), and K. Giboni (Columbia University).

as well as the end of the center pipe that carries the LXe flow from the cooling tower funnel to the cryostat. The recirculation line, a copper pipe that runs from the bottom of the cryostat and out through double-wall pipe connection to the cooling tower, serves as the input to the Xe recirculation system (Sec. 3.3.6).

Fig. 3.16 (right) presents a closer view of the bell and cryostat lid connection (upside down). As mentioned earlier, the two supports with left-right threaded screws serve both to share the load of the future inner detector structure attached to the bell and to level it with respect to the cryostat lid. The semi-cylindrical cavity in the side of the cryostat lid lines up with the double-wall pipe connection to the cooling tower. The liquid level adjustment mechanism is also seen from up close in this picture. A small 0.25 in. stainless steel tube runs horizontally from the larger pipe connection to the bell and then vertically to the side of the bell. The LXe level adjustment tube is bellowed near its connection to the larger pipe and can be vertically adjusted with a linear motion feedthrough. Since the GXe volume inside the bell is at a higher pressure than the GXe volume above it, the LXe level inside the bell is maintained at fixed height and can be adjusted by raising or lowering the level adjustment tube .

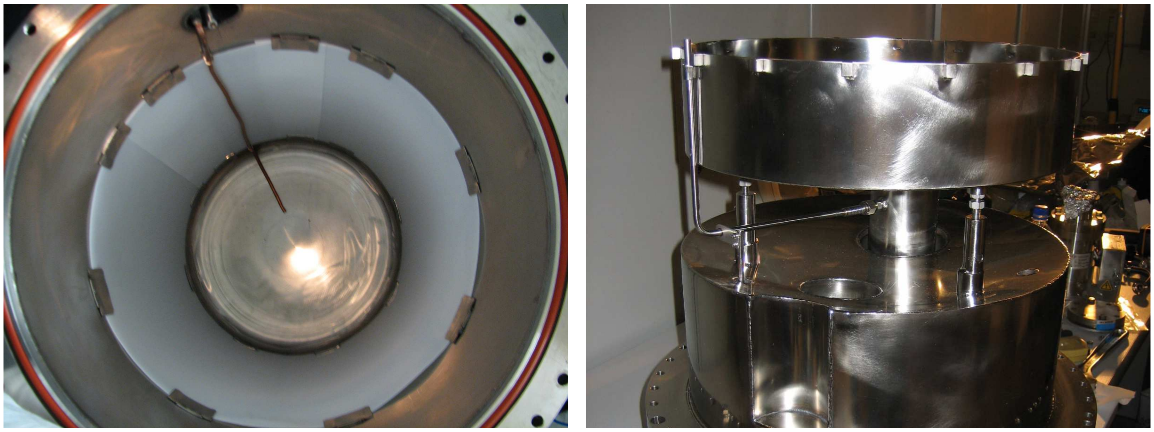

Figure 3.16: Picture of the inside of the cryostat (left) and picture of the cryostat lid and bell coupling (right). The veto PTFE lining is maintained in place by welded steel holders. LXe flowing from the cooling tower funnel reaches the main cryostat and drips down at the end of center pipe. LXe from the bottom of the detector is extracted via the recirculation line. The LXe level inside the bell can be adjusted by raising or lowering the LXe level adjustment tube via a linear motion feedthrough.

Fig. 3.17 (left) shows a picture of the top of the cryostat lid. On the left in black is the linear motion feedthrough for the LXe level adjustment. Behind the motion feedthrough (not visible) and on the double-wall pipe to the cooling tower are two pumping ports for the cryostat lid and cooling tower pipe insulation vacua, respectively. The CF-16 flange in the middle of the picture will be for the future anode high-voltage feedthrough while the one on the right will be for the cathode feedthrough. Fig. 3.17 (right) shows a picture of the cryostat after closing all flanges, ready for pumping down operations. The white wooden construction simulates the passive shield door for the installation underground. As mentioned earlier, the cooling tower, the double-wall pipe connecting it to the main cryostat, and the bottom part of the main cryostat are foreseen to remain permanently underground after the initial installation. If repairs or upgrades are necessary, the cryostat top assembly and the future inner detector structure can be transported in a special transport vessel to a clean room above ground.

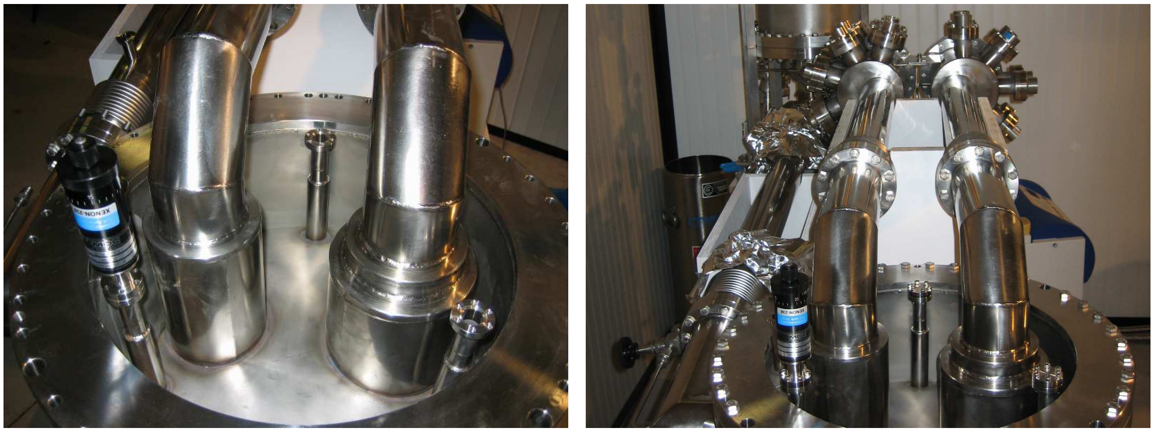

Figure 3.17: A top view of the cryostat lid (left) and of the entire top assembly and cooling tower connection (right). The LXe level adjustment motion feedthrough is visible on the left along with the two flanges for the future anode and cathode high-voltage feedthroughs. The white wooden support represents the position of the passive shield door underground.

After the assembly of the cryostat above ground a first leak test of the vessel was performed. One of the outer vessel feedthroughs of the cooling tower vessel and one of the inner vessel feedthroughs were found to leak at rates of $3 \times 10^{-3}\,\mathrm{mbar\,L\,s^{-1}}$ and $7 \times 10^{-7}\,\mathrm{mbar\,L\,s^{-1}}$, respectively. Given the low leak rate from the insulation volume to the internal volume a first test of the cooling system was performed on December 17th 2007, with the successful liquefaction of 18 kg of Xe into the empty cryostat vessel. The initial filling speed achieved was 1.7 kg/h but increased to 2.4 kg/h towards the end of the filling operation. A test of the recirculation system above ground was also performed and resulted in stable detector parameters. The maximum recirculation speed tested was ~5 SLPM. This test allowed to verify the operation and short term stability of the cooling system. The test revealed that the actual cooling power of the PTR with the helium compressor used was much larger than the available power to the electrical heaters. The temperature control system was thus modified to employ an external power supply with enough power to counteract the PTR (Sec. 3.3.5).

The cooling tower was disassembled and the damaged feedthroughs repaired and a new leak check of the cryostat vessel was performed on January 20th 2008, with no sizeable leaks detected. A new cooling test followed on the 22nd with the modified temperature control system and its successful completion concluded the first commissioning phase of the cryostat vessel. The cryostat and the cooling tower would be installed underground and the passive shield modified over the next weeks while the inner structure of the detector was being assembled.

3.2.3 TPC Assembly

The first component of the inner detector structure assembled was the TPC. Fig. 3.18 shows the top and bottom copper ring frames of the TPC during the installation of the side PTFE panels. The PTFE support rods were first fixed to both rings and then each panel was inserted in a slot in the bottom ring and screwed to the top ring. PTFE panels have vertical grooves such that each successive panel interlocks in the next. After all PTFE side panels were installed the next step was the field shaping wires. The TPC has 40 horizontal grooves for the field shaping wires, both inside and outside the PTFE panels. Additionally, each panel has two holes per groove that connect the inside and outside grooves. A single wire makes up each field shaping “ring” but makes the equivalent of two turns around the circumference going inside and outside of each successive hole.

The completed field cage is shown in Fig. 3.19 also with the bottom, anode and top meshes installed (left). Eight PTFE holding structures maintain the meshes in place and are secured to the TPC top copper ring with screws. The bottom mesh is held at ground potential by being firmly set against the copper ring, also at ground potential, by the PTFE holders. The bottom mesh and the copper ring have a hole through which the anode positive high-voltage connection is made. A threaded copper rod screwed firmly in the anode ring extends below the ring and is insulated from it with a PTFE cylinder. Fig. 3.20 (left) shows

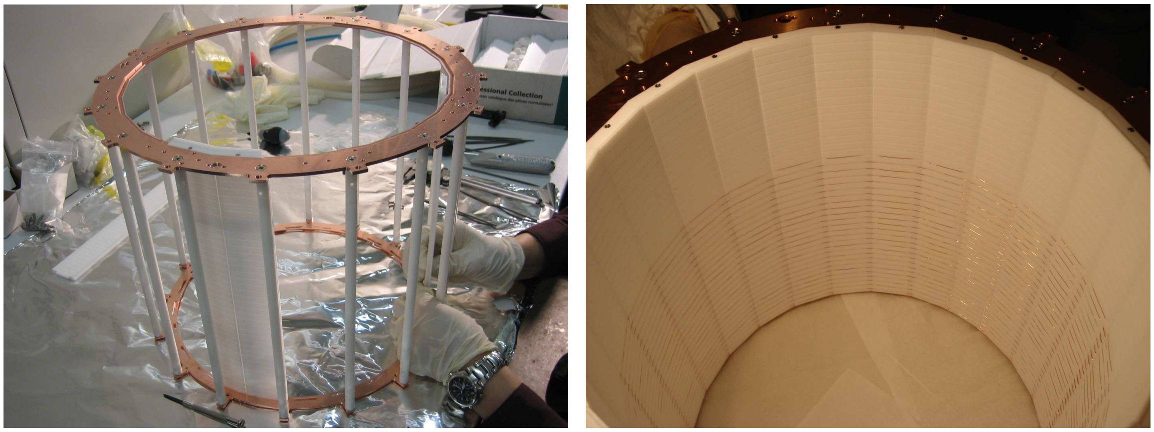

Figure 3.18: Picture of the top and bottom copper ring frames of the TPC, along with its 16 PTFE support rods, during the installation of the PTFE panels (left), and a picture of the TPC during the installation of the field shaping copper wires (right). Each panel is inserted in a slot in the bottom copper ring and screwed to the top copper ring.

the assembled connection. The high-voltage connection to the copper rod will be in LXe, a material with a very good dielectric strength (Sec. 2.1), and consequently that connection can be left uninsulated. This is in contrast to the anode ring connection, which lies in GXe and needs to be insulated.

The field shaping wires are connected to a resistive voltage divider circuit to provide each wire with the appropriate graded potential and thus ensure the uniformity of the drift field. The shaping wires are connected to each other with 700 MΩ resistors. The resistors used are Japan Finechem precision plate resistors type SM5D. A picture of the original arrangement is shown in Fig. 3.20 (right) but was later modified (see Sec. 3.2.9). The cathode high-voltage appropriately biases the circuit.

3.2.4 PMT Arrays Assembly

The second component of the inner detector structure assembled was the top, bottom, and veto PMT arrays. The PMT HV and signal cables are connected directly from the PMT base to multipin electrical feedthroughs at the end of the two pipes that serve as cable conduits (see Fig. 3.17). For the PMT HV, MDC KAP1 Kapton® insulated silver-plated copper wires were used. For the PMT signal, 50 Ω Belden 83265 RG178/U coaxial cables were used with silver-plated copper conductor and braid. The dielectric is PTFE. The outer fluorinated ethylene propylene (FEP) jackets of the RG178 cables were removed to prevent

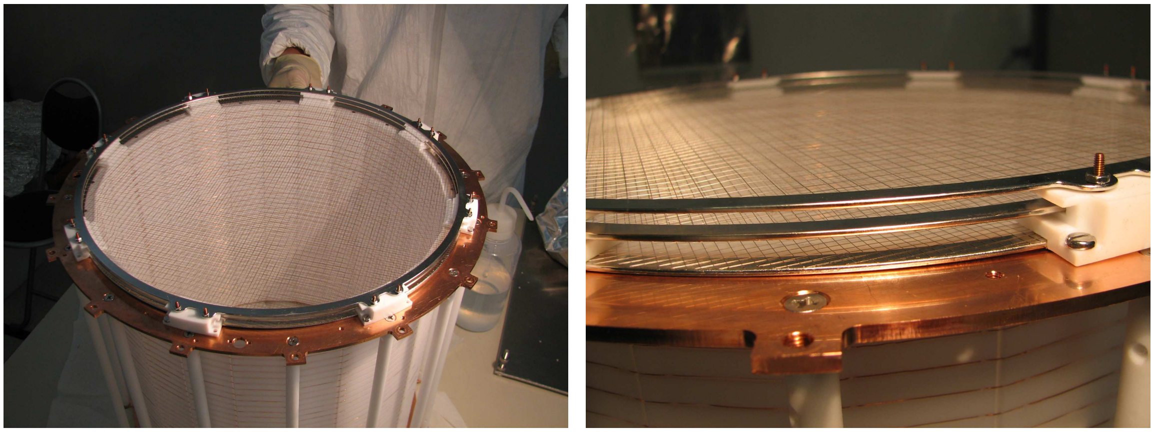

Figure 3.19: Picture of the TPC after the installation of the field shaping wires and with the square mesh top, anode, and bottom meshes (left), and a close up of the mesh stack of the proportional amplification region (right). The meshes are maintained in place by eight PTFE holders with screws fixed to the top TPC copper ring. During operation the LXe level is maintained between the bottom mesh and the anode.

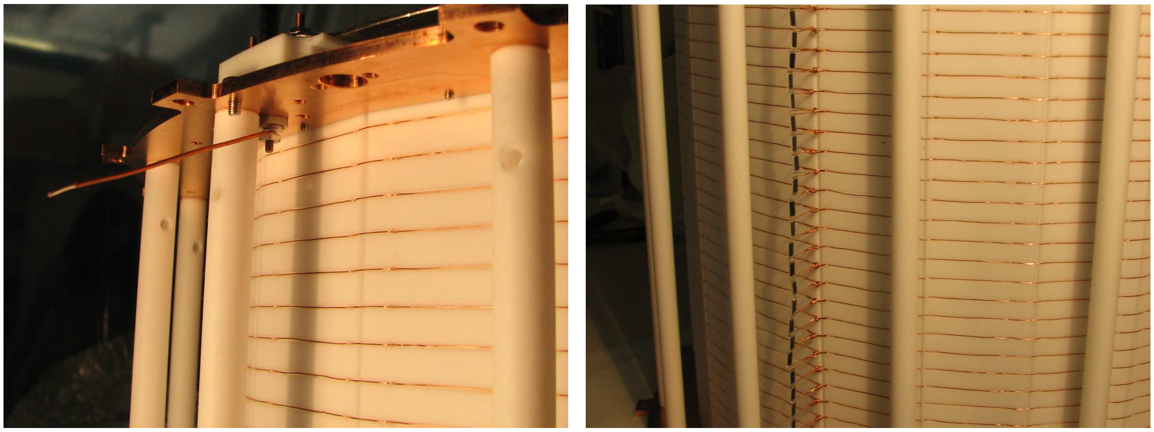

Figure 3.20: Picture of the anode connector below the TPC top copper ring (left) and of the TPC field shaping wires resistive voltage divider circuit (right).

the potential outgassing of trapped gases between the jacket and the braid. To easily keep track of each PMT HV and signal cable and its associated position within the PMT arrays all PMT bases were installed sequentially in their respective PMT arrays. Both HV and signal cables were first cut to length, soldered to the PMT base, and had their connector pins soldered. The multipin feedthrough used is a Kyocera 16522 48-pin type feedthrough. The in-vacuum connector is a ceramic piece into which each push pin is locked and the whole in-vacuum connector is inserted on the feedthrough.

The top array was assembled first. Fig. 3.21 (top left) shows a picture of the PTFE top array PMT holder. The PMT bases were all placed in their corresponding cavity in the PTFE holder and the HV and signal cables were grouped into bundles of 48 for the HV feedthroughs and 24 for the signal feedthroughs. The pins of each base were sequentially inserted into the in-vacuum ceramic connector making it easier to manage by simply labelling the connector instead of each individual cable. To install the top array the cryostat top assembly was positioned on a working table upside down, with the bell under surface facing up. The in-vacuum connectors were then fed one by one through the bell cable conduit. Fig. 3.21 (top right) shows the end of the cable conduit after all ceramic connectors had been fed through. The PTFE holder with the individual bases in each cavity (and the other end of their cables) rested on a platform next to the bell during this operation. Subsequently the PMTs of the top array were inserted one by one into their corresponding bases and placed into the correct PTFE holder cavities. Once all PMTs were placed, they were secured with copper rings onto the PTFE holder. Each PMT base of the top array has a small PTFE spacer that prevents the braids of the signal cable to accidentally touch any of the PMT pins. The PTFE top array PMT holder with secured PMTs is shown in Fig. 3.21 (bottom left). Finally, with all PMTs secured, the PTFE holder was turned upside down, and lowered into the bell. The positions of the four threaded stands to which the top array is fixed were indicated by four stainless steel rods as the PTFE holder was lowered. After the PTFE holder was fixed to the bell and the in-vacuum connectors were pushed onto the feedthroughs the cryostat top assembly, now including the top PMT array, was rotated into its intended position and placed on a custom-built stand designed to hold the assembly during transport underground. The previously assembled TPC with top, anode, and bottom meshes installed was then fixed to the bell.

The bottom array was assembled next. In a procedure analogous to that of the assembly

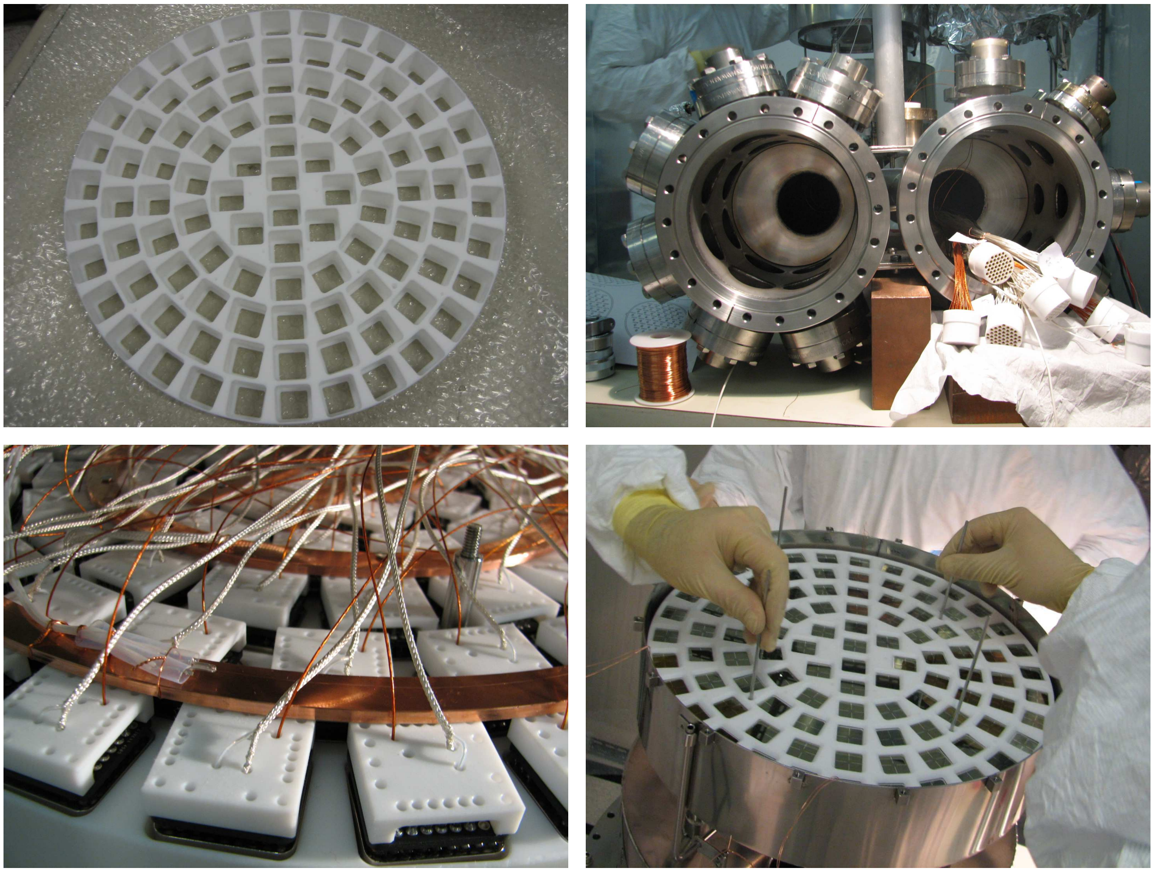

Figure 3.21: Picture of the PTFE top array PMT holder (top left). Each top array PMT base was put in its corresponding cavity in the PMT holder and its HV and signal cable connected to the desired multipin feedthrough connector before being fed through the cable conduit. The PMT HV and signal cables after having been fed through the bell cable conduit (top right). All PMTs were then inserted in the top array bases and put back into the PTFE PMT holder. The top array PMTs are held in place in the PTFE holder by copper rings (bottom left). With the copper ring holders preventing the PMTs from falling off of the PTFE holder, the top array was turned upside down and lowered (gently) into the bell. The assembled top PMT array after the delicate lowering operation (bottom right). Four rods indicate the position of the threaded stands which will later on hold the top array.

of the top array, all PMT bases were first fixed to the bottom array copper plate and their cable pins inserted into the in-vacuum connectors to easily follow the designed feedthrough pin to PMT channel mapping. Next, all PMTs were inserted into their bases and each PMT was properly aligned with the three mount point screws and PTFE spacers mentioned earlier. Fig. 3.22 shows the bottom array during (left) and after (right) its assembly. After all PMTs were installed, the lower PTFE panels and copper ring frames were joined together to form the bottom PMT array holding assembly and the bottom veto copper PMT supports were attached to it. The bottom PMT copper plate was then fixed to the array holding assembly and the whole structure was attached to the bottom copper ring of the TPC. The cathode mesh was installed prior to this step as it is pressed between the bottom copper ring of the TPC and the top copper ring of the bottom PMT array holding assembly. Fig. 3.23 (left) shows the result. At this point all PMT cables were still grouped and inserted into their proper in-vacuum connectors but not yet fed through the cable conduit.

Figure 3.22: Picture of the bottom PMT array during assembly (left) and of the completed array (right). The three screws and PTFE spacers that allow the alignment of the bottom array PMTs can be seen on both pictures.

The bottom and top veto PMTs were installed last. The top veto copper supports were fixed to the bell and the PMT bases were attached to both the bottom and top veto supports. After the installation of all PMT bases of the bottom and top veto the PMT HV and signal cables were grouped into four cable bundles that would run along the TPC side upwards before entering the cable conduit. This ensured that if subsequent disassemblies of the inner detector were required, one could easily reach the TPC and separate the bottom array from it and slide the TPC horizontally to access the top array. The arrangement of the cables into few separate bundles also allows an easier routing of the cables to avoid that their braids, held at ground potential, touch any of the field shaping wires or the bottom copper ring of the TPC, which is biased to the cathode potential. The last step involved feeding the cables of the top and bottom veto arrays and their in-vacuum connectors all at once through the cable conduit, and connecting them to the multipin feedthroughs. The operations was much simpler than that of the top array cables in which the in-vacuum connectors were fed one by one. Fig. 3.23 (top right) shows two of the cable bundles next to the completed bottom veto array. Fig. 3.23 (bottom right) shows a view of the top veto after the PMTs were installed.

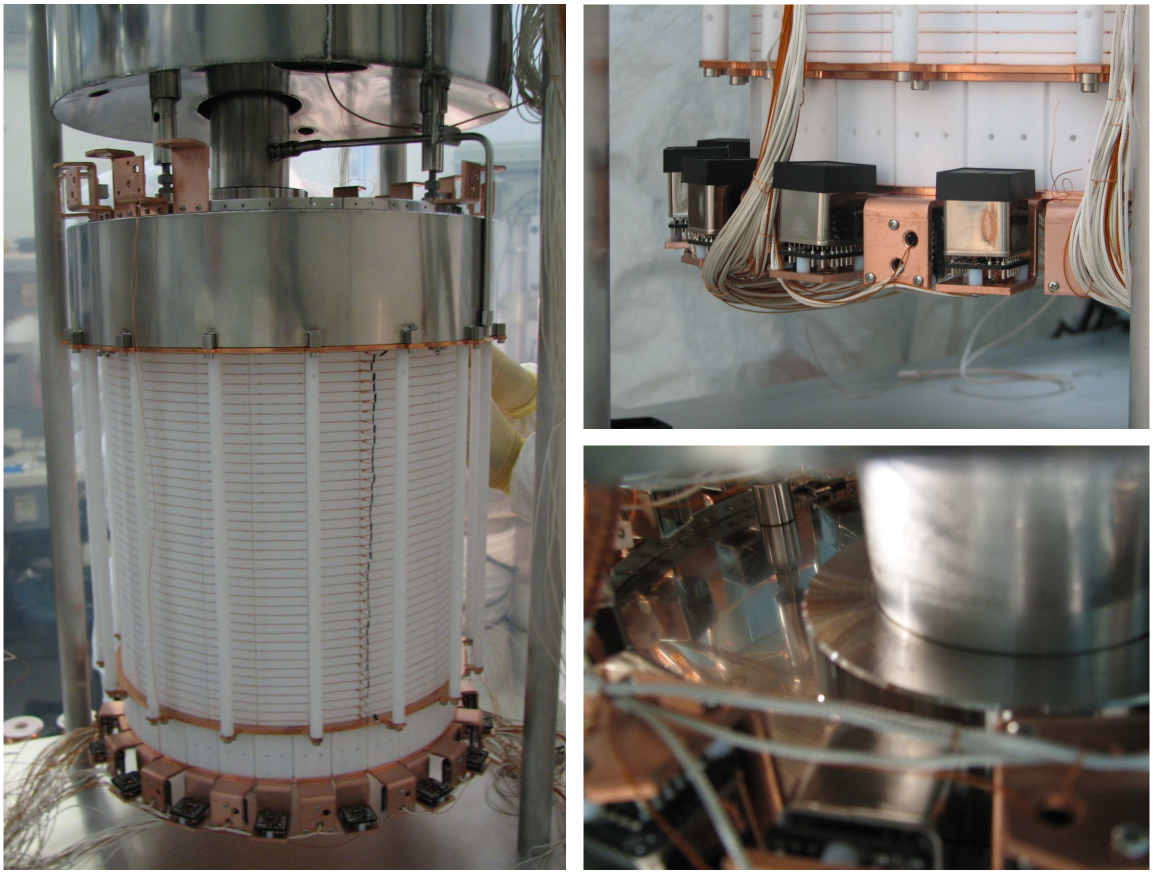

Figure 3.23: Picture of the inner detector structure after the installation of the bottom array and during the veto PMT installation (left). Two pictures of the completed bottom veto ring of upwards/inwards alternating PMTs (top right) and of the top veto PMT ring of downwards/inwards alternating PMTs (bottom right).

3.2.5 High Voltage Connections

The anode and cathode meshes feedthrough connections were made after the PMT arrays were assembled. The feedthroughs are custom-made low radioactivity feedthroughs. The inner cores of the anode and cathode feedthroughs consist, respectively, of 0.125 in. and 0.0625 in. diameter stainless steel rods inserted into a 0.25 in. diameter PTFE tube. During the construction of the feedthrough the PTFE tube is heated to facilitate the sliding of the stainless steel rod. The air side of the feedthrough is composed of a 0.25 in. Swagelok® male connector welded onto a CF-16 flange. The PTFE insulation and stainless steel rod assembly is simply inserted into the connector such that the desired length extends above and below the flange. When tightened, the female nut presses the front ferrule and creates a seal on the outside diameter of the PTFE tube. A copper braid is slid over the PTFE tube and acts as the outer conductor of the feedthrough. A flexible stainless steel rod is welded to the bottom of the CF-16 flange and wound around the braid to hold it firmly in place and provide an adequate electrical connection between the braid and the flange. This simple construction combined with the low radioactivity and very high dielectric strength of PTFE provides an elegant solution to the problem of biasing electrodes inside a vacuum vessel while simultaneously minimizing the background radioactivity in the vicinity of the detector.

Fig. 3.24 shows a picture of the cathode (left) and anode (right) high voltage feedthrough connections. Both connections are made below the LXe level to benefit from the high dielectric strength of LXe. The cathode HV connection is made with a bare copper wire fixed to the feedthrough core, wound around a PTFE support rod and pressed between a copper screw and the bottom TPC copper ring. Similarly, the anode HV connection is made with a bare copper wire wound around the feedthrough core and around a PTFE support rod, and connected to the anode copper rod extending below the top TPC copper ring.

3.2.6 Assembled Inner Structure

The assembly of the XENON100 detector inner structure was completed on February 5th 2008. A picture of the completed structure is shown in Fig. 3.25 (left). The bell LXe level adjustment tube is visible on the right. Two of the four PMT HV and signal cable bundles can be seen on the left and right of the TPC. Bare copper wires stretched between bottom and top veto PMT supports were used as stays for the cable bundles. Thin copper wires

Figure 3.24: Pictures of the cathode (left) and anode (right) feedthrough connections. The connection of both feedthroughs are made below the LXe level with their copper braids reaching below the LXe. The connections are made with bare copper wires. The cable bundles from the bottom and bottom veto PMT arrays are also visible.

were used to tie the cables into bundles. As mentioned earlier, great care must be taken that the grounded braids of the PMT signal cables do not touch any PMT bodies, PMT base pins, field shaping wires, or the bottom TPC copper ring which is at the cathode potential.

Two redundant systems were installed to perform the gain calibration of PMTs: light emitting diodes (LEDs) and optical fibers connected to two optical feedthroughs. A total of ten LEDs were installed at various positions such that all PMTs of the detector could be illuminated. Small PTFE blocks or holes into existing PTFE structures were used as light diffusers. Similarly, a total of ten optical fibers were positioned throughout the different volumes. Two quartz fibers are used to carry the light signal from the optical feedthroughs to the top veto where the two fibers are split into four and six plastic fibers, respectively.

Fig. 3.25 (top and bottom right) present close views of the top and bottom veto PMT rings. The bottom and top veto PMTs that are directed upwards and downwards, respectively, are positioned between the PTFE support rods of the TPC to maximize their light detection efficiency. The PMT HV and signal cables were attached to the copper PMT supports and routed to the nearest cable bundle. The three screws used to mount the PMT bases onto the copper supports can be seen in the picture. The two holes of the copper supports, behind the PMT base, allow to route the signal cable away from the base to prevent it from accidentally touching one of the HV pins.

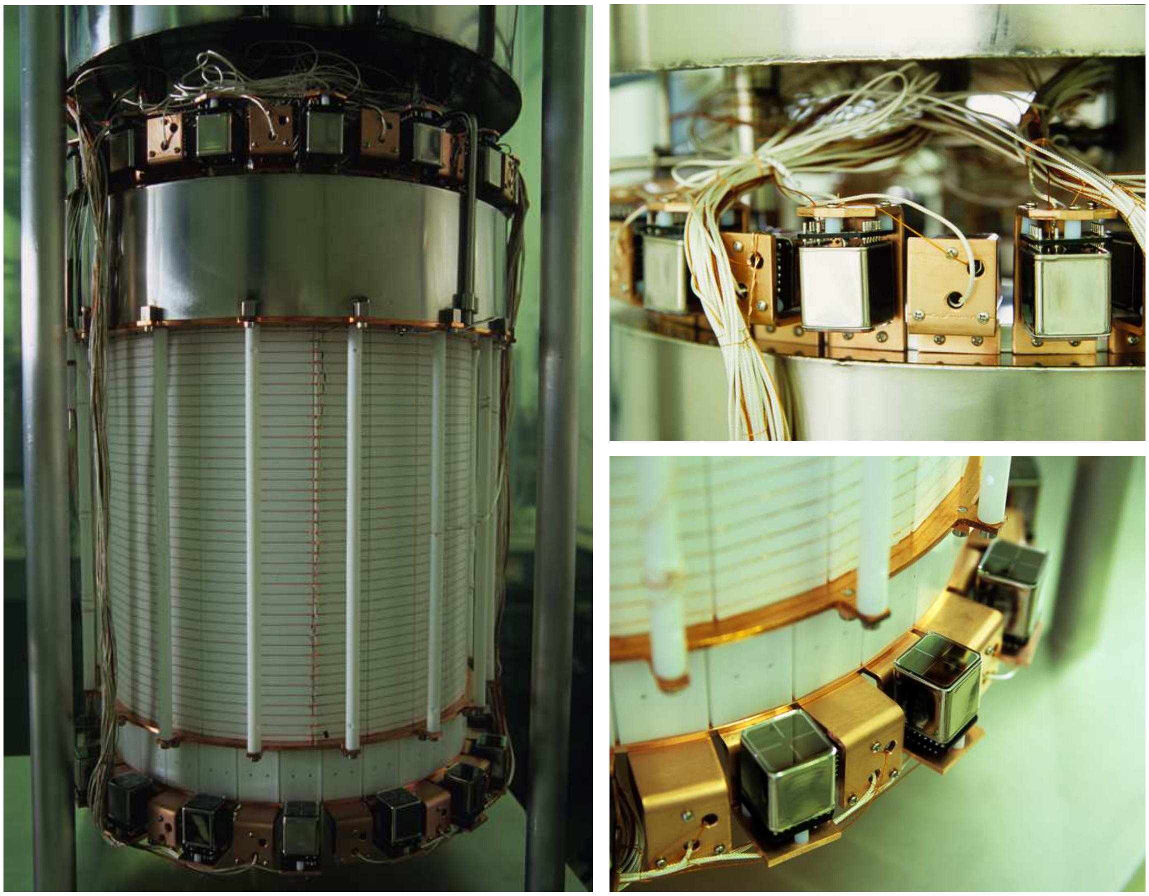

Figure 3.25: Picture of the completed XENON100 inner detector structure (left), and close up views of the top veto PMT ring (top right) and bottom PMT veto ring (bottom right).

3.2.7 Initial Installation Underground

The completed XENON100 detector inner structure was transported underground and installed in the cryostat vessel on February 6th 2008. Fig. 3.26 (left) shows a picture of the detector inner structure, ready to be transported underground. The lowering operation can be seen in Fig. 3.26 (right). The cryostat top assembly with the attached inner structure is lifted from the custom-built transportation stand with the XENON box crane and lowered into the bottom part of the cryostat. Four stainless steel rods and a spirit level maintain the alignment with the top flange while the assembly is lowered.

Fig. 3.27 shows the completed XENON100 detector inside the passive shield. The external cathode connection to the feedthrough can be seen on top. A current limiting resistor

Figure 3.26: The XENON100 detector inner structure, ready to be transported underground, surrounded by curious physicists and the transportation company workers. From left to right: the author, D. Rubin (Columbia University), transportation worker, E. Tziaferi (Zurich University), transportation worker , A. Ferella (Zurich University), K. Lim (Columbia University), M. Schumann (Rice University), K. Giboni (Columbia University), transportation worker. The lowering of the cryostat top assembly with the attached detector inner structure into the bottom part of the cryostat (right). From left to right: M. Schumann (Rice University), A. Ferella (Zurich University), and the author.

is connected in series for a safe discharge of the accumulated charge in case of an accidental breakdown at the feedthrough. The anode connection can also be seen between the two pipes carrying the PMT and sensor cabling. A flexible vacuum line with Kwik-Flange$^{\mathrm{TM}}$ ISO KF connections allow the cryostat lid insulation to be evacuated using a pump outside of the shield through the insulation of the double-wall pipe between the main cryostat and the cooling tower. The bottom part of the cryostat insulation is connected in the same manner but is not visible on the picture. The recirculation line can also be seen exiting the cryostat near the bend of the pipe to the cooling tower. A straight tube going through the shield door and connected to a circular copper tube going around the detector is used to insert calibration sources from outside the passive shield and irradiate the detector at various azimuthal positions.

Fig. 3.28 shows the interior of the XENON box with the XENON100 detector and all its subsystems installed and the passive shield door closed. The cooling tower rests on a shelf attached to the shield door. The turbo molecular pump and the diaphragm pump used to evacuate and maintain the vacuum in the insulation are connected to the cooling tower. Similarly, the pumping station used to evacuate the cryostat and a host of equipment, a Bourdon pressure gauge, a safety rupture disk, a pressure transducer, and a vacuum gauge,

Figure 3.27: The XENON100 detector inside the passive shield with anode, cathode, and vacuum connections completed. The circular copper tube can be used to irradiate the detector at various azimuthal positions when the shield door is closed.

are connected to the main volume through the cooling tower.

The ends of the two cable conduit pipes, with the PMT HV, signal, and instrumentation feedthroughs, can be seen protruding from the shield door. The stack of lead bricks and polyethylene above it can be removed easily if a need to open the detector arises. The red cables supply PMT HV biases while the black cables carry the PMT signals to the data acquisition (DAQ) system (Sec. 3.3.10). A lower shelf supporting two NIM crates used for the DAQ system is also attached to the shield door. The XENON100 DAQ can be seen on the left of the shield. The equipment rack on the far left houses the detector temperature controlling system (Sec. 3.3.5), pressure and temperature process meters, the PMT HV distribution system (Sec. 3.3.2), the anode and cathode HV power supplies (Sec. 3.3.3), and HV filtering boxes. The Xe recirculation system (Sec. 3.3.6) is located on the right side of the shield, next to the air conditioning unit.

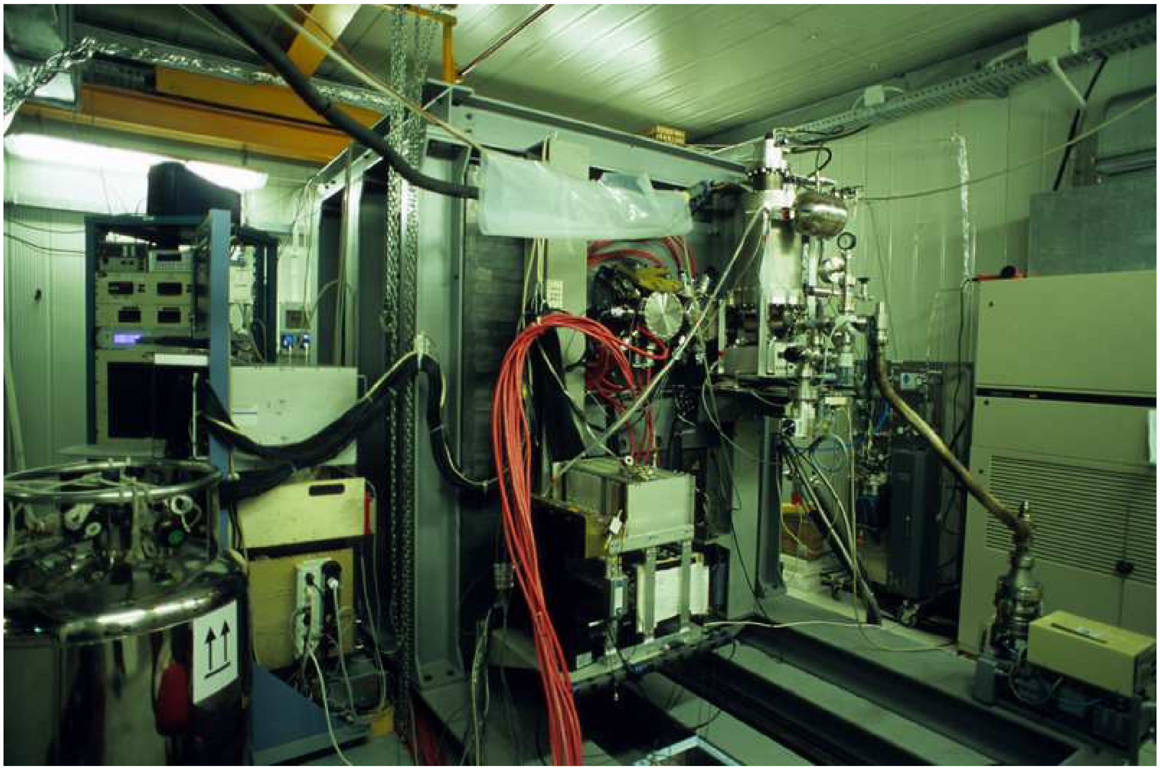

Figure 3.28: Picture of the interior of the XENON box with the XENON100 detector and all its subsystems installed and the passive shield door closed.

The XENON100 detector was first filled with LXe on March 25th 2008. A total mass of 46 kg of LXe was used. This mass corresponded to a LXe level below the design level and not high enough to cover the anode and cathode feedthroughs. Nevertheless, this initial run allowed several subsystems to be checked, the cryogenic system in particular, now that the inner structure of the detector was installed in the cryostat. This run was also the first opportunity to operate the newly acquired PMTs in LXe. Tests unfortunately lead to the discovery of a sealing problem with some of the tubes. A plan to replace them at the next detector opening was thus set in motion. The XENON100 DAQ system had already been tested in part with the XENON10 detector before the end of its final run but this XENON100 first run provided the occasion to test it with all its channels and with signals from the new detector. A period of intensive work followed on the optimization of the PMT HV filtering circuits to reduce the amplitude of the baseline electronic noise on the signal lines. Once the PMT replacements were acquired, the first run was terminated and the Xe recuperated from the vessel on April 30th, 2008. The planning started for which upgrades would be performed during the first detector opening.

3.2.8 First Opening: New Meshes, Level Meters, Temperature Sensors

The XENON100 detector cryostat was first opened to perform some upgrades on May 8th 2008. The cryostat top assembly and the inner structure were raised out of the bottom part of the cryostat and brought above ground. The planned upgrades were: replacement of PMTs that do not work or with poor performance, installation of new meshes, installation of a long and four short LXe level meters, and installation of four temperature sensors throughout the LXe volume.

A total of twenty-four PMTs were replaced in the bottom array. Eight were replaced because their vacuum seal had failed during the first filling while the remaining were replaced with tubes of higher QE. Additionally, seven PMTs of the top array had to be replaced because of their vacuum seal.

The meshes originally installed in the XENON100 detector were square grid etched stainless steel meshes welded to a stainless steel ring wire by wire. The S2 spectroscopic performance of these meshes was never tested but several other tests concluded that this production technique would fulfill the requirements of operation at LXe temperature and resistance to thermal cycling. In the meantime, however, another mesh geometry was proposed whose characteristics should outperform the original geometry, a hexagonal grid geometry. Simulations showed that the spectroscopic performance should be improved and that the deformation of the mesh from thermal contraction should be smaller than for the square meshes. Consequently the anode, bottom, and top meshes were replaced with hexagonal meshes (Sec. 3.3.3).

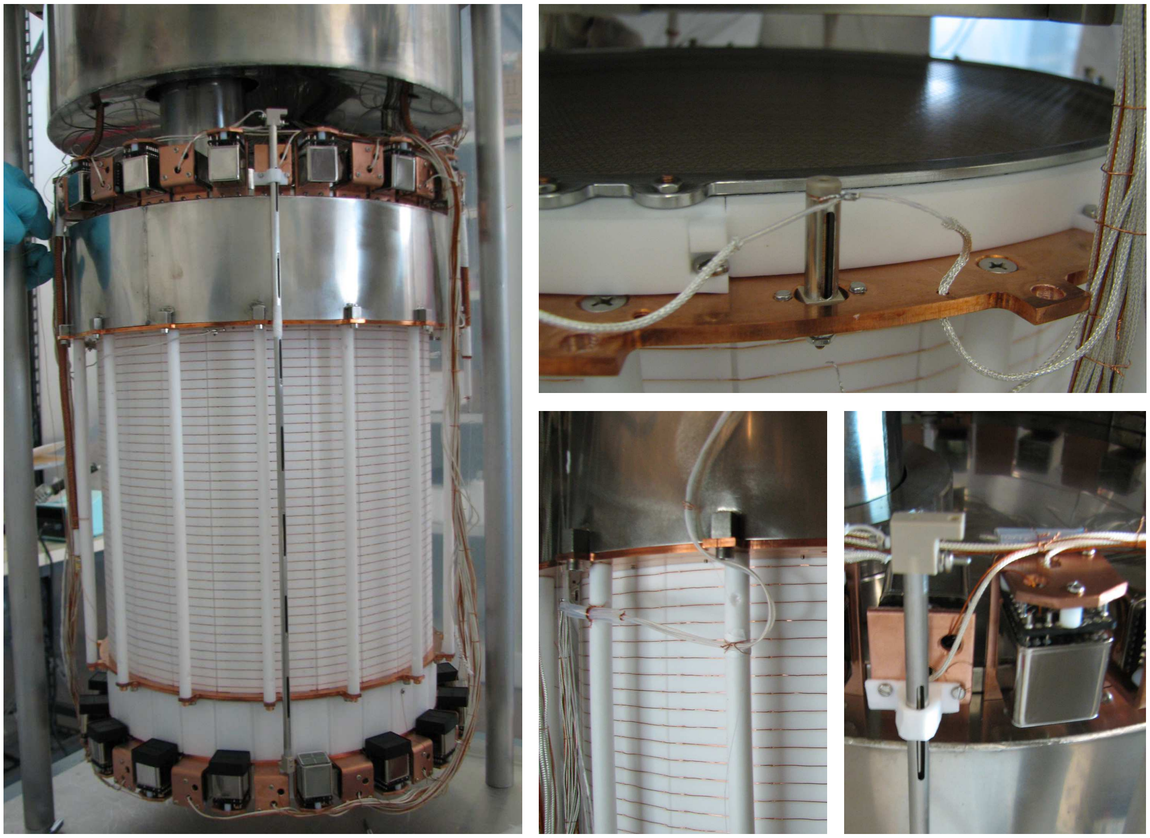

Figure 3.29: Picture of the long level meter (left), one of the short level meters (top right), and two of the temperature sensors (bottom right) installed during the first opening of the XENON100 cryostat after its original installation.

A long capacitive level meter was installed on the detector inner structure to monitor the LXe level during filling and long term operation. The original plan was to mount it on the cryostat but it proved much easier to fix it on veto PMT copper supports, one at the bottom and one at the top. Fig. 3.29 (left) shows the long level meter after its installation on the detector inner structure. The top fixture allows the level meter to slide vertically in it since the thermal contraction of the PTFE panels is larger than that of the level meter. Additionally three short capacitive level meters were installed inside the bell to measure precisely the position of the liquid-gas interface. A fourth meter filled with polyether ether ketone (PEEK), and whose capacitance should consequently not change as the LXe varies, was also installed. Fig. 3.29 (top right) shows one of the short level meters. The level meters are described in more detail in Sec. 3.3.4.

Four Pt-100 temperature sensors were installed to measure the temperature at various points within the LXe and GXe volume. One temperature sensor was fixed on a bottom veto PMT copper support and gives the *bottom* temperature, one on a PTFE support rod for the *below bell* temperature, one above the PTFE top array PMT holder for the *inside bell* temperature, and one on a top veto PMT copper support for the *top* temperature. Fig. 3.29 (bottom right) shows the location of the *below bell* and *top* temperature sensors.

Before connecting back the HV feedthroughs a test of the cathode HV feedthrough was performed in air, with the in-LXe tip moved away from the TPC. The voltage could be raised to 18.4 kV before breakdown occured near the tip of the feedthrough, a part which would normally be submersed in LXe. Considering the good dielectric strength of LXe and the cathode-ground distance inside the detector the conclusion was that the feedthrough should allow the application of the design voltage of 30 kV on the cathode.

The cryostat top assembly and the detector inner structure were brought back underground and the cryostat closed on May 13th 2008. The XENON100 detector was filled for a second time on May 20th 2008, this time with a total of 138 kg of LXe, a quantity large enough to allow tests of the cathode HV feedthrough in its design conditions. During the test the cathode HV could be raised to 20 kV without any discharges or appearance of leakage current. Tests of the anode followed and the first XENON100 S2 signals could be observed at an anode voltage of 2.3 kV. At the operating conditions of the test, this corresponded to a field of $\sim 3\,\mathrm{kV\,cm^{-1}}$ in the LXe above the bottom mesh, enough to extract electrons into the gas phase (Aprile *et al.*, 2006a). The field in the GXe ($\sim 2.7\,\mathrm{kV\,cm^{-1}\,atm^{-1}}$) was also high enough for the production of proportional scintillation. Unfortunately, it was later discovered that a high rate signal reminiscent of LXe scintillation photons appears, mostly on the veto PMTs near the resistor chain of the voltage divider circuit, when a voltage higher than 4 kV is applied on the cathode. The effect had not been observed during the first cathode test as the PMTs were not in operation at that time. The decision was taken then to open the cryostat and attempt a modification of the resistor chain underground. The Xe recuperation started on July 1st 2008 and was completed on July 3rd.

3.2.9 Second Opening: Resistor Chain Modification

The XENON100 cryostat was opened for a second time on July 4th 2008 to modify the resistor chain of the field shaping wires voltage divider circuit. As mentioned earlier, tests had shown that high rate (~10 kHz) light signals would appear on some PMTs, mostly those of the bottom veto ring facing upwards and near the resistor chain. The cryostat top assembly and the detector inner structure were placed on the custom-built stand normally used for transportation and work in the clean room above ground.

After inspection of the resistor chain, the conclusion reached was that the likely cause of the problem was that the field near the tips of the field shaping copper wires might have been too high and the signals observed were those of pre-breakdown conditions in LXe. Additionally, it was concluded that the situation could be improved by bending the copper wires that support the resistors, bringing them closer to the PTFE panels and further away from the cryostat wall at ground potential, and by modifying the solder points such that none of the sharp edges of the cut copper wires would be apparent. Fig. 3.30 shows a picture of the resistor chain after the modification. It can be compared to the original arrangement shown in Fig. 3.20 (right).

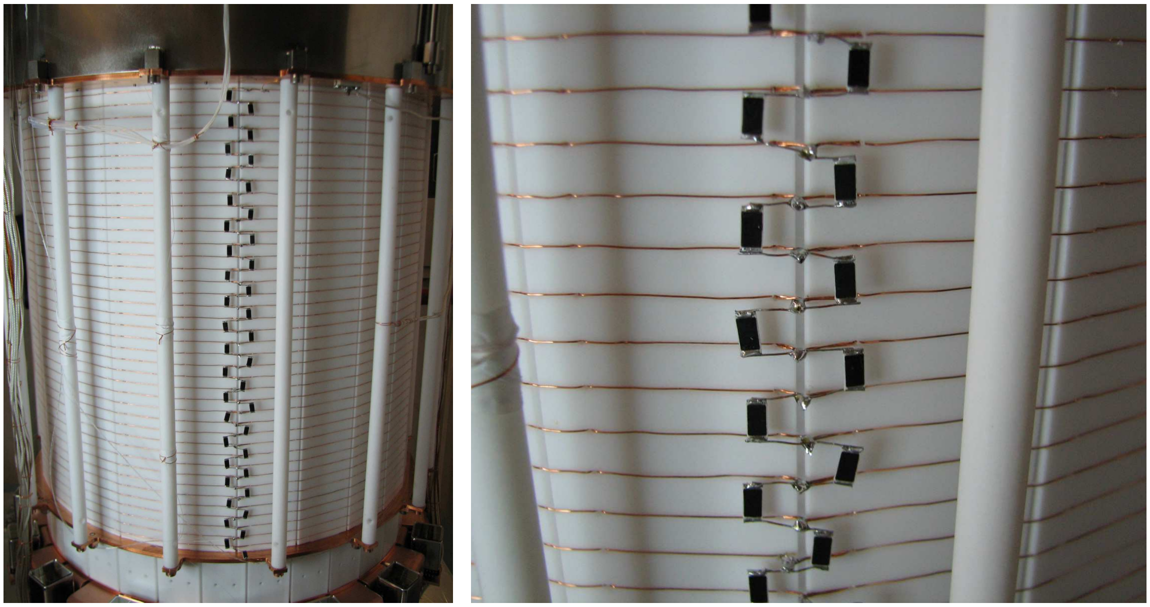

Figure 3.30: Picture of the resistor chain of the field shaping wires voltage divider circuit after the modification underground (left). A closer view of the modified solder points of the resistors to the field shaping copper wires (right).

The inner detector structure was lowered back into the cryostat on July 5th 2008. After evacuating the cryostat and a short period of pumping the detector was filled again on July 9th 2008. A total mass of 154 kg of LXe was used. Naturally the first test performed was that of the cathode HV. Encouragingly, the appearance of high rate light signals in the veto volume with the cathode at 4 kV was solved. Unfortunately, a similar effect was found to occur inside the TPC when the cathode HV reached ~14 kV.

3.2.10 Third Opening: Screening Mesh Installation

The last time the XENON100 detector inner structure was taken out of the cryostat, as of 2011, was on December 3rd 2008. Different upgrades were planned on the inner structure and, most importantly, a screening mesh was to be installed below the cathode to shield the PMTs of the bottom array from the high electric field created by the cathode.

Figure 3.31: Picture of the lower PTFE panels and the bottom PMT array before the replacement of the panels and the installation of the screening mesh (left). The new lower PTFE panels and the screening mesh after the upgrade (right).

During the cathode HV tests of the previous run a curious feature was observed. The rate of light signals was highest on PMTs neighbouring PMTs whose bias voltage was at ground. Since the PMTs are operated in the grounded anode scheme the metal PMT body is normally at a negative potential in the vicinity of −800 V. It was noted then that the strongest electric field near the cathode, also biased at negative potential, is near PMTs with no HV bias applied. It was therefore concluded that the PMT signals seen at high cathode voltages were caused by electrons whose trajectories are deformed due to the high electric field near the PMT and are striking the PMT quartz window and creating scintillation light. The solution adopted was to install a mesh at ground potential between the cathode and the bottom PMT array. This required the machining of new, longer lower PTFE panels, with a notch to hold the screening mesh in place. Fig. 3.31 shows a picture of the bottom array holding assembly before and after the installation of the screening mesh. The PTFE panels were replaced one by one and the mesh was subsequently inserted into the notch.

The additional upgrades performed were the replacement of twenty-four PMTs, mostly to exchange them with PMTs with a lower measured activity, the installation of copper pieces to block the top PMT array from light signals created outside the radius of the sensitive volume, and the installation of PTFE reflector pieces in the bottom veto volume to increase its light collection efficiency. Fig. 3.32 shows the top of the TPC after the installation of the copper light blocking pieces.

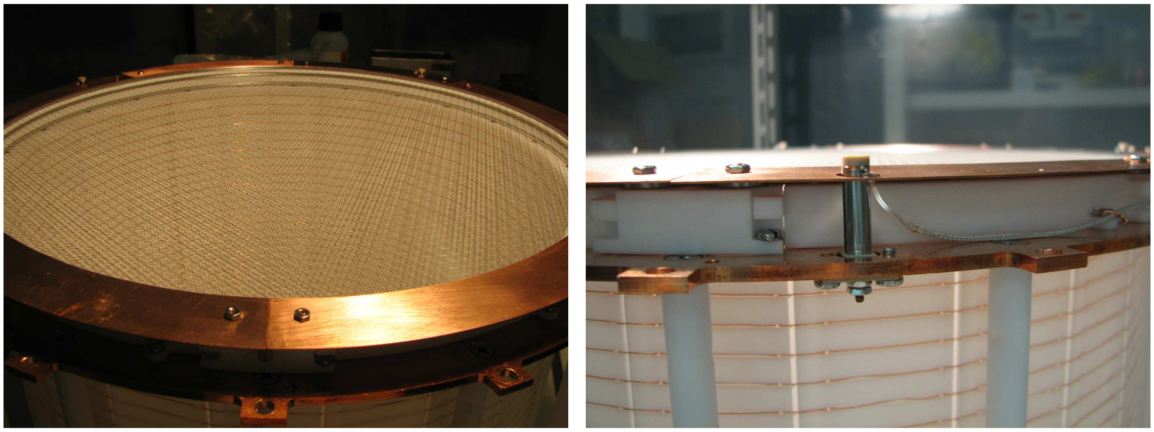

Figure 3.32: Picture of the top of the XENON100 TPC after the installation of the copper light blocking pieces (left) and a closer view near a short level meter (right).

The upgrades were completed on December 9th 2008 and the cryostat top assembly and detector inner structure were brought underground that day. After closing, the cryostat was evacuated and a bake-out at the maximum permissible temperature, limited to ~50°C by the PMTs, was initiated. After this bake-out period the detector was filled for a sixth time. The filling was completed on January 24th 2009 and a total mass of 146 kg of LXe was used. The cathode HV tests resumed quickly and a higher cathode potential of ~17 kV could now be applied before the appearance of the light signals on bottom PMTs. The decision was made then to try and reproduce this effect in a R&D setup and find a solution there before any further modifications of the XENON100 detector.

This run was to be the one in which the focus would be on the achievement of long drift of the charge signals. In fact, in previous runs no sizeable rate of charge signals with drift times larger than a few microseconds had been observed. After the multiple verifications of many of the detector subsystems it became clear that the effect was likely due to a high concentration of electronegative impurities in the LXe (Sec. 2.4.2). The Xe was eventually recuperated on March 13th 2009 and an intense period started where several purification techniques were employed to reduce the outgassing of materials of the detector and to measure precisely the change in their concentration. Finally a breakthrough was made when the measurement of permeation of N_2 and Ar gas through the cryostat top seal was measured with a residual gas analyzer (RGA).

3.2.11 Fourth Opening: Cryostat Seal Replacement

The last time the XENON100 cryostat was opened and exposed to air, as of 2011, was on April 15th 2009. The cryostat top flange o-ring was replaced with a Viton® o-ring with a lower permeation than the one used previously. This last modification enabled the measurement, during the subsequent run, of S2 signals from interactions at the bottom of the TPC, with their ionization electrons drifting the full 30 cm of the TPC. This milestone marked the beginning of the transformation of the XENON100 detector into a fully operational research instrument.

3.3 The XENON100 Detector

In the previous section we described the construction and assembly of the XENON100 detector, from its original design into its concrete realization. We also described the four additional openings of the cryostat for modifications to the inner detector structure and the various tests which led to those modifications. In this section we will describe in more details the XENON100 detector itself and its various subsystems. In Sec. 3.3.1 we discuss the TPC, in Sec. 3.3.2 the PMTs, in Sec. 3.3.3 the electric field configuration, in Sec. 3.3.4 the LXe level meters and temperature sensors, in Sec. 3.3.5 the cryogenic system, in Sec. 3.3.6 the gas system, in Sec. 3.3.6 the Xe purity, in Sec. 3.3.8 the passive shield, in Sec. 3.3.9 the krypton distillation column, and finally in Sec. 3.3.10 we discuss the DAQ system.

3.3.1 TPC

The target volume of the XENON100 TPC has a radius of 15.3 cm, a drift length of 30.5 cm, and contains 62 kg of LXe. Twenty four 0.25 in. thick interlocking PTFE panels define the radius of the target volume. The PTFE panels are held in place on the top and on the bottom by two copper plates. The cathode mesh, mounted below the bottom copper ring, and the bottom mesh, mounted above the top copper ring and slightly below the liquid level, close the TPC and define the 30.5 cm drift region. As mentioned earlier, the top and bottom qualifiers for the meshes refer to their positions with respect to the anode mesh. The uniformity of the drift field is ensured by a set of forty field shaping wires, mounted inside and outside the PTFE panels. The field shaping wires also rigidify the PTFE and copper rings assembly. The top and bottom TPC copper rings are also joined by sixteen PTFE support rods to distribute the weight that needs to be held by the TPC. The PTFE panels interlock to optically separate the target volume from the veto volume.

The bottom, anode, and top meshes, separated by 5 mm from each other, are held in place by a PTFE structure fixed to the top TPC copper ring. The diving bell houses the three meshes and stabilizes the LXe liquid level between the bottom mesh and the anode. The level height can be adjusted with a linear displacement motion feedthrough. The TPC assembly is attached to the bell via its top copper ring. Two PMT arrays are used to detect the light emitted in the TPC volume, one inside the bell, in the gas phase, and one below the cathode mesh, in the liquid. An assembly of thirty-two shorter PTFE panels held together by copper rings isolates the bottom PMT array from the veto volume and is fixed to the bottom copper ring of the TPC.

The target volume is surrounded by a veto volume containing 99 kg of LXe. It is instrumented by PMTs that detect light below and on the sides of the TPC, and above the bell. As discussed in Sec. 3.1, the veto volume acts essentially in the same way as fiducialization in reducing background (see Sec. 4.4) but with the added benefit of reducing the total trigger rate inside the sensitive volume. The cost of instrumenting the veto volume to reach an acceptable lower energy threshold is also lower than having the entire volume as a TPC. The liquid level outside the bell covers the PMTs of the top veto. The LXe level can be maintained at this height with a positive pressure difference between the GXe volumes inside and outside the bell. The diaphragm pump of the Xe recirculation system (Sec. 3.3.6) provides the pressure difference through its connection to the bell cable conduit.

The original intent was to replace the TPC PTFE pieces machined from commercially procured PTFE with known low activity PTFE that was obtained beforehand, and assemble the TPC in a N_2 atmosphere to avoid Rn contamination. However, after the original PTFE used was measured to have low intrinsic radioactivity (Aprile *et al.*, 2011d), the decision was made not to replace the PTFE pieces. As we saw earlier, the TPC structure is supported by the bell and is enclosed in a double-wall vacuum vessel made of 316Ti stainless steel. The steel was selected for its low activity, especially in ^{60}Co (Aprile *et al.*, 2011d).

3.3.2 PMTs

The XENON100 PMTs are $2.5\,\mathrm{cm} \times 2.5\,\mathrm{cm}$ metal-channel type R8520-AL Hamamatsu PMTs with low intrinsic radioactivity (Aprile *et al.*, 2011d). The PMTs have a special bialkali photocathode for low temperature operation down to -110° C and optimized for detection of the Xe 178 nm scintillation light. They have also been selected due to their compact size which allows improved (x, y) position resolution compared to what can be obtained with larger tubes.

The top array is composed of 98 tubes disposed in circular patterns to enable a better reconstruction of the radial coordinate while minimizing the number of tubes required. The tubes are held by a PTFE structure fixed to the top plate of the bell. The light collection efficiency is enhanced even if the number of PMTs is reduced compared to a square grid arrangement since the PTFE holding structure acts as a UV reflector. The average QE of the top array PMTs is ~23%. The bottom array is composed of 80 tubes arranged on a square grid to maximize light collection. The bottom array PMTs have been selected for higher QE. Their average QE is ~33%. The top and bottom veto arrays each have 32 tubes arranged in alternating inward and down, and inward and up directions, respectively, to allow a simultaneous view of the top, bottom and side portions of the active veto volume.

The PMTs are operated in the grounded anode scheme, that is, with the photocathode at negative potential. The PMT base circuits are printed on a Cirlex® board. The PMT base voltage divider resistor chain has a total resistance of $125\,\mathrm{M\Omega}$, chosen to minimize the heat influx from the PMTs to the LXe. At the maximum operating voltage of $-900\,\mathrm{V}$ this corresponds to a current of $i_b = 7.2\,\mu\mathrm{A}$ and a power dissipation of $6.5\,\mathrm{mW/PMT}$. The total cooling power required to compensate for the heat influx from PMT arrays is thus 1.6 W.

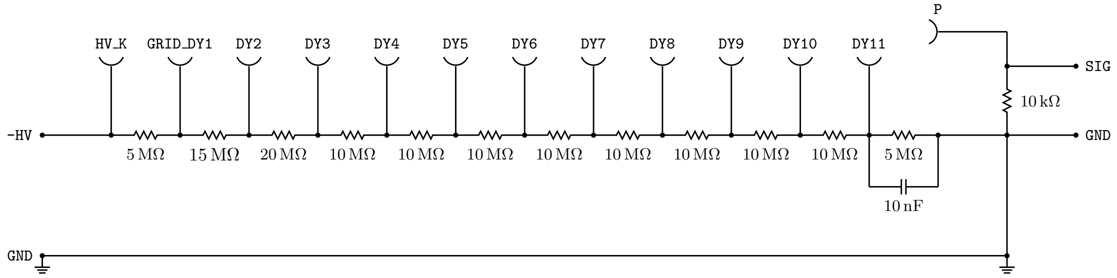

Figure 3.33: Schematic of the XENON100 grounded-anode scheme PMT base voltage divider.

The schematic of the PMT base electrical circuit is shown in Fig 3.33. The PMT bias voltages are supplied by a CAEN SY1527LC Universal Multichannel System with seven CAEN A1733N 12 channels 3 kV HV boards and seven CAEN A1535N 24 channels 3.5 kV HV boards.

When operating PMTs one must ensure that the signal current from the last dynode to the anode is always much lower than the voltage divider biasing current. The rule of thumb is that the signal current should not exceed 0.5%-1% of the voltage divider biasing current (Hamamatsu Photonics K.K., 2006), which leads to a maximum signal current of $i_{s,\max} = 36\,\mathrm{nA}$. Assuming a gain of $2 \times 10^6\,\mathrm{e^-/pe}$, this limits the linear response of the PMT to single photoelectron rates below ~100 kHz. However, in a dual-phase LXe TPC, the S2 signal is much larger than the S1 signal due to the amplification of the ionization signal. If no additional measures were taken, considering a typical S2 signal duration of $1\,\mu\mathrm{s}$ and that the PMT immediately above the interaction typically measures a 20% fraction of the S2 signal, then this PMT would enter a non-linear regime during every S2 pulse. The capacitor on the final amplification stage stores a reserve charge of

$$Q_C = 10\,\mathrm{nF} \cdot 700\,\mathrm{V} \cdot \frac{5\,\mathrm{M\Omega}}{125\,\mathrm{M\Omega}} = 280\,\mathrm{nC}, \tag{3.1}$$

where we have set the PMT voltage more or less at the lower limit of the operational range. Again, for the PMT response to remain linear the total charge drawn should not exceed 1% of Q_C (Hamamatsu Photonics K.K., 2006). This results in a maximum S2 signal on any given PMT of ~8700 pe. As an estimate, if ones assumes a S2 amplification of $20\,\mathrm{pe/e^-}$ (Sec. 4.2.4) and a charge collection of 50%, then ionization signals from electron recoils above ~14 keV will induce a non-linear response in the PMT immediately above the interaction. In practice however, the only consequence of that effect is that the position resolution will start to degrade. The energy measurement uses the signal on the bottom PMT array where the S2 light is distributed evenly and the non-linear regime thus appears at much higher energies. Moreover, for nuclear recoil events, this non-linear regime would appear above nuclear recoil energies of 200 keV, well outside of the typical energy range of interest for WIMP searches.

As mentioned earlier the PMTs can be calibrated by a redundant system of optical fibers and LEDs positioned throughout the LXe volume. The PMTs are calibrated in the single photoelectron regime and PMT gains were adjusted to a mean value of $2 \times 10^6\,\mathrm{e}^-/\mathrm{pe}$ by varying their biasing voltages. The standard deviation in gain values is $1.7 \times 10^5\,\mathrm{e}^-/\mathrm{pe}$. In practice only the optical fibers are used to perform the gain calibration.

3.3.3 Electric Field

High optical transparency meshes are used to create the drift field and the proportional amplification field while simultaneously allowing the measurement of the S1 and S2 signals with both top and bottom PMT arrays. All meshes have a hexagonal wire pattern. They were fabricated by chemically etching the hexagonal pattern on a stainless steel foil, stretching the foil and spot-welding it to a stainless steel ring. The rings used for the bottom, anode, and top mesh have an inner radius of 161.3 mm, a width of 6.4 mm, and a thickness of 2.5 mm. The ring of the cathode is pressed between the bottom copper ring of the TPC and the top copper ring of the lower PTFE panels assembly. The cathode ring has the same inner radius as the TPC, 152.4 mm, a width of 6.4 mm, and a thickness of 1.5 mm. The ring used for the screening mesh has a square cross section with a 3 mm width and an inner radius of 152.4 mm. All mesh rings were machined out of the same low-activity stainless steel as that used for the cryostat (Aprile *et al.*, 2011d).

The bottom, anode, and top mesh are all $125\,\mu$m thick, with wire pitches[1] of 2.5 mm, 2.5 mm, and 5.0 mm, respectively. The optical transparency of the proportional amplification meshes, averaged over all incident angles, is 47.7%. The cathode has a thickness of $75\,\mu$m and a pitch of 5 mm, for increased optical transparency. Similarly, the screening mesh, placed 12 mm below the cathode and 5 mm above the windows of the bottom array PMTs, has a thickness of $50\,\mu$m and a pitch of 5 mm. The combined optical transparency

---

[1] The pitch here is defined as the distance between two parallel sides of the hexagonal pattern.

of the cathode and the screening mesh is 83.4%.

All meshes were tested for thermal deformations at LXe temperature and an upper limit of 240 μm was obtained. This should translate into S2 signal corrections of less than 10% across the surface. Indeed the measured S2 width variation across the xy plane is ~3% (σ/μ) (Sec. 4.2.3). The anode was also tested for stability in a N_2 and an Ar atmosphere up to 6 kV with a grounded plate 4.6 mm below and no discharges were observed.

In normal operation the anode is biased at +4.5 kV/cm and creates an extraction field of ~6 kV/cm in the LXe and a proportional amplification field of ~12 kV/cm in the GXe. Strictly speaking these values are the values one obtains by approximating the meshes as continuous surfaces but they are not far from the mean field along electron trajectories. Fig. 3.34 shows the expected variation of the field between the bottom mesh and the anode. Under those conditions, the transparency of the bottom mesh for drifting electrons is ~100%. The electron extraction efficiency into the gas phase should also be close to 100% (Aprile *et al.*, 2004).

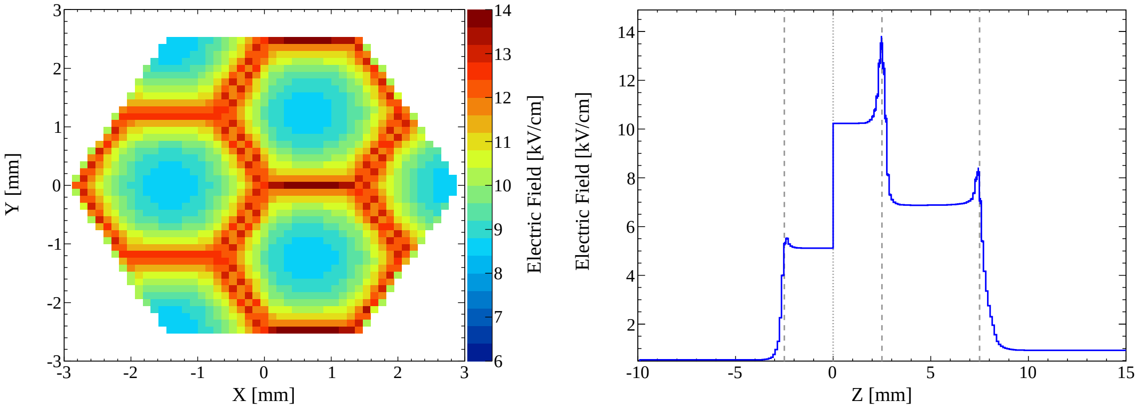

Figure 3.34: (left) Mean electric field in the proportional amplification region (between the liquid level and the anode) as a function of x and y. In this region the field is strongest near the wires of the anode due to their small radius. The field is shown in the hexagonal unit cell of the proportional amplification meshes (see Fig. 3.35). (right) Mean electric field in the hexagonal unit cell as a function of depth. A discontinuity in the electric field occurs at the liquid level (dotted line) due to the different relative permittivities of GXe and LXe. The dashed lines are, from left to right, bottom mesh, anode, top mesh.

As can be seen in Fig. 3.34, the electric field in the proportional amplification region, that is, between the liquid level and the anode, is highest near the wires of the anode. Since the electroluminescence yield per unit distance is proportional to the electric field (Eq. 2.13), and since the electron drift velocity increases with increasing field, we expect the time distribution of emitted proportional photons to also exhibit the distribution between the liquid level and the anode in Fig. 3.34 (right). It is also worth noting that the electric field above the top mesh, and below the top PMT array, has a value of $\sim 1\,\mathrm{kV\,cm^{-1}}$. This is due to the fact that the metal bodies of the PMTs are at a negative potential, the photocathode bias potential, and that the top mesh is grounded. Ionization electrons created in that region can thus drift down in the direction of the anode and produce a proportional scintillation signal between the top mesh and the anode .

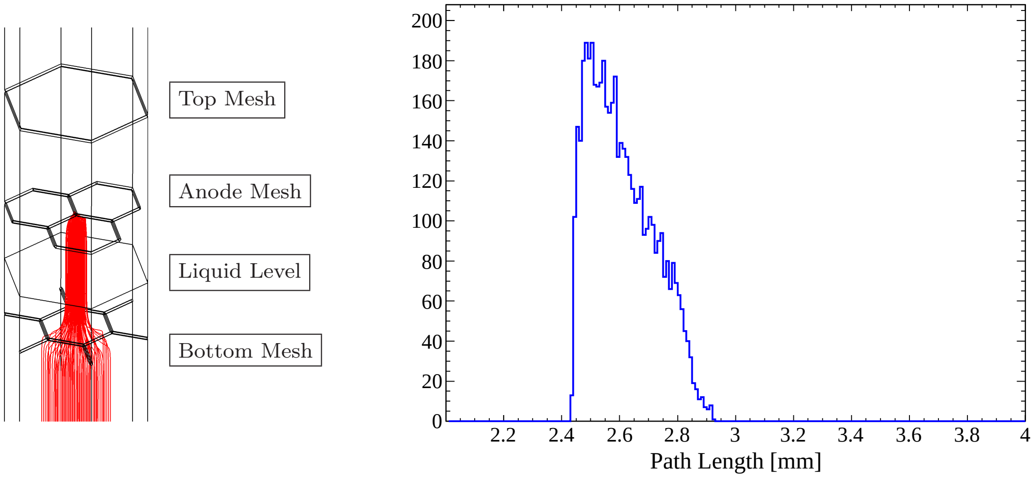

Figure 3.35: Unit cell of the proportional amplification region meshes with electron paths from the drift region to the anode (left) and path length distribution for 5000 electron paths (right). The focusing effect can clearly be seen on the left.

Fig. 3.35 (left) shows the hexagonal unit cell of the proportional amplification region meshes and the field lines from the volume below the bottom mesh to the anode. This offers a visual explanation for the high electron transmission efficiency, since the field is higher above the bottom mesh then very few field lines from the drift region terminate on the bottom mesh and hence very few electrons travelling along the field lines are not transmitted. Because of this focusing effect, ionization electrons, and thus reconstructed event positions, are subject to lateral displacements of up to half a pitch of the bottom mesh, 1.25 mm in the case of XENON100. Fig. 3.35 (right) shows the distribution of path lengths in the proportional amplification region of 5000 electron paths. The small spread of the path length distribution should imply superior spectroscopic performance with the S2 signal.

As mentioned earlier, the design cathode voltage of −30 kV could not be reached in earlier detector configurations. The extension of the lower PTFE panels and the addition of the screening mesh allowed to raise the maximum cathode voltage from 14 kV to 17 kV before apparition of the high rate signals on bottom PMTs. The cathode is biased at 16 kV to ensure stable operation and thus establishes a drift field of 0.53 kV/cm. The anode voltage is supplied by a CAEN A1526P 6 channels 15 kV HV board inside the SY1527LC crate system. The cathode voltage is supplied by a Heinzinger PNC 100000-3neg $-100\,\mathrm{kV}$ power supply.

The problem of constructing TPCs with simultaneous measurement of scintillation and ionization with an energy threshold as low as possible and a uniform drift field translates into an optimization problem of the optical transparency of meshes and field shaping wire and mesh configuration. The 5 mm pitch and the 75 μm wire thickness of the cathode mesh were chosen to maximize the optical transparency of the mesh and maintain a good mechanical stability at low temperatures. Due to an omission in the electrostatic simulations of the drift field during the design phase, the loss in shielding efficiency went unnoticed. The first measured (r, z) distributions of events within the TPC showed that the drift field near the cathode was bending inwards slightly.

Fig. 3.36 shows a cylindrically symmetric approximation of the drift field and its curvature in the lower right corner. The anode bias was set to $+4.5\,\mathrm{kV}$, the cathode to $-16\,\mathrm{kV}$, and the PMT casings to $-850\,\mathrm{V}$. Since this effect only induces a continuous displacement map, that is, for each true position (r, z) corresponds one and only one apparent position (r', z') and vice-versa, then this effect can be corrected for. Sec. 4.3.1 discusses the correction applied.

3.3.4 Level Meters, Temperature Sensors

The LXe level inside the bell is measured with 3 short cylindrical capacitive level meters and the level outside the bell in the veto volume is measured with a long level meter. A copper rod with a radius of 1.1 mm serves as the inner conductor of the short level meters while the outer conductor is a stainless steel cylinder with an inner radius of 2.53 mm. The inner and outer conductors are mounted on a PEEK support. A vertical slit 2.03 mm wide and 14.73 mm long allows the LXe to fill the cylindrical capacitor. The theoretical capacitance per unit length is $2\pi\epsilon_0/\ln(r_>/r_<) \approx 0.067\,\mathrm{pF/mm}$, neglecting the effect of the slit. The total capacitances when filled with GXe and LXe are $C_{\mathrm{slm,GXe}} = 0.98\,\mathrm{pF}$ and

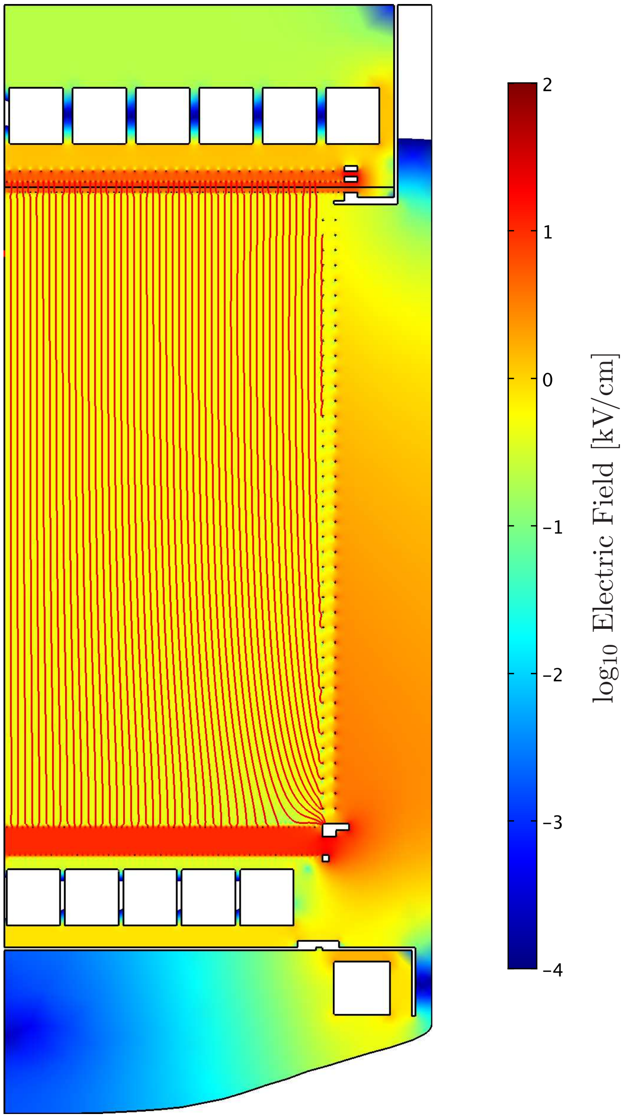

Figure 3.36: Cylindrically symmetric approximation of the XENON100 drift field. A slight curvature in the bottom right corner can be observed. The lateral displacement in true and apparent positions within the TPC is corrected for with the results of a finite element analysis simulation of the drift field (Sec. 4.3.1).

$C_{\mathrm{slm,LXe}} = 1.9\,\mathrm{pF}$, respectively.

The long level meter inner conductor is a stainless steel rod with a radius of 1.05 mm. The cylindrical outer conductor is also made out of stainless steel and has an inner radius of 2.77 mm. The active range of the long level meter is 500 mm. Four cylindrical PEEK spacers with height 4.98 mm and separated by 94.49 mm keep the inner conductor centered. Fifteen slits 2.03 mm wide and 32.26 mm long that alternate between the front and back of the level meter allow the LXe to fill the structure. The PEEK spacers create portions of the long level meter where the capacitance does not vary with the liquid level. Under a constant LXe level rising speed, during a filling or emptying of the detector, the long level meter can be calibrated using the known inter-spacer distance. The theoretical capacitance per unit length of the long level meter is $0.057\,\mathrm{pF/mm}$, neglecting the effect of the spacers and the slit. The total capacitances when filled with GXe and LXe are $C_{\mathrm{llm,GXe}} = 28.7\,\mathrm{pF}$ and $C_{\mathrm{llm,LXe}} = 55.9\,\mathrm{pF}$, respectively.

Four PT-111 Lake Shore Cryotronics Pt-100 temperature sensors measure the LXe or GXe temperature within the volume. Under normal operation three of them are in the liquid, one at the bottom of the inner detector structure, one below the bell, and one above the top veto PMT array, and one of them is in the gas, inside the bell above the top PMT array. Each sensor uses two Kapton®-insulated wires on each platinum lead to compensate for the resistance of the wires and provide an accurate measurement. The temperature sensors can also be used as crude “binary” level meters whose temperature reach the LXe temperature as the liquid level rises above their position.

3.3.5 Cryogenic System

The stability of the pressure inside a LXe dual-phase TPC is crucial since the S2 amplification factor is a function of the pressure (Sec. 2.4.6). As mentioned earlier, the cooling power for the XENON100 detector is provided by a PTR coldhead coupled to the gas volume through a copper cold finger (Sec. 3.1.4 and Sec. 3.2.1). The PTR used is an Iwatani PC150 driven by a Leybold Coolpak 6000 6.5 kW water-cooled He compressor. This combination delivers 200 W of cooling power at 170 K.

A PTR is a regenerative cryocooler that improves over the Stirling and Gifford-McMahon refrigerators in that it has no moving parts in its low temperature stage. This ensures long term reliable operation and no vibrations, two important requirements for the operation of dual-phase TPCs. Fig. 3.37 shows the principle of operation of a PTR. The system consists of an oscillating pressure source, like a piston, a heat exchanger, where heat is released to the surroundings, a regenerator, a heat exchanger at the cold end, where heat from the object being cooled is extracted, a pulse tube, a heat exchanger at the hot end, where heat is also released to the surroundings, an orifice, and a reservoir volume. The regenerator usually consists of a porous material with a large specific heat capacity.

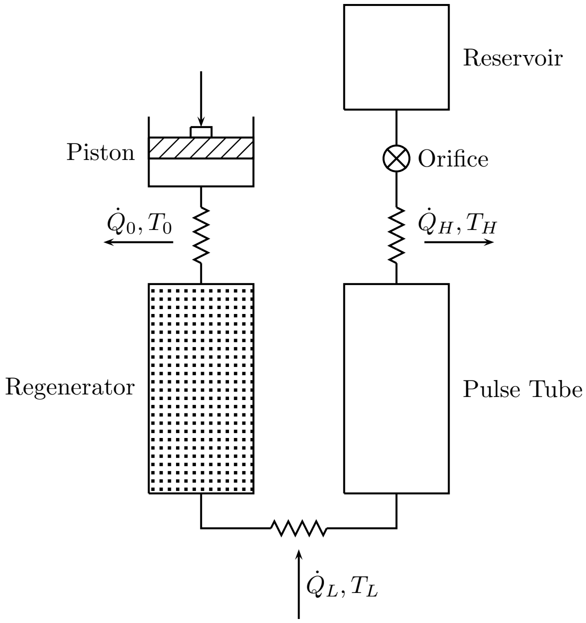

Figure 3.37: Schematic of the operating principle of a pulse tube refrigerator.

The cooling cycle consists of four steps. In the first step the piston compresses the gas in the pulse tube. The heat due to the compression is transferred to the environment via the heat exchanger and the gas passes through the regenerator where is it cooled to the cold end temperature T_L. In the second step, the compressed gas in the pulse tube gas flows through the orifice into the reservoir since it is at a higher pressure than the pressure in the reservoir. Heat is transfered to the environment at the hot end heat exchanger during the process and the gas cools to T_H. The flow stops when the pressure in the pulse tube reaches the average pressure. In the third step the piston expands the gas adiabatically in the pulse tube. In the fourth step, the now colder gas in the pulse tube is forced through the heat exchanger at the cold end by the higher pressure in the reservoir. In the process, heat from the object being cooled is transfered to the gas and the motion of the gas stops when the pressure in the pulse tube reaches the average pressure. The heat stored in the regenerator is transfered back to the gas as it flows through it. The pulse tube must be large enough such that the gas from the hot end never reaches the cold end in one oscillation and vice-versa. In effect the gas in the middle of the pulse tube acts as the displacer in the Stirling and Gifford-McMahon refrigerators. The name "pulse" tube is actually misleading since there are no pressure pulses occurring in the tube.

In the case of the XENON100 cooling system, the pressure oscillation is generated by the use of a rotary valve, also sometimes called motor valve, that switches between high- and low-pressure sources. The frequency of "pulsing" is thus determined by the rotary valve. The compressor is connected to the rotary valve with stainless steel braided flexible lines with low fluid loss Aeroquip pressure fittings. The rotary valve is connected to the PTR with a 0.5 in. copper tube with Aeroquip fittings. The hot end heat exchanger of the PC150 PTR is water cooled.

The temperature of the cold finger is maintained at the desired value by resistive heaters ($23\,\Omega$) glued to a copper piece between the PTR coldhead and the cold finger. The temperatures of the coldhead and the cold finger are measured with two Lakeshore Cryotronics PT-111 Pt-100 temperature sensors and monitored by a Lakeshore 340 temperature controller. The controller uses a PID control loop to adjust the power supplied to the heaters with the cold finger temperature as feedback. A Kepco JQE100-5M 500 W DC power supply is used as the power source for the heaters. As the pressure in the GXe volume is directly related to the temperature, the pressure is stabilized by the thermal coupling of the GXe to the cold finger.

As described in Sec. 3.1.4, the remote cooling principle of the XENON100 detector uses a funnel to collect LXe droplets that condensed on the cold finger and an inclined pipe from the cooling tower to the main cryostat to let gravity drive the LXe flow. The total heat load when the detector is full but without recirculation was measured to be $\sim$70 W.

An emergency cooling system using LN_2 is integrated in the cooling tower (see Sec. 3.2.1) and is comprised of a stainless steel tubing coil above the cooling tower funnel. The coil is connected to a pressurized external dewar, always kept full during operation. The LN_2 flow through the coil is controlled by an actuated valve and triggered when the detector pressure increases above a defined setpoint. The most fragile component of the inner detector are the PMTs, with a maximum pressure rating of 5 atm. The actuated valve and the process meter monitoring the pressure are powered by an uninterruptible power supply. The effectiveness of the emergency cooling system was tested by turning off the PTR He compressor and measuring the rate of pressure increase inside the detector and the LN_2 consumption without Xe recirculation (see Sec. 3.3.6). The duration of the test was 4 hours. During the first cycle the pressure increased to 2.92 atm but remained between 2.1 and 2.5 atm afterwards, a perfectly secure range for the PMTs. The LN_2 consumption was such that the system is estimated to be able to operate without human intervention for close to two days.

3.3.6 Gas System

The Xe used to fill the XENON100 detector is stored in four Spectra Gases high-pressure 2A aluminium cylinders. Each cylinder has an internal volume of 30 L and a pressure rating of 140 atm. Each bottle typically contains ~8000 standard liters of GXe (~43 kg) at a pressure of ~50 atm. The bottles are connected together with 0.25 in. stainless vacuum tubing and high-purity bellows-sealed valves. A pipe connects the Xe storage system to the Xe purification system. The purification system, or Xe recirculation system, consists of a diaphragm pump, a mass flow controller, and a high-temperature getter.

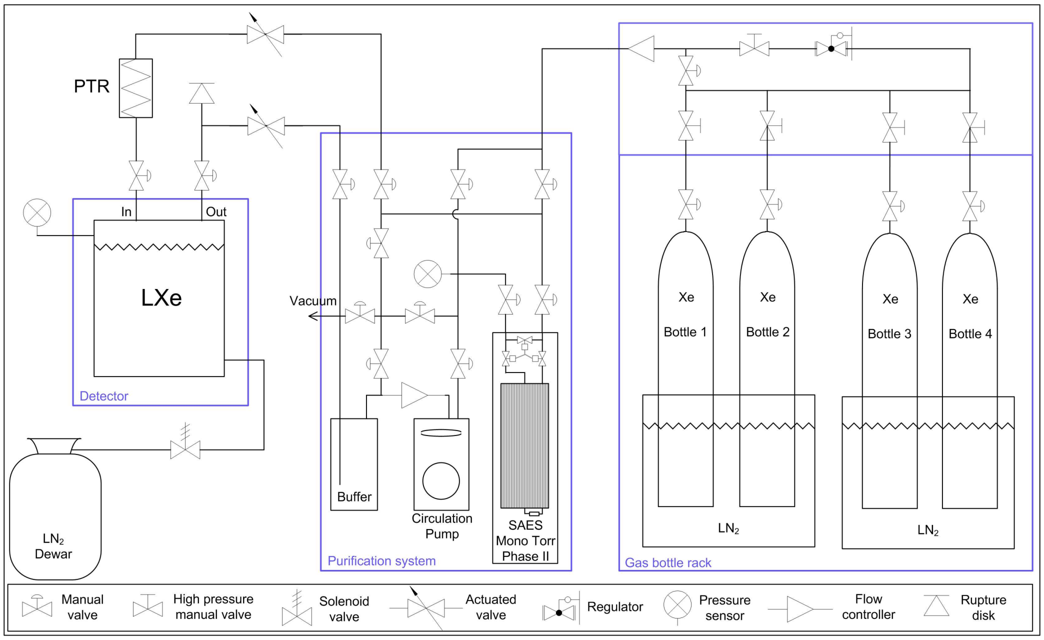

Figure 3.38: Schematic of the XENON100 gas system. Drawing by L. Coelho.

LXe from the bottom of the detector is evaporated in the gas line connecting the detector to the buffer volume of the recirculation system. The diaphragm pump draws GXe from the buffer volume and circulates the gas through the getter for purification. The model used is a KNF N 143 AN.12E double-diaphragm pump. The getter used is a SAES Mono Torr® PS4-MT15-R-1 heated getter purifier, certified to reduce concentrations of H_2O, O_2, CO, CO_2, N_2, H_2, and CH_4 to below 1 ppb for flow rates below 15 SLPM. The GXe at the output of the getter is fed back into the bell volume of the detector to provide the pressure difference that maintains the LXe level above the bell. The recirculation flow is kept stable with a Teledyne Hastings HFC-302 flow controller installed at the input of the diaphragm pump. The recirculation system is equipped with three actuated valves, two normally closed for the input and output, and one normally opened that connects both, and that act as a bypass mechanism that isolates the detector volume. Fig. 3.38 shows a schematic of the XENON100 gas storage, recirculation, and purification system.

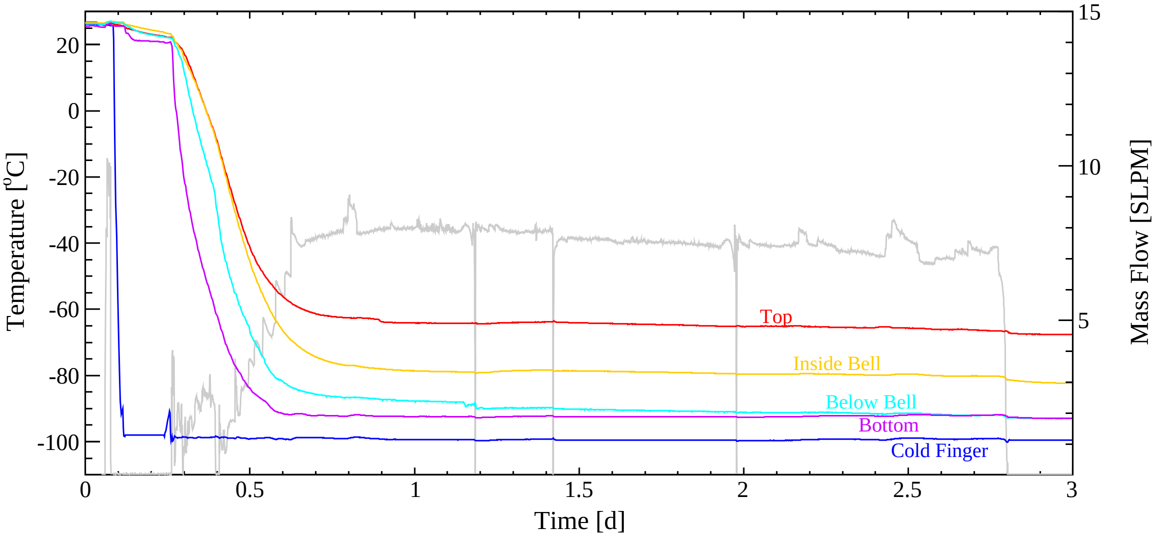

Figure 3.39: Evolution of the top (red), inside bell (orange), below bell (cyan), and bottom (violet) temperatures inside the XENON100 detector while filling, along with the GXe mass flow (gray). Except for the initial stage, the entire process is done at an almost constant pressure of 2.3 atm.

Filling from the cylinders to the detector or recovery into the cylinders occurs in the gas phase. Before filling, the detector is evacuated to reduce the amount of impurities to below the typical amount liberated by outgassing during the filling. Fig. 3.39 shows the evolution of the temperatures inside the XENON100 detector while filling and the Xe mass flow into the detector. After evacuation the detector is filled with GXe to a pressure of ~2.3 atm and the cryocooler started. Both events can be seen in Fig. 3.39 around a time of 0.1 d. The first mass flow spike (grey line) corresponds to the initial fill with GXe and the cold finger temperature sudden drop (blue line) is due to the cryocooler startup.

A period of pre-cooling where GXe is circulated through the detector volume usually precedes the actual filling. The time required to lower the temperature of the whole inner detector structure solely with GXe circulation would be very long due to the low heat conductivity of GXe, coupled with the decrease in conductivity with decrease in pressure. This can be seen on the figure by looking at the temperature slopes between times of 0.1 and 0.3 d. As soon as more gas is filled the temperatures decrease much faster. The filling initially starts with cycles of pressure increases from the addition of GXe (spikes in the mass flow) and pressure decreases from its liquefaction. This process is rather slow at the beginning as the LXe droplets immediately vaporize upon contact with the warmer cooling tower funnel surface. The LXe essentially cools down the funnel and the LXe flow path pipe to LXe temperature by successive evaporation of droplets. Once the pipe is completely cooled the LXe can flow to the detector vessel and begin the same process with the cryostat inner vessel. The filling speed gradually increases as the mass of the inner detector structure is progressively cooled. A maximum filling speed of ~2.8 kg/hr is attained after 10 h of filling, limited by the available cooling power of the PTR. The initial slope of the filling speed is roughly $0.5\,\mathrm{kg\,hr^{-2}}$. The total mass of 161 kg can thus be transfered into the detector in about 2.5 days.

For the Xe recovery operation, custom-made insulated steel dewars are used to cool down the aluminium cylinders with LN_2. The output of the recirculation system is then simply switched from the detector to the storage system. Recuperation is slightly faster (~2 days) since the LN_2 bath provides a very high cooling power. The mass flow is then essentially limited by the pressure in the detector vessel and the length of the pipe to the storage cylinders since the pressure in the cylinders is almost zero (the Xe gas freezes into the bottles).

3.3.7 Xe Purity

Scintillation and ionizations signals in LXe can be attenuated if the purity of the liquid is not at extremely high levels. As discussed in Sec. 2.3.4, the common impurity with the highest absorption cross-section for LXe scintillation light is H_2O, followed by O_2. For example, with H_2O concentrations at the ppm level one would expect scintillation light absorption lengths of

$$\lambda_{\mathrm{abs,H_2O}} = \frac{1}{10^{-6} \cdot n_{\mathrm{Xe}} \sigma_{\mathrm{H_2O}}} = \frac{131\,\mathrm{g\,mol^{-1}}}{10^{-6} N_A \cdot 2.83\,\mathrm{g\,cm^{-3}} \cdot 2 \times 10^{-18}\,\mathrm{cm^2}} \approx 38\,\mathrm{cm} \qquad (3.2)$$

clearly unacceptable. At the same time, the ionization signal is even more sensitive to the presence of impurities, especially electronegative impurities. Among common impurities, O_2 has the highest electron attachment cross-section. For example, for O_2 concentrations at the level of ppb, and at a drift field of $0.5\,\mathrm{kV\,cm^{-1}}$ where the electron attachment rate constant is $k_{O_2} = 1 \times 10^{11}\,\mathrm{mol^{-1}\,L\,s^{-1}}$ (Bakale *et al.*, 1976), the corresponding electron lifetime is

$$\tau_e = \frac{1}{10^{-9} \cdot n_{\mathrm{Xe}} k_{O_2}} = \frac{131\,\mathrm{g\,mol^{-1}}}{10^{-9} \cdot 2.83\,\mathrm{g\,cm^{-3}} \cdot 1 \times 10^{11}\,\mathrm{mol^{-1}\,L\,s^{-1}}} \approx 463\,\mu\mathrm{s}. \qquad (3.3)$$

With a maximum drift time of ~175 μs, clearly ppb O_2-equivalent concentrations are required. The Xe gas used to fill the XENON100 detector is research grade 99.999% purity Xe hence the need of the Xe recirculation system to purify it to ppb impurity levels.

Common impurities, here, refers to molecules that can typically be found in stainless steel vacuum systems for which great care was taken to clean them prior to their evacuation. Usually, they will consist of H_2O, N_2, O_2, CO_2, and Ar, most of which are present in air at the percent level. Due to its high binding energy to surfaces, the desorption of H_2O in vacuum systems is not ruled by the pumping speed. Typically vacuum systems will be baked at high temperatures (~180°C) to increase the desorption rate of H_2O. Unfortunately, dual-phase LXe TPCs with PMTs cannot withstand this high temperature, the R8520 PMTs for example are limited to a temperature of 50°C. The materials in contact with LXe being at such a low temperature have very low outgassing rates. In the case of XENON100, not all surfaces are at LXe temperature. The PMT signal and HV pipes for example are close to room temperature. This has the consequence that the concentrations of impurities in the liquid are function both of the recirculation speed and the outgassing rate of the warm surfaces. Sec. 4.2.2 discusses this topic further in the context of the measurement of the electron lifetime.

3.3.8 Passive Shield

The XENON100 detector was designed to be installed inside the XENON10 passive shield, after a few modifications to the shield door to accommodate the cooling tower. The XENON100 passive shield consists of, from outer layers to inner layers, a 20 cm thick water layer on the top and three sides, a 25 cm thick slab of polyethylene on which the shield rests, a 20 cm thick layer of polyethylene, and a 5 cm thick layer of OFHC copper. The lead and polyethylene layers attenuate the background from external γ rays and neutrons, respectively, while the copper layer attenuates the γ background from the polyethylene. Finally the external water and polyethylene layer further reduces the background contribution from neutrons from the cavern rock. The inner cavity is accessed by rolling on rails one wall, the shield door, onto which the detector cryostat is secured. When the shield door is closed the inner cavity is continuously purged with boil-off N_2 gas at a rate of 17 SLPM to prevent Rn penetration into the cavity. The Rn concentration is monitored with a commercial Rn monitor via an external tube that connects to the inner cavity and yields values below the detection limit of the instrument ($1\,\mathrm{Bq/m^3}$). The design, construction, and shielding performance of the XENON10 shield are discussed in detail in Sorensen (2008).

As described earlier in Sec. 3.2.7, a straight tube penetrating the shield door and connected to a circular tube that goes around the detector is used to insert calibration sources from outside the shield and irradiate the detector from various azimuthal positions. A lead brick arrangement is installed at a fixed azimuth to attenuate high energy γ rays produced by the AmBe neutron source. This source is used for the nuclear recoil band calibration of the detector (Sec. 4.5). The γ rays mostly come from the de-excitation of ^{12}C after the ^{9}B$(\alpha, n)^{12}$C reaction.

3.3.9 Krypton Distillation Column

Xenon, as mentioned in Sec. 2.1, is a particularly appropriate material for low-background rare event searches as it is the element with the second largest number of stable isotopes (tin is the first) and has no long lived isotopes. The longest-lived isotope is ^{127}Xe with a half-life of 36.3 d. As a condensed noble gas, is it also readily purifiable for most radioactive impurities. One exception, however, is ^{85}Kr, present in $^{\mathrm{nat}}$Kr with an isotopic abundance of $\sim 10^{-11}$. ^{85}Kr decays into ^{85}Rb with a half-life of 10.76 y through a beta decay with a 687 keV

Figure 3.40: Picture of inner cavity of the XENON100 passive shield. A copper support holds the lead brick arrangement used to attenuate high energy γ rays from the AmBe neutron source used for calibration. Also visible in the lower right corner is a mount of the cryostat and the mechanical coupling (Sec. 3.2.2) that allows the leveling (Sec. 4.2.3) of the cryostat from outside the passive shield.

endpoint. ^{85}Kr is produced in small quantities in the atmosphere from the capture of cosmic ray neutrons on ^{84}Kr but most of its abundance in the atmosphere is a result of nuclear fission, of which it is a product. As ^{85}Kr is uniformly distributed in the LXe volume and contributes to the background in the energy region of interest it thus presents a potentially serious background for a dark matter search with LXe. $^{\mathrm{nat}}$Kr, present in commercial Xe gas at the ppm (mol/mol) level, would generate an electronic recoil background rate of $\sim$20 events keV^{-1} kg^{-1} d^{-1} through decays of ^{85}Kr.

The $^{\mathrm{nat}}$Kr concentration of the gas used for the XENON100 detector, procured from Spectra Gases Inc., was reduced to $\sim$10 ppb by the company using their cryogenic distillation plant. In the XENON100 detector, the ^{85}Kr concentration can be measured directly through β-γ delayed coincidences $^{85}\mathrm{Kr}\,(\beta, 173\,\mathrm{keV}) \longrightarrow {}^{85m}\mathrm{Rb}\,(\gamma, 514\,\mathrm{keV}) \longrightarrow {}^{85}\mathrm{Rb}$ with a $1.46\,\mu$s time difference and a 0.454% branching ratio. The analysis of the first XENON100 background data run confirmed the specified concentration with a measurement of the $^{\mathrm{nat}}$Kr concentration at 7 ppb.

A $^{\mathrm{nat}}$Kr concentration of 100 ppt would contribute a rate of $\sim$0.002 events keV^{-1} kg^{-1} d^{-1}

from decays of ^{85}Kr and would make the ^{85}Kr contribution to the electronic recoil background level sub-dominant. In order to reduce the $^{\mathrm{nat}}$Kr concentration in the gas used for the experiment, a small-scale cryogenic distillation column is installed underground near the XENON100 detector. The column was procured from Taiyo Nippon Sanso (Taiyo Nippon Sanso). The column is a 3 m tall, 6 theoretical cell stages, distillation column designed with the McCabe-Thiele method (McCabe and Smith, 1976) to provide a ×1000 reduction in the $^{\mathrm{nat}}$Kr concentration at a purification speed of 0.6 kg/hr and a collection efficiency of 99%. The input and output Xe are in the gas phase. A small sample of Xe gas processed with a column of similar design, and analyzed by mass spectroscopy, was reported to have a Kr level of 3 ppt (Abe *et al.*, 2009).

After the installation underground and a commissioning run of the column, the entire XENON100 gas inventory was processed through the distillation column. For the commissioning run that led to the first XENON100 dark matter results (Sec. 4.6), the ^{85}Kr concentration was measured with the delayed coincidence method and a value of 143^{+130}_{-90} ppt (mol/mol) (90% c.l.) was obtained for the $^{\mathrm{nat}}$Kr concentration.

3.3.10 Data Acquisition System

As mentioned in Sec. 3.1, the design chosen for the DAQ was the digitization of PMT signals with FADCs for the versatility and large amount of information present in digitized time traces. The XENON100 data acquisition system is divided into three subsystems, the trigger, the waveform acquisition subsystem, and the rate and time accounting subsystem. The trigger uses a S2-based trigger scheme to limit the rate to events within the TPC. The waveform acquisition subsystem is composed of 31 CAEN V1724 14 bit 100 MS/s FADCs. The FADCs have an input bandwidth of 40 MHz and a full scale range of 2.25V. The modules are housed in two VME crates and connected to the DAQ computer via an optical fiber connection. The format into which events are stored is described in Sec. 3.4.2. Fig. 3.41 shows a diagram of the XENON100 DAQ system.

The signals from all 242 PMTs are fed into Phillips 776 ×10 amplifiers. The Phillips 776 ×10 amplifier has two amplified outputs per channel and thus also allows to get two copies of the analog signal. The first copy of each channel is digitized by the FADCs. The second copy of 68 inner PMT channels of the top array and 16 inner PMT channels of the bottom array are summed in Phillips 740 fan-ins. The summed signal is amplified and filtered with

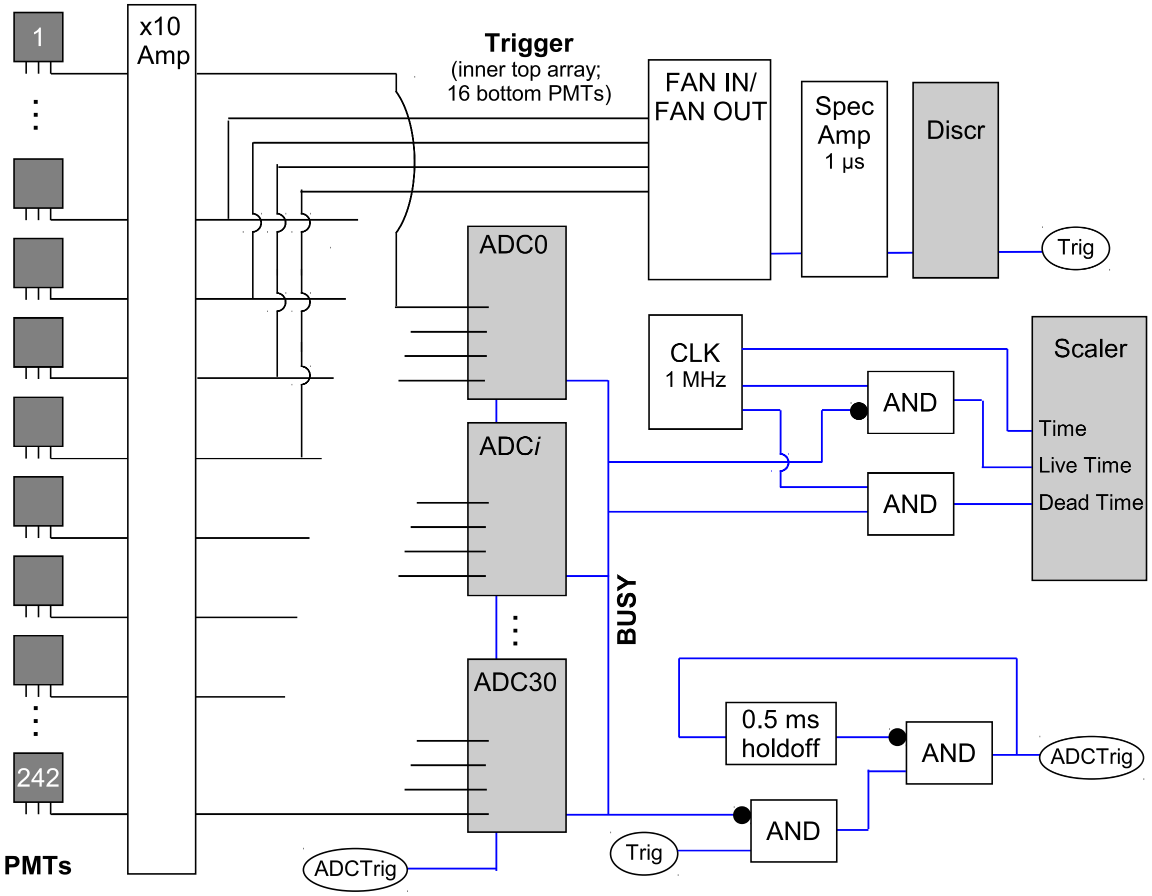

Figure 3.41: XENON100 DAQ and trigger diagram. Figure from Aprile *et al.* (2011f).

an ORTEC model 450 research amplifier with an integration time constant of 1 μs. The integrated signal is discriminated and constitutes the preliminary trigger logic signal. This trigger signal is combined into an AND gate with a logic signal indicating whether or not the FADCs are in a busy state and subsequently combined with a holdoff logic signal that prevents the generation of a secondary trigger signal for 0.5 ms. The resulting logic signal is distributed simultaneously to the 31 FACDs modules.

At low trigger rates, the CAEN V1724 FADC permits operation in a deadtime-less mode where data is written to a circular buffer with 512 kB memory per channel and where multiple events can be stored before they are read via the VME bus. Additionally, an on-board FPGA allows on-line "zero-length encoding" of the digitized samples, that is, only the relevant portions of the signal trace are stored to the module memory and transfered from the module to the data acquisition computer. S1 and S2 signals have typical time scales of < 150 ns and 1 μs, respectively, but the time the ionization electrons take to travel from the interaction site to the liquid level ranges from 0 to ~175 μs at a drift field of 0.530 kV/cm. The acquisition window is set at 400 μs, more than twice the maximum drift time, with the trigger positioned in the middle of the window, such that all features of an event are recorded, whether the trigger occurred due to a S1 signal or a S2 signal. Thus, large portions of the digitized waveform are essentially free of signals and consist mostly of baseline samples. This is where the zero-length encoding algorithm can greatly reduce the size of events.

The zero-length encoding algorithm implemented on the on-board FPGA includes only portions of the waveform where the voltage exceeds a predefined threshold, with a fixed number of samples before and after the excursion above threshold. For XENON100 the encoding threshold is set at 30 digitizer counts (~4 mV) and pre- and post-excursion segments of 50 samples (500 ns). The threshold corresponds to ~0.3 photoelectrons. The digitized trace is represented by a sequence of two types of control words, a *skip* control word and a *samples* control word. The *skip* control word indicates how many digitized samples are not present in the stream because they were below threshold while the *samples* control word indicates that a sequence of samples above threshold are present and follow the control word. Due to a bandwidth limitation of the FADC module a maximum of 14 *skip* → *samples* or vice-versa control word transitions can occur within an event. Fig. 3.42 shows an example of a zero-length encoded waveform. The digital representation of the zero-length encoded format is described in Sec. 3.4.2.

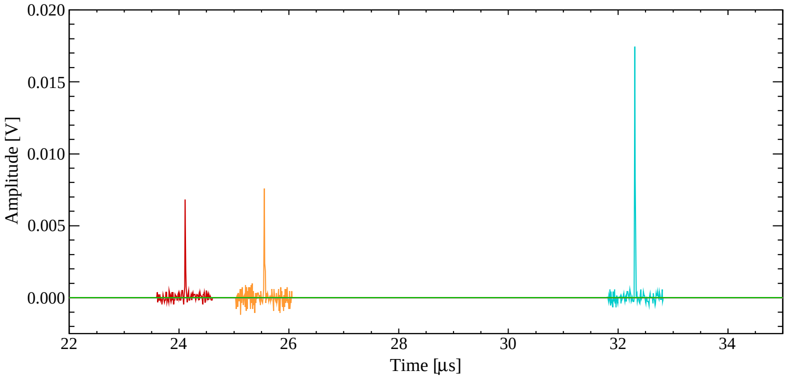

Figure 3.42: Zero-length encoded XENON100 PMT waveform. Three different PMTs record single photoelectrons at different times and only the samples around the excursions above threshold are included in the waveforms.

For low energy events, this zero-length encoding results in a reduction of the event size by a factor ten. PMT waveforms from veto PMTs essentially take no space as they do not record any S2 signals. At higher energies however, large S2 signals followed by a series of few electron S2 signals (see Sec. 4.2.4) result in larger event sizes and the reduction is not as dramatic. Nevertheless, this data reduction allows much higher calibration rates as the data volume to be transfered to the host computer is reduced. For high energy γ sources the maximum rate achievable is ~30 Hz. The VME crate optical fiber maximum transfer rate and the RAID array maximum writing speed are the limiting factors for the transfer speed to the DAQ computer. Sec. 3.4.1 discusses in more details the DAQ computing infrastructure and these issues. One should note however that calibration rates higher than that are not advisable in any case as the accidental coincidence probability within the event window is already approximately at the $30\,\mathrm{Hz} \cdot 400\,\mu\mathrm{s} \approx 1\%$ level.

The CAEN V1724 FADC modules have low-voltage digital signalling (LVDS) I/O ports that can communicate the status of the board to other devices. The *memory full* output status of the module signals that the module will ignore all subsequent triggers until some events are transfered from the module memory. The *memory full* status of the 31 FADC modules are combined with an OR function using a CAEN V1495 programmable general purpose VME logic module and constitutes the *busy* logic signal. Since channel data are spread among multiple modules and transfered in sequence from each module, a mismatch could occur if a module with memory recently freed would accept a trigger when another module still has a *memory full* condition. This situation is avoided by inhibiting triggers when the *busy* logic signal is true.

The DAQ trigger also includes a high energy veto subsystem that inhibits triggers if the energy of the event exceeds a certain threshold. Since the data transfer rate between the VME crates with the FADCs and the DAQ computer is limited by a combination of the fiber optical connection and the writing speed to disk, it is clearly advantageous to prevent the transfer of events which are outside of the energy range of interest. The high-energy veto is used for all low-energy calibrations such as the electronic recoil band and nuclear recoil band calibrations (Sec. 4.5). The threshold is set a value high enough so that no distortion of the spectrum at low energies occurs.

The rate and time accounting subsystem of the DAQ is responsible for measuring the time, live time, dead time, trigger rate, and event rate of the measurement. A clock module that generates a logic signal at a frequency of 1 MHz and is combined with the *busy* signal and its complement to compute the dead time and live time, respectively. A CAEN V830 scaler is used to count the number of clock cycles, dead cycles and live cycles. The scaler also counts the number of triggers, before any inhibition due to the *busy* signal or a *high energy veto* signal, and the number of events of the measurement.

The efficiency of the XENON100 trigger was measured initially by feeding a square voltage pulse with a width of $1\,\mu$s width and variable height to the research amplifier. At a pulse height of 24 mV a trigger was generated for every voltage pulse. At a PMT gain of $2 \times 10^6\,\mathrm{pe/e^-}$ and after the $\times 10$ amplification, a photoelectron corresponds to a charge signal of $160\,\mathrm{mV\,ns}$ in the $50\,\Omega$ input resistor of the FADC. This means that the $24\,\mathrm{mV}\,\mu$s square pulse was equivalent to a 150 pe signal. Since the PMTs used for the trigger collect ~52% of the S2 light the ~100% efficiency trigger threshold is 290 pe. This value was verified subsequently by a direct measurement. Events were triggered by energy deposits in the veto instead of the normal trigger and the normal trigger was digitized along with the PMT signals. This allowed the computation of the fraction of S2 signals of a given size that are generated a trigger compared to the total number of S2 signals of a given size.

3.4 Computing Infrastructure

In this section we will describe the computing infrastructure deployed for the XENON100 experiment, both the hardware and software side, with respect to the acquisition (Sec. 3.4.1), storage (Sec. 3.4.2), and processing (Sec. 3.4.3) of data.

3.4.1 Data Acquisition

The data acquisition system, in proximity to the XENON100 detector, consists of the DAQ computer and its communication interface to the VME crates containing the FADCs. It is responsible for the transfer of digitized waveforms from the FADCs to a local data storage, while it awaits the transfer to the main data storage resources above ground. In normal circumstances, for example when acquiring background data for a dark matter search, the trigger rate is such that none of the FADCs enter the *memory full* condition. The DAQ program periodically checks for the presence of data in one of the modules and proceeds to transfer the data acquired by all modules. The raw data is stored locally in a versatile, custom, indexed data format described in Sec. 3.4.2. The hardware selected for the local storage was a four drive RAID10 array to accommodate both fast read and write operations and redundancy in the case of hard drive failures. As mentioned earlier, the baseline samples of the waveforms are already encoded as skip control words on the FADCs to reduce the data rates between the VME crates and the DAQ computer.

A measurement of a given duration and for which the acquisition is subsequently stopped is called a dataset. Dark matter search datasets are typically uninterrupted one day long datasets while γ calibration datasets are usually a few hours. PMT calibration datasets are less than an hour. A run refers to a collection of datasets usually separated in time by a recuperation and filling of the detector or an event that changed detector conditions. The transfer of datasets from the DAQ computer underground is automated and performed by a custom data transfer program based on the `rsync` program. The transfer program maintains a list of datasets that exist on the DAQ machine and synchronizes modified data files acquired to the storage above ground. When a dataset no longer changes, typically because the acquisition was stopped and a new dataset was started, the transfer program will protect the dataset on the main storage against modifications and later delete the dataset from the DAQ local storage (after a certain delay). In this way there is no dead time incurred from data transfers to the main storage during high data rate γ calibrations, as the DAQ computer storage acts as a buffer. The transfer program also implements the blinding protocol by making the raw data acquired unreadable until the decision is explicitly made to "unblind" the dataset.

3.4.2 Data Storage

The XENON100 data storage system consists of a collection of storage nodes with large data capacity totalizing ~100 TB. The nodes use RAID5 and RAID6 arrays for redundancy in the event of hard drive failures. As mentioned earlier, the data transfer program is responsible for the transfer and integrity of raw datasets from the DAQ computer underground to the main storage. The raw data of the XENON100 detector is stored in a general purpose detector-independent data format designated as the XENON data input-output (XDIO) format. Fig. 3.43 shows a schematic representation of the headers of the XDIO format with byte offsets indicated on top for each header.

The format is defined by three logical layers, the *file* layer, the *event* layer, and the *chunk* layer. An XDIO file contains multiple events and events contain multiple chunks. A dataset will typically contain many files. All multiple byte types are stored in little-endian format. The file layer stores the original dataset name (`FILENAME`), the time of creation (`TIME`), first event number (`FIRST EVENT NB`), and number of events (`NB EVENTS`) of the file. It also maintains an index of the positions (`INDEX[]`) of events within the file for fast extraction of single events from large files.

The event layer stores the original dataset name the event is part of (`FILENAME`), the Coordinated Universal Time (UTC) of the event in seconds (`TIME SEC`) and a fractional part in microseconds (`TIME USEC`), the event number within the dataset (`EVENT NB`), and the number of chunks the event holds (`NB CHUNKS`). Typically a chunk type will be associated with the data from an instrument, for example the digitized waveforms from an FADC or the counts from a scaler.

The chunk layer contains a header describing the type of chunk (`TYPE`) and the actual data, digitizer samples, or any other form defined through a chunk type. The format currently implements only two types of chunks, `RAW0` and `ZLE0`, for sequences of digitizer samples from a generic FADC and "zero-length" encoded digitizer samples from the CAEN V1724 FADC, respectively. The chunk layer stores the chunk size (`SIZE`), the type of

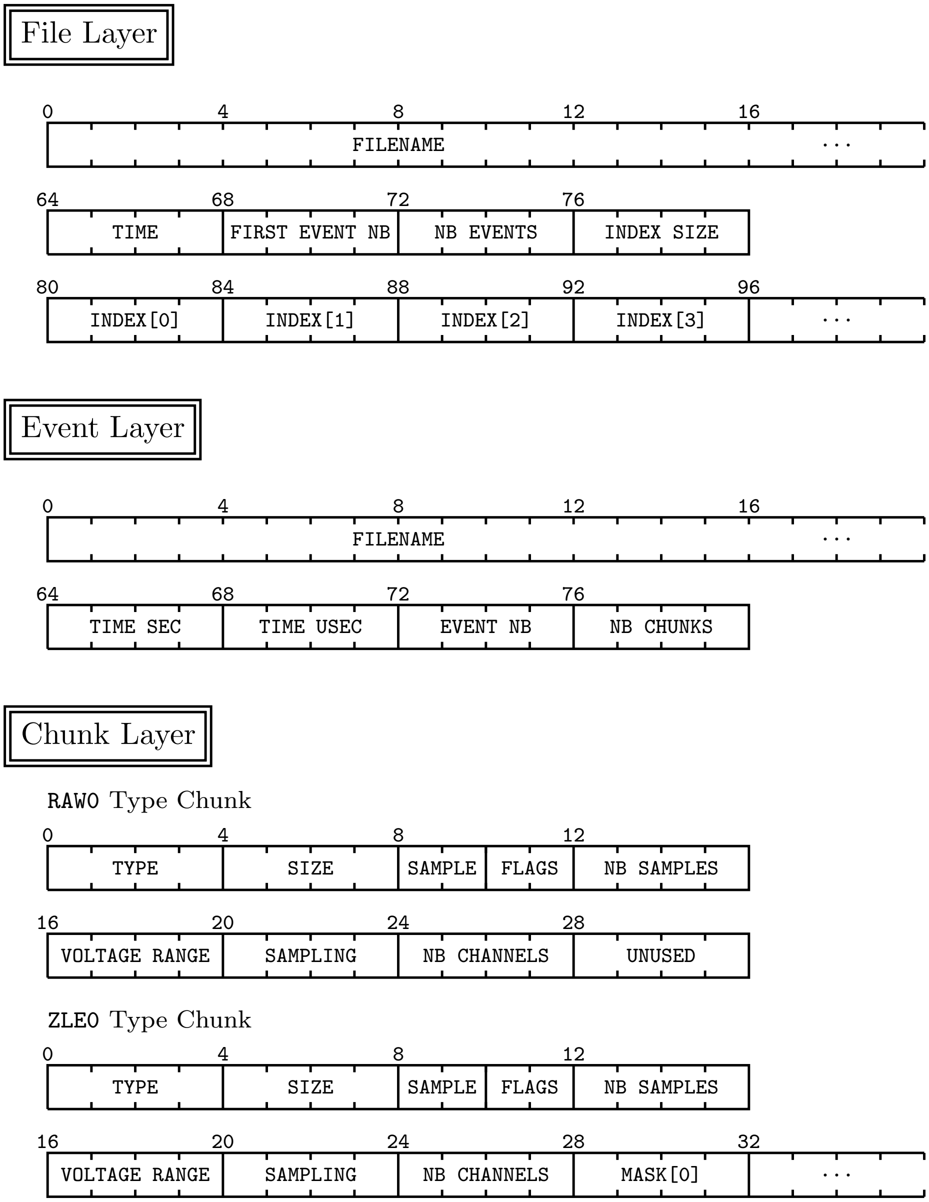

Figure 3.43: Schematic representation of the headers of the XDIO format used to store raw data from the XENON100 detector. Byte offsets are indicated on top for each header.

samples (`SAMPLE`), flags (`FLAGS`), the number of digitizer samples included (`NB SAMPLES`), the voltage range (`VOLTAGE RANGE`), the sampling frequency (`SAMPLING`), and the number of channels (`NB CHANNELS`) of the FADC. The sample type is stored as a signed integer and indicates the precision in bits of a sample. The voltage range and sampling frequency are both encoded as single precision IEEE 754 floating point numbers. In the case of the `RAW0` chunk, a sequence of `NB CHANNELS` × `NB SAMPLES` digitizer samples follows the header, starting with the first channel and so on. In the case of the `ZLE0` chunk, a binary mask (`MASK[]`) encodes which channels are included. The data that follows is the channel data from each V1724 FADC, composed of a size header for the channel data (`CHANNEL DATA SIZE`) and a sequence of zero-length encoded samples (see Fig. 3.44). The data for each channel included in the `MASK[]` appears sequentially.

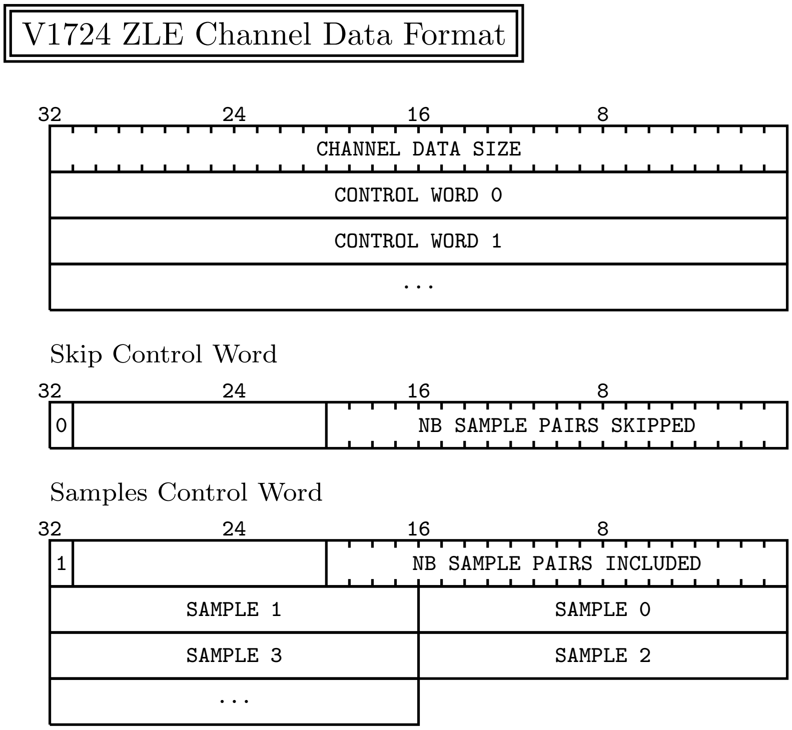

Figure 3.44: Schematic representation of the V1724 ZLE channel data format. Bit offsets are indicated on top. The size of the channel data is given in number of 32 bit words. Similarly, the number of skipped or good samples is also given in 32 bit words. Since FADC samples are written on 16 bits, each 32 bit word contains a pair of samples.

A C library, libxdio, has been written for input and output operations on XDIO files. Operations on the chunk layer are abstracted and follow a defined interface such that additional chunk specifications can easily be added without breaking compatibility with previous definitions. The library is also designed such that copy operations are minimized to handle large data rates without overhead.

3.4.3 Data Processing

The raw data for a XENON100 event consists of 242 waveforms of (usually) 40000 samples and is stored in the general-purpose XENON event data (XDIO) file format using the libxdio library. This raw data is converted to physical parameters using a program specifically written for XENON100 data analysis, the XENON raw data processor, *xerawdp*, but with a design that should allow processing of raw data from other liquid xenon detectors. High reusability is achieved by making most of the module interfaces as generic as possible and making each module highly configurable. With nearly all parameters specified via an input xml configuration file the program can be used to convert raw data from varying detector conditions or even other detectors, as mentioned earlier. The data conversion proceeds in three stages: i) preprocessing the waveforms, ii) searching for peak candidates, and finally iii) computing the reduced quantities associated with each peak candidate.

Preprocessing

In the preprocessing stage, the event attributes from the XDIO event layer are read, and the `ZLE0` or `RAW0` chunk containing the channel waveforms is read. For all channels included, the baseline of each zero-length encoded block is computed on 46 samples (*nb_baseline_samples*) and the digitizer samples are converted from ADC counts to volts. The *nb_baseline_samples* value was chosen such that it is smaller than the number of pre-samples included in the zero-length encoded block. The waveforms of all target volume channels are added into a summed waveform that is used to search for S1 and S2 peak candidates. The waveforms of veto volume channels are also added into a summed veto waveform that is used to search for S1 peak candidates. It is possible to exclude channels from the S1 or S2 peak finding summed waveform via the *excluded_pmts* parameter.

Fig. 3.45 shows TPC and veto summed waveforms for a typical low-energy event. The blue triangle indicates the S1 peak candidate found and the red triangles the S2 peak candidates. Zooms of the largest S1 and S2 peaks are shown in insets.

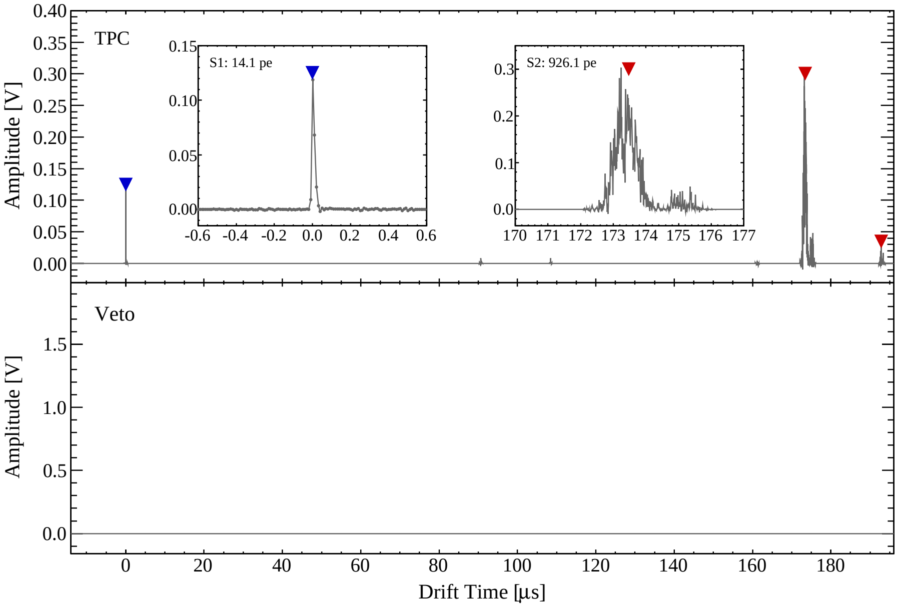

Figure 3.45: TPC and veto summed waveforms for a typical low-energy event. The blue triangle indicates the S1 peak candidate found and the red triangles the S2 peak candidates. The event is deep within the detector with a drift time of 173.5 μs.

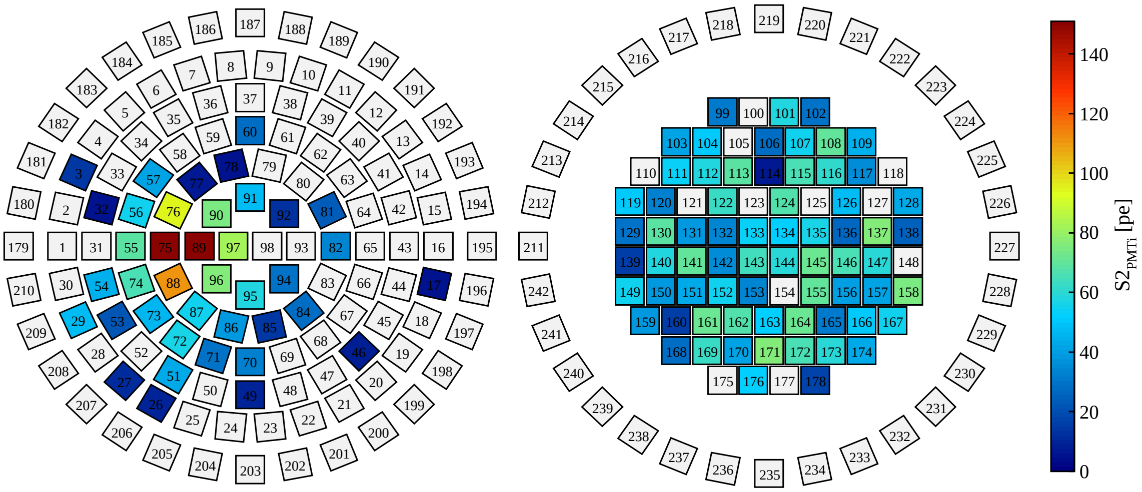

Figure 3.46: Distribution on PMTs of the S2 signal of a typical low-energy event.

S1 and S2 Peak Finding

The target volume peak finding stage operates in two steps: it first looks for S2-like peaks in the entire summed waveform and then looks for S1-like peaks in between all S2 peak candidates found in the first step but not beyond a S2 peak that exceeds a 50 mV threshold (*s1_right_limit_height_threshold*). This condition is used since we expect the S1 signal to precede any S2 signal if the two signals arise from the same energy deposit. This also avoids the selection as S1 peak candidates of any of the many photoelectrons that typically follow a large S2 peak such as PMT afterpulses and single electron S2 signals (see Sec. 4.2.4).

The S2 peak finding algorithm starts by applying a digital filter (*s2_large_peak_filter*) to the entire waveform to smooth out the high frequency components which facilitates the detection of the extent of S2 peaks (see Fig. 3.47, bottom). The filter used is a raised cosine filter low-pass filter with a cut-off frequency at 3 MHz. The algorithm then searches the filtered waveform for regions where the signal exceeds a threshold of 10 mV (*s2_large_peaks_signal_threshold*) for at least $0.6\,\mu$s (*s2_large_peaks_min_interval_width*), a time interval large enough to contain at least one S2 peak. The average of the $0.21\,\mu$s of the waveform (*s2_large_peaks_pre* and *s2_large_peaks_post_interval_avg_window*) preceding and following the interval must also not exceed 5% (*s2_large_peaks_pre_interval_avg_threshold*) of the maximum within the interval. Because of the long afterpulsing tails that follow large S2 peaks the interval above threshold will often contain multiple S2 peaks.

The algorithm then recursively searches for S2-like peaks within that interval. This is done by computing the extent of any potential peak by starting from its maximum sample in the interval and going backwards in the trace until either the signal drops below 0.5% (*s2_large_peaks_left_height_fraction_threshold*) of its maximum or the slope of the signal changes sign. This defines the left boundary of this peak. The same procedure is repeated going forward in the trace to find the right boundary. If the peak found has a FWHM larger than $0.35\,\mu$s (*s2_large_peaks_min_width*), much smaller than typical S2 widths observed , it will be considered as a valid S2 peak candidate and its location and boundaries will be saved. The recursive search for S2 peaks then continues within the interval, excluding the regions where any peaks might already have been found. The stopping condition is that the new sub-interval width be large enough to hold a S2 peak (*s2_large_peaks_min_interval_width*). Fig. 3.48 shows a graphical representation of the recursive search for S2 peaks. This first part of the algorithm will detect S2-like peaks down to very low energies (~150 pe) with close to 100% efficiency. The division of intervals above threshold into sub-intervals and the detection of slope changes in the summed waveform also allows a very good double S2 peak resolution.

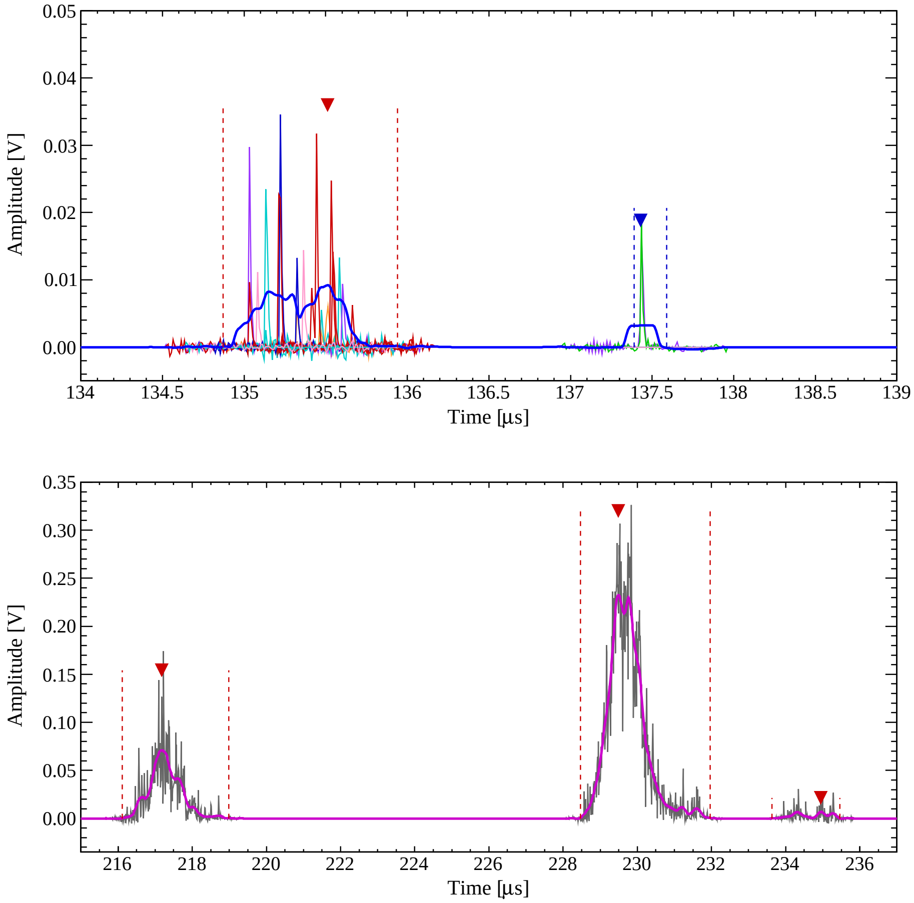

Figure 3.47: Graphical representation of the filtered waveforms used for the search of S1 and S2 peak candidates. The *s2_tiny_peaks_filter* filtered waveform (top, thick blue line) is used to detect small S2 peaks (left, red marker). The much faster S1 peaks (right, blue marker) have a response very close to the impulse response of the digital filter. The *s2_peaks_filter* filtered waveform is used to detect the extent of larger S2 peaks (bottom, thick magenta line).

After searching for large S2 peak candidates, the S2 peak finding algorithm proceeds to search for the smallest of S2 peaks from tens all the way down to single electron S2 peaks. A digital filter (*s2_tiny_peaks_filter*) with a higher frequency cut-off is applied (see Fig. 3.47, top) to the summed waveform to identify intervals where its average height exceeds what is expected for a single electron S2 signal. An estimate can be obtained from

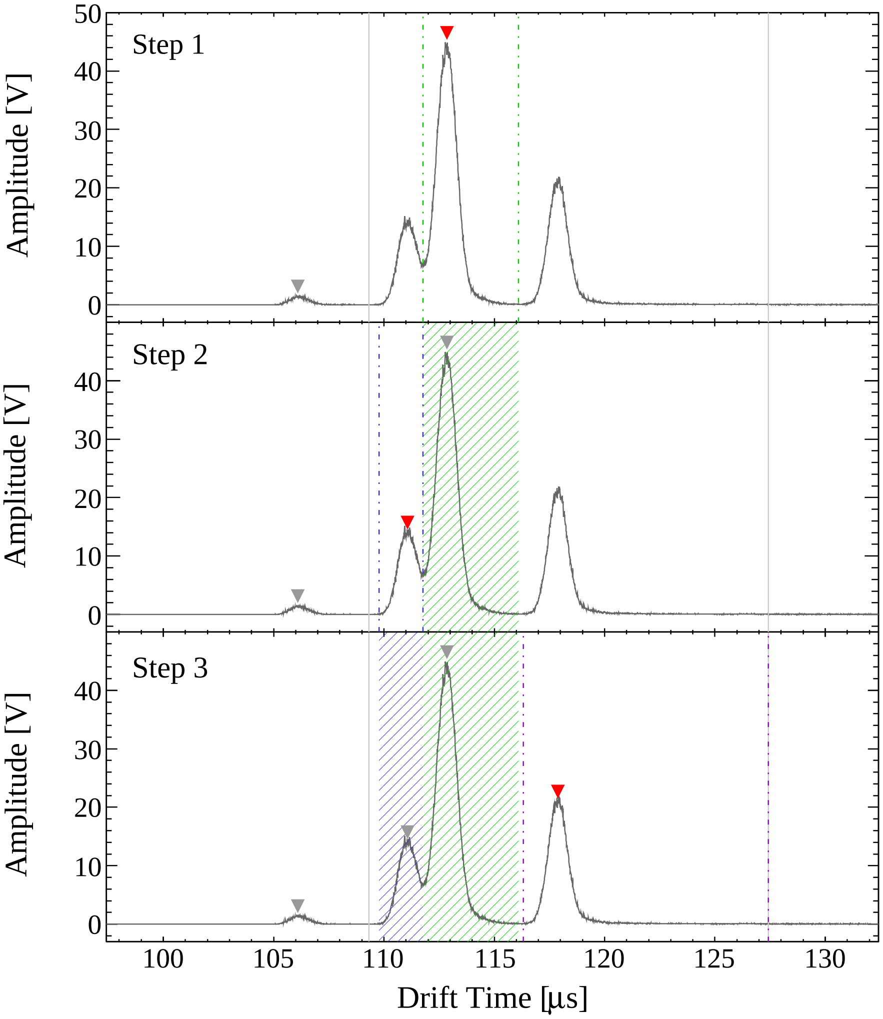

Figure 3.48: Graphical representation of the recursive S2 peak search. The solid grey lines represent the interval bounds. In step 1, the largest sample of the interval is selected as the position of a potential S2. The extent of the peak, represented by the green dash-dotted lines, is found on the left via the slope change condition and on the right via the threshold condition. The peak fulfills all requirements and is accepted as an S2 peak. In step 2, the algorithm moves on to the sub-interval to the left of the previous peak and discovers the second S2 peak. The recursive search then skips the sub-interval on the left and the right of the current peak since they are smaller than the minimum width condition. Finally in step 3 the last S2 peak is found.

Eq. 2.13 with $E = 12\,\mathrm{kV\,cm^{-1}}$, $p = 2.25\,\mathrm{atm}$ and $d = 2.5\,\mathrm{mm}$, giving $N_{\mathrm{ph}} \approx 170$ photons. Assuming a S2 light collection efficiency of 28% and a QE of ~25% one arrives at ~12 pe, so roughly tens of photoelectrons over $0.4\,\mu$s, that is, the time an electron takes to travel across the 2.5 mm proportional amplification gap with a drift velocity of $6.86\,\mathrm{mm}/\mu\mathrm{s}$ at $12\,\mathrm{kV\,cm^{-1}}$ and 2.25 atm. Several conditions must be met for an interval above threshold to be considered a S2 peak candidate. The filtered waveform must exceed 1 mV (*s2_tiny_peaks_signal_threshold*) for more than $0.4\,\mu$s (*s2_tiny_peaks_min_interval_width*) and the average of the $0.1\,\mu$s (*s2_tiny_peaks_pre* and *s2_tiny_peaks_post_interval_avg_window*) preceding and following the interval must not exceed 5% of the maximum within the interval. Finally, the ratio of the interval maximum to its width must be larger than 0.1 mV/ns (*s2_tiny_peaks_aspect_ratio_threshold*).

All S2 peaks found, both large and tiny, are sorted in decreasing order of size (in mV ns) and the positions and boundaries of the 32 (*s2_max_nb_peaks*) largest S2 peak candidates are kept.

The S1 peak finding algorithm searches the total waveform for signal excursions of at least 3 mV (*s1_signal_threshold*) above the baseline. The boundaries of the peak candidate are defined as the points where the signal drops below 0.5% (*s1_height_fraction_threshold*) of its maximum, for more than 20 ns (*s1_samples_below_threshold*). If all of the following conditions are met the location and boundaries of the S1 peak candidate will be kept: the $0.5\,\mu$s (*s1_pre_peak_avg_window*) preceding the peak and the 100 ns (*s1_post_peak_avg_window*) following the peak respectively have an average signal less than 1% (*s1_pre_peak_avg_threshold*) and 4% (*s1_post_peak_avg_threshold*) of the maximum; the full-width at quarter maximum (FWQM) of the filtered (*s1_filter*) waveform near the peak candidate is smaller than $0.5\,\mu$s (*s1_filtered_width_threshold*), to distinguish them from single electron S2s; the maximum is at least 3 times larger (*s1_negative_excursion_fraction_threshold*) than the largest negative excursion in the vicinity of the peak. The parameters of the 32 (*s1_max_nb_peaks*) largest S1 peaks identified are kept.

Parameter Computation

Once all peaks have been identified, the conversion enters its last stage, the computation of the quantities of interest for each peak. This proceeds in five steps: computation of quantities that do not depend on PMT gains, computation of quantities that do depend

Algorithm 1 find_s2_peaks()

```
apply s2_large_peak_filter low-pass filter on summed waveform
while there are samples left do
  if sample > s2_large_peak_signal_threshold and we weren't above threshold then
    above_threshold ← true
    left_edge ← position
  end if
  if sample < s2_large_peak_signal_threshold and we were above threshold then
    above_threshold ← false
    right_edge ← position
    push the (left_edge, right_edge) interval on the stack
    while the stack of intervals is not empty do
      pop a (left, right) interval off the stack
      if right − left > s2_large_peaks_min_interval_width then
        left_boundary, right_boundary ← compute_s2_extent()
        fwhm ← full-width half maximum of the filtered waveform
        pre_peak_avg ← average over s2_pre_peak_avg_window samples
        post_peak_avg ← average over s2_post_peak_avg_window samples
        if fwhm < s2_filtered_width_threshold and pre_peak_avg < s2_pre_peak_avg_threshold and post_peak_avg < s2_post_peak_avg_threshold then
          record peak_position, left_boundary, right_boundary, and peak_area
          push the subinterval right of the peak on the stack
          push the subinterval left of the peak on the stack
        end if
      end if
    end while
  end if
  move to the next sample
end while
sort peak candidates by peak_position
apply s2_tiny_peak_filter low-pass filter on summed waveform
for all regions between S2 peaks do
  search for tiny S2 peaks with the same loop as describe above
end for
order peak candidates by peak_area
return the first s2_max_nb_peaks peak candidates
```

Algorithm 2 compute_s2_extent()

```
height_threshold ← s2_height_fraction_threshold · maximum
start from maximum_position
minimum_so_far ← maximum
loop
  if sample < minimum_so_far then
    minimum_so_far ← sample {keep track of the minimum and its position}
    minimum_position ← position
  end if
  if sample < height_threshold then
    exit loop
  end if
  if position is too far from maximum_position or slope < −s2_slope_threshold then
    position ← minimum_so_far {we reached the interval border or a slope change}
    exit loop
  end if
end loop
left_boundary ← position
do the equivalent to find the right_boundary
return left_boundary, right_boundary
```

Algorithm 3 find_s1_peaks()

```
apply s1_filter low-pass filter on summed waveform
for all regions between S2 peaks do
  if previous S2 peak was higher than s1_right_limit_height_threshold then
    return peaks found
  end if
  while there are samples left do
    if sample > s1_signal_threshold then
      left_boundary, right_boundary ← compute_s1_extent()
      fwqm ← full-width quarter maximum of the filtered waveform
      pre_peak_avg ← average over s1_pre_peak_avg_window samples
      post_peak_avg ← average over s1_post_peak_avg_window samples
      largest_negative_excursion ← minimum value around sample
      if peak_height > largest_negative_excursion and fwqm < s1_filtered_width_threshold and pre_peak_avg < s1_pre_peak_avg_threshold and post_peak_avg < s1_post_peak_avg_threshold then
        record peak_position, left_boundary, right_boundary, and peak_area
      end if
      move to right_boundary
    else
      move to the next sample
    end if
  end while
end for
order peak candidates by PMT coincidences and peak_area
return the first s1_max_nb_peaks peak candidates
```

Algorithm 4 compute_s1_extent()

```
height_threshold $\leftarrow$ $s1\_height\_fraction\_threshold \cdot$ maximum
start from maximum_position
count $\leftarrow 0$
while sample $<$ maximum do
  if position is too far from maximum_position or sample $<$ height_threshold then
    count $\leftarrow$ count $+ 1$ {increase the count of samples below threshold}
    if count $>$ $s1\_samples\_below\_threshold$ then
      exit loop
    end if
  else
    $c \leftarrow 0$ {we are not below threshold anymore}
  end if
  move position to the left
end while
left_boundary $\leftarrow$ position
do the equivalent to find the right_boundary
return left_boundary, right_boundary
```

on PMT gains, reconstruction of the (x, y) position of each S2 peak candidate (which obviously also depends on PMT gains), correction of the position using the simulated drift field, correction of the position dependence of the S1 and S2 signals for each peak candidate, and finally computation of any extra quantities that depend on the position of events within the target volume.

Each PMT waveform is integrated over the boundaries of the S1 and S2 peak candidates identified by the S1 and S2 peak finding algorithms and the values are converted into photoelectrons using the PMT gains. For each peak a number of quantities are computed: FWHM, 10% height full width, height, mean arrival time, number of PMT coincidences, number of digitizer channels saturating, etc. A few parameters of the entire waveform are also computed: its total area, the average and RMS of the baseline before any peaks, and the total S1 and S2 signals.

The (x, y) position of each S2 peak candidate is computed using three different position reconstruction algorithms. The first is based on support vector machines regression, the second on neural networks, and the third on χ^2 minimization. All three algorithms compute the (x, y) position of the S2 peak by comparison of the distribution of the S2 signal on top array PMTs to a Monte Carlo light propagation simulation of the expected distribution. The simulation assumes that the electroluminescence light emission is isotropic, point-like, and situated midway between the LXe level and the anode mesh. As most of the S2 light detected by the top array PMTs is direct, the influence of simulation parameters such as the LXe scintillation light attenuation length and the PTFE reflectivity should be minimal, except maybe near the edges of the sensitive volume. Nevertheless, these effects are included. The support vector machine and the neural network algorithm both require training on the Monte Carlo data. Since each PMT waveform is integrated for each S2 peak candidate independently, the (x, y) position of every S2 peak candidate stored is available.

The true position of each event within the target volume is computed from the (r, z) coordinates obtained from the S2 pattern and drift time via the electric field position correction (Sec. 4.3.1). The various signal corrections applied are: the S1-(r, z) correction, the S2-z correction (electron lifetime), the S2-(x, y) correction (independent corrections for top and bottom PMT arrays).

Chapter 4

Calibration of the XENON100 Detector

In Chap. 3, we described the elements incorporated in the design of the XENON100 detector, chronicled the steps of the construction and assembly stage, and finally gave an overview of the experiment and its subsystems. We now turn to the next step, the calibration of the instrument as a low-background nuclear recoil detector.

In Sec. 4.1, we describe the calibration of some of the hardware components, in Sec. 4.2 the basic scintillation and ionization calibrations, and in Sec. 4.3 we describe the corrections applied to the signals measured. Next, building upon the results of the previous sections, we look at the comparison of the expected electronic recoil background and the measured background in Sec. 4.4, the electronic and nuclear response of the detector in Sec. 4.5, and finally at the first dark matter results from a commissioning run in Sec. 4.6.

4.1 Hardware Components

Several hardware components of the detector need to be calibrated properly before they can be used. The most important, as they provide the signals from which we will reconstruct the energy of the interactions and their positions within the detector, are the PMTs.

Additional components that require a dedicated calibration and are almost required before one can measure proportional signals in a LXe TPC are the LXe level meters. Without knowing exactly the position of the liquid surface it is very time consuming to try and extract electrons from the liquid. To proceed without any information about the liquid level one can increase slowly the LXe mass in the detector and be on the lookout for the appearance of light signals with durations on the order of ~1 μs, typical of electroluminescence signals. This is commonly done with small scale detectors but impractical for large scale ones, also because the initial purity of the LXe might not allow for electrons to drift long distances before attaching to impurities.

4.1.1 Level Meters

We saw in Sec. 3.3.4 the geometry and the expected capacitance of the short level meters and the long level meter. Theses values however differ from the actual values and it is simpler to calibrate the level meter from two known configurations. Typically one measures the capacitance when the level is below the level meter and when it is above, and uses the known length of the meter to calculate its capacitance per unit length. The XENON100 long level meter having PEEK spacers at fixed positions gives intermediate calibrations, without the need to cover it with LXe. The XENON100 long LXe level meter was calibrated during a recovery operation since this provides a much more constant Xe mass flow (Sec. 3.3.6). Fig. 4.1 shows a plot of the capacitance of the long level meter as a function of time, along with the Xe mass flow to the bottles.

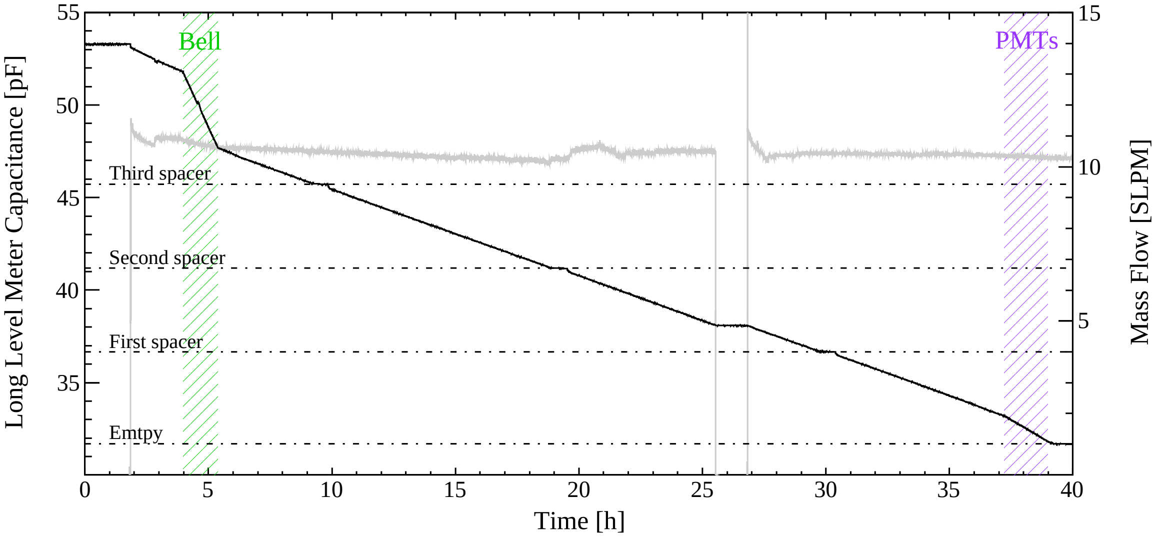

Figure 4.1: Long level meter calibration during a Xe recovery operation showing the capacitance of the long level meter (solid black line) and the Xe mass flow (gray line) as a function of time.

The initial period where the capacitance does not vary is before the start of the recuperation. As soon as the Xe recovery to the bottles starts the capacitance decreases. At the beginning the LXe level is above the bell. When the liquid level reaches the top the bell (green hatched region) the capacitance decreases much more rapidly. These abrupt slope changes are present because the LXe surface varies discontinuously as a function of height in the detector. In this case the bell is filled with GXe and only a small amount of LXe surrounds it (see Fig. 3.11). Below the bell the capacitance decreases with roughly the same slope as above the bell. The position of the first three spacers is marked on the plot. The capacitance per unit length obtained from the calibration is 0.045 pF/mm.

4.1.2 PMTs

As mentioned before, the PMTs are calibrated in the single photoelectron regime using a pulse LED. The LED is outside of the detector and the light is carried inside by optical fibers. The LED intensity is chosen such that in most events acquired ($> 95\%$) a PMT does not register a signal. This guarantees that the contamination in multiple photoelectron events is negligible. Fig. 4.2 shows a typical PMT calibration spectrum. The PMT gains were equalized to a mean value of 2×10^6 pe/e$^-$ and are measured weekly to monitor any deviations. The PMT calibration procedure is described in detail in Kish (2011).

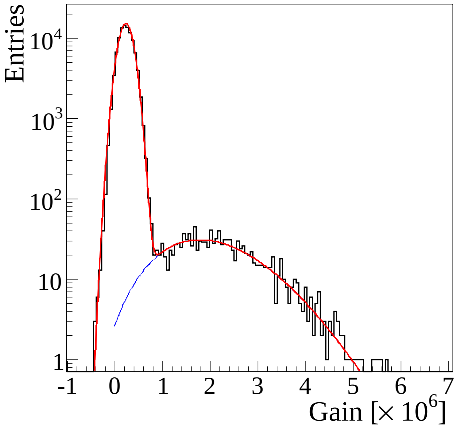

Figure 4.2: Typical PMT calibration spectrum. The PMT response shows a noise peak on the left, when no signal is present in the waveform, and the single photoelectron peak on the right. Figure from Aprile *et al.* (2011f).

4.2 Basic Calibration and Optimization

The two signals measured with the XENON100 detector are the S1 direct scintillation signal and the S2 proportional scintillation signal. The efficiency at which the scintillation light can be detected ultimately determines the energy threshold of the detector. As discussed earlier, both the light and the charge signals can also be attenuated due to the presence of impurities in the LXe. The basic calibrations performed early on and regularly throughout are thus on these two signal: the number of photoelectrons measured from the scintillation signal per unit energy, the S1 light yield, and the number of photoelectrons measured from the proportional signal per unit energy, the S2 light yield. By investigating the S2 light yield one can also obtain the number of photoelectrons measured per electron from the proportional signal.

4.2.1 S1 Light Yield

Several γ-ray sources have been used to calibrate the light yield response of the XENON100 detector, ^{137}Cs, ^{60}Co, ^{57}Co, and ^{232}Th. In addition, the response at several other γ-ray energies can be measured during and after a neutron calibration, from neutron inelastic interactions on Xe (Sec. 2.2.3). Fig. 4.3 shows the volume averaged S1 light yield at several γ-ray energies, after correcting the S1 signal for its spatial dependence (Sec. 4.3.2). The nonlinear response, and the increase in yield at lower energies, are due to the variation in the fraction of electron-ion pairs that recombine as a function of energy.

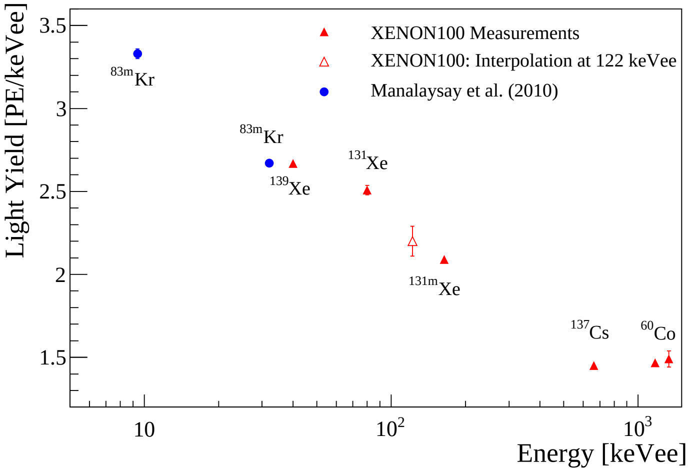

Figure 4.3: XENON100 volume averaged S1 light yield for different γ-ray energies at the operating drift field of 0.530 kV/cm. Figure from Aprile *et al.* (2011f).

4.2.2 Electron Lifetime

Calibrations with an external ^{137}Cs source are routinely taken to infer the electron lifetime, a measure of the concentrations of electronegative impurities in the LXe (Sec. 3.3.7). Since the electron lifetime is defined as the time after which $1/e$ drifting electrons will have been captured by impurities it can be inferred from a distribution of the S2 signal as a function of drift time. Fig. 4.4 shows such a distribution. The band appearing around S2 $\sim 200 \times 10^3$ pe corresponds to the full absorption peak of the 662 keV γ ray. The tail that extends to lower S2 values is due to events where the energy is not fully absorbed and the scattered γ escapes the detection. This contribution diminished drastically as the interaction occurs closer to the center of the TPC. To reduce this contribution to the minimum while retaining enough statistics, events with $r < 120\,\mathrm{mm}$ are selected. This calibration yields an electron lifetime of $\tau_e = 333 \pm 11\,\mu$s. The rate is higher is the center of the drift time distribution simply because the source calibration tube is positioned in the middle of the height of the TPC.

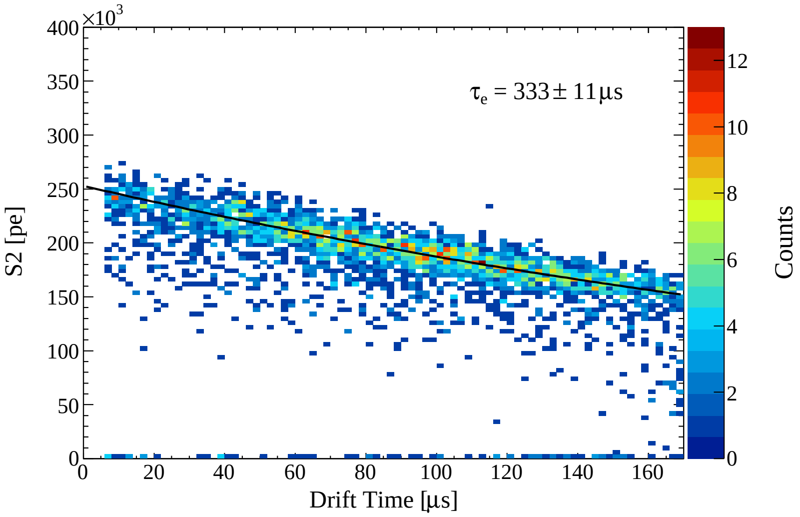

Figure 4.4: Distribution of S2 values of single scatter events as a function of drift time from a ^{137}Cs calibration. Only events with $r < 120\,\mathrm{mm}$ are selected to avoid events due to backscattered γ rays. The attenuation of the signal is interpreted as electron attachment to impurities. This calibration yields an electron lifetime of $\tau_e = 333 \pm 11\,\mu$s.

Fig. 4.5 shows the variation of the electron lifetime during a commissioning run (`run_07`) and during the WIMP search (`run_08`), as inferred from regular ^{137}Cs calibrations. The electron lifetime is increasing due to the continuous purification through the Xe recirculation system (Sec. 3.3.6). If the process through which impurities are dissolving into the LXe volume was a process that takes place at constant rate one would expect the electron lifetime to reach asymptotically the maximum value attainable, given by the impurity outgassing rate divided by the Xe recirculation speed. The time scale governing this increase would be a function of the outgassing rate, the recirculation speed, and the total Xe mass. However this is not the case, in fact the trend observed is consistent with a linear increase during the WIMP search period. This could be expected as it is well know that the outgassing rate decreases as a function of time in vacuum vessels.

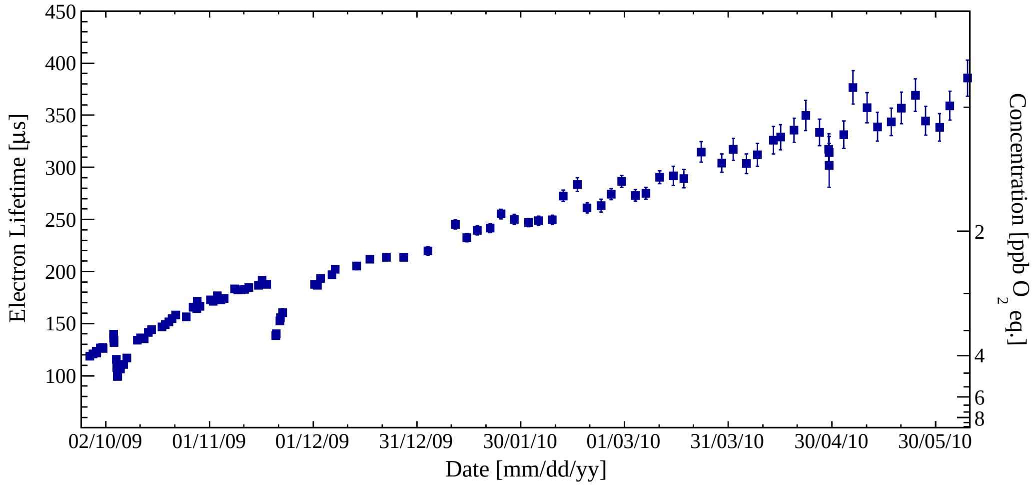

Figure 4.5: Variation of the electron lifetime during a commissioning run (`run_07`) and during the WIMP search (`run_08`). During the WIMP search the electron lifetime increased from 230 μs to 380 μs.

The two instances in which the electron lifetime is seen to decrease substantially in the commissioning run are due to maintenance operations where the Xe liquid level changed: the S2 signal optimization and the replacement of the recirculation pump. Two very interesting features are present in these occurrences. First, the decrease in the electron lifetime is sudden, and that even for very small changes of the liquid level on the order of few millimeters. Second, the trend at which the electron lifetime increases after this initial decrease is consistent with an exponential increase on a time scale compatible with that of the total Xe mass divided by the recirculation speed. This can be explained in the following manner. The rate at which impurities are dissolving in the LXe is a function of their outgassing rate, and this is seen to decreases with time. During those periods the electron lifetime seems to increases linearly, at intermediate values of τ_e at least, and the electron lifetime increase is driven by the decrease in the outgassing rate. The impurity dilution rate can be drastically increased however, if the LXe becomes in contact with previously untouched surfaces for example. This releases a large amount of impurities in the liquid. The limiting factor in the purification process is then the recirculation speed and the total Xe mass, not the impurity outgassing rate, and the electron lifetime increases at a much faster rate.

If no measures were taken, this variation of the electron lifetime would results in a time varying S2 detector response, clearly an undesired effect. To reduce the variance of the S2 signal from this effect, the S2 signal is corrected for its drift time (z) dependence (see Sec. 4.3.3).

4.2.3 S2 Optimization

Detector Levelling

As described in Sec. 2.4.6, the proportional amplification of the ionization signal through electroluminescence depends on several factors, the pressure in the amplification region, the electric field, and the path length of the electron. The resolution of the S2 signal can thus be optimized by varying some of the parameters.

The first parameter whose variance should be minimized is the electron path lengths. Variations in electron path lengths from the mesh geometry are unavoidable but those due to a tilt of the detector with respect to the liquid level inside the bell can be minimized by levelling the detector. That is, an inclination creates regions in the proportional amplification region with longer electron paths lengths where the liquid level is further from the anode and vice-versa. As mentioned in Sec. 3.2.2, the detector main cryostat can be raised or lowered on two of its three supports from outside the passive shield. Since the bell is rigidly connected to the cryostat top flange and since the detector inner structure is fixed to the bell, then one can align the detector such that the anode mesh becomes parallel to the LXe level. One very sensitive technique to measure the inclination is to measure the distribution of widths of S2 signals as a function of their position in the xy plane. The widths are directly proportional to the electron path lengths in the proportional amplification region.

Fig. 4.6 shows four steps during the detector levelling operations of a previous commissioning run[1] (`run_06`). The distributions are fitted with planes and the negative gradients are shown as arrows. The slope of the plane, α, is also indicated. At the first step (top left) the width distribution is wide and the slope in the northwest direction is obvious.

---

[1] The detector levelling adjustments needed at the beginning of commissioning `run_07` were too minute to exemplify the procedure.

After each step (not all shown), where the knobs that raise or lower the two the cryostat mount points are gently rotated, the situation gradually improves. This procedure requires carefulness and patience since one has to minimizes the creation of any waves on the liquid surface and wait for it to stabilize before proceeding further.

After the final step (bottom right), the slope in the mean S2 width response across the plane is 0.02 ns/mm. The variation in S2 widths is 35 ns (1-σ), which corresponds to variations in liquid level and anode distance of ~200 μm. The remaining variations are probably due to small deformations in the anode mesh ring.

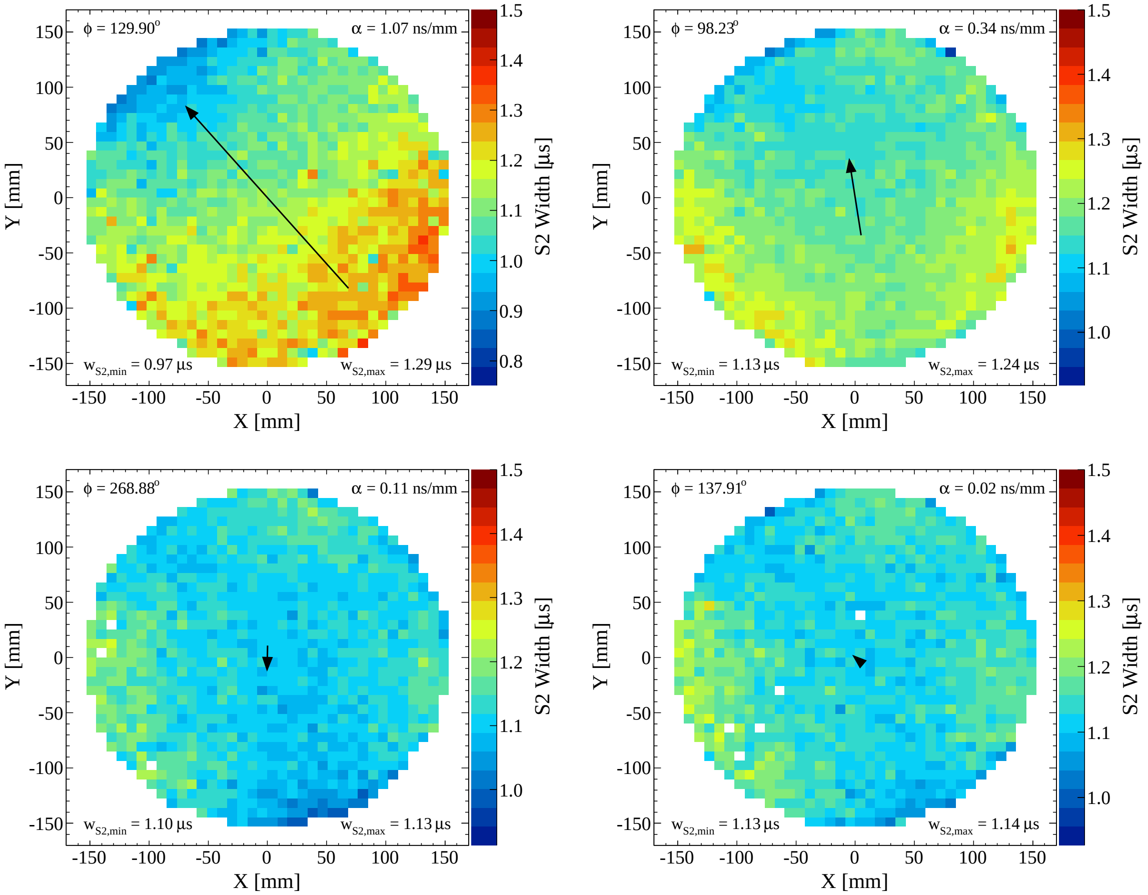

Figure 4.6: S2 width variations across the xy plane through steps of a detector levelling operation during a previous commissioning run (`run_06`, see footnote). The arrow indicates the negative gradient of the planar component of the response. From the first step (top left), through some intermediate steps (top right, bottom left), and the final step (bottom right) the tilt of the detector is gradually adjusted such that the anode mesh becomes parallel to the liquid level.

4.2.4 Single Electron S2 Signals

At very low energies, the proportional scintillation spectrum displays a sharp rise that peaks at about ~20 pe. Fig. 4.7 shows a zoom at low energies of a S2 spectrum from the irradiation with a neutron source. One can also notice a second feature near 40 pe. This is indicative of some form of quantized phenomenon being responsible for these very low energy S2 signals. The low energy spectrum is fitted using a sum of Gaussian functions multiplied by an efficiency curve with the constraint $\mu_n = n\mu_1$ and $\sigma_n = \sqrt{n}\sigma_1$. The assumption is that the low energy spectrum is a sum of 1-electron S2 peaks, 2-electron S2 peaks, etc, and that each electron produces an independent S2 peak distributed as $N(\mu_1, \sigma_1)$ and that the raw data processor has a rolling efficiency to detect such low energy S2 peaks. The mean S2 produced by a single electron obtained is 17.5 pe with a 6.4 pe standard deviation. Trying to perform the same fit without accounting for the detection efficiency gives fits that do not correctly describe the spectrum between the 1-electron and 2-electron peaks. The value obtained is not far from the estimate of the expected number of photoelectrons per electron accelerated in the proportional region of 12 pe calculated in Sec. 3.4.3.

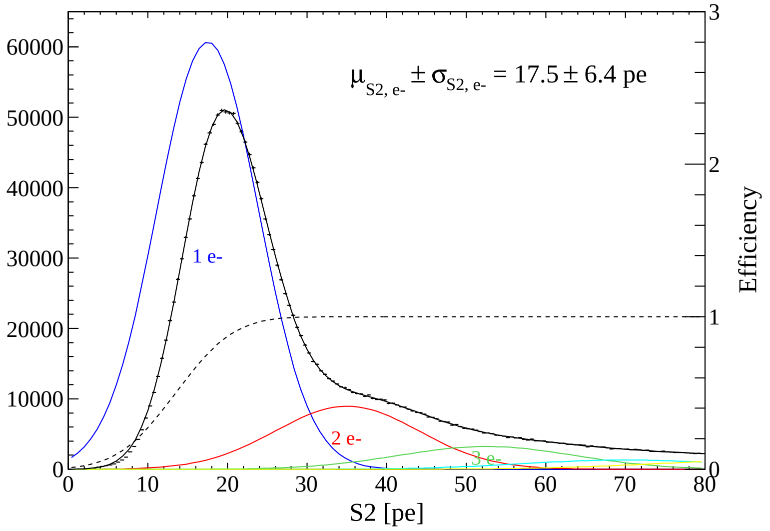

Figure 4.7: Ultra-low energy S2 spectrum, along with a fit to a sum of Gaussian functions with constrained means $\mu_n = n\mu_1$ and standard deviations $\sigma_n = \sqrt{n}\sigma_1$, where μ_1 and σ_1 are the mean and standard deviation of the S2 signal of a single electron, respectively.

In Fig. 4.8, the total S2 is separated into its top and bottom PMT array contributions. The previously inferred detection efficiency is taken into account by correcting the spectrum for it along the $S2_{top} + S2_{bottom}$ axis. The values obtained are 9.8 pe for the mean $S2_{top}$

signal and 7.3 pe for the mean S2$_{\text{bottom}}$. The mean top to bottom ratio is consistent with the value measured for higher energy S2 signals (∼1.3), a proof that these very low energy S2-like peaks are indeed true proportional light signals.

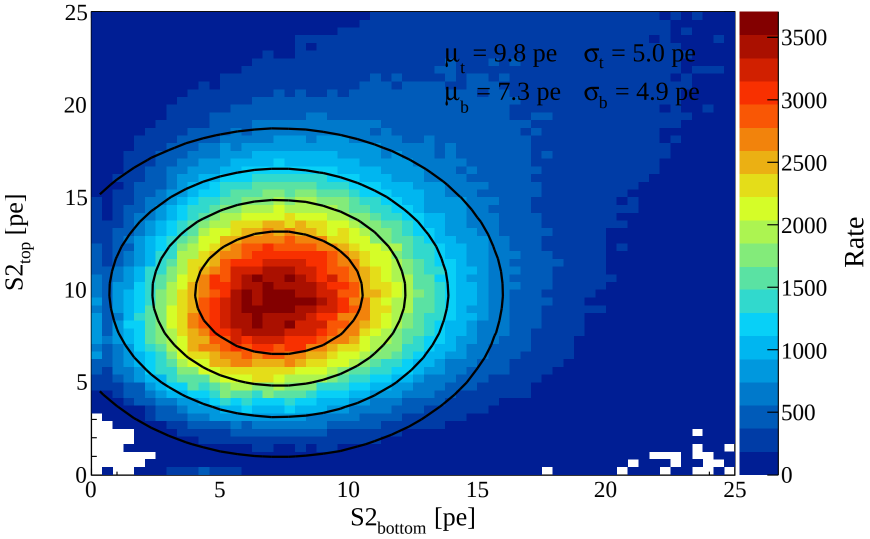

Figure 4.8: Separation of the single electron S2 signal into its top and bottom PMT array contributions.

4.3 Position Dependent Corrections

Events within the XENON100 TPC can be localized with a resolution on the order of millimeters. This results in a special ability to measure the response of the detector as a function of position within the TPC and to ultimately obtain a uniformized response by applying different corrections. The S1 light collection efficiency, for example, is expected to vary substantially within the volume since the solid angle subtended by both PMT arrays drastically changes as a function of position. By measuring the response function as a function of position one can then easily build a correction.

This section describes the four corrections applied to the signals measured. In Sec. 4.3.1 we describe the correction of measured positions into physical positions, in Sec. 4.3.2 the S1 (r, z) correction, in Sec. 4.3.3 the S2 (z) correction, and in Sec. 4.3.4 the S2 (x, y) correction.

4.3.1 Position Correction

As described earlier, the high optical transparency of the cathode mesh results in a distorted drift field near the outward bottom corner of the TPC and above the mesh. This situation does not result in any charge insensitive regions within the TPC but simply that electron trajectories from the lower part of the TPC bend towards the center of the TPC. Positions inferred from the S2 distribution on the top array, however, are the displaced positions. This implies that the reconstructed positions at longer drift times will tend to be shifted inwards. The effect is most pronounced immediately above the cathode mesh and near its outer ring.

The important element to realize is that such systematic shifts can be corrected for with the knowledge of the electric field configuration within the TPC. That is, one can construct a function that maps between true event positions and reconstructed event positions from the lateral displacement of the field line. The systematic shift is very close to being purely radial since only field lines with much longer drift times could create a substantial shift along the z coordinate. Regions of higher or lower electric field alone cannot vary substantially the shift in the z coordinate due to the mild dependence of the electron drift velocity with electric field at the operating field of 0.530 kV/cm. As the map between true event positions and reconstructed event positions is invertible, the physical event positions can be calculated from the reconstructed positions.

The position correction was determined from a numerical finite element analysis simulation of the electric field within the TPC (Mei, 2011). The map of the position shifts is shown in Fig. 4.9 at different points within the TPC. The dots represent physical interaction points whereas the lines indicate the position of the reconstructed position. The correction uses the inverse of this map to transform reconstructed event positions into physical positions.

The accuracy of the position correction was verified with different independent measurements: the drift time distribution of events near the bottom of the TPC, the radial position of the outermost detected events and the event density of uniformly distributed γ rays following the decays of the metastable states ^{129m}Xe and ^{131m}Xe.

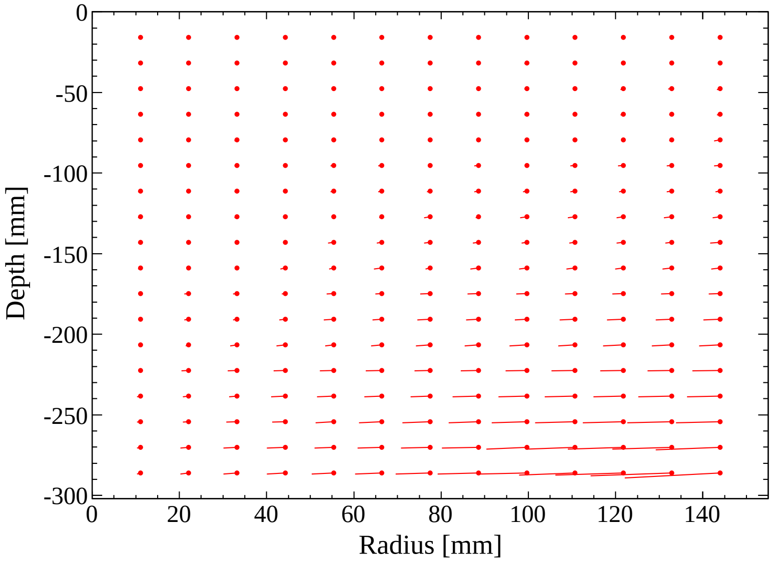

Figure 4.9: Graphical representation of the position correction at different points within the TPC. The correction uses the inverse of this map to transform reconstructed event positions into physical positions.

4.3.2 S1 (r, z) Correction

A correction for the spatial dependence of the S1 light collection within the TPC is also applied to reduce the variance in the direct scintillation signal. In principle a light propagation simulation accounting for the absorption length and Rayleigh scattering of scintillation photons in LXe, PTFE and copper reflectivities, optical transparencies of meshes, etc, could yield the variation of the relative light collection efficiency in the volume. However, since the correction map can also be measured from data it is probably more straightforward to proceed in this way. Since the TPC is to a great degree cylindrically symmetric, the correction is computed within that approximation.

The S1 (r, z) correction can be obtained from multiple monoenergetic calibration sources since the light collection does not depend on the amount of scintillation light produced. However, since the quantity of interest is the relative light yield as a function of position, the accuracy of the map does depend on the resolution of the position reconstruction. The correction is obtained from three separate measurements, an irradiation of the detector with an external ^{137}Cs at various azimuthal positions, 40 keV γ rays produced via the inelastic reaction $^{129}\text{Xe}\,(n, n'\gamma)^{129}\,\text{Xe}$ during the neutron calibration, and finally with the 164 keV and 236 keV γ rays produced during decays of metastable ^{131m}Xe and ^{129m}Xe, respectively, produced during the neutron calibration. The corrections inferred from these independent calibrations differ by less than 3% and improve the energy resolution (σ/E) at 662 keV from 24% to 13% using the scintillation signal alone. The relative light yield, with respect to the volume averaged light yield, as a function of radius and depth in the TPC, is shown in Fig. 4.10.

The S1 signal from an event at position (r, z) is corrected by dividing it by the relative light yield at that position. However, since multiple scatter events have a S1 signal which is effectively the sum of multiple separate light signals at different positions, the corrected signal for those events is not optimal. The correction applied will be the one for the position with the largest S2 signal. A more appropriate correction for multiple scatter events could be a S2-weighted position correction but this would also introduce uncertainties from the S2 corrections (Sec. 4.3.3 and Sec. 4.3.4). This topic has not been investigated further given the reduced importance of accurate spectroscopy of multiple scatter events in the context of direct dark matter detection.

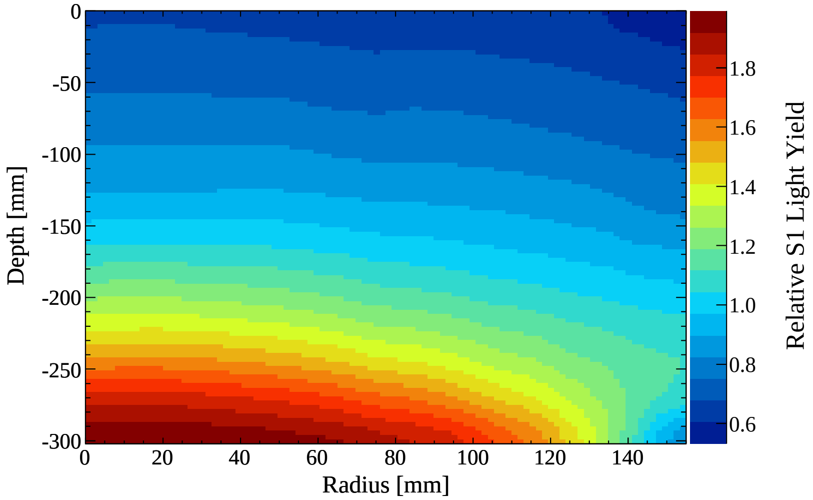

Figure 4.10: The relative light yield, with respect to the volume averaged light yield, of the XENON100 detector as a function of radius and depth within the TPC. The relative light yield is clearly higher for events near the bottom of the TPC above the bottom PMT array. The S1 signal from an event at position (r, z) is corrected by dividing it by the relative light at that position.

Since a degradation of the position reconstruction performance is expected for large S2 signals due to the non-linear response of PMTs (Sec. 3.3.2), the ^{137}Cs calibration used to infer the S1 (r, z) correction is performed at a lower proportional amplification. This is achieved by lowering the anode voltage to ~2.2 kV. Under those conditions the position reconstruction bias from a non-linear PMT response is negligible. This reduced anode voltage has no adverse effects on the accuracy of the map obtained. The correction used for the results presented in Sec. 4.6 is the one inferred from the ^{137}Cs low-anode calibration.

The advantage of the γ rays from the ^{129m}Xe and ^{131m}Xe metastable states is that they constitute a source which is truly homogeneously distributed within the volume. The disadvantage, however, is that the intensity of the 164 keV and 236 keV γ-ray lines is not dominant compared to the γ background from detector materials in all regions of the TPC, notably at the edge. For this reason, a more appropriate γ source is the 40 keV γ rays produced by inelastic neutron scatterings on ^{129}Xe. The longer mean free path of MeV neutrons compared to that of γ rays in LXe results in a higher event rate at the center of the TPC. The correction inferred from the 40 keV γ rays during the AmBe neutron calibration is the one used for the results presented in Chap. 6.

4.3.3 S2 (z) Correction

Calibrations with ^{137}Cs were taken bi-weekly during the WIMP search to infer the electron lifetime (see Sec. 4.2.2) and to subsequently correct the S2 signal for its drift time dependence. As electrons drifting have a probability of being captured by electron negative impurities, a measured S2 signal is corrected by an exponential weighting factor of e^{t_d/τ_e}, where t_d is the drift time of the event and τ_e is the electron lifetime. During the WIMP search (`run_08`) the electron lifetime increased from 230 μs to 380 μs (Fig. 4.2.2). A linear fit to the electron lifetime evolution yields the z correction for the S2 signals with a negligible systematic uncertainty ($< 2.5\%$).

For the results presented in Sec. 4.6, calibrations with ^{137}Cs were taken daily. The electron lifetime in that period increased from 154 μs to 192 μs, resulting in the average S2 z-correction decreasing from 75% to 60%.

4.3.4 S2 (x, y) Correction

The S2 signal is also corrected for its (x, y) variation, mostly due to light collection effects near the edge of the TPC. This dependence is determined using the 40 keV γ rays from the neutron calibration data and computing the proportional scintillation light yield in (x, y) cells. Only insignificant differences ($< 2\%$) were observed between corrections obtained using other calibration datasets of various γ-ray energies (164 keV, 662 keV). The S2 signals from the top and bottom PMT arrays are corrected independently with two different correction functions. The measured S2 signals of the top and bottom array from an event at position (x, y) are corrected by dividing them by the corresponding relative response at that position. S2 signals from multiple interactions each have possibly different (x, y) positions and are thus corrected independently. The energy resolution (σ/E) at 662 keV using the S2 signal alone is improved from 7.3% to 6.5% after applying the S2 spatial corrections (including the S2 (z) correction).

Fig. 4.11 shows the relative response of the proportional scintillation signal as a function of position in the xy plane for both the top and bottom PMT arrays. Since the S2 signal is produced very close to the top array PMTs, positions close to non-functional top array PMTs suffer a greater reduction in response. In contrast, the S2 is distributed much more uniformly on the bottom array PMTs, resulting in a much more smoothly varying response function. This smaller uncertainty in the correction function led to the choice of using only the bottom PMT array S2 signal for the dark matter analysis presented in Chap. 6.

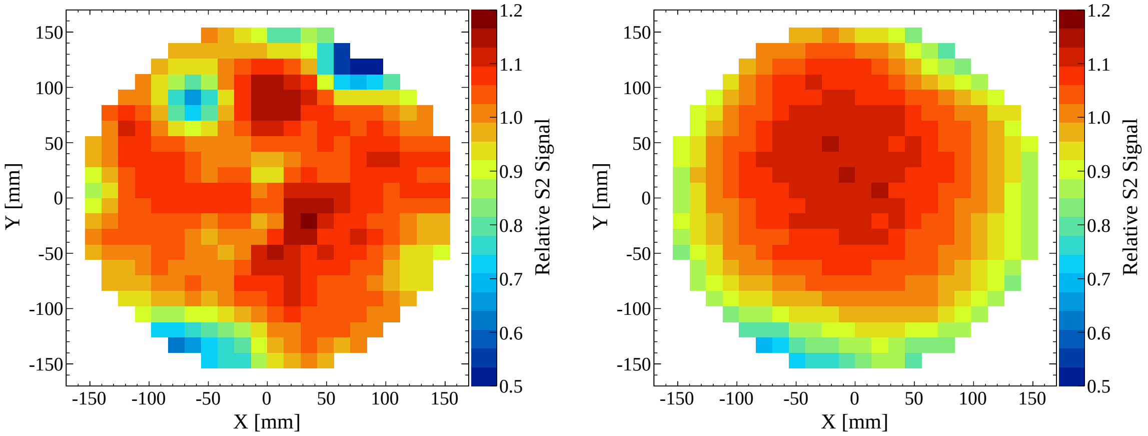

Figure 4.11: Relative proportional scintillation response as a function of (x, y) for the top (left) and bottom (right) PMT arrays. The S2 signals from the top and bottom PMT arrays are corrected independently using their respective correction functions. The measured S2 signal of the top or bottom array from an event at position (x, y) is corrected by dividing it by the relative response at that position.

The (x, y) variation of the S2 signal could also possibly be due to charge losses near the PTFE panels. The hypothesis of an additional mechanism for the reduction of the S2 signal near the PTFE panels beyond the light collection effect rests in the observation that even after the correction of the S2, the variance of the S2 signal near the edge is still larger than that in the center of the TPC.

4.4 Electronic Recoil Background

Once the basic calibration of the detector has been performed and the variance-reducing corrections to be applied have been calculated, a reliable comparison of the electronic recoil background from detector materials with simulation can be performed. Detailed GEANT4 simulations similar in nature to those described in Sec. 3.1 were performed to estimate the electronic recoil background of the XENON100 detector, taking into account the detailed geometry of the concrete realization of the detector. The inputs to the simulation are the radioactive screening measurements listed in Aprile *et al.* (2011d). The results obtained are presented in Aprile *et al.* (2011e). The analysis of the results is described in more details in Kish (2011). Fig. 4.12 shows the comparison of the measured single scatter electronic recoil background in a 30 kg fiducial volume with the prediction from simulation. The veto coincidence cut is not applied here to increase the available statistics. No scaling is applied except for three sub-dominant contributions from intrinsic radioactive impurities in the LXe, ^{85}Kr, ^{222}Rn, and ^{136}Xe[2]. The agreement between the prediction and the measurement below 1.5 MeV is very good. The agreement is actually expected to worsen at higher energies since most of the analysis data selection cuts (Sec. 4.6.1) are tailored to have a high acceptance at much lower energies ($\lesssim 100\,\mathrm{keV}$). The parameters of the raw data processor `S1` and `S2` peak finding routines are also optimized for high efficiency at low energies.

The predicted rate of single scatter electronic recoil events in the energy region below 100 keV, without veto coincidence cut, is $15.8 \times 10^{-3}\,\mathrm{events\,keV^{-1}\,kg^{-1}\,d^{-1}}$ for the 40 kg fiducial volume used in the results presented in Sec. 4.6. With the application of the veto coincidence cut with an energy threshold of 100 keV, the rate reduces by almost a factor of three to $6.1 \times 10^{-3}\,\mathrm{events\,keV^{-1}\,kg^{-1}\,d^{-1}}$. The background reduction factor of the veto coincidence cut, as also observed in the electronic recoil background simulations of Sec. 3.1, is only mildly sensitive to the veto volume energy threshold if the threshold is below ~200 keV (Aprile *et al.*, 2011e). The energy threshold in the veto volume depends on the positions of interactions since the light collection efficiency varies substantially, especially

---

[2] The scaling for the ^{136}Xe two-neutrino double-β decay contribution is misquoted in Aprile *et al.* (2011e) and corresponds to that of ^{136}Xe with a half-life of 1.1×10^{22} y. In the meantime the half-life of ^{136}Xe has been measured to be $2.11 \pm 0.04 \pm 0.021 \times 10^{21}$ y (Ackerman *et al.*, 2011). The contribution is thus indeed sub-dominant.

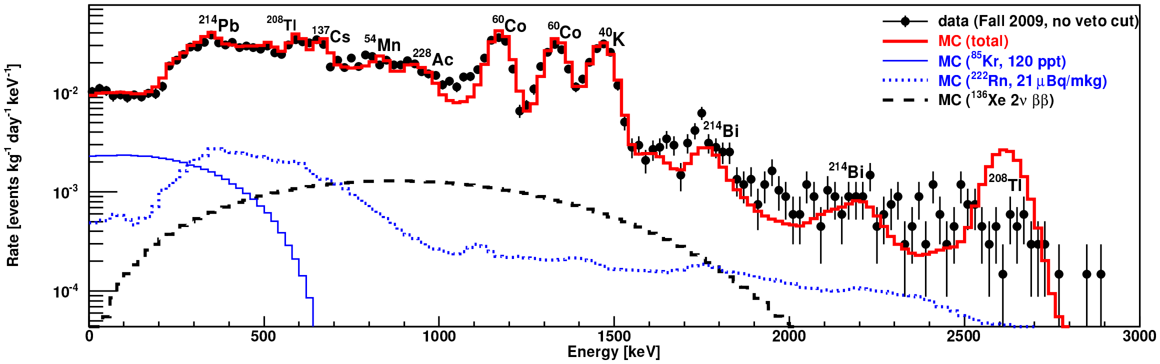

Figure 4.12: Measured electronic recoil background (points) from single scatter events in a 30 kg fiducial volume during the commissioning run (`run_07`) and the predicted rate from simulation (solid red line). The agreement is very good considering that no scaling is applied except for three sub-dominant contributions, ^{85}Kr, ^{222}Rn, and ^{136}Xe. See footnote concerning the ^{136}Xe contribution. Figure from Aprile *et al.* (2011e).

in the side part of the veto, as interactions get closer to the veto PMT rings. The detection thresholds (90%) have been measured with a collimated ^{137}Cs source and are lower than ~230 keV throughout the veto volume (Kish, 2011).

4.5 Electronic and Nuclear Recoil Band Calibration

Background rejection in XENON100 is achieved mainly through the use of fiducialization and subsequently via the identification of the type of recoil based on the ratio of ionization and scintillation, S2/S1. An accurate knowledge of the response of the detector to both types of recoils is essential to define a signal region where WIMP-induced nuclear recoils can be measured and to compute the fraction of electronic recoils that should appear as signal events. The response to nuclear recoils is also needed to estimate the acceptance of the different data selection criteria used.

As discussed earlier, the main background from detector materials that can mimic nuclear recoils is from single Compton scatters in the fiducial volume which have uncharacteristically low S1/S2 values. Multiple Compton scatter interactions can easily be rejected via their multiple S2 signals signature and thus do not constitute a background for a WIMP search with dual-phase LXe TPCs.

Statistics for the low energy electronic recoil calibration are accumulated at regular intervals with a 1 kBq ^{60}Co source. Clearly, high energy (> 1 MeV, see Fig. 2.2) γ rays have a much higher probability of interacting only once through a Compton scatter and exiting the target volume than lower energy γ rays. This results in a more efficient calibration, as more events are of the desired topology, and is the main motivation for using ^{60}Co over ^{137}Cs for example. The simple use of a higher activity source to perform faster calibrations is not possible due to the inherent TPC dead time associated with the drift of electrons from the interaction point to the liquid surface, a point mentioned earlier in Sec. 3.3.10. The important element here is that the low energy electronic recoil calibration serves to define the probability distribution of the S2/S1 discrimination parameter for electronic recoils and hence any contamination of the distribution from accidental coincidences, even at the sub-% level, will result in a prediction of background events leaking into the WIMP-induce nuclear recoil signal region.

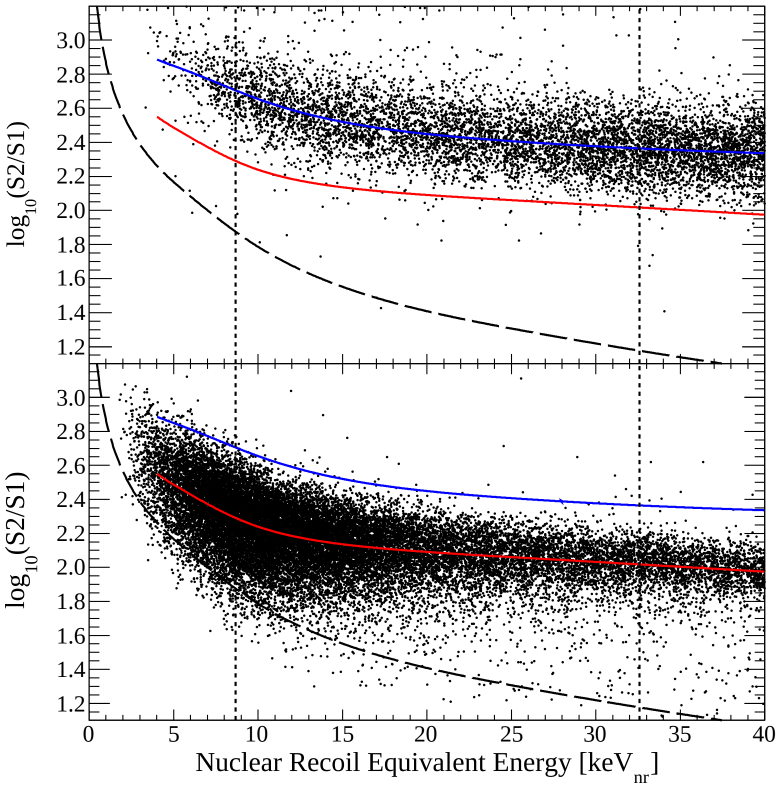

Figure 4.13: Electronic (top) and nuclear (bottom) recoil bands from ^{60}Co and ^{241}AmBe calibration data, respectively, after data selection and the 40 kg fiducial volume cut. Colored lines correspond to the median $\log_{10}$(S2/S1) values of the electronic (blue) and nuclear (red) recoil bands. The energy range of the WIMP analysis of Sec. 4.6 (vertical dashed line) and the 300 pe (uncorrected, see footnote) S2 software threshold (long dashed) are shown. Figure from Aprile *et al.* (2010).

Fig. 4.13 (top) shows the $\log_{10}(\mathsf{S2}/\mathsf{S1})$ distribution of single scatter electronic and nuclear recoils in the 40 kg fiducial volume used for the dark matter search analysis presented in Sec. 4.6, as function of nuclear recoil energy. The S1 and S2 signals are corrected according to the corrections described in Sec. 4.3. The solid blue line indicates the energy dependence of the median of the distribution. The vertical dashed lines are the energy range chosen for the dark matter analysis. The long dashed line corresponds to a S2 software threshold[3] of 300 pe, representative of the estimated $> 99\%$ efficiency curve of the S2 trigger threshold. The solid red line corresponds to the median of the response of the XENON100 detector to low energy nuclear recoils (read below). The nuclear recoil equivalent energy scale used is the one described in Sec. 4.6.2.

In each energy slice, the electronic recoil band is empirically found to be consistent with a Gaussian distribution in $\log_{10}(\mathsf{S2}/\mathsf{S1})$, at the ~99.5% level. It is important to make a distinction between two types of non-Gaussian events. The first type, *type I* non-Gaussian events, shall label events whose actual microscopic ratio of ionization and scintillation follows the empirical Gaussian distribution but who appear non-Gaussian due to detector response effects. The second type, *type II* non-Gaussian events, shall label events whose actual ratio of ionization and scintillation is non-Gaussian in nature, from non-Gaussian tails in recombination for example. The largest source of *type I* non-Gaussian events are events where a second scatter occurs in a charge insensitive region of the target volume, mostly below the cathode. So far we have no proof that type II non-Gaussian events are present. The different types of leakage events and estimates of their rates are discussed in Sec. 6.1.3.

The response of XENON100 to single elastic nuclear recoils is obtained by irradiating the detector with a 220 n/s ^{241}AmBe source. A subset of the entire 72 h irradiation is shown in Fig. 4.13 (bottom), for the 40 kg fiducial volume. The solid red line corresponds to the median of the nuclear recoil band. As mentioned earlier, this calibration is essential to define the signal region for WIMP-induced nuclear recoils, the assumption being that for a given nuclear recoil energy they are indistinguishable from neutron-induced nuclear recoils. Consequently, this calibration dataset is also used to estimate the acceptance of data cuts on WIMP-induced nuclear recoils.

The higher event density at lower energies is expected from the elastic interactions of

---

[3] Strictly speaking this software threshold applies to uncorrected S2 values, consequently in the corrected S2 space plotted here the threshold is not a line.

neutrons with Xe nuclei (Sec. 2.2.3). The separation in $\log_{10}(\mathtt{S2}/\mathtt{S1})$ between the electronic recoil band and the nuclear recoil band results in a discriminating power between both types of recoils. The distribution in $\log_{10}(\mathtt{S2}/\mathtt{S1})$ for nuclear recoils of a fixed energy has a much larger non-Gaussian tail at low $\log_{10}(\mathtt{S2}/\mathtt{S1})$ values. Its source is not entirely clear but a large fraction is likely to be attributable to the same mechanism as the one described for electronic recoils earlier, that is, events where a second interaction occurs in a charge insensitive region of the target volume. The larger mean free path of ~MeV neutrons compared to that of ^{60}Co γ rays could explain the higher rate in this low $\log_{10}(\mathtt{S2}/\mathtt{S1})$ tail.

4.6 First Dark Matter Results

A first dark matter analysis with 11.2 live days of XENON100 background data acquired between October 20th and November 12th 2009, during the `run_07` commissioning run, was carried out to test the potential of the recently calibrated instrument. The background data was taken prior to the neutron calibration and its aim was originally to confirm the Monte Carlo prediction for the single scatter electronic recoil rate at low energies. Although the data acquired was not formally taken in a blind mode where events from a predefined signal region are unaccessible, the data selection cuts were derived from the ^{60}Co and ^{241}AmBe calibration data. The cuts were being developed for the eventual analysis of the first science run (`run_08`), which was under way at the time.

The energy window for the dark matter search analysis was chosen between $8.7 - 32.6\,\mathrm{keV_{nr}}$. The energy scale used to convert the scintillation signal in photoelectrons into nuclear recoil equivalent energies was defined on the basis of new measurements of $\mathcal{L}_{\mathrm{eff}}$ available at the time. The procedure used to build the energy scale is described in Sec. 4.6.2. The lower bound of the energy range was chosen at 4 pe since the acceptance of the `S1` two-fold coincidence requirement at that value was estimated to be larger than 90%. The upper bound was chosen to correspond approximately to the one used for the XENON10 blind analysis (Angle *et al.*, 2008a), after its conversion into the newly defined energy scale[4]. The $\log_{10}(\mathtt{S2}/\mathtt{S1})$ upper bound of the WIMP signal region was chosen as the median of the nuclear recoil band while the lower bound was chosen at a fixed 300 pe `S2` value. The choice of the median as the upper discrimination bound results in an energy-independent nuclear

---

[4] The XENON10 limit was derived using a constant $\mathcal{L}_{\mathrm{eff}} = 0.19$

recoil acceptance of 50%, not accounting for the acceptance of data quality selection cuts.

4.6.1 Data Selection Cuts

The data selection cuts used for the analysis can be classified into four categories: basic quality cuts, multiple scatter cuts, fiducial volume cuts, and finally signal consistency cuts. They are motivated by the physical properties of xenon scintillation light, the characteristics of proportional light signals, and the expected WIMP-induced single-scatter nuclear-recoil signature.

Basic quality cuts put minimal requirements on S1 and S2 signals, reject events with a high electronic noise level, or extraneous PMT signals outside identified S1 and S2 peaks, for example. These cuts typically have high acceptance as they are meant to remove non-events or events rendered useless due to infrequent spurious signals. For this analysis four basic quality cuts were used, a S1 coincidence cut, a S2 threshold cut, a signal to noise cut, and cuts for specific event types not related to energy deposits within the fiducial volume. The S1 coincidence cut requires a twofold PMT coincidence of the S1 signal. For a PMT signal to be considered in the coincidence computation it must exceed 0.35 pe and must appear 20 ns or less away from the S1 peak found in the summed waveform. This allows true low energy events to be distinguished from events with random single photoelectrons from PMTs or accidental coincidences. For the S2 signal the lower threshold set was 300 pe, which corresponds to about 15 ionization electrons (see Sec. 4.2.4). The signal to noise cut requires events outside of the detected S1 and S2 signals to contribute less than a certain fraction of the total area of the waveform. This typically rejects events with excessive noise of with very large energy depositions.

The multiple scatter cuts applied required the presence of a single S1-like peak in the waveform, a single S2 peak above the 300 pe threshold, and no energy deposit in the veto in coincidence with the S1 signal in the TPC. The S1 multiple scatter cut rejects events with delayed decays or accidental coincidences within the event digitization window where two S1 signals can appear. The S2 multiple scatter cut rejects events with multiple energy deposits at different z positions.

The fiducial volume chosen for the analysis was a cylinder with a radius of 13.5 cm and a height of 24.3 cm. This choice was motivated by the consistency of the reconstructed (x, y) event positions from the three algorithms used up to a radius of $r < 14\,\text{cm}$.

Finally, the only signal consistency cut used for this analysis was a S2 width consistency cut. Ionization electrons diffuse as they are drifted to the liquid surface in the detector and thus produce a proportional signal with a larger width that that observed at shorter drift times. The cut requires the width of the S2 signal to be consistent with the reconstructed event depth.

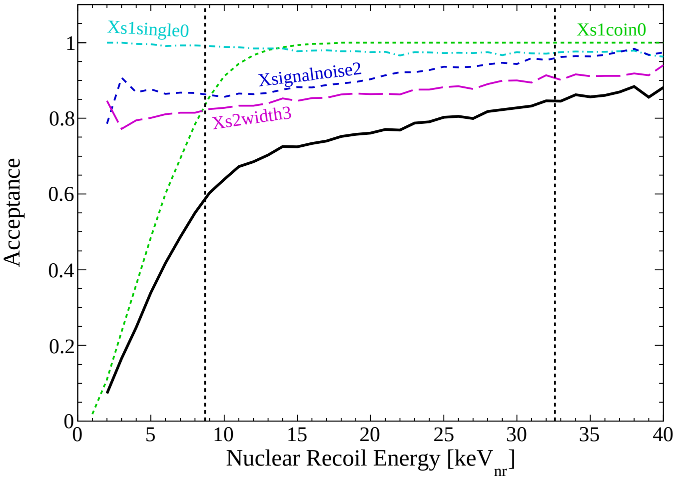

Figure 4.14: Cumulative and individual software cut acceptances for single scatter nuclear recoil events estimated from the ^{241}AmBe neutron calibration, as described in the text.

The cumulative software cut acceptance for single scatter nuclear recoils was estimated using the elastic recoil events from the ^{241}AmBe calibration. The procedure used assumes that single scatter nuclear recoil events within the fiducial volume which pass all cuts but one are valid events. It estimates the acceptance for a given cut as the ratio of single scatter nuclear recoil events within the fiducial volume which pass the cut under study to those which pass all other cuts. This is a conservative estimate since a larger number of events who fail only one cut are actually events which should be rejected than events failing multiple cuts are events which should not have been rejected. Fig. 4.14 shows the estimated cumulative and individual cut acceptances. The estimated cumulative cut acceptance varies between 60% (at 8.7 keV$_{\mathrm{nr}}$) and 85% (at 32.6 keV$_{\mathrm{nr}}$).

4.6.2 Nuclear-Recoil Equivalent Energy

The nuclear recoil equivalent energy scale (Sec. 2.5.3) used for this WIMP analysis was based on a fit to all direct measurements of the relative scintillation efficiency of nuclear recoils in LXe, $\mathcal{L}_{\mathrm{eff}}$, available at the time (see Fig. 4.15). The two different techniques, direct and indirect, used to measure $\mathcal{L}_{\rm eff}$ were described in Sec. 2.3.3. As mentioned in that section, direct measurements are typically less likely to suffer from large systematic uncertainties than those inferred from a comparison of broad energy neutron source calibration spectra with Monte Carlo simulations.

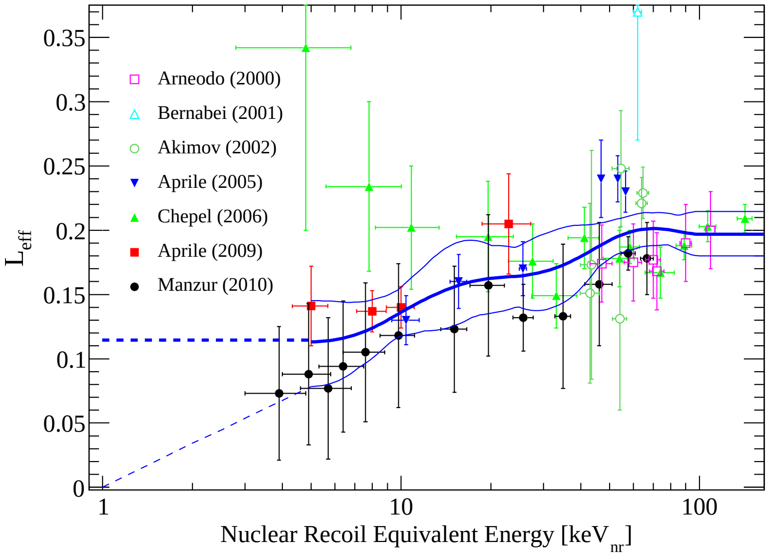

Figure 4.15: Parametrization of the energy dependence of $\mathcal{L}_{\rm eff}$ used for the analysis of the XENON100 `run_07` commissioning run background data (thick solid blue line) with its extrapolation below 5 keV$_{\rm nr}$ (thick dashed blue line), along with direct measurements of $\mathcal{L}_{\rm eff}$ available prior to 2011 from different groups (Akimov *et al.*, 2002; Aprile *et al.*, 2005, 2009; Arneodo *et al.*, 2000; Bernabei *et al.*, 2001; Chepel *et al.*, 2006; Manzur *et al.*, 2010). Also shown, the 90% confidence contour (thin solid blue lines) of the fit along with a logarithmic extrapolation to zero scintillation at 1 keV$_{\rm nr}$ (thin dashed blue line). Figure from Aprile *et al.* (2010).

The light yield L_y at 122 keV$_{\rm ee}$ at 530 V/cm was calculated from a fit to all γ-ray lines mentioned in Sec. 4.2.1. This procedure was employed since 122 keV$_{\rm ee}$ γ rays cannot penetrate far in the sensitive volume due to their short attenuation length of 3 mm in LXe. The light yield obtained was $L_y(122\,\mathrm{keV_{ee}}) = (2.20 \pm 0.09)\,\mathrm{pe/keV_{ee}}$.

The energy dependence of $\mathcal{L}_{\rm eff}$ and its uncertainty were determined through a cubic-spline fit to the direct $\mathcal{L}_{\rm eff}$ measurements of Fig. 4.15. The procedure employed to calculate the energy dependence is described in Manalaysay (2010). The energy range for the fit was limited to a region where at least two measurements existed, specifically, from $5-100$ keV$_{\rm nr}$. The spline knots were fixed at 5, 10, 25, 50 and 100 keV$_{\rm nr}$. This leaves a region below 5 keV$_{\rm nr}$ where only a single measurement exists, that of Manzur *et al.* (2010) at 4 keV$_{\rm nr}$.

The decision was taken then to use a constant extrapolation for the energy dependence of $\mathcal{L}_{\text{eff}}$ below $5\,\text{keV}_{\text{nr}}$, a trend that seemed supported by both the direct measurement of Aprile *et al.* (2009) and the indirect measurement of Sorensen *et al.* (2009). Fig. 4.15 shows the resulting parametrization (thick solid blue line) along with its extrapolation (thick dashed blue line). The 90% confidence contour of the fit is also shown (thin solid blue lines) along with a logarithmic extrapolation to zero scintillation at $1\,\text{keV}_{\text{nr}}$ (thin dashed blue line). The logarithmic slope was chosen as the slope between the two lowest energy measurements of Manzur *et al.* (2010).

4.6.3 Results

The measured event distribution in $\log_{10}(\mathtt{S2}/\mathtt{S1})$ versus nuclear recoil energy space for the 11.2 live days of XENON100 background data taken during the `run_07` commissioning run is shown in Fig. 4.16. Twenty-two events were observed within the $8.7 - 32.6\,\text{keV}_{\text{nr}}$ energy window. No events were observed in the pre-defined signal acceptance region. This was consistent with the prediction of the number of events that should leak into the signal region. At 50% nuclear recoil acceptance, assuming a $\log_{10}(\mathtt{S2}/\mathtt{S1})$ electronic recoil discrimination better than 99%, a total of 0.2 events would be expected to leak. The approximately uniform rate in energy observed was consistent with the expectation from Monte Carlo for the electronic recoil background energy distribution.

The spatial distribution of events passing all cuts (not considering the fiducial volume cut) is shown in Fig. 4.17 as black dots. Red circles correspond to events below the nuclear recoil median. The event rate near the edge of the sensitive volume is much higher than in the fiducial volume, showing the power of LXe self-shielding and fiducial volume cuts as a background reduction technique. The much lower electronic recoil background obtained with the XENON100 detector is clear when comparing Fig. 4.17 with the spatial distribution of events from the XENON10 results (Angle *et al.*, 2008a), which corresponds to a similar exposure. Events below the nuclear recoil median are more frequent near the edge of the sensitive volume probably due to incomplete charge collection, between wires of the cathode mesh or near the field shaping ring grooves on the PTFE side panels of the TPC for example. Again, this demonstrates the usefulness of the precise three-dimensional localization of events and fiducial cuts to reject artificially produced WIMP-like events.

With no events observed in the energy range chosen, an upper limit on the spin-

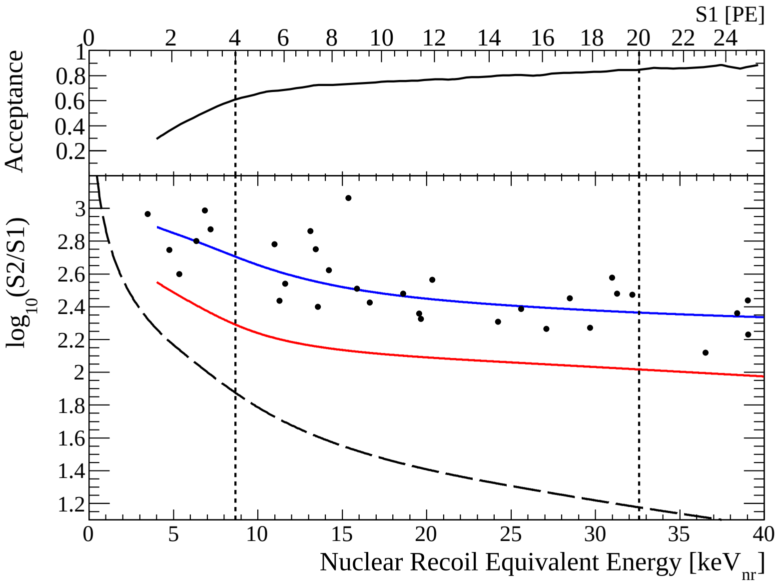

Figure 4.16: $\log_{10}(\mathsf{S2}/\mathsf{S1})$ as a function of nuclear recoil energy for events passing all cuts observed during the 11.2 live days of XENON100 background data of the `run_07` commissioning run. Colored lines correspond to the median $\log_{10}(\mathsf{S2}/\mathsf{S1})$ values of the electronic (blue) and nuclear (red) recoil bands. The energy range of the WIMP analysis (vertical dashed line) and the 300 pe $\mathsf{S2}$ software threshold (long dashed) are shown. Figure from Aprile *et al.* (2010).

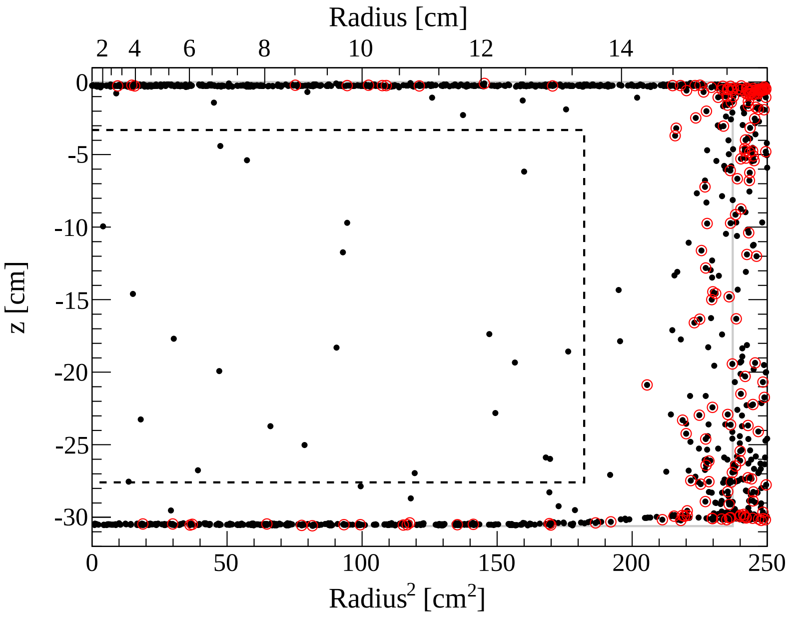

Figure 4.17: Spatial distribution of all events (black dots) and events below the nuclear recoil band (red circles) passing all data selection cuts (not considering the fiducial volume cut) and observed during the 11.2 live days of XENON100 background data of the `run_07` commissioning run inside the TPC (gray line). The 40 kg fiducial volume chosen for the analysis is represented by the dashed line. Figure from Aprile *et al.* (2010).

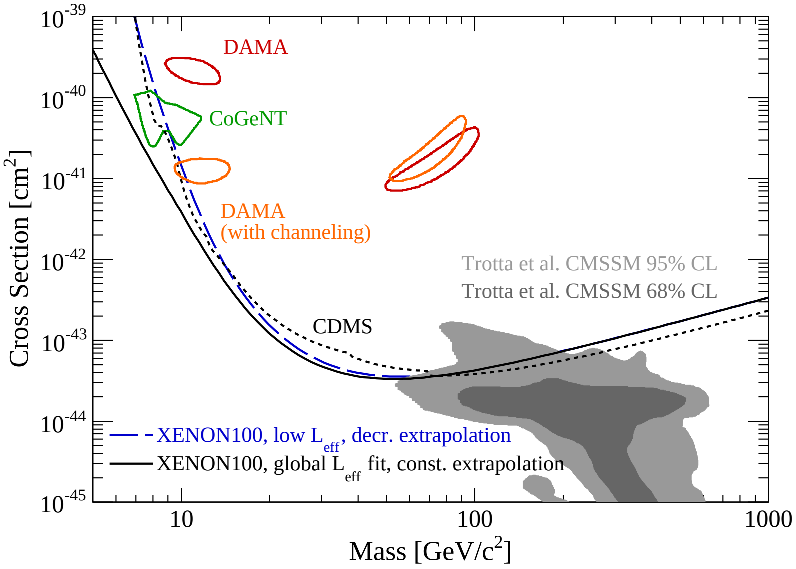

Figure 4.18: 90% confidence upper limit on the spin-independent elastic scattering WIMP-nucleon cross section (solid and long dashed lines), together with the best limit at the time from the CDMS II experiment (dotted) (Ahmed *et al.*, 2010), re-calculated assuming an escape velocity of 544 km/s and $v_0 = 220$ km/s. Also shown, the favored parameter space from a theoretical model (Trotta *et al.*, 2008) and the 90% confidence contours compatible with the signals from CoGeNT (green) (Aalseth *et al.*, 2011a) and DAMA (red/orange) (Savage *et al.*, 2009). Figure from Aprile *et al.* (2010).

independent WIMP-nucleon elastic scattering cross section was derived. WIMPs were assumed to be in an isothermal halo with velocity $v_0 = 220\,\mathrm{km/s}$, local energy density $\rho_0 = 0.3\,\mathrm{GeV}\,c^{-2}\,\mathrm{cm}^{-3}$, and galactic escape velocity of $544\,\mathrm{km/s}$ (Lewin and Smith, 1996). The expected WIMP-induced nuclear recoil spectrum was converted to a signal in photoelectrons in the detector using the $\mathcal{L}_{\mathrm{eff}}$ parametrization shown in Fig. 4.15 (thick solid blue line), with the constant extrapolation below $5\,\mathrm{keV_{nr}}$. Since the detector signal consists of discrete photoelectrons, the finite detector resolution was taken into account by convolving the expected spectrum with Poisson statistics. The acceptance-corrected exposure in the energy range considered, weighted by the spectrum of a $100\,\mathrm{GeV/c^2}$ WIMP, is 172 kg days. The resulting 90% confidence upper limit is shown in Fig. 4.18 (solid black line). The limit has a minimum at a cross section of $3.4 \times 10^{-44}\,\mathrm{cm}^2$ for a WIMP mass of $55\,\mathrm{GeV/c^2}$. The effect of taking the lower 90% confidence contour on the $\mathcal{L}_{\mathrm{eff}}$ parametrization shown in Fig. 4.15 (lower thin solid blue line) and the logarithmic extrapolation to zero scintillation at $1\,\mathrm{keV_{nr}}$ (thin dashed blue line) is also shown. The limit obtained challenged the interpretation of the CoGeNT (Aalseth *et al.*, 2011a) and DAMA (Savage *et al.*, 2009) signals as being due to light mass WIMPs. These initial results, based on only 11.2 live days of data, demonstrated the potential of the XENON100 detector as a low-background WIMP detector.

Chapter 5

Measurement of the Scintillation Efficiency of Low Energy Nuclear Recoils

In recent years, LXe particle detectors (Alner *et al.*, 2007; Angle *et al.*, 2008a; Aprile *et al.*, 2010; Lebedenko *et al.*, 2009a; Minamino, 2010) have achieved a large increase in target mass and a simultaneous reduction in backgrounds and are now among the leading technologies in the search for dark matter WIMPs. The XENON100 detector, with its 62 kg target mass and its low electronic recoil background of $< 10^{-2}\,\mathrm{events\,keV^{-1}\,kg^{-1}\,d^{-1}}$ (Aprile *et al.*, 2011e), is one of the most sensitive dark matter search in operation. Key to its performance is the ability to detect low-energy recoiling nuclei in LXe. As mentioned in Chap. 1, since WIMPs are expected to interact primarily with atomic nuclei, the nuclear recoil energy scale is based on the LXe direct scintillation signal and thus requires knowledge of the scintillation yield of nuclear recoils.

The relative scintillation efficiency of nuclear recoils in LXe, $\mathcal{L}_{\mathrm{eff}}$, was discussed in Chap. 2. The different methods used to measure $\mathcal{L}_{\mathrm{eff}}$ and their advantages and disadvantages were also presented. Fig. 5.1 shows the status of low-energy direct and indirect measurements at the time of the publication of the first dark matter results from the XENON100 experiment (Aprile *et al.*, 2010), also presented in Sec. 4.6. The more recent direct measurement of Manzur *et al.* (2010) indicated a decreasing $\mathcal{L}_{\mathrm{eff}}$ with decreasing energy while the direct measurement of Aprile *et al.* (2009) and the indirect measurement of Sorensen *et al.* (2009) were more supportive of a constant $\mathcal{L}_{\mathrm{eff}}$ at low energies. This uncertainty in the low energy behavior of $\mathcal{L}_{\mathrm{eff}}$ was taken into account in the analysis by presenting limits with two different extrapolations at low energies, a constant extrapolation and a logarithmic extrapolation to zero scintillation at 1 keV, as indicated in Fig. 5.1.

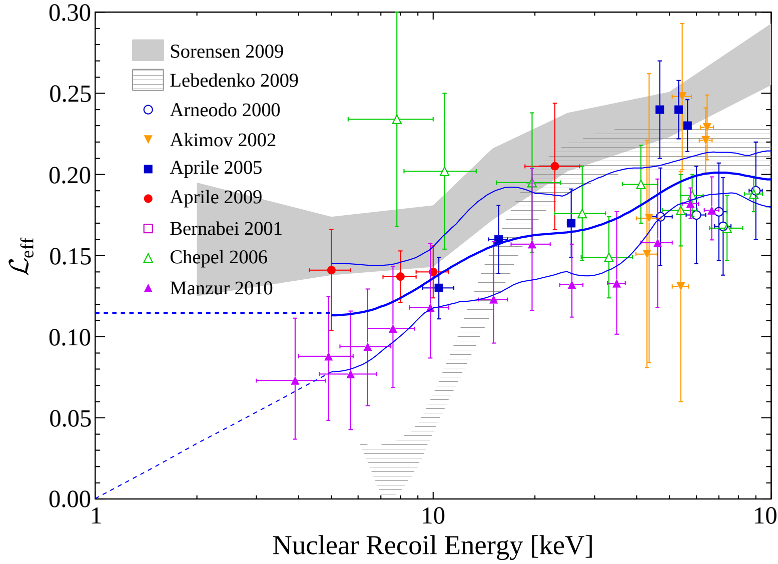

Figure 5.1: Direct and indirect measurements of $\mathcal{L}_{\mathrm{eff}}$ prior to 2011, along with the parameterization (thick line) used for the energy dependence of $\mathcal{L}_{\mathrm{eff}}$ used in Aprile *et al.* (2010).

As we saw in Sec. 4.6.3, the uncertainty in the nuclear recoil energy scale at low energies was the largest systematic uncertainty in the reported results from XENON100 (Aprile *et al.*, 2010, 2011c). Since the start of the XENON dark matter project, our group has performed two direct measurements of $\mathcal{L}_{\mathrm{eff}}$, in 2005 and 2007. Given the uncertainty in the low energy behavior of $\mathcal{L}_{\mathrm{eff}}$ and the implications for LXe dark matter searches it was clear that a new measurement was needed. We undertook the task of designing a new special purpose LXe detector in 2009 with the goal of measuring $\mathcal{L}_{\mathrm{eff}}$ with more precision and at the lowest energies possible. We finished the construction of the new detector in May 2010 and started operating it immediately to assess its performance.

With the renewed interest in the low WIMP mass region, motivated by the interpretation of the DAMA results (Bernabei *et al.*, 2008) and the recent CoGeNT signals (Aalseth *et al.*, 2011a) as being compatible with spin-independent elastic light mass WIMP interactions, an improvement in the robustness of future XENON100 results at low WIMP masses, or of any search with a LXe target, would of course help to clarify the situation.

In this chapter we describe results from a new measurement of $\mathcal{L}_{\text{eff}}$, with an improved apparatus and elaborated control of systematic uncertainties. The experimental setup used for the measurement, and a description of LXe detector and all associated subsystems are presented in Secs. 5.1-5.9, the measurement itself in Sec. 5.10, and the analysis procedure in Secs. 5.11-5.12. Finally, the results, discussion and conclusions are presented in Secs. 5.13-5.15.

5.1 Experimental Setup

Figure 5.2 shows a schematic of the experimental setup for the measurement of $\mathcal{L}_{\text{eff}}$ at low energies. Approximately monoenergetic neutrons produced with a neutron generator are incident on a special purpose LXe scintillation detector with high light detection efficiency. Part of the neutrons that scatter in the LXe detector at an angle θ with respect to their original direction are tagged by liquid scintillator neutron detectors placed on azimuthally symmetric positions. The energy E_r transferred to a Xe nucleus by a neutron of energy E_n, elastically scattering at an angle θ, can be computed kinematically and is given by

$$E_r = \frac{2E_n m_n}{\left(m_n + M_{\text{Xe}}\right)^2}\left[M_{\text{Xe}} + m_n\left(1-\cos^2\theta\right) - \cos\theta\sqrt{M_{\text{Xe}}^2 + m_n^2\left(\cos^2\theta - 1\right)}\right] \tag{5.1}$$

where m_n and M_{Xe} are the neutron and the Xe nucleus masses, respectively. Since $M_{\text{Xe}} \gg m_n$ and $E_n \ll m_n c^2$ the energy of the recoiling Xe nucleus is well approximated by

$$E_r \approx 2E_n \frac{m_n M_{\text{Xe}}}{\left(m_n + M_{\text{Xe}}\right)^2}\left(1-\cos\theta\right). \tag{5.2}$$

This provides a source of nuclear recoils of a known energy distribution in the LXe detector. By measuring the response of the LXe detector at different scattering angles, one can thus measure the energy dependence of $\mathcal{L}_{\text{eff}}$.

The total event rate R_{total} from neutron elastic scattering in the LXe detector when the neutron generator is operating can be approximated as $R_{\text{total}} = \phi \cdot \sigma \cdot nV$, where ϕ is the incident neutron flux on the LXe active volume, σ is the total neutron elastic scattering cross section on Xe, n is the number density of Xe atoms, and V the volume of active LXe. Active in this context means a LXe volume whose scintillation signals are measured by PMTs. Similarly, the tagged event rate, the event rate of neutrons that scatter in the direction of one of the EJ301 detectors, can be approximated by

$$R_{\text{tagged}} = \phi \cdot \int_{\Omega_{\text{EJ301}}} \frac{d\sigma}{d\Omega} d\Omega \cdot nV, \tag{5.3}$$

where $d\sigma/d\Omega$ is the neutron differential elastic scattering cross section on Xe. With the EJ301 detectors at a nominal distance of 1 m, the solid angle subtended by two EJ301 detectors is $\Delta\Omega_{\text{EJ301}} = 2 \cdot (3 \cdot 2.54\,\text{cm})^2 / \left[4\pi\,(100\,\text{cm})^2\right] = 9.2 \times 10^{-4}\,\text{sr}$. In order to accumulate a dataset of 10^4 events in one day, with a nominal recoil energy of 5 keV, which corresponds to a scattering angle of 30°, one thus needs a total neutron scattering rate in the LXe detector of

$$R_{\text{total}} = R_{\text{tagged}} \cdot \sigma \left[\int_{\Omega_{\text{EJ301}}} \frac{d\sigma}{d\Omega} d\Omega\right]^{-1} \approx \frac{10^4}{86400\,\text{s}} \cdot \frac{3.7\,\text{b}}{1.5\,\text{b}\,\text{sr}^{-1} \cdot 9.2 \times 10^{-4}\,\text{sr}} \approx 300\,\text{Hz}, \tag{5.4}$$

where we assumed that the differential scattering cross section does not vary much over the extent of the solid angle subtended by the EJ301 detectors. If the LXe detector is placed at a distance of 40 cm from the neutron generator then the generator needs to achieve yields of $300\,\text{Hz} \cdot 4\pi\,(40\,\text{cm})^2 / \left[3.7\,\text{b} \cdot 1.3 \times 10^{22}\,\text{cm}^{-3} \cdot (2.6\,\text{cm})^3\right] \approx 7 \times 10^6\,\text{n}\,\text{s}^{-1}$.

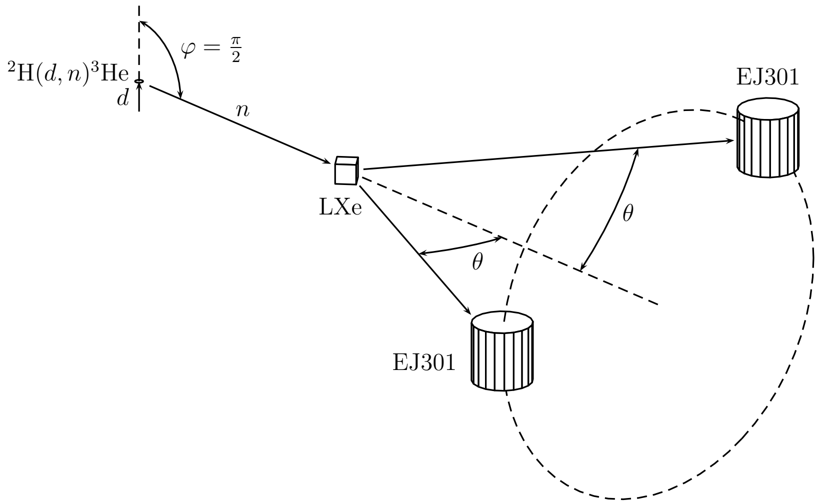

Figure 5.2: Schematic of the experimental setup. A sealed-tube neutron generator, where deuterons of energy E_d are incident upon a titanium deuteride target, produces neutrons at various angles φ. Some of the neutrons emitted at an angle $\varphi = \frac{\pi}{2}$ scatter in the LXe detector at an angle θ and are tagged by two EJ301 organic liquid scintillators neutron detectors. Figure from Plante *et al.* (2011).

The measurement of $\mathcal{L}_{\text{eff}}$ was performed at the Columbia University Nevis Laboratories.

Neutrons with an average energy of 2.5 MeV were produced via the $^{2}\mathrm{H}(d,n)^{3}\mathrm{He}$ reaction in a compact sealed-tube neutron generator provided by the Schlumberger Princeton Technology Center. The generator was operated at deuteron energies of 60, 65, 75, or 80 keV and with deuterium beam currents ranging from 60 to 100 μA. Sec. 5.3 describes the principle, operation, and modelling of the neutron generator yield. Sec. 5.2 describes in detail the design of the LXe detector.

The organic liquid scintillator neutron detectors used are Eljen Technologies M510 detector assemblies filled with EJ301. The EJ301 liquid scintillator is identical to the more commonly known proprietary names of NE213 and BC501A, all commercial names for $C_6H_4\,(CH_3)_2$. The liquid scintillator is encapsulated in a 3 in. cylindrical aluminium container, coupled to a 3 in. ET Enterprises 9821B PMT. EJ301 has excellent pulse shape discrimination (PSD) properties and is especially adapted to fast neutron counting in the presence of γ radiation. Sec. 5.7 discusses the calibration of the EJ301 neutron detectors.

5.2 Detector Design

The precise measurement of $\mathcal{L}_{\mathrm{eff}}$ at energies lower than previously achieved is a challenging exercise. To achieve a low energy threshold one needs a very high light detection efficiency. At the same time, to accumulate enough statistics in a reasonable amount of time the detector should be large enough. A practical way to satisfy both constraints is to cover the active LXe volume with photosensors. Equally important is to maximize the probability that neutrons travel from the neutron generator to the active LXe volume without interacting in other materials, and similarly travel without interactions from the LXe detector to the EJ301 neutron detector. The emphasis for the design of the LXe detector has thus been placed on the reduction of non-active LXe and other materials in the immediate vicinity of the active LXe volume, and on the maximization of the scintillation light detection efficiency.

5.2.1 Detector Inner Structure

Fig. 5.3 shows a schematic of the detector. The active volume of the LXe detector is a cube with sides of length 2.6 cm viewed by six 2.5 cm × 2.5 cm Hamamatsu R8520-406 SEL PMTs. The PMTs are the same type as used in the XENON100 experiment (Aprile *et al.*, 2011f) (see Sec. 3.3.2) but were selected for QE. The PMTs have a special bialkali photocathode,

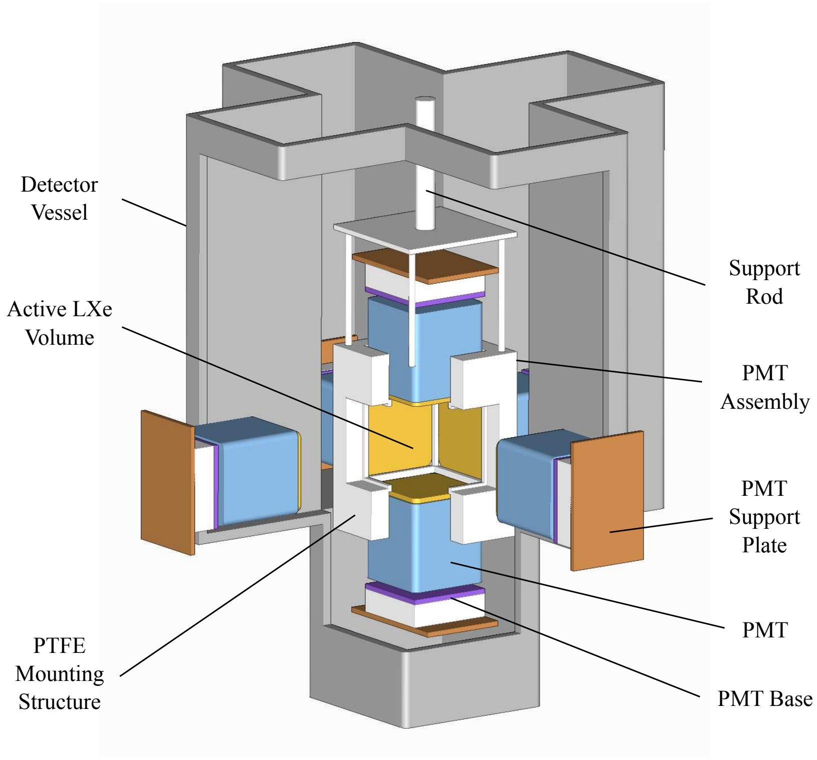

Figure 5.3: Schematic drawing of the LXe detector. The cubic active LXe volume is covered by PMTs on each side. Figure from Plante *et al.* (2011).

optimized for low temperature operation down to −110°C. The room temperature QE at a wavelength of 178 nm was measured by Hamamatsu. The values obtained for the six PMTs used are listed in Tab. 5.2 and give an average QE of 32%. The PMTs are operated with positive high voltage bias (grounded-cathode scheme) so that the metal body of the PMT and photocathode are both at ground potential. The schematic of the PMT base voltage divider network used to bias the dynodes is shown in Fig. 5.5. In this configuration the active volume remains at zero electric field, a prerequisite of the $\mathcal{L}_{\rm eff}$ measurement since $\mathcal{L}_{\rm eff}$ is defined as the relative scintillation efficiency of nuclear recoils at zero electric field.

A PTFE frame serves as a mounting structure and alignment guide for the PMTs. Each PMT covers one side of the cubic active volume. Small 1 mm edges in the PTFE frame block the PMTs and define the 2.6 cm cubic active volume. These edges also partially cover with PTFE the outer part of the PMT not covered by the photocathode. The PMT bases are mounted on aluminium PMT support plates with a PTFE block between the base and the support plate. The support plates are fixed to the PTFE frame with four threaded stainless steel rods. The rods can be used to precisely adjust the PMT positions and hold the support plates firmly in place. The PMT assembly is housed in a stainless steel detector vessel, surrounded by a vacuum cryostat. The detector vessel has a special cross shape that closely follows the contours of the PMT assembly. This is to reduce to a minimum the materials in the vicinity of the active volume and thus minimize the probability that neutrons scatter before or after an interaction in the active volume. The PTFE mounting structure is suspended from the top by a stainless steel rod fixed to a linear displacement motion feedthrough. The vertical position of the assembly within the detector vessel can be adjusted from the outside with the motion feedthrough.

An extra rectangular PTFE piece, not shown in Fig. 5.3, is fixed on top of the PTFE mounting structure and holds a blue LED used to calibrate the PMT gains. PTFE is partially transparent to the LED light and acts as a diffuser. A single intensity for the LED pulse is enough to generate an appropriate amount of light and calibrate all PMTs simultaneously.

PMT signal and high voltage cables share a common multipin electrical feedthrough. 50 Ω RG178 coaxial cables with their outer FEP jacket removed are used to carry the signals from the PMT bases to the feedthrough. MDC Vacuum KAP3 in-vacuum insulated wires are used for the high voltage connections.

5.2.2 Cryogenic System, Gas Handling and Purification System

The LXe temperature is kept constant with an Iwatani PDC08 pulse tube refrigerator (PTR) delivering 24 W of cooling power at 165 K with an air-cooled 1.5 kW helium compressor. The active volume consists of only 50 g of LXe but the detector needs ~1.6 kg of LXe for the level to reach the top PMT. The PTR is mounted on a separate double-wall vacuum insulated vessel above the detector vessel. The PTR coldhead is coupled to the Xe gas through a cylindrical copper piece that acts as a cold finger. The part in contact with the gas has a comb-like structure to maximize the contact surface. This cylindrical copper piece closes off the top of the PTR vessel. It is sealed to the vessel with an aluminium wire in a “v” groove machined on a stainless steel flange. A copper piece with resistive heaters is inserted between the PTR coldhead and the cold finger. Two Pt100 temperature sensors placed above and below the heaters monitor the temperatures of the coldhead and the cold finger, respectively. A Lakeshore 340 temperature controller regulates the temperature of the cold finger by controlling the heaters, thus maintaining the temperature and pressure of the detector at the desired value. A funnel below the cold finger collects LXe droplets and a pipe connected to the funnel guides the liquid flow to the bottom of the detector vessel. The design is similar to the cooling tower design of the XENON100 detector (Sec. 3.1.4).

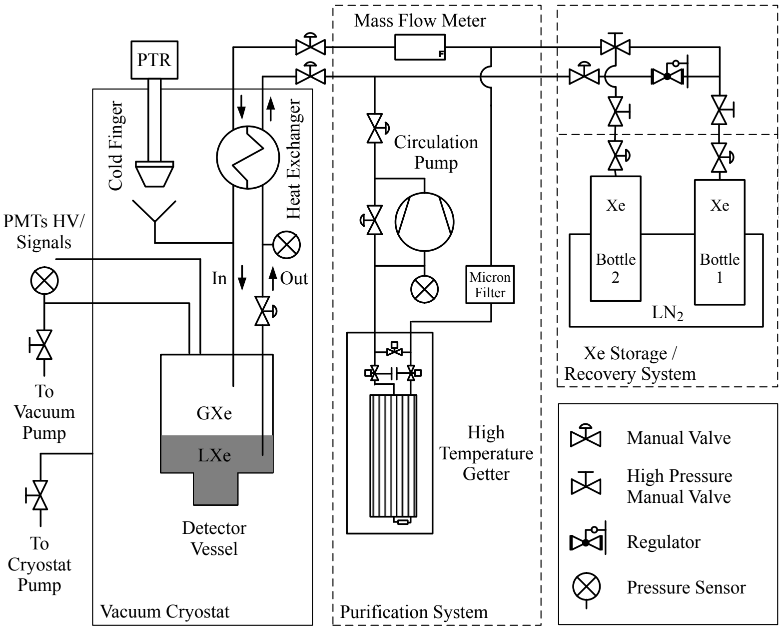

Figure 5.4: Xe gas system used for continuous LXe purification and storage. Figure from Plante *et al.* (2011).

A schematic of the gas handling, liquefaction and recirculation system developed for this detector is shown in Fig. 5.4. An Enomoto MicroPump Model MX-808ST-S diaphragm pump pulls the LXe out of the detector through a pipe from a separate buffer volume, connected to the detector vessel at a height of 9.4 cm from the bottom of the detector vessel. The pipe runs to a separate double-wall vacuum insulated chamber with a heat exchanger. Xe in the liquid state reaches the heat exchanger and is evaporated inside the heat exchanger. After the diaphragm pump, the GXe is circulated through a SAES MonoTorr PS4-MT3-R1 high-temperature getter and re-liquefied efficiently in the heat exchanger. Further details on the design and performance of the cooling system developed for this detector are presented in Giboni *et al.* (2011).

Fill or recovery operations are carried out with GXe. When the detector is not in operation, the Xe gas is stored in a 16 L stainless steel cylinder. Filling the required 1.6 kg of LXe takes about ~8 h. The initial stage of the filling cannot proceed at a fast rate because the PTR is essentially cooling the detector vessel and the PMT assembly via cycles of Xe condensation on the cold finger and evaporation on warm surfaces. This is similar, although not as substantial, as the effect observed for the much larger XENON100 detector and described in Sec. 3.3.6. When filled, 10.5 W of PTR cooling power are required to keep the detector temperature stable when recirculating the Xe at a speed of 1.64 SLPM.

Thanks to the PTR stability and low maintenance, the cooling system developed for this detector has enabled us to acquire data over a two month long, uninterrupted run. During the measurements, the LXe temperature was maintained at −94°C which corresponds to a vapor pressure of 2 atm.

5.2.3 PMTs

The small form factor of the R8520 PMTs allowed a compact design of the inner structure of the detector and consequently satisfied the requirement of minimized materials in the vicinity of the LXe active volume. Trying to create a detector geometry with high photocathode coverage area with larger PMTs would obviously require more materials, which reduces the probability of the neutron reaching the active volume (and exiting) without any interactions.

As mentioned in Sec. 5.2.1, the PMTs were operated with positive high voltage to ensure a zero electric field configuration in the active LXe volume. Prototype XENON10 PMT bases, originally designed for negative high voltage operation, were modified to enable positive high voltage operation. Two 22 nF decoupling capacitors and two 12 kΩ resistors were added to the base. Fig. 5.5 shows the schematic of the modified base voltage divider circuit.

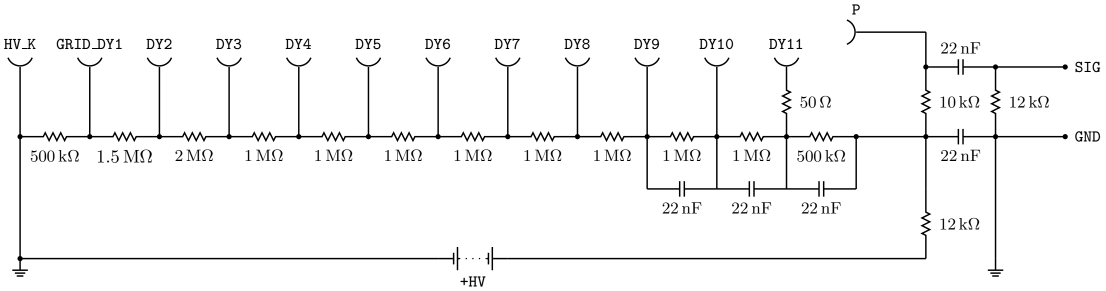

Figure 5.5: Schematic of the modified grounded-cathode scheme PMT base voltage divider.

At the recoil energies measured, the PMT response remains far from the non-linear regime. Repeating the estimate of Sec. 3.3.2, one obtains a voltage divider biasing current of $i_b = 72\,\mu\text{A}$ which leads to a recommended maximum signal current of $i_{s,\max} = 0.36\,\mu\text{A}$. Again, for a PMT gain of 2×10^6 pe/e$^-$, this implies a linear PMT response at single photoelectron rates below 1 MHz. This limit is above the expected nuclear recoil scintillation signals on a single PMT at the neutron fluxes achievable with the neutron generator. Additionally, the reserve charge on the last amplification stage is more than enough to buffer the larger instantaneous signal currents drawn during the short time of the scintillation signal.

5.2.4 Scintillation Light Detection Efficiency

The expected scintillation light detection efficiency (photoelectrons/photon) of the LXe detector was examined with a light propagation simulation based on the GEANT4 Monte Carlo simulation framework. A detailed geometry of the PMTs and the PTFE inner structure was included. Unfortunately, many of the parameters needed to obtain an accurate prediction of the scintillation light detection efficiency are not known to the desired accuracy. The measured light detection efficiency is often found to be higher than the predicted value. The result of the simulation is shown in Fig. 5.6 (left). Another effect which has an impact on the light detection efficiency is the angular response of PMTs. Fig. 5.7 shows an example from the Hamamatsu PMT Handbook (Hamamatsu Photonics K.K., 2006). Photons with an angle of incidence larger than zero have an effectively higher probability of being detected. Fig. 5.6 (right) shows the result of the light detection simulation once this effect is taken into account. In both cases we see that the expected light detection efficiency is very uniform throughout the volume.

Table 5.1: Parameters with an effect on the light detection efficiency and values used in the simulation.

Parameter	Value
PMT Quantum efficiency, η	0.32[a]
PMT Collection efficiency, ζ	0.75
Quartz refraction index, n_{quartz}	1.56
LXe refraction index, n_{LXe}	1.61
LXe absorption length, λ_{abs}	100 cm
LXe Rayleigh scattering length, λ_R	30 cm
PTFE reflectivity, ϱ_{PTFE}	0.95
Aluminium reflectivity, ϱ_{Al}	0.90

[a] Room temperature measurement at 178 nm from Hamamatsu.

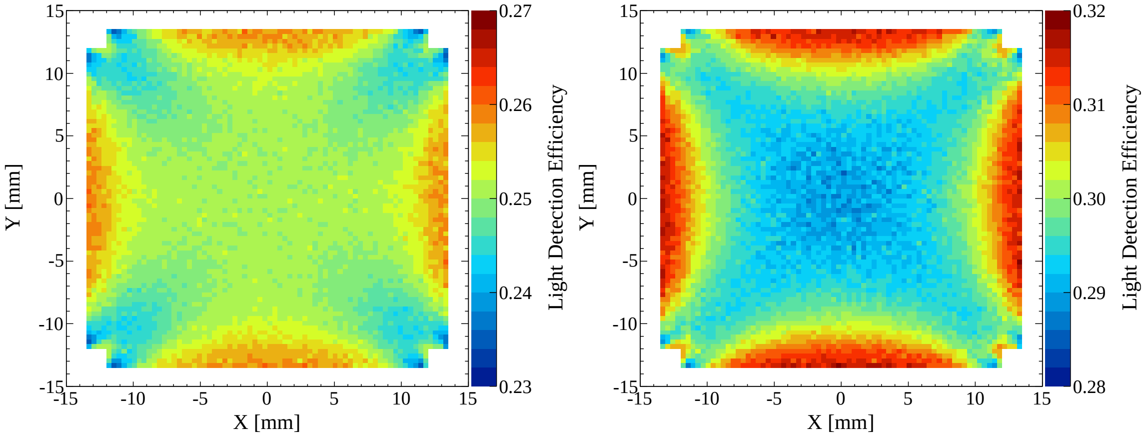

Figure 5.6: Simulated average scintillation light detection efficiency as a function of (x, y) without (left) and with (right) taking into account the angular response of PMTs.

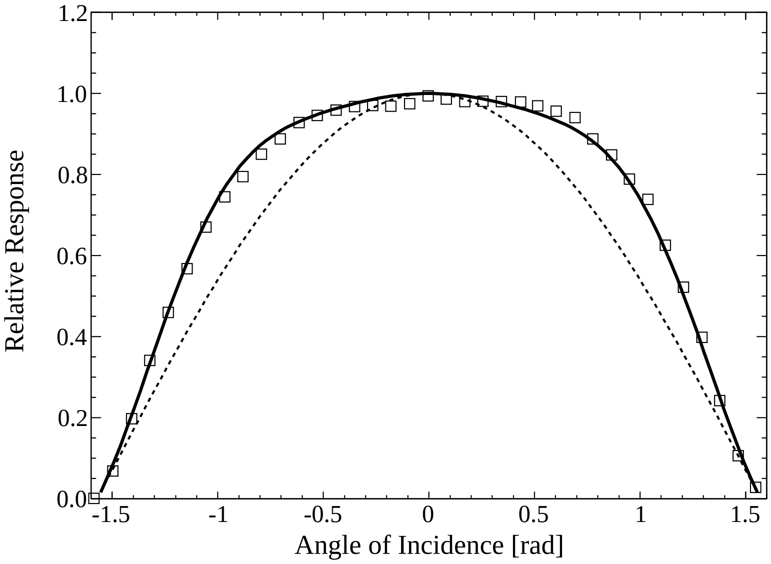

Figure 5.7: Typical PMT angular response (squares), taken from the Hamamatsu PMT Handbook (Hamamatsu Photonics K.K., 2006), together with a $\cos\theta$ response (dashed line) and the model used to parameterize the angular response (solid line).

5.3 Neutron Generator

The neutron generator used for the $\mathcal{L}_{\text{eff}}$ measurement is a deuterium-deuterium compact sealed-tube generator supplied by the Schlumberger Princeton Technology Center. The tube itself is a ~11 cm long cylinder with a diameter of 2.5 mm. This small form factor allows easy placement near the LXe detector and additionally helps reduce the amount of scattering materials near the detector. Since recoil energies are directly proportional to the neutron energy, the energy spread of the incident neutrons should be minimized as much as possible.

Sec. 5.3.1 describes the operation of the neutron generator, Sec. 5.3.2 details the model of its neutron yield as a function of its operating parameters, and Sec. 5.3.3 discusses the expected energy spread of neutrons incident on the LXe detector.

5.3.1 Operation

Neutrons are produced in the generator via the $^{2}\text{H}(d,n)^{3}\text{He}$ reaction. Deuterium gas is released in the inner volume of the generator by heating a replenisher filament with an electric current, the filament current I_{filament}. Another electric current, the cathode current I_{cathode}, circulates in another filament near a conducting grid held at positive electrical potential. As the cathode filament heats up, electrons are extracted to the grid and create an electric current from the cathode filament to the grid, the grid current I_{grid}. Atomic and molecular ions, D_1^+, D_2^+, or D_3^+, are created when the grid current ionizes deuterium gas molecules, sometimes breaking them apart in the process. The deuteron ions are accelerated towards a titanium deuteride (TiD_2) target on a copper backing held at high negative potential, $V_{\text{high voltage}}$. The deuteron ions, accelerated to an energy $E_d = eV_{\text{high voltage}}$, eventually collide with deuterium atoms in the target and produce neutrons or are stopped in the target. The target is a self-regenerating thick target, that is, deuterons lose all their energy in the target and those that do not produce neutrons replenish the target in deuterium. The thickness of the target is $10\,\mu$m, larger than the penetration depth of ~$0.56\,\mu$m of 100 keV deuterons in TiD_2 (see Fig. 5.9). Prior to the first operation the target does not contain any deuterium but gets loaded in deuterium after a short initial loading time. The deuteron ion beam current, I_{beam} is measured on the high voltage power supply providing the accelerating voltage. Fig. 5.8 (left) shows a sketch of the operating principle of the neutron generator.

The neutron generator was held in place by a custom made PTFE holder inside a vertical stainless steel tube closed at the bottom. The stainless steel tube was held a ground potential and filled with mineral oil to avoid corona discharges at the high voltage connection to the neutron generator. The neutron production point, the TiD_2 target, was set at the same height as the center of the LXe detector, 62.5 cm from the floor. Fig. 5.8 (right) shows a schematic of the generator holding apparatus.

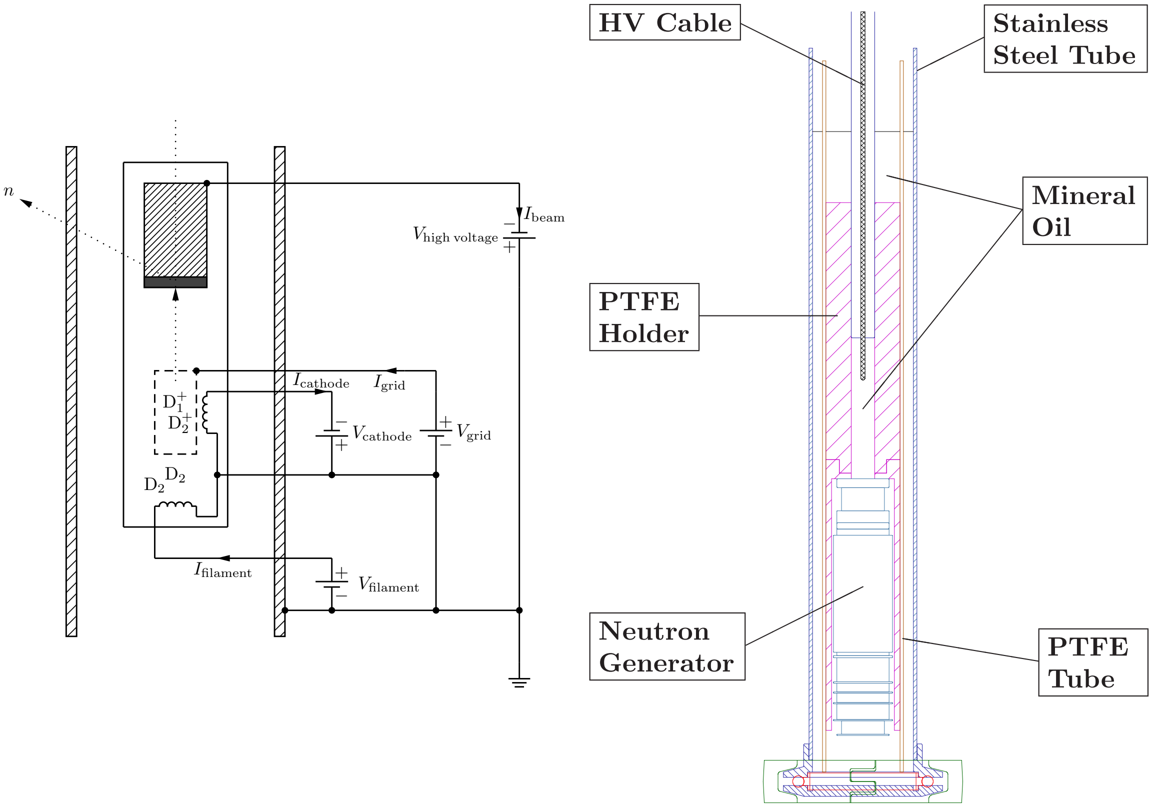

Figure 5.8: Operating principle of the neutron generator (left) and schematic of the holding apparatus (right).

The deuteron ions striking the target produce a large amount of heat that needs to be dissipated. The deuterium number density in the target is a function of the target temperature and decreases as the temperature increases, thereby reducing the neutron yield of the generator. An electrical fan was used to cool the stainless steel tube holding the neutron generator to keep its temperature at acceptable levels.

Prior to each neutron scattering measurement, the neutron generator was brought to stable operating conditions, i.e., a set accelerating voltage and a stable beam current. The beam current was monitored throughout the measurement and maintained at the desired value by adjusting I_{filament} manually.

5.3.2 Neutron Yield

The expected neutron yield from the generator can be computed from its operating conditions, specifically the deuteron energy, the monoatomic/diatomic deuterium beam composition, and the deuterium beam current. We follow the computation of the neutron yield in Chap. 1, Sec. 1.C of (Csikai, 1987).

For non-relativistic deuterons ($E_d < 20\,\mathrm{MeV}$), the energy of neutrons emitted in the $^2\mathrm{H}(d,n)^3\mathrm{He}$ reaction is given by

$$E_n^{1/2} = \frac{\left(m_d m_n E_d\right)^{1/2}}{m_{\mathrm{He}} + m_n}\cos\varphi + \frac{\left\{m_d m_n E_d \cos^2\varphi + \left(m_{\mathrm{He}} + m_n\right)\left[m_{\mathrm{He}} Q + \left(m_{\mathrm{He}} - m_d\right) E_d\right]\right\}^{1/2}}{m_{\mathrm{He}} + m_n} \tag{5.5}$$

where m_d and m_{He} are the deuteron and ^{3}He nucleus masses, respectively, Q is the Q-value of the reaction (3.269 MeV), and φ is the neutron emission angle in the laboratory frame.

The number of neutrons per second per steradian produced by a deuteron flux ϕ, incident upon an infinitely thin titanium deuteride target of thickness dx, and with deuteron energies E_d, is given by

$$dY(E_d,\varphi) = \phi\sigma(E_d,\varphi)\, n_d dx, \tag{5.6}$$

where n_d is the number density of deuterium atoms in the target, and $\sigma(E_d,\varphi)$ is the $^2\mathrm{H}(d,n)^3\mathrm{He}$ differential neutron production cross section. Since the deuterons are slowing down in the target, their energy is actually a function of x. Using the deuteron (mass) stopping power of the target, $(dE/dx)_d$, we can rewrite Eq. 5.6 as

$$dY(E_d,\varphi) = \phi\sigma(E_d,\varphi)\, n_d \left[\rho\left(\frac{dE}{dx}\right)_d dE_d\right]^{-1}, \tag{5.7}$$

where ρ is the target density. Since the deuterons lose all their energy in the target, the total neutron yield is the integral of the above expression over the entire penetration depth in the target and is given by

$$Y(E_d, \varphi) = \frac{\phi\, n_d}{\rho} \int_0^{E_d} \sigma\left(E'_d, \varphi\right) \left[\left(\frac{dE}{dx}\right)_d \left(E'_d\right)\right]^{-1} dE'_d. \tag{5.8}$$

So far we have assumed that the deuteron flux is a monoenergetic flux with deuterons of energy E_d. However, since deuterons from D_2^+ molecular ions reach the target with half the kinetic energy of the D_1^+ ions but can produce two neutrons, then the yield has to take into account these two components. The total neutron angular yield is thus given by

$$Y_{\text{tot}}(E_d, \varphi) = xY(E_d, \varphi) + 2yY(E_d/2, \varphi)\,, \tag{5.9}$$

where x and y are the D_1^+ and D_2^+ beam composition fractions, respectively.

The stopping power of TiD_2 for deuterons is computed from Bragg's rule (Bragg and Kleeman, 1905), from the atomic mass number weighted sum of the stopping powers of titanium and deuterium,

$$\left(\frac{dE}{dx}\right)_d = \frac{48}{52}\left(\frac{dE}{dx}\right)_{d,\text{Ti}} + \frac{4}{52}\left(\frac{dE}{dx}\right)_{d,\text{D}}. \tag{5.10}$$

Finally, using the stopping power scaling law (Leo, 1994)

$$\frac{dE_2}{dx}(T_2) = \frac{z_2^2}{z_1^2}\frac{dE_1}{dx}\left(T_2\frac{M_1}{M_2}\right) \tag{5.11}$$

we can obtain the stopping power of titanium and deuterium for deuterons from the stopping power for protons. Consequently

$$\left(\frac{dE}{dx}\right)_d(E) = \frac{48}{52}\left(\frac{dE}{dx}\right)_{p,\text{Ti}}\left(\tfrac{1}{2}E\right) + \frac{4}{52}\left(\frac{dE}{dx}\right)_{p,\text{H}}\left(\tfrac{1}{2}E\right). \tag{5.12}$$

The mean deuteron range is found simply by integrating the reciprocal of the stopping power over energy

$$R_d\left(E_d\right) = \int_0^{E_d} \left[\left(\frac{dE}{dx}\right)_d \left(E'_d\right)\right]^{-1} dE'_d. \tag{5.13}$$

Fig. 5.9 shows the stopping power and range of deuterons in titanium, hydrogen, and TiD_2. The stopping power in TiD_2 and the ranges are computed using Eqs. 5.12 and 5.13 and the stopping power for protons is taken from the PSTAR database (Berger *et al.*). Dividing the range of a 100 keV deuteron in TiD_2 by a density of $\rho = 4.0\,\mathrm{g\,cm^{-3}}$ one gets a value of $0.56\,\mu$m for the range in the target. Since the maximum deuteron energy used for the $\mathcal{L}_{\mathrm{eff}}$ measurement is 80 keV the assumption that deuterons are stopped in the target is valid.

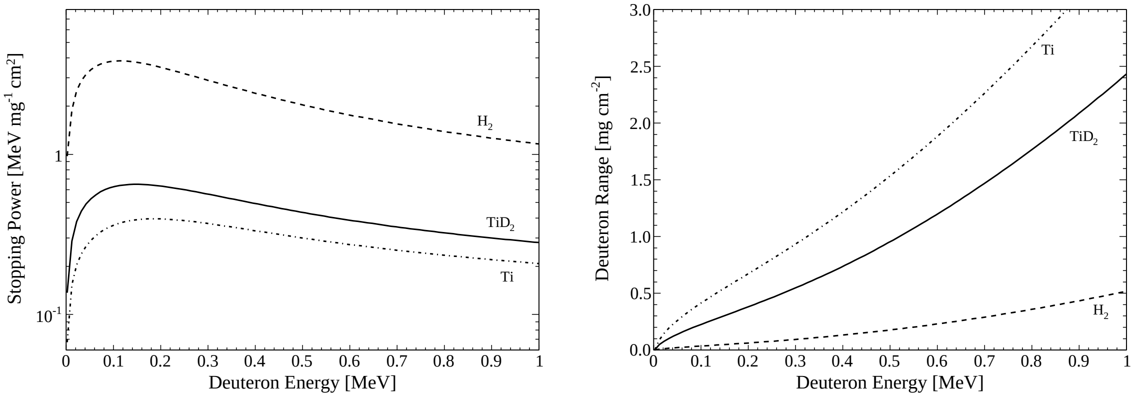

Figure 5.9: Deuteron stopping power (left) and range (right) in Ti, H_2, TiD_2. The stopping power and range of deuterons in TiD_2 are calculated from Eqs. 5.12 and 5.13 and using the stopping power for protons from the PSTAR database (Berger *et al.*).

The expected neutron yield from the generator is computed from Eqs. 5.9, 5.8, and 5.12. The $^2\mathrm{H}(d,n)^3\mathrm{He}$ neutron production cross section is taken from the ENDF/B-VII.0 database (Chadwick *et al.*, 2006), and the monoatomic/diatomic deuterium beam fraction is taken as 0.05/0.95[1]. The result of the computation is shown in Figs. 5.10 and 5.11 (solid lines).

Measurements of the neutron flux under various operating conditions were also carried out using a Nuclear Research Corporation NP-2 portable neutron monitor. The NP-2 neutron monitor is a boron trifluoride proportional counter surrounded by a low density polyethylene cylinder to moderate the neutron flux before capture by boron. We used the NP-2 neutron monitor scaler output to perform the flux measurements. The scaler output is proportional (6000 cts/mrem) to the neutron dose rate incident on the front of the monitor. The neutron flux is obtained from the dose rate through the fluence to dose conversion factor of $29 \times 10^6\,\mathrm{n\,cm^{-2}\,rem^{-1}}$ for 2.5 MeV neutrons (ICRP, 1987). The accuracy of the NP-2 neutron monitor is ±10%. The measurements of the neutron flux as a function of the deuteron accelerating voltage, deuterium beam current, and distance are shown in Figs. 5.10 and 5.11 (points).

The result of the computation shows remarkable agreement with the measurement as a

---

[1] Andrew Bazarko (personal communication, 2010)

function of high voltage (maximum deuteron energy). The agreement with the measurement as a function of beam current is also good but worsens as the beam current increases. This discrepancy can have several sources, the growth of an electronic current between the target and the ground, undistinguishable in the apparatus from the measured deuterium beam current, or the increased unloading of deuterium in the target at higher power on target for example. The measurement of the neutron flux as a function of distance also shows a discrepancy, with an apparent excess at larger distances. This could be due to the effect of the concrete floor of the laboratory, where a part of the flux is reflected, enhancing the contribution of the direct flux and not taken into account in the theoretical calculation.

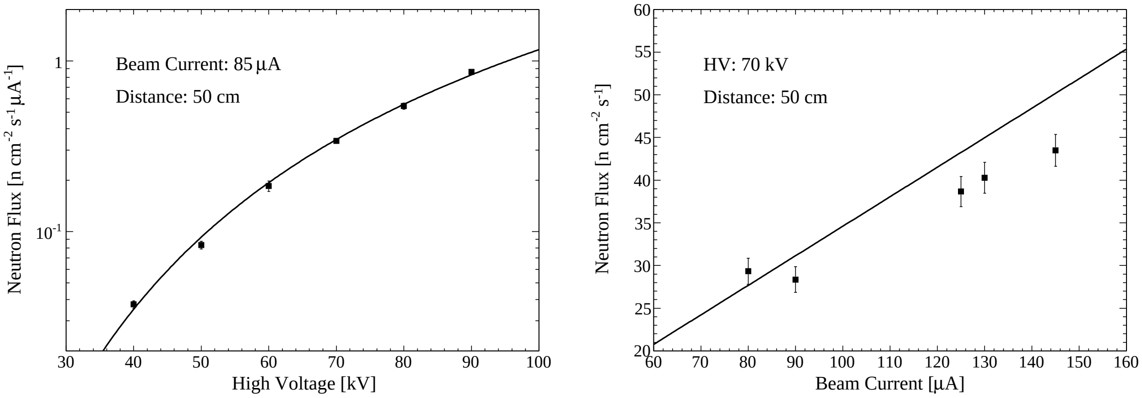

Figure 5.10: Measured (points) and calculated (solid line) neutron flux as a function of deuteron accelerating voltage (left) and deuterium beam current (right). Figure from Plante *et al.* (2011).

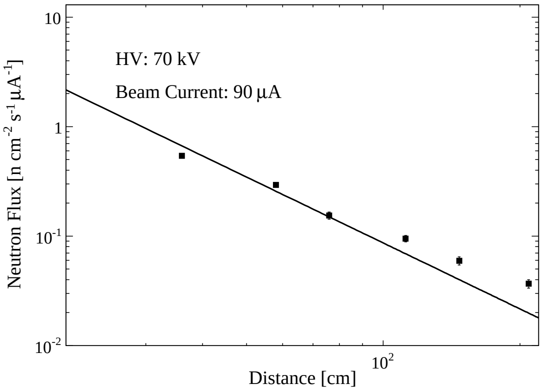

Figure 5.11: Measured (points) and calculated (solid line) neutron flux as a function of distance.

5.3.3 Neutron Energy Spread

As we saw through Eq. 5.5, the neutron energy is a function of the deuteron energy. Since deuterons lose energy as they are stopped in the target, neutrons are produced in a continuum of energies. Fig. 5.12 (left) shows the energy of the produced neutron as a function of the deuteron energy, calculated via Eq. 5.5. At small and large emission angles the neutron energy depends significantly on the deuteron energy. However, there is a minimum in $\partial E_n/\partial E_d$ and a maximum in $\partial E_n/\partial\varphi$ at $\varphi \sim 100°$, and consequently the energy spread of neutrons produced is minimal near this angle (see Fig. 5.12 (right)).

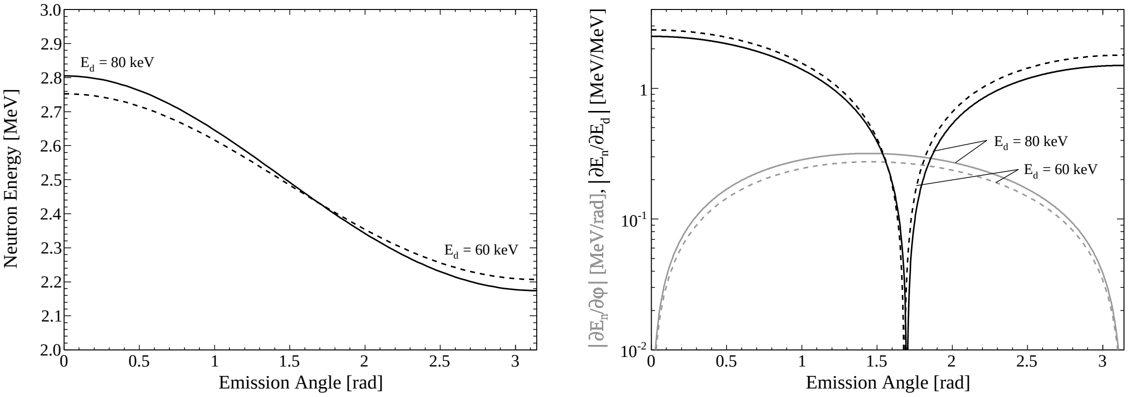

Figure 5.12: Neutron energy (left) and neutron energy variation with respect to deuteron energy or emission angle (right), as a function of the neutron emission angle, for the ^{2}H$(d, n)^3$He reaction.

To minimize the neutron energy spread from the energy loss of deuterons, the neutron generator was operated in a configuration where deuterons are accelerated vertically and where the neutrons incident on the LXe detector are those produced at $\varphi = \frac{\pi}{2}$ (see Fig. 5.2).

Several variables can influence the energy spread of neutrons incident on the LXe detector, (i) the ratio of atomic and molecular ions in the beam (since the energy of the two deuterons are significantly lower for D_2^+), (ii) the energy spread of the accelerated ions, (iii) the slowing down of ions in the target, (iv) the angular straggling of deuterons due to multiple scattering in the target, (v) the finite solid angle subtended by the LXe detector with respect to the neutron source, and (vi) the scattering of neutrons back into the LXe detector direction that were produced at different angles. We took into account effects (i) and (iii) in the modelling of the neutron generator. In the GEANT4 simulation of the experiment (see Sec. 5.11), the energy and direction of the primary neutron is sampled from the calculated energy-angle distribution of neutrons produced by the generator (Eq. 5.16) and propagated through the experimental setup geometry therefore effects (v) and (vi) are taken into account in that step.

To calculate the energy-angle distribution of neutrons produced by the generator we start with the number of neutrons produced at an angle φ by deuterons of energy E_d to $E_d + dE_d$, from Eq. 5.8,

$$N(E_d, \varphi)\, dE_d = \frac{\phi\, n_d}{\rho} \sigma(E_d, \varphi) \left[\left(\frac{dE}{dx} \right)_d (E_d) \right]^{-1} dE_d. \tag{5.14}$$

Since E_d is a function of E_n, the number of neutrons with energy between E_n and $E_n + dE_n$ produced at a fixed angle φ can be obtained by the expression for the number of neutrons produced at that angle by deuterons of energy E_d to $E_d + dE_d$,

$$N(E_n, \varphi)\, dE_n = N(E_d, \varphi)\, \frac{\partial E_d}{\partial E_n} dE_n \tag{5.15}$$

Summing contributions from D_1^+ and D_2^+ deuterium beam constituents, we get

$$N_{\mathrm{tot}}(E_n, \varphi)\, dE_n = \big[x N(E_d, \varphi) + 2y N(E_d/2, \varphi) \big] \frac{\partial E_d}{\partial E_n} dE_n. \tag{5.16}$$

From Eq. 5.16 one gets the energy distribution of neutrons at all angles produced by a deuterium beam with maximum energy $E_d = eV_{\text{high voltage}}$. Fig. 5.13 shows the result for $E_d = 80\,\mathrm{kV}$.

5.4 Data Acquisition System

The data acquisition system for the measurement of the scintillation efficiency of nuclear recoils needs to fulfill several requirements. It needs to record the waveforms of the six PMT channels of the LXe detector and the waveforms of the two PMTs of the neutron detectors, achieve a very low triggering threshold in the LXe, and measure the neutron time-of-flight between the LXe detector and the neutron detectors. In addition it is important to have a good knowledge of the efficiency of the trigger subsystem, the behavior of the efficiency loss at low energies, the dead time incurred at high event rates, etc.

In Sec. 5.4.1 we describe the data acquisition system used for the measurement of $\mathcal{L}_{\mathrm{eff}}$,

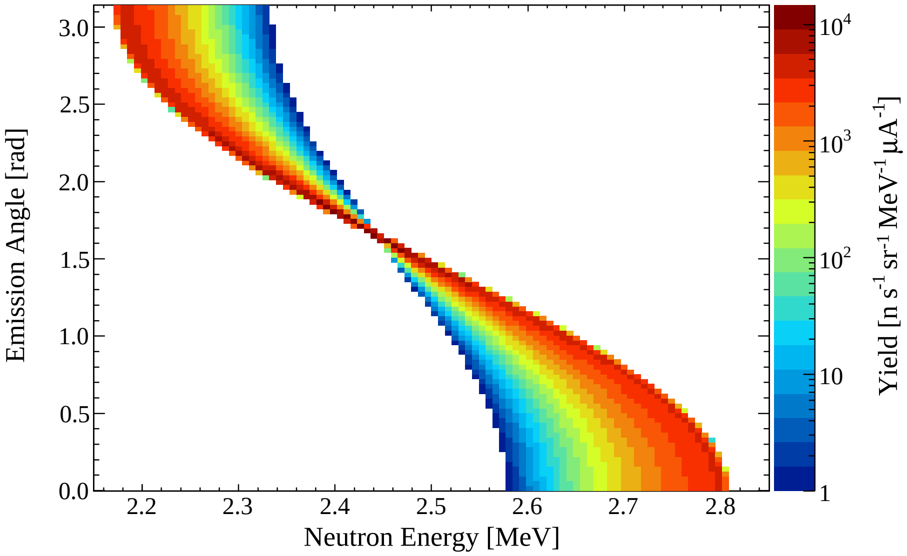

Figure 5.13: Calculated neutron energy distribution as a function of the neutron emission angle φ.

in Sec. 5.4.2 we describe the setup used to directly measure its trigger efficiency, and in Sec. 5.4.3 we describe the simulation performed to obtain the expected trigger efficiency.

5.4.1 Data Acquisition System and Trigger Description

The data acquisition system is divided in two subsystems, the trigger and the acquisition subsystems. The triggering scheme is quite simple. To obtain the lowest possible energy threshold while minimizing the trigger rate of uninteresting events we require a twofold coincidence on any of the six LXe PMTs. In addition, we require a coincident signal in one of the two neutron detectors. Fig. 5.14 shows a diagram of the data acquisition system used in for the $\mathcal{L}_{\mathrm{eff}}$ measurement. Many of the electronics used for the acquisition subsystem are the same as those used for the XENON100 experiment (Sec. 3.3.10).

The signals from the six LXe PMTs are first fed to a Phillips 776 ×10 amplifier. Without the amplification, the fast single photoelectron signal from a PMT is not large enough to be accurately measured by the flash ADC used. The Phillips 776 ×10 amplifier has two amplified outputs per channel and thus also allows to get two copies of the analog signal. The first copy of each LXe channel is digitized by a 14-bit CAEN V1724 100 MS/s flash ADC with 40 MHz bandwidth. The second copy goes to a Phillips 706 leading edge discriminator. The discriminator thresholds are set at a level of $-15\,\mathrm{mV}$, which corresponds

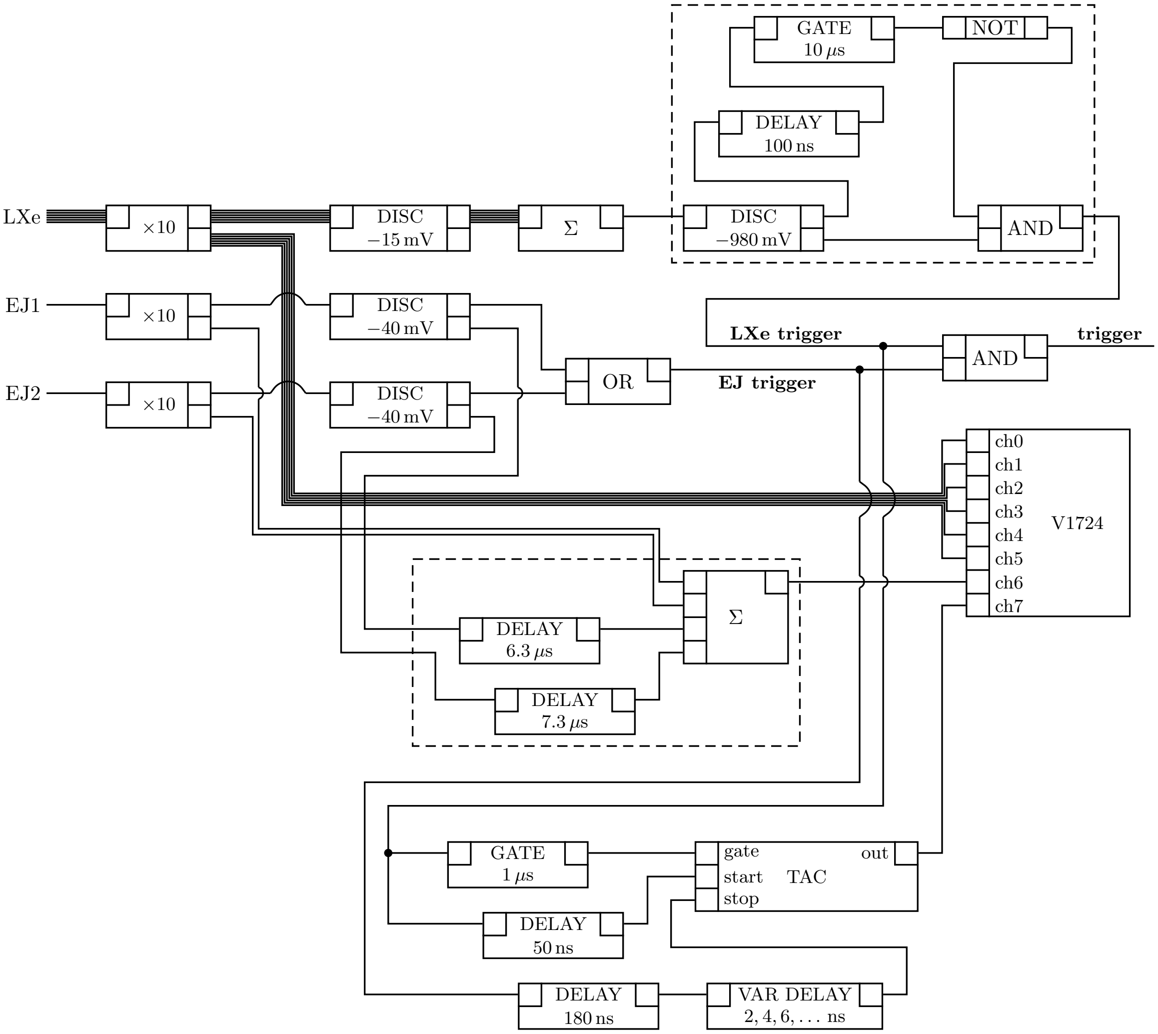

Figure 5.14: DAQ and trigger diagram for the $\mathcal{L}_{\text{eff}}$ measurement.

to approximately 0.5 pe. The logic signals of the six discriminator outputs are summed in a CAEN N625 linear fan-in. The output of the fan-in is discriminated at a level of -980 mV, lower than the -700 to -900 mV level of a true NIM logic signal, to obtain a twofold PMT coincidence condition. A copy of the twofold PMT coincidence logic signal is then delayed slightly and used to start a 10 μs gate. The delay is long enough so that the gate starts after the original twofold PMT coincidence logic signal. The gate logic signal is negated and combined into an AND gate with the second copy of the twofold PMT coincidence logic signal. This subcircuit serves as a holdoff circuit that prevents re-triggering on the tail of the LXe scintillation signal. The output of the holdoff circuit constitutes the LXe trigger.

The signals from the two EJ301 PMTs are also fed into the amplifier. The first amplified copy is digitized by the flash ADC unit and the second copy is discriminated at a level of -40 mV. Valid events where a neutron scatters in the LXe detector and subsequently interacts in one of the EJ301 neutron detectors do not have signals in both EJ301 PMTs, and if an event were to have a signal in both EJ301 detectors it should be discarded. We can thus multiplex both EJ301 PMT channels in a single digitizer channel as long as we keep the information required to determine which of the two EJ301 PMT channels had a signal. This is done by delaying the discriminator outputs of the two EJ301 PMT channels by different amounts, 6.3 μs and 7.3 μs, and adding them to the analog signal to be digitized. The delays are large enough so that the logic signals do not overlap with each other or with the EJ301 scintillation signal. A copy of the discriminator outputs is combined into and OR gate to trigger when one of the two EJ301 neutron detectors has a signal, and forms the EJ301 trigger.

The neutron time-of-flight (TOF) is measured with an Ortec 566 time to amplitude converter (TAC). A first copy of the LXe trigger generates a 1 μs logic gate signal to operate the TAC in gated mode. A slightly delayed second copy of the LXe trigger is used as the "start" signal and a delayed copy of the EJ301 trigger as the "stop" signal. An Ortec 425A variable delay generator is introduced before the TAC on the EJ301 "stop" line to calibrate the TOF measurement. The TAC calibration is described in Sec. 5.8. The full scale time measurement range is chosen as 2 μs to allow a wide range of TOF values and to keep the TAC signal smaller than the FADC input range of 2.25 V. The TAC has a time resolution (FWHM) better than 0.01% of the full scale plus 5 ps, corresponding to a TAC time resolution of ~0.2 ns in our case. The TAC output signal is also digitized by the flash

ADC unit and the TOF is computed at a later stage by the event processing program.

Finally, for neutron scattering measurements, the trigger is taken as a coincidence within a 200 ns window of the LXe trigger and the EJ301 trigger. For ^{57}Co measurements, obviously the trigger signal used is the LXe trigger.

The digitized window chosen has a length of 1024 samples, corresponding to $10.2\,\mu$s, with 950 post-trigger samples ($9.5\,\mu$s). This is to ensure the proper digitization of the LXe signal, the EJ301 signal with its "digital" code, and the TAC output signal. Fig. 5.15 shows the digitized traces for a typical event. Event waveforms are transferred from the flash ADC unit to a computer via a VME interface. The maximum achievable trigger rate is limited by the speed at which events can be written to disk and is approximately 5 kHz.

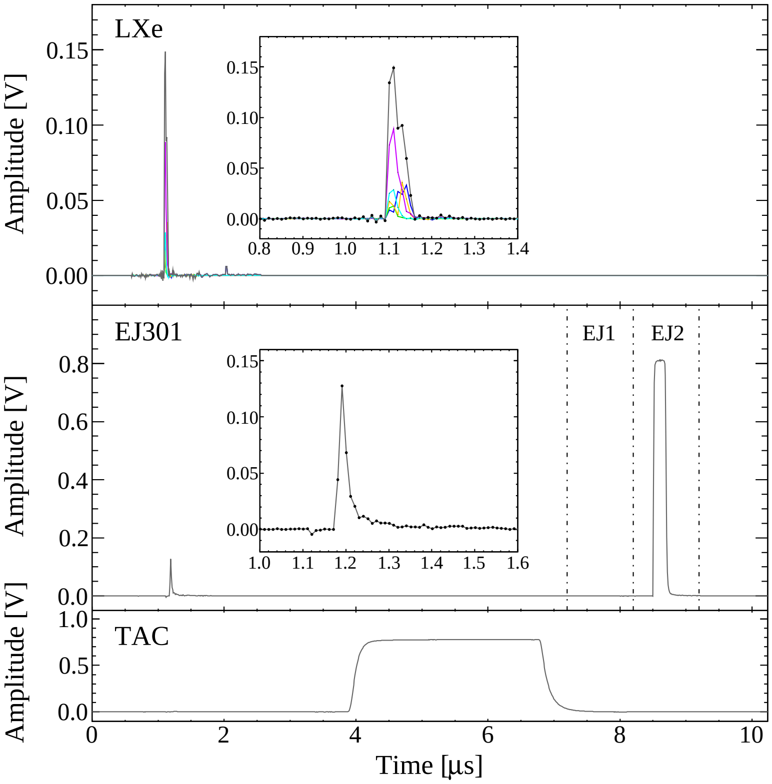

Figure 5.15: Recorded waveforms for a typical neutron scattering event. The total LXe scintillation signal (black) and the individual PMT signals (color) are shown in the top panel. The EJ301 neutron detector signal and its "digital" identification code, detector EJ2 in this case, are shown in the middle panel. The bottom panel shows the TAC signal.

5.4.2 Measurement of the Trigger Efficiency

We are interested to measure $\mathcal{L}_{\rm eff}$ down to energies as low as possible. Inevitably, we will reach a region where elastic neutron scatters in the LXe deposit a very small amount of energy and where the probability to trigger on such a small energy deposit is not unity. The roll-off of the trigger probability, or trigger efficiency, at low energies can contribute significantly (Manalaysay, 2010) to the systematic uncertainty on $\mathcal{L}_{\rm eff}$, if it is not understood properly.

The efficiency of the trigger setup described in Sec. 5.4 was measured, as directly as possible, in an attempt to improve over previous measurements of $\mathcal{L}_{\rm eff}$ where the trigger efficiency was based solely on simulations.

The setup used to measure the trigger efficiency is shown in Fig. 5.16. A ^{22}Na source, a β^+ emitter, was placed between the LXe detector and a Bicron 3M3/3 sodium iodide NaI(Tl) detector. The source was fixed on the LXe detector cryostat outer wall. Over this distance, the back-to-back pair of 511 keV γ rays from the β^+ annihilation then interact effectively at the same time in the LXe and NaI(Tl) detectors. The NaI(Tl) detector was positioned such that the solid angle it subtended at the source was larger than the one subtended by the active volume of the LXe detector. This ensured that 511 keV γ rays could interact in the whole active volume of the LXe detector if the corresponding γ ray interacted in the NaI(Tl) detector. For this measurement, the data acquisition system was triggered using the discriminated signal of the NaI(Tl) PMT. In addition to the signals of the six LXe PMTs, the trigger logic signal of the normal LXe trigger was digitized with the flash ADC.

To infer the trigger efficiency, the number of photoelectrons of the LXe signal is computed for each event and whether or not a LXe trigger signal was present. The trigger efficiency for a signal with a given number of measured photoelectrons is then simply given by the fraction of events accompanied by a LXe trigger signal. Fig. 5.17 shows the result of the measurement, along with the expected trigger efficiency from simulation, as described in Sec. 5.4.3. The errors bars are statistical only.

The statistical uncertainty in the trigger efficiency measurement is very small because a large number of low energy events are present in the spectrum. The source of these low energy events is not entirely clear but most likely they are attributable to energy

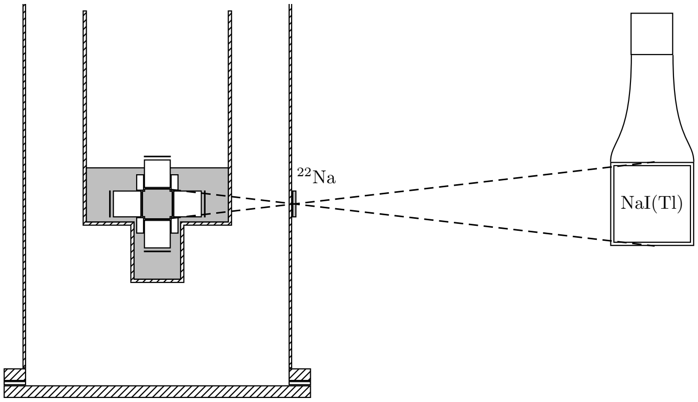

Figure 5.16: Setup used for the measurement of the trigger efficiency of the twofold coincidence LXe trigger. A ^{22}Na source is place between the LXe detector and a NaI(Tl) detector such that one of a pair of 511 keV back-to-back γ rays interacting in the NaI(Tl) detector is likely to be coincident with an interaction of the associated γ ray in the LXe detector.

deposits outside of the active LXe volume where a small number of scintillation photons leak inside the active volume. The position dependence of the light collection efficiency was estimated in Sec. 5.2.4 via a light propagation Monte Carlo simulation and the average probability for a photon outside the active LXe volume to reach a PMT photocathode was estimated at 1×10^{-4}. We expect that, alone, the statistical uncertainty would not have any substantial systematic effect on $\mathcal{L}_{\text{eff}}$, hence the main effect would come from any systematic uncertainty in the measured trigger efficiency. Some possible systematic effects are discussed in Sec. 5.4.3.

The trigger efficiency could also be measured by irradiating the detector with any source producing low energy events and randomly triggering the data acquisition system, still digitizing the normal LXe trigger signal, and applying the same analysis. Using the NaI(Tl) and the ^{22}Na has the advantage of increasing substantially the probability that a signal is indeed present in the LXe detector. Randomly triggering the detector would only result in useful events when a chance coincidence occurs between the random trigger and the γ interaction in the LXe.

5.4.3 Simulation of the Expected Trigger Efficiency

The expected efficiency of the twofold coincidence LXe trigger has also been computed via a detailed Monte Carlo simulation. The simulation starts by randomly choosing the total number of photons produced, N_{ph}, anywhere between 0 and $N_{\text{ph,max}} = 100$, and a random

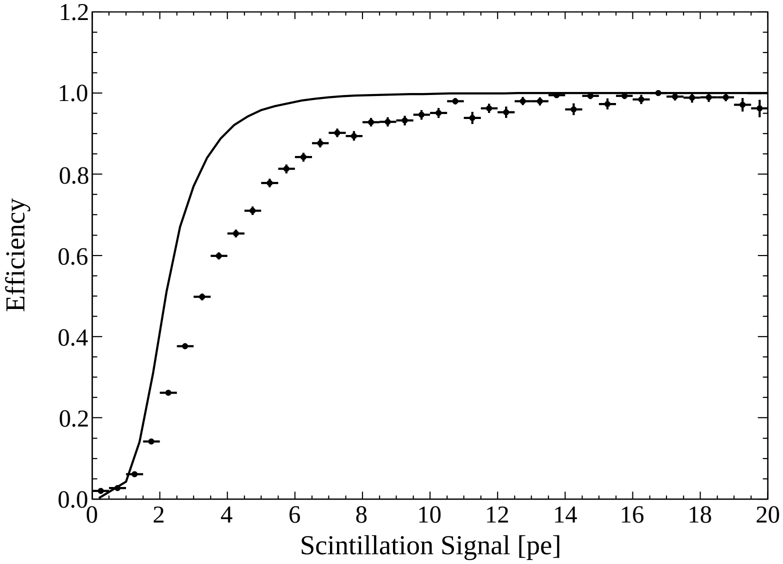

Figure 5.17: Measured (points) and simulated (solid curve) efficiency of the twofold coincidence LXe trigger. Error bars on the measurement are statistical only. Figure from Plante *et al.* (2011).

position $\vec{r}_0$ within the active volume of the LXe detector. For each PMT i, the number of photoelectrons $N_{\mathrm{pe},i}$ reaching the first dynode is calculated through binomial variates with probability $p_i = \alpha_i(\vec{r}) \cdot \zeta \cdot \eta_i$, where $\alpha_i(\vec{r})$ is the PMT light collection efficiency at position $\vec{r}$, ζ is its first dynode collection efficiency, and η_i is its quantum efficiency. The measured number of photoelectrons at PMT i, $\bar{N}_{\mathrm{pe},i}$ is then computed from normal variates with a mean of 1 pe and a standard deviation of $R_{\mathrm{spe},i}$ pe, where $R_{\mathrm{spe},i}$ is the single photoelectron resolution (σ/μ) of PMT i, as inferred from the PMT calibration (see Sec. 5.5). Next, the PMT signal height (after the ×10 amplifier), h_i, is computed by assuming that single photoelectron current pulses at the output of the PMT can be modelled as

$$\frac{\bar{N}_{\mathrm{pe},i} G_i}{\sqrt{2\pi}\sigma_w} \exp\left(-\tfrac{t^2}{2\sigma_w^2}\right), \tag{5.17}$$

where $\sigma_w = 1.9\,\mathrm{ns}$ is the observed width of a single photoelectron pulse[2], and G_i is the gain of PMT i, also inferred from the PMT calibration. Finally, the coincidence level, the number of PMT signal heights h_i that go above threshold, and the total number of measured photoelectrons $\bar{N}_{\mathrm{pe}}$ are computed. The expected trigger efficiency is obtained by calculating

---

[2] This is the width as observed directly from the PMT base on a high-bandwidth scope to prevent any attenuation from lower bandwidth components.

the fraction of simulated events for which the coincidence level is higher or equal to 2 as a function of the number of measured photoelectrons. The result of the simulation with the parameter values listed in Tab. 5.2 is shown in Fig. 5.17 (solid curve).

Table 5.2: Parameter values used for the trigger efficiency simulation. The PMT QE values were measured at room temperature by Hamamatsu. The PMT gains and single photoelectron resolutions were measured at −94°C.

Parameter	PMT1	PMT2	PMT3	PMT4	PMT5	PMT6
Quantum efficiency, η_i	0.328	0.317	0.324	0.329	0.317	0.323
Collection efficiency, ζ	0.75					
Gain, G_i, $\times 10^6$	0.93	2.33	2.50	2.13	1.97	2.02
Resolution (σ/μ), $R_{\mathrm{spe},i}$	103%	55%	57%	61%	56%	106%
Discriminator threshold	$-15\,\mathrm{mV}$					

The PMT single photoelectron resolution $R_{\mathrm{spe},i}$, the position dependence of the light collection efficiency $\alpha_i(\vec{r})$, and variations among PMT gains G_i and PMT QEs η_i are responsible for smearing the trigger efficiency function from the ideal case. If $R_{\mathrm{spe},i} \approx 0$ and each PMT had the same probability of detecting a photon the trigger efficiency would simply be given by combinatorics.

The discrepancy between the expected trigger efficiency and the measured efficiency is substantial. The discrepancy can be due to incorrect assumptions in the simulation or a systematic bias in the measurement. However, because of the direct way in which the trigger efficiency was inferred, the measurement can only be systematically biased to lower trigger efficiency values, not higher ones.

Two possible effects that could systematically lower the trigger efficiency measured were investigated: interactions of 511 keV γ rays in PMT dynode structures and large deviations from a uniform photon spectrum inside the active volume. Obviously, if γ rays from the ^{22}Na source can interact in the PMT dynode structure and produce a signal, then these events would rarely (if ever) produce twofold PMT coincidences and thus bias the measurement. However, no rate increase could be observed when irradiating PMTs at room temperature with the ^{22}Na source so this effect was discarded as a possible bias.

A more subtle effect is related to the effect of the actual photon spectrum to which the PMT are exposed during the trigger efficiency measurement. We are interested in the probability that a signal with a certain number of *measured* photoelectrons generates a trigger, since this is how we can correct a measured scintillation spectrum for a trigger efficiency roll-off. However, a variety of scintillation signals can give rise to the same number of measured photoelectrons, upward fluctuations from signals with fewer photons or downwards fluctuations from signals with a larger number of photons. Since it will always be more likely that a scintillation signal with more photons generates a twofold coincidence trigger then this means that the photon spectrum has an effect on the inferred trigger efficiency. It is illustrative to take the extreme case of a light source that produces single photons. By definition the source will never generate any twofold coincident triggers. However, due to the finite single photoelectron resolution a fraction of events will register 2 or 3 measured photoelectrons and thus attribute a zero triggering probability to those values as well. Theoretically this has an effect on the trigger efficiency inferred from the measurement. However, bias from this effect is always more pronounced at lower values of measured photoelectrons while the observed discrepancy grows from one to three photoelectrons.

Failing to find a plausible systematic effect in the measurement, the discrepancy between the simulated and measured efficiency is attributed to the limited accuracy in modeling hardware components of the trigger. Consequently, the measured trigger efficiency is used to extract $\mathcal{L}_{\text{eff}}$ (Sec. 5.12) from the neutron scattering measurements.

5.5 PMT Calibration

The LXe PMT gains are measured under single photoelectron conditions by pulsing the blue LED embedded in the PTFE mounting structure. Fig. 5.18 shows the results of a typical gain calibration. The light intensity is adjusted such that the probability of measuring a PMT signal with 1 or more photoelectrons within a $3\,\mu$s window following the LED pulse is 5%-10%, for each PMT. Under these conditions, assuming that the probability of detecting a photon is governed by Poisson statistics,

$$\sum_{k=1}^{\infty} \frac{\lambda^k e^{-\lambda}}{k!} = 0.10 \tag{5.18}$$

and one obtains $\lambda \approx 0.105$. From this we can conclude that the 2 or more photoelectron contribution to the single photoelectron distribution is

$$\left(\sum_{k=2}^{\infty} \frac{\lambda^k e^{-\lambda}}{k!} \right) \left(\sum_{k=1}^{\infty} \frac{\lambda^k e^{-\lambda}}{k!} \right)^{-1} = \frac{e^{-\lambda} - 1 - \lambda}{e^{-\lambda} - 1} \approx 0.05, \tag{5.19}$$

a negligible fraction.

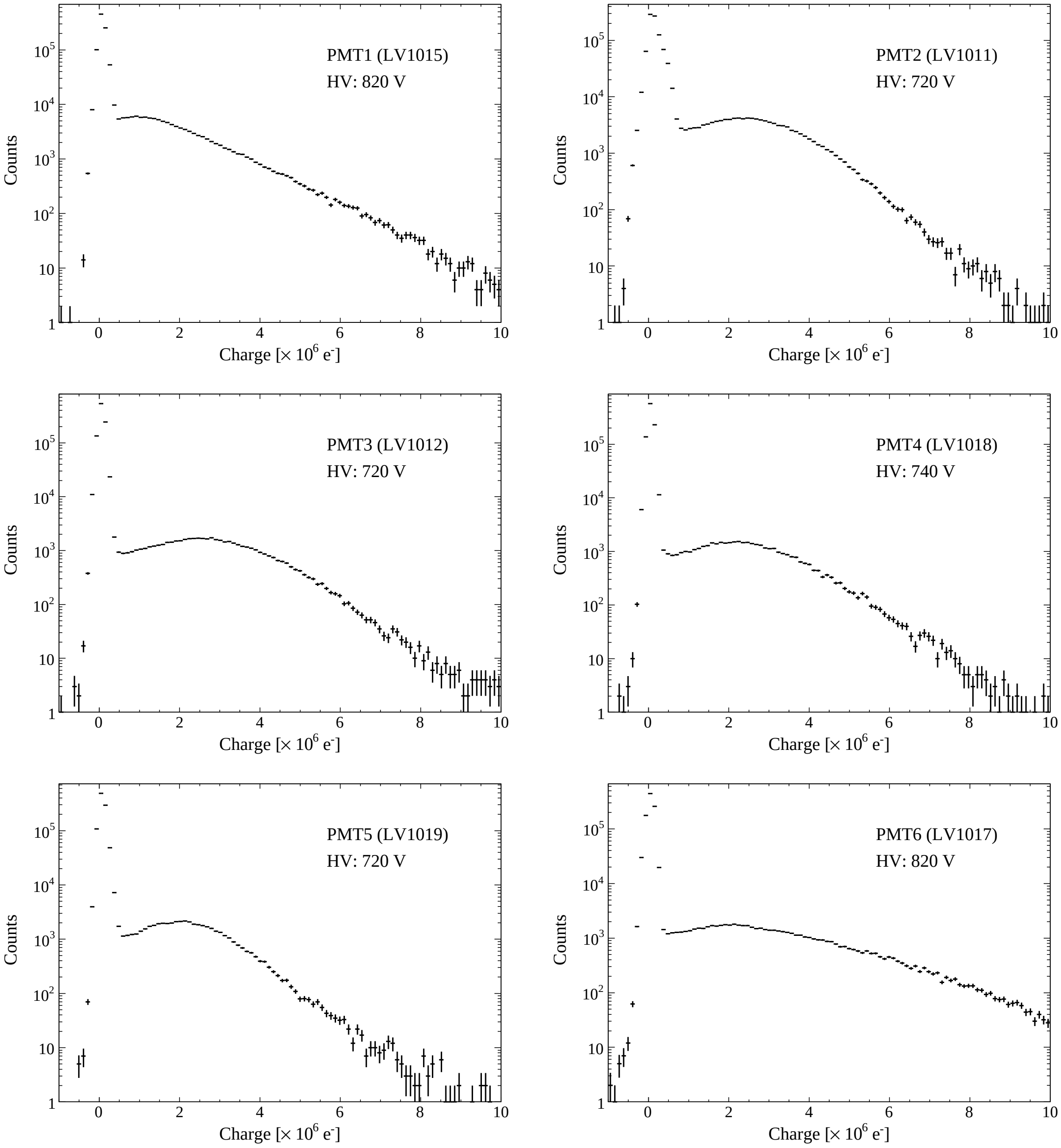

Figure 5.18: PMT single photoelectron spectra from an LED calibration dataset.

At the beginning of the experiment, the PMT gains were equalized to a mean value of 2.0×10^6 pe/e$^-$ by adjusting the individual PMT anode bias voltages. The power supply used allowed only ±20 V adjustments. PMTs 2-5 show the best performance. Fig. 5.19 shows the PMT gains versus applied high voltage and the operating conditions chosen. The PMT gains were monitored regularly throughout the neutron scattering measurements.

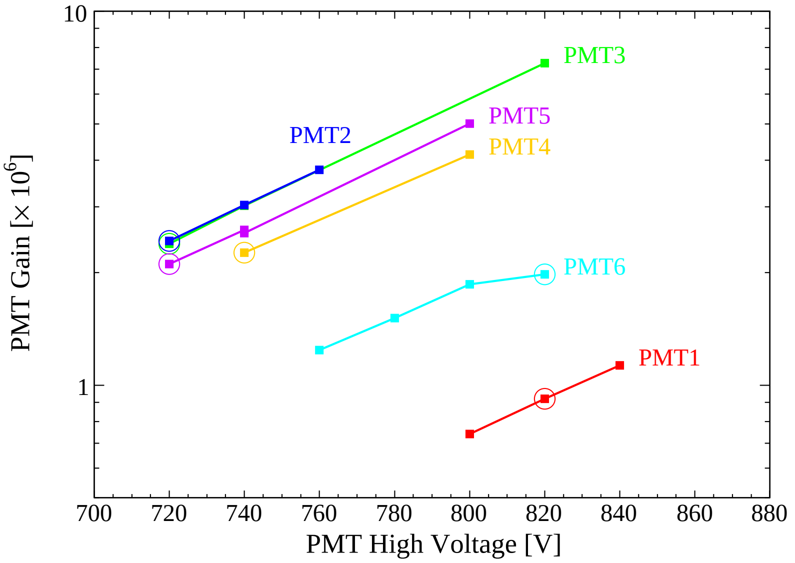

Figure 5.19: PMT gain versus applied high voltage for the six PMTs used in the detector. The point of operation (solid circle) chosen is shown for each PMT.

5.6 Light Yield

The electronic recoil energy scale is calibrated using 122 keV γ rays since $\mathcal{L}_{\mathrm{eff}}$ is defined as the scintillation light yield of nuclear recoils relative to the yield of γ rays of that energy (see Sec. 2.3.3). Calibrations with an external 100 μCi ^{57}Co source were taken regularly throughout the duration of the experiment. Fig. 5.20 shows the scintillation spectrum of a calibration with the ^{57}Co source. The scintillation light yield was measured to be $L_y = 24.14 \pm 0.09(\mathrm{stat}) \pm 0.44(\mathrm{sys})\,\mathrm{pe/keV_{ee}}$ with a resolution (σ/E) of 5%. The statistical uncertainty is the combination of the statistical uncertainties of the individual light yield calibrations while the systematic uncertainty comes from the variation throughout the calibrations.

Since the attenuation length of 122 keV γ rays in LXe is 3 mm (Berger *et al.*, 2010) the external ^{57}Co source mostly probes the light yield in the outer layers of the active volume. However, since the elastic scattering mean free path of 2.5 MeV neutrons in LXe is ~20 cm, the expected spatial distribution of nuclear recoils is uniform. Hence, the quantity of interest is the average light yield over the whole volume. Some precautions need to be taken when analyzing data from a ^{57}Co calibration to ensure that the light yield inferred is the volume averaged light yield. For example, if the ^{57}Co is placed such that most of the event rate is in the cavity between the side of a PMT and the PTFE mounting structure

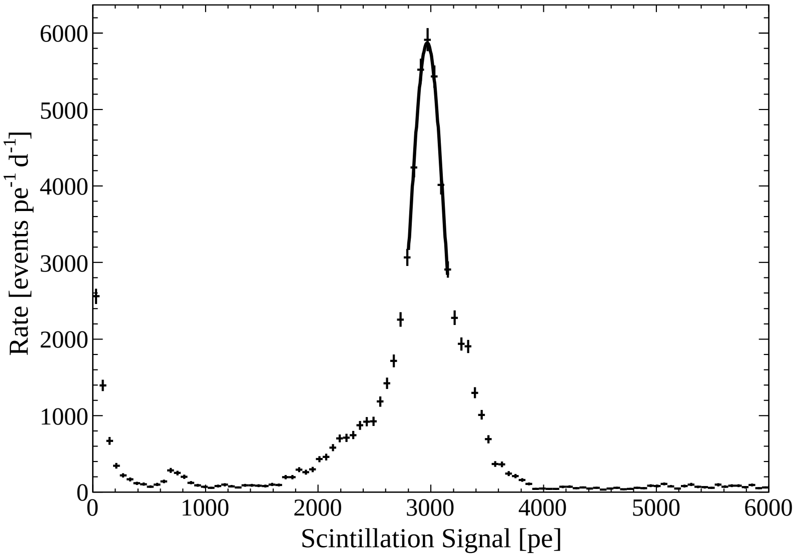

Figure 5.20: Scintillation light spectrum of the 100 μCi ^{57}Co source used to calibrate the LXe light yield, L_y. The peak at ~3000 pe is the 122 keV photoelectric absorption peak. Also visible is the Xe 30 keV characteristic X-ray at ~700 pe. This calibration gives a scintillation light yield of $L_y = 24.3\,\text{pe/keV}_{\text{ee}}$. Figure from Plante *et al.* (2011).

the light yield would be underestimated.

The spatial uniformity of the light detection efficiency has been investigated with the light propagation simulation described in Sec. 5.2.4. The relative light yield variation over the active volume is expected to be very small, due to the high photocathode coverage of the volume. The relative light yield variation over the active volume was calculated to be less than 2%, with a maximum variation of 5% near the edge. If the angular response of the PMTs is included in the simulation, the relative light yield variation over the volume increases to 3%, with a maximum variation of 7% near the edge.

This very high light yield, combined with the 90% trigger efficiency at 7 pe (Sec. 5.4.2), implies that energy spectra do not suffer from efficiency losses down to energies as low as 0.3 keV$_{\text{ee}}$, with the electronic recoil energy scale calibrated at 122 keV.

5.7 Liquid Scintillator Calibration

The response of EJ301 liquid scintillator to electronic recoils and proton recoils, from γ and neutron interactions, respectively, allows a very efficient discrimination between the two type of recoils. The characteristic scintillation decay time for proton recoils is much longer than for electron recoils. The decay times of the three main components of EJ301 are 3.2 ns, 32 ns, and 270 ns (Kuchnir and Lynch, 1968). The slow component is due to delayed fluorescence from excited molecules in the singlet state created by bimolecular interactions of longer-lived triplet states. The bimolecular reaction yield depends on the square of the triplet states density and consequently particles with a higher rate of energy loss, such as proton recoils, induce longer scintillation pulse (Knoll, 2000).

The PSD parameter is defined as the fraction of the total EJ301 scintillation signal contained within the tail of the pulse. The tail of the pulse is defined as a region with a lower boundary at 30 ns after the pulse peak and an upper boundary at the time where the pulse returns to 1% of the peak amplitude. A PSD cut is therefore defined to select neutron interactions in EJ301 with high efficiency. However, since this cut is based on the scintillation signal, the discrimination power degrades with decreasing energy and it is preferable to also apply an energy threshold cut on the EJ301 scintillation signal. This reduces the background from neutrons that scattered in other materials, in addition to the scatter in the LXe detector, since the neutron energy was reduced and hence cannot deposit the maximum energy expected. Fig. 5.21 shows the events selected by the combination of the PSD cut and the EJ301 energy threshold cut for one of the two EJ301 neutron detectors.

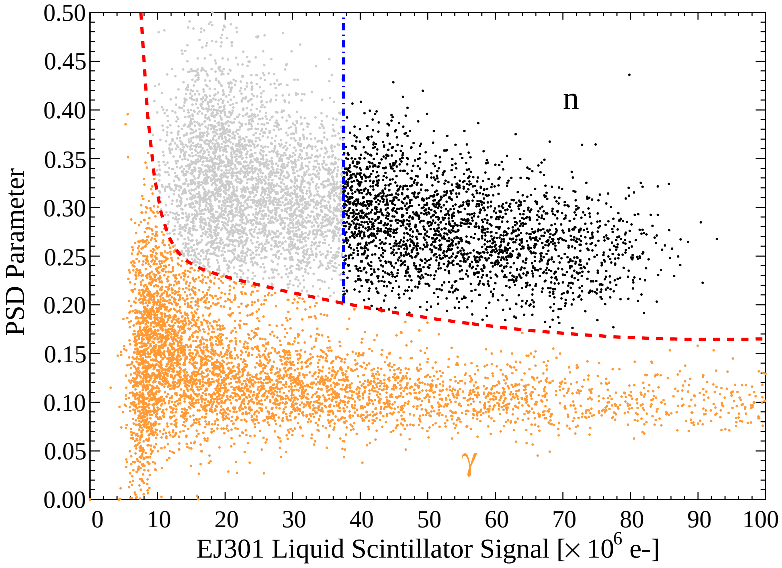

Figure 5.21: Neutron interactions (gray/black) and γ interactions (orange) for one of the two EJ301 neutron detectors. The neutron events selected by the PSD cut (red dashed line) and the EJ301 energy threshold cut (blue dash-dotted line) are shown in black. Figure from Plante *et al.* (2011).

5.8 Time of Flight Calibration

The TOF parameter is an important data selection parameter for tagged neutron scattering $\mathcal{L}_{\text{eff}}$ measurements. Since the neutron energy is known, and thus its speed, the travel time between the LXe detector and the EJ301 neutron detectors can substantially reduce backgrounds by selecting the proper time window. In Sec. 5.8.1 we describe the calibration of the TAC module to compute the TOF and in Sec. 5.8.2 we discuss a correction applied to the TOF value to account for a systematic bias of the TOF value with the scintillation signal size.

5.8.1 TAC Calibration

The TOF calibration was performed with the ^{22}Na source placed between the LXe detector and the EJ301 neutron detectors. The two 511 keV γ rays emitted interact in both LXe and EJ301 detectors at the same time and give a TOF $= 0$ calibration point. The time delay between the LXe and EJ301 triggers was varied with the delay generator over a range of 32 ns to obtain the TOF calibration of the TAC pulse. Fig. 5.22 shows a calibration without additional delay. The TAC pulse height is non-zero even without additional delay due to the cable lengths of the LXe and EJ301 trigger signal paths. The peak in the spectrum corresponds to coincident γ-ray interactions in the LXe detector and a neutron detector where the γ ray was fully absorbed in the LXe. The tail on the left of the peak is caused by γ rays that Compton scatter in the LXe detector. The smaller TAC pulse heights are due to a systematic shift of the LXe trigger signal to later times when the scintillation signal size decreases. This effect and its correction are discussed in Sec. 5.8.2.

The TOF calibration is obtained for each EJ301 detector from the set of TAC pulse height spectra taken with different delays. Fig. 5.23 shows the result of the calibration for the two EJ301 neutron detectors. For a LXe detector and EJ301 neutron detector distance of 1 m, the typical neutron TOF is 45 ns.

5.8.2 Time of Flight Correction

A subtle effect can be observed in the TOF calibration data. Since the LXe trigger comes from the coincidence of two LXe scintillation photons, the LXe scintillation light decay time systematically shifts the TOF measurement of scintillation signals with fewer photons to

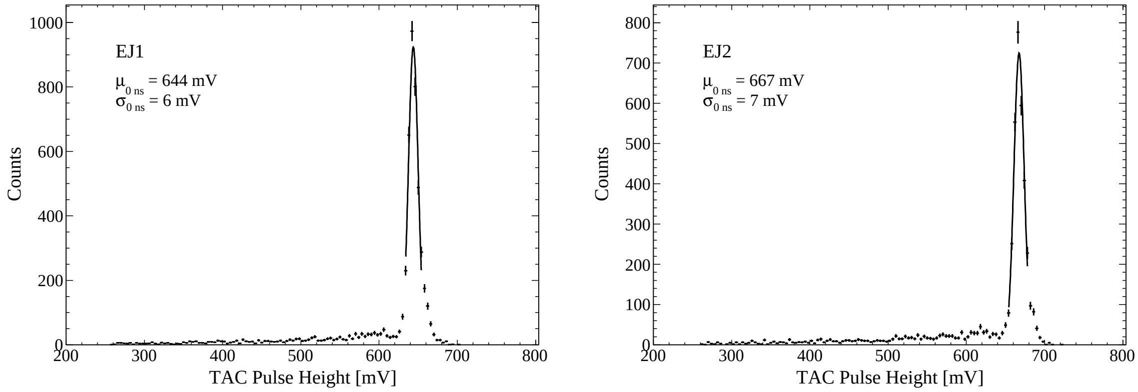

Figure 5.22: ^{22}Na TAC pulse height spectra for the time difference between the LXe signal and the two EJ301 neutron detector signals. The cable lengths of the LXe and EJ301 trigger signal paths in the DAQ yield TAC signals of 644 and 647 mV for the first and second EJ301 neutron detectors, respectively.

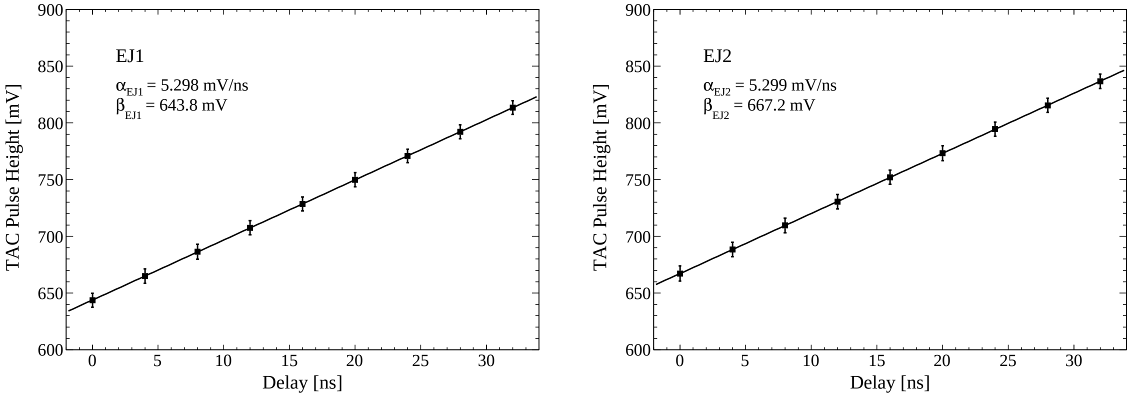

Figure 5.23: TOF calibration of the TAC pulse for the two EJ301 neutron detectors. The standard deviation in the TAC pulse heights is indicated as an error bar on each measurement.

lower TOF values. The effect is likely more pronounced for γ rays interacting in LXe due to the slower recombination time for electron recoils (Hitachi, 2005; Hitachi *et al.*, 1983). Additionally, since the TAC calibration has been performed with a ^{22}Na γ source, the TOF $= 0$ reference point is really the time difference between the twofold coincidence LXe trigger and the EJ301 trigger for scintillation signals of 511 keV$_{\mathrm{ee}}$ in each detector.

Fig. 5.24 shows the distribution of uncorrected TOF values obtained with the TAC calibration inferred in Sec. 5.8.1 as a function of the scintillation signal in the LXe detector. The mean of each slice of constant scintillation signal is also shown. For the typical scintillation signal of a fully absorbed 511 keV γ ray (about 9×10^4 pe) the zero of the TOF calibration is accurate. However, it is clear that as the scintillation signal decrease the mean TOF values are systematically biased to lower values.

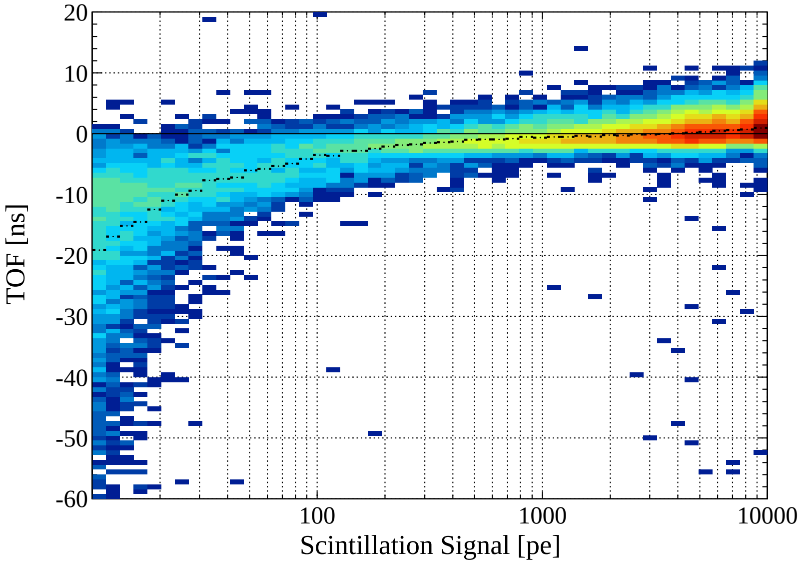

Figure 5.24: Uncorrected TOF values as a function of the scintillation signal in the LXe detector for the ^{22}Na TAC pulse height calibration data.

For the neutron scattering measurements, the TOF value is corrected for this effect in the event processing software. The correction was determined by requiring that the position of the neutron peak in the TOF spectra correspond to the position inferred from the simulation of the neutron scattering measurements (see Sec. 5.11). This correction, however, does not eliminate the spread in TOF values also caused by this effect. To eliminate any possible bias where recoils of lower energies would not be selected, we chose TOF cuts (see Sec. 5.10) that contain the full neutron TOF peak for each scattering angle measurement, even if doing so results in a higher contamination of the recoil spectrum by neutrons that scattered in other materials (see Sec. 5.11).

5.9 Data Processing and Event Selection

Events consist of the six LXe PMT waveforms, the waveform of the triggered EJ301 neutron detector, as well as the waveform of the TAC output (see Fig. 5.15). The processing software used is the same as the one developed for XENON100 data, as described in Sec. 3.4.3, with some additions to compute parameters for the EJ301 detectors and the TAC module. For each event, the processing software searches the LXe PMT waveforms for scintillation signals and records several parameters for each pulse found: position, area, height, etc. The same procedure is applied to the EJ301 neutron detector waveform with the addition of the PSD parameter (Sec. 5.7). Finally, the TOF is computed from the height of the TAC output and the TOF calibration values, and corrected. Three selection cuts are applied to the data: a PSD cut to select neutron interactions in the EJ301 neutron detectors, a lower energy threshold cut on the EJ301 scintillation signal (Sec. 5.21), and a TOF cut. The TOF cuts used for each scattering angle measured are listed in Tab. 5.3.

Table 5.3: TOF cut ranges used to select neutrons that travelled between the LXe detector and the EJ301 neutron detector and TOF windows used to estimate the energy spectrum of recoils from accidental coincidences of the LXe trigger and the EJ301 trigger, for each scattering angle measurement.

θ	TOF Cut Range (ns)	Accidentals Windows (ns)
23°	$[20, 65]$	$[-70, -20]$, $[80, 150]$
26.5°	$[25, 62]$	$[-70, -20]$, $[80, 150]$
30°	$[28, 62]$	$[-70, -20]$, $[80, 150]$
34.5°	$[20, 55]$	$[-70, -20]$, $[80, 150]$
39.5°	$[17, 45]$	$[-70, -20]$, $[80, 150]$
45°	$[17, 40]$	$[-70, -20]$, $[80, 150]$
53°	$[37, 60]$	$[-70, -20]$, $[100, 150]$
120°	$[10, 27]$	$[50, 150]$

5.10 Measured Nuclear Recoil Distributions

Neutron scattering data were acquired at eight different angles: 23°, 26.5°, 30°, 34.5°, 39.5°, 45°, 53°, and 120°, corresponding respectively to recoil energies E_{nr} of 3.0 ± 0.6, 3.9 ± 0.7,

5.0 ± 0.8, 6.5 ± 1.0, 8.4 ± 1.3, 10.7 ± 1.6, 14.8 ± 1.3, and 55.2 ± 8.8 keV. The experimental setup for the 3 keV measurement is shown in Fig. 5.25. The uncertainty in nuclear recoil energies, dominated by the angular acceptance of the detectors, is extracted from the results of the GEANT4 Monte Carlo simulation described in Sec. 5.11.

Figure 5.25: Experimental setup for the $\mathcal{L}_{\text{eff}}$ measurement at 3 keV (23°). For this angle both EJ301 neutron detectors are in the horizontal plane of the neutron generator and the LXe detector.

For most angles, the first EJ301 neutron detector was placed in the horizontal plane of the neutron generator and the LXe detector, while the second was placed at the same distance to the LXe detector but higher above the laboratory floor, with an azimuthal angle of about 45°. The alignment of the LXe detector and the neutron generator was performed with an auto-levelling laser mounted on a tripod. The horizontal line and the vertical line projected by the laser were used to set the height of the neutron generator target to the center of the LXe detector and to mark the position of both on the laboratory floor. The laser was also used to align the two EJ301 neutron detectors with respect to the LXe detector. For each angle, the distance between the LXe detector and the two EJ301 neutron detectors was chosen to produce a recoil energy spectrum with a spread due to the angular acceptance of the detectors of 10% to 20%. The desired EJ301 neutron detector positions were marked on the floor using 1.5 m aluminium rules, while their height was set with the help of the laser and a vertical rule. The EJ301 neutron detectors were supported at the desired positions around the LXe detector by their own laboratory stands. The horizontal distance between the neutron generator and the LXe detector was fixed at 40 cm. The distance from the LXe detector to the EJ301 liquid scintillators varied from 100 cm, for the scattering angles corresponding to low-energy recoils, to 40 cm, for the scattering angles corresponding to higher energies. The positions of the EJ301 neutron detectors for each scattering angle are listed in Tab. 5.4. The positioning accuracy of the EJ301 neutron detectors is estimated to be better than 5 mm.

Table 5.4: EJ301 detector positions for each scattering angle measurement. The procedure used to position the detectors is described in the text.

θ	E_{nr} (keV)	EJ1 Position[a] (cm)			EJ2 Position[a] (cm)		
		x	y	z	x	y	z
23°	3.0 ± 0.6	−39.1	−92.1	0.0	+39.1	−92.1	0.0
26.5°	3.9 ± 0.7	−44.6	−89.5	0.0	+31.5	−89.5	+31.5
30°	5.0 ± 0.8	−50.0	−86.6	0.0	+35.4	−86.6	+35.4
34.5°	6.5 ± 1.0	−32.0	−65.9	+32.0	+32.0	−65.9	+32.0
39.5°	8.4 ± 1.3	−30.9	−54.0	+32.0	+30.9	−54.0	+32.0
45°	10.7 ± 1.6	−41.7	−41.7	0.0	+20.9	−41.7	+36.1
53°	14.8 ± 1.3	−79.9	−60.2	0.0	+69.2	−60.2	+40.0
120°	55.2 ± 8.8	−34.6	+20.0	0.0	+34.6	+20.0	0.0

[a] The origin is the center of the LXe detector and the neutron generator is at $(0, 40, 0)$.

As mentioned earlier, the neutron generator was operated at deuteron energies of 60, 65, 75, or 80 keV and with deuterium beam currents ranging from 60 to 100 μA. A summary of the operating conditions for each scattering angle is listed in Tab. 5.5. In ideal circumstances the deuteron energy should be kept constant throughout and as high as possible since the neutron yield increases almost exponentially with deuteron energy. At high voltages – 80 or 90 kV – our holding apparatus has proven to be less reliable than at lower voltages. In two occasions, a large electronic leakage current developed and led to a measured current that exceeded the trip setting of the power supply. As the deuterium beam erodes the target some sharp points can appear near which the electric field can grow to large values. The proximity of the ground surface to the generator (see Fig. 5.8) and the choice of running small radii low voltage wires next the ground surface also probably accentuated the problem. A better design would have an electrical feedthrough at the bottom for the low voltage wires and a larger diameter stainless steel tube casing. However, since the LXe detector was placed at the $\varphi = \frac{\pi}{2}$ neutron emission angle (Fig. 5.2), the operation at different deuteron energies had a very small impact on the incident neutron energy (Fig. 5.12 (right)). The variation in the neutron yield due to the different operating conditions is taken into account in the analysis (Sec. 5.12).

Table 5.5: Neutron generator high voltage and beam current used during each scattering angle measurement. The dates of operation and the measurement live time is also indicated for each scattering angle.

θ	High Voltage (kV)	Beam Current (uA)	Dates	Live time (s)
23°	-60	102	10/29-11/23	313202
26.5°	-80	80	10/05, 10/06	43732
	-75	61	10/10	19267
	-65	60	10/08	11851
30°	-80	81	10/01-10/04	50620
34.5°	-60	100	12/01-12/06	107818
39.5°	-60	103	12/09-12/14	96051
45°	-80	69	09/30	25345
53°	-75	65	10/21-10/22	34499
	-65	100	10/23-10/26	53309
	-60	95	10/27	26554
120°	-60	97	12/16-12/17	43581

Figures 5.26, 5.27, and 5.28 show the measured recoil energy and TOF spectra for all scattering angles. The spectra are scaled by the live time of the measurements. For the nuclear recoil energy spectra, black histograms are spectra after the PSD and TOF cuts applied, and after subtraction of the neutron accidental background (described below), with the neutron accidental background spectra shown as green histograms. A vertical red dashed line indicates the position of the 90% measured trigger efficiency. For the TOF spectra, black histograms are neutron TOF spectra while orange histograms are spectra where the PSD cut is chosen to select γ-ray interactions in the EJ301 neutron detectors. The TOF cut range for each recoil energy spectrum is shown as vertical dash-dotted lines and is also listed in Tab. 5.3.

Nuclear recoil spectra have two components, a peak and an exponential background. The peak is due to neutrons that elastically scatter in the LXe and then interact in one of the EJ301 neutron detectors. The width of the peak comes from the finite size of the

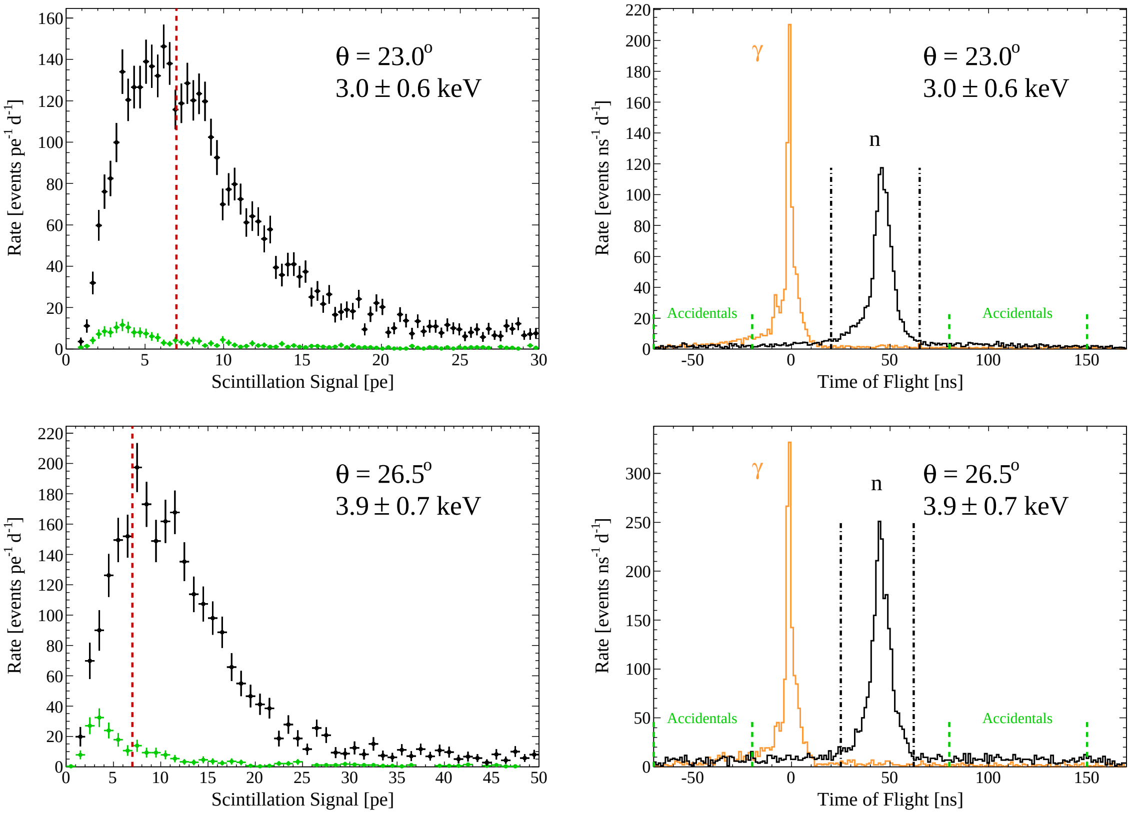

Figure 5.26: (left) Recoil energy spectra for the 23° and 26.5° scattering angles, with PSD and EJ301 energy threshold cuts applied, for the TOF window indicated in the TOF spectrum by the vertical dash-dotted lines (right). The black histogram is the recoil energy spectrum, after subtraction of the accidental spectrum shown as a green histogram. As a reference, the 90% measured trigger efficiency is indicated by the vertical red dashed line. The accidental spectrum expectation is obtained from the TOF windows before and after the main TOF peak, as indicated in the figure by the vertical green dashed lines. The accidental spectrum in the window before the peak is in agreement with the one after the peak. The orange histogram is the TOF spectrum where the PSD cut is chosen to select γ-ray interactions in the EJ301 neutron detectors. Figure from Plante *et al.* (2011).

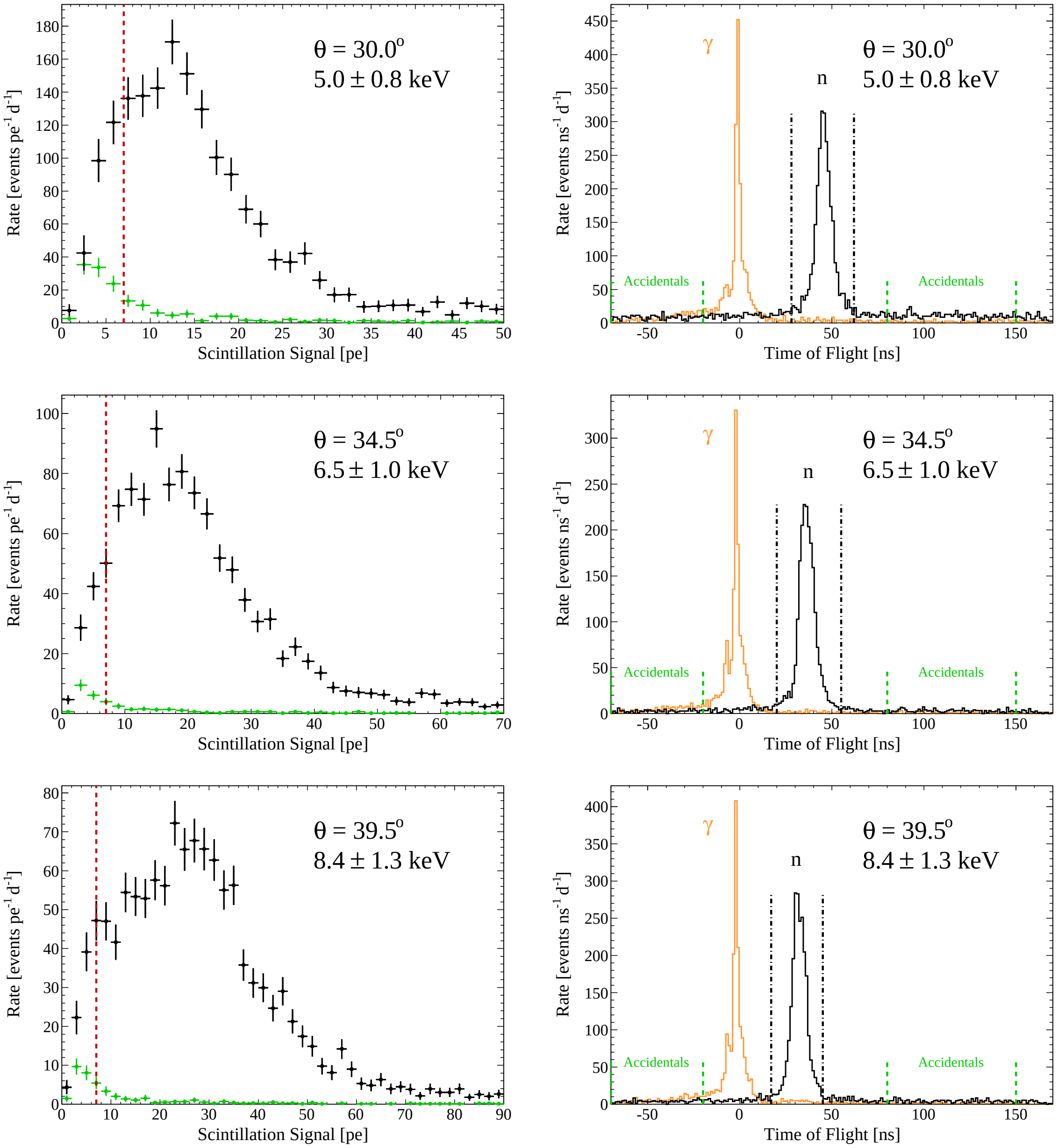

Figure 5.27: (left) Recoil energy spectra for the 30°, 34.5°, and 39.5° scattering angles, with PSD and EJ301 energy threshold cuts applied, for the TOF window indicated in the TOF spectrum by the vertical dash-dotted lines (right). Colors as in Fig. 5.26. Figure from Plante *et al.* (2011).

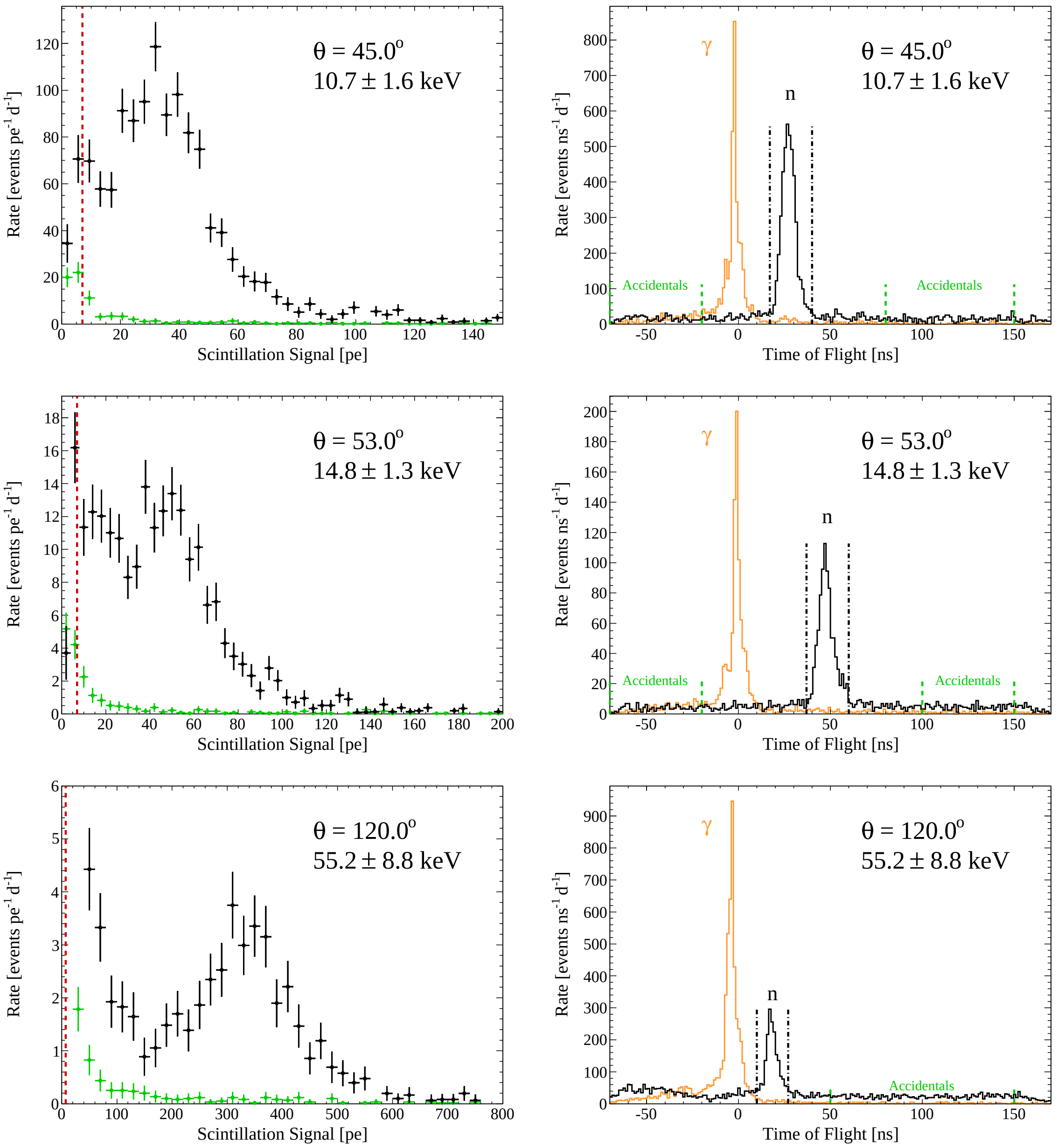

Figure 5.28: (left) Recoil energy spectra for the 45°, 53° and 120° scattering angles, with PSD and EJ301 energy threshold cuts applied, for the TOF window indicated in the TOF spectrum by the vertical dash-dotted lines (right). Colors as in Fig. 5.26. Figure from Plante *et al.* (2011).

detectors and the range of scattering angles allowed. The spread in the measured response of the LXe detector also depends on the intrinsic energy resolution of LXe, on the PMT photon detection statistics, and on variations in the PMT amplification. The exponential background is due to neutrons that scatter in other materials before or after the interaction in the LXe, and hence with a random scattering angle in the LXe detector, or at least a scattering angle very different from the angle at which the EJ301 detector was placed. In Sec. 5.11 the different components of the nuclear recoil energy spectra are examined using the results of the GEANT4 Monte Carlo simulation of the neutron scattering measurements.

All measurements show two very clear peaks in the TOF spectrum. The peak at TOF = 0 corresponds to γ rays that Compton scatter in the LXe detector before interacting in the EJ301 neutron detectors, while the peak at later TOF values corresponds to neutrons. For the lower recoil energies the effect discussed in Sec. 5.8.2, which spreads the TOF distribution to lower values, is noticeable in Figs. 5.26 and 5.27. A smaller peak, about 5 to 10 ns earlier than the γ TOF peak, is also present in the γ TOF spectra of most scattering angle measurements. This peak comes from low energy (<10 pe) events whose TOF measurement is shifted to lower values. The source of these events is likely γ-ray interactions in the LXe surrounding the active volume whose scintillation photons only have a small probability of reaching a PMT (see Sec. 5.2.4).

The neutron accidental background arises from accidental coincidences between the LXe trigger and the EJ301 trigger, specifically, from energy energy deposits in the LXe detector not correlated to neutron interactions in the EJ301 detector. Since these events pass the neutron PSD cut we know they correspond to neutron interactions in the EJ301. Also, since this background scales with the yield of the neutron generator, the interactions in the LXe detector are likely from neutrons as well or γ rays produced by inelastic scattering or capture in the surrounding materials. Such a background appears as a flat component in the TOF spectra since the two triggers are uncorrelated. The expectation for this background is thus taken far from the neutron TOF peak, as indicated in the TOF spectra by the vertical green dashed lines. The windows chosen for the accidental spectra are also listed in Tab. 5.3. The contamination of the nuclear recoil spectra by the accidental background is small – 7% on average – but it is subtracted nonetheless since it is not uniform in energy. The assumption is that this background is stationary in time for a given scattering angle measurement. This assumption was verified by comparing the spectra before and after the neutron TOF peak and both were found to be compatible for each scattering angle measurement.

For all measurements the recoil energy and TOF distributions of the two EJ301 neutron detectors are compatible. Consequently, all distributions shown are for neutrons that interacted in any of the two EJ301 detectors.

For energies of 6.5 keV and above, the peak in the recoil spectrum is clearly above the beginning of the low-energy trigger efficiency roll-off. For these energies, $\mathcal{L}_{\text{eff}}$ could even be computed directly without much uncertainty, simply by fitting a Gaussian to the peak over an exponential background. For energies below 6.5 keV, to avoid the bias of the low-energy trigger efficiency roll-off, a more sophisticated procedure that takes into account the trigger efficiency is warranted. The procedure used to extract $\mathcal{L}_{\text{eff}}$ from the measured recoil energy spectra is detailed in Sec. 5.12.

5.11 Monte Carlo Simulation

Extensive GEANT4 simulations of the expected neutron scattering rate, nuclear recoil energy distribution and neutron TOF distribution were performed for each scattering angle. Each simulation takes into account a realistic description of the neutron generator, LXe detector, detector vessel, vacuum cryostat, support frame, as well as the measured positions of the two EJ301 neutron detectors (Tab. 5.4). The geometry of the simulation of the 3 keV neutron scattering measurement is shown in Fig. 5.29. The live time of each scattering angle simulation is calculated from the expected neutron yield of the generator at the operating conditions of the measurement (Tab. 5.5) and the results are scaled accordingly.

The information recorded in the simulation includes the energy, position, time, type of particle, and physical process responsible for each energy deposit in the LXe detector, as well as the energy, time, and type of particle for each energy deposit in the EJ301 neutron detectors. The energy and direction of the primary neutron is sampled from the calculated energy-angle distribution of neutrons produced by the generator, as given by Eq. 5.16.

Neutrons that interact in the active LXe volume can deposit energy via elastic or inelastic scattering, once or multiple times, and may additionally scatter in materials outside of the active volume. The contributions from all these classes of events has been inferred from the Monte Carlo simulation. Figs. 5.30, 5.31, and 5.32 show the simulated recoil energy and

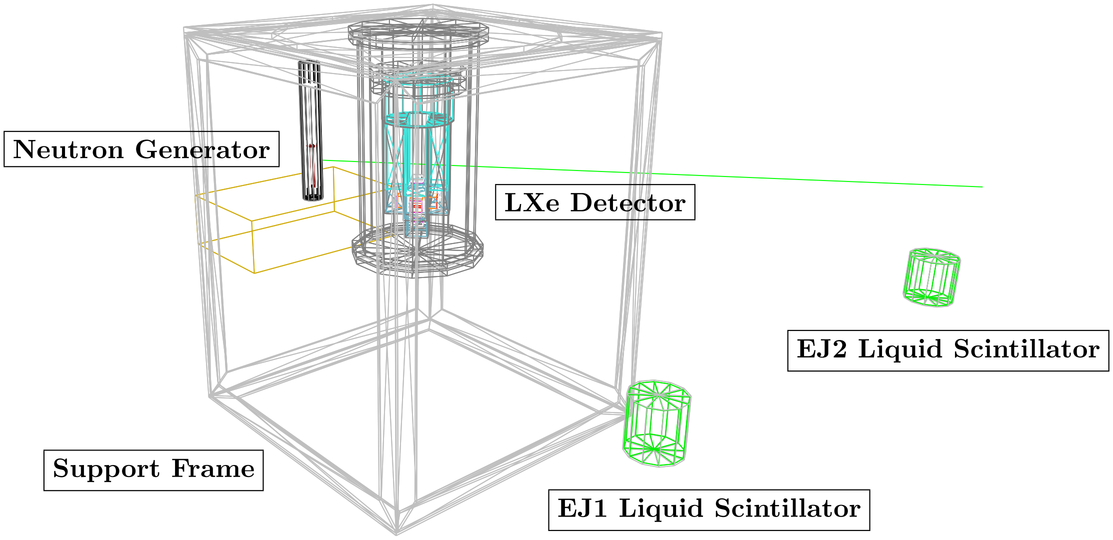

Figure 5.29: Geometry of the GEANT4 Monte Carlo simulation of the 3 keV (23°) neutron scattering measurement.

TOF distributions for all measured scattering angles.

As described earlier, the energy spectrum of elastic recoils consists of a peak, roughly centered at the recoil energy corresponding to the angle at which the EJ301 neutron detectors have been placed, and an approximately exponentially distributed background. The peak is due to neutrons that elastically scatter once in the LXe detector and interact nowhere else (pure single elastic scatters), while the exponential background is due to neutrons that additionally scatter in other materials surrounding the active volume, that is, their energy deposit in the LXe is essentially that of a recoil with a random scattering angle. At the energies we are interested in, the contribution from inelastic scattering is negligible. This is due to the fact that γ rays from the inelastic scattering of neutrons on Xe are very likely to be photoabsorbed and thus push the total deposited energy to much higher values.

In Figs. 5.30, 5.31, and 5.32 the black histogram is the spectrum of energies deposited in the LXe active volume for events where a neutron interacts both in the LXe detector and the EJ301. Multiple energy deposits can occur in the LXe active volume or in other materials. The red dotted histogram is the spectrum of energies deposited in the LXe active volume when the neutron elastically scatters multiple times in the LXe active volume (multiple elastic scatters), the energy deposited is thus the sum of all scatters. There is no need to consider mixed multiple elastic-inelastic events as the inelastic interaction again would push the energy deposited outside of the range of interest. The violet dashed histogram is

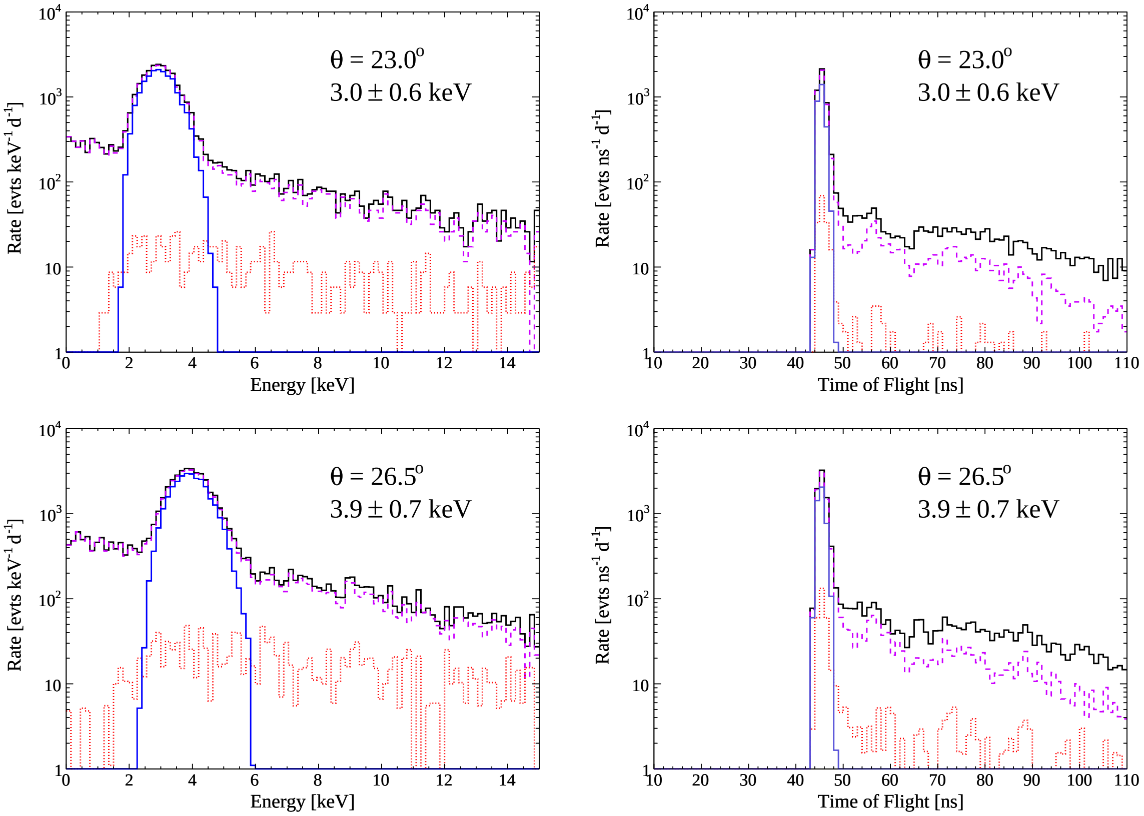

Figure 5.30: (left) Simulated LXe nuclear recoil energy spectrum of neutrons interacting in the active LXe volume and in the EJ301 neutron detector, not including accidental coincidences, for the 23° and 26.5° scattering angles, and for the TOF window used in the analysis; and TOF spectrum (right). The solid black histogram is the total spectrum while the violet dashed histogram is the spectrum of neutrons that elastically scatter once in the LXe active volume and maybe elsewhere. The red dotted histogram is the spectrum of neutrons that elastically scatter multiple times in the active volume. The blue histogram is the spectrum of neutrons that interact only via a single elastic scatter in the active LXe volume. Figure from Plante *et al.* (2011).

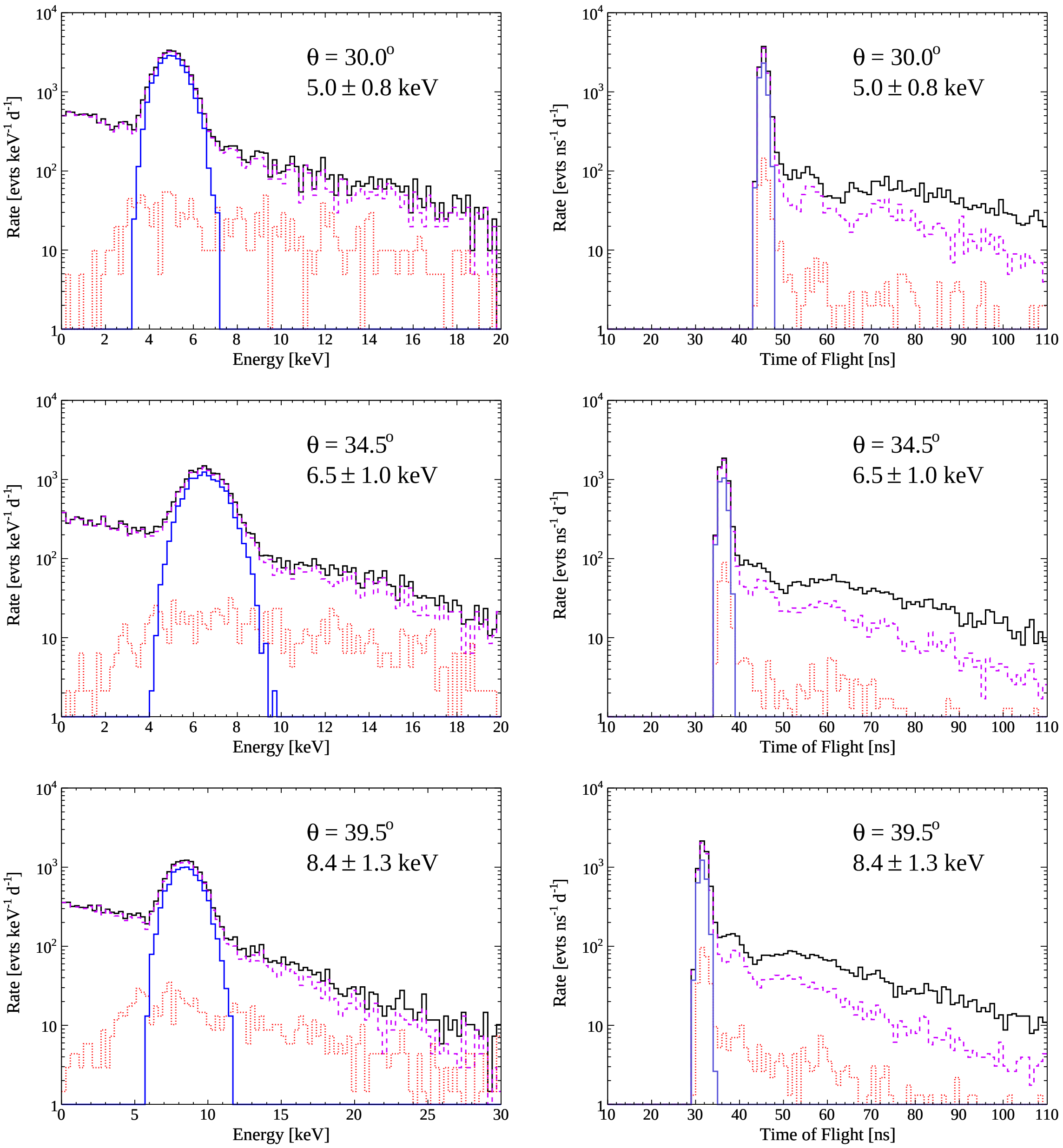

Figure 5.31: (left) Simulated LXe nuclear recoil energy spectrum of neutrons interacting in the active LXe volume and in the EJ301 neutron detector, not including accidental coincidences, for the 30°, 34.5°, and 39.5° scattering angles, and for the TOF window used in the analysis; and TOF spectrum (right). Colors as in Fig. 5.30. Figure from Plante *et al.* (2011).

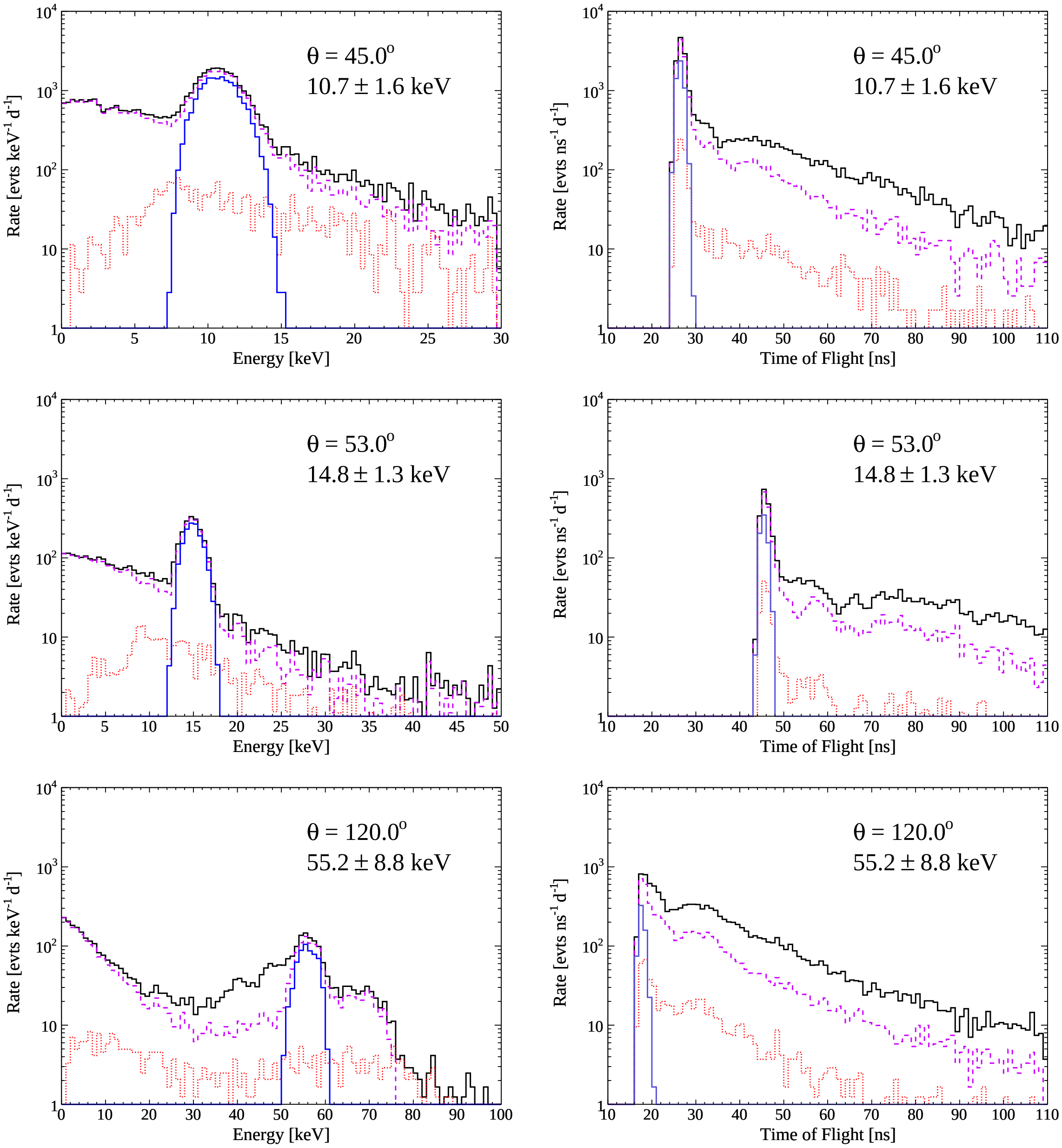

Figure 5.32: (left) Simulated LXe nuclear recoil energy spectrum of neutrons interacting in the active LXe volume and in the EJ301 neutron detector, not including accidental coincidences, for the 45°, 53°, and 120° scattering angles, and for the TOF window used in the analysis; and TOF spectrum (right). Colors as in Fig. 5.30. Figure from Plante *et al.* (2011).

the spectrum of energies deposited in the LXe active volume by neutrons that elastically scatter only once in the LXe active volume, but possibly scatter somewhere else as well (materials scatters). The blue histogram is the spectrum of energies deposited in the LXe active volume by neutrons that elastically scatter only once in the LXe active volume, and nowhere else, before interacting in the EJ301.

For the smaller angles the nuclear recoil energy spectrum is clearly dominated by pure single elastic recoils with 61% at 23°, but the proportion gradually decreases, reaching 49% at 39.5° and 17.8% at 120°. The multiple scatter contribution is negligible at all angles, from 3.7% at 23° up to 7.0% at 120°, due to the small dimensions of the active LXe volume compared to the neutron elastic scattering mean free path. These simulation results demonstrate clearly that the design goal of minimizing the amount of materials in the vicinity of the active LXe volume has been achieved.

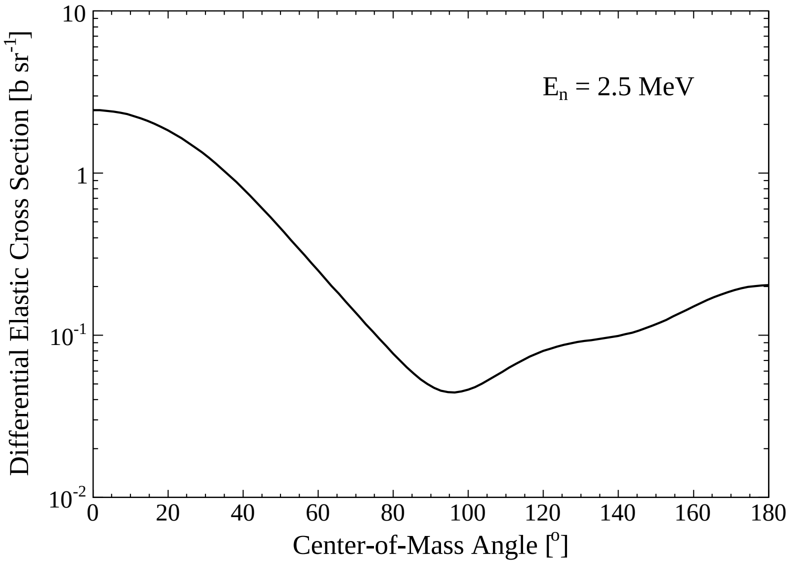

Figure 5.33: Neutron differential elastic scattering cross section on Xe for 2.5 MeV neutrons as a function of the center-of-mass scattering angle.

As mentioned earlier, the spread in energies in the pure single elastic scatter spectrum is (mostly) due to the finite size of the LXe detector and EJ301 neutron detector. The uncertainty in nuclear recoil energies for each scattering angle measurement is obtained by fitting a Gaussian to the single elastic recoil peak in the total energy spectrum (black histogram) – the spectrum which should be measured by the detector – over the energy range of kinematically allowed single elastic recoils (blue histogram). The only exception is for the 120° scattering angle measurement (see Fig. 5.32, bottom). In this case the region near the elastic recoil peak is contaminated heavily and the spread in energies in the total spectrum is much wider than the kinematically allowed spread. The contamination mostly comes from scatters outside the LXe active volume. That is, the neutron differential elastic scattering cross section on Xe is so small near 120° (see Fig. 5.33) that it is more likely for neutrons to scatter multiple times that add up to something close to 120° than to do it in a single scatter. The energy spread in this case is also obtained by fitting a Gaussian to the total energy spectrum but over a much larger energy range. The values obtained for the uncertainty are listed in Tab. 5.4 and in Figs. 5.30, 5.31, and 5.32.

The TOF spectra clearly show that the pure single elastic recoils are in a narrow TOF band, about 5 ns wide, as one would expect. Events where neutrons scatter in other materials become dominant at later TOF values. Neutrons that scatter in other materials, in addition to the scatter in the LXe active volume, lose energy and take a longer path and hence take longer to travel from the LXe detector to the EJ301 neutron detector. A carefully chosen TOF cut can therefore enhance the single elastic recoil peak over the exponential background due to materials scatters. The measured TOF distributions (Figs. 5.26, 5.27, and 5.28) are wider than the simulated distributions due to the finite TOF resolution, an energy dependent quantity as we saw in Sec. 5.8.2. When applying the TOF cut to the simulated recoil energy spectra, the simulated TOF values are convoluted with a Gaussian resolution function with 3 ns standard deviation, the mean of the measured TOF resolutions for the neutron scattering measurements.

5.12 Extracting $\mathcal{L}_{\mathrm{eff}}$

The energy dependence of $\mathcal{L}_{\mathrm{eff}}$ is obtained by minimizing the χ^2 statistic between the measured recoil distribution and the simulated distribution with respect to two free parameters, $\mathcal{L}_{\mathrm{eff},j} \equiv \mathcal{L}_{\mathrm{eff}}(E_{\mathrm{nr},j})$ and $R_j \equiv R(E_{\mathrm{nr},j})$, respectively the scintillation efficiency and the energy resolution at the recoil energy measured $E_{\mathrm{nr},j}$. Explicitly, the χ^2 statistic is computed from

$$\chi^2(\mathcal{L}_{\mathrm{eff},j}, R_j) = \sum_{i=0}^{N} \frac{[h_i - g_i(\mathcal{L}_{\mathrm{eff},j}, R_j)]^2}{\sigma_{h,i}^2 + \sigma_{g,i}^2(\mathcal{L}_{\mathrm{eff},j}, R_j)} \tag{5.20}$$

where h_i and g_i are the measured and simulated event rates in energy bin i, respectively, and $\sigma_{h,i}$ and $\sigma_{g,i}$ the uncertainties of the measured and simulated event rates in bin i, respectively. The bins over which the χ^2 statistic is computed varies depending on the scattering angle so that the χ^2 does not become dominated by effects in the higher energy tail of the recoil distribution, nor the low trigger efficiency region. The values used are summarized in Tab. 5.6.

Table 5.6: Scintillation signal range used to extract $\mathcal{L}_{\rm eff}$ for each scattering angle measured as well as the resulting number of degrees of freedom and the minimum χ^2 obtained.

θ	χ^2 Fit Range (pe)	d.o.f	$\chi^2_{\rm min}$
23°	$[3, 20]$	44	63.2
26.5°	$[4, 25]$	20	19.2
30°	$[4, 30]$	15	14.4
34.5°	$[7, 40]$	16	32.1
39.5°	$[10, 50]$	19	21.1
45°	$[10, 70]$	15	34.5
53°	$[10, 100]$	22	20.9
120°	$[20, 500]$	23	21.4

The steps involved in transforming the simulated recoil energy distributions of Figs. 5.30, 5.31, and 5.32 into the simulated recoil energy distribution h, in photoelectrons, are detailed below.

The recoil energy spectrum obtained from the simulation is first multiplied by the $\mathcal{L}_{\rm eff}$ value under test to convert it to a spectrum with energies in keV (electron-equivalent) and convolved with a Gaussian energy resolution with standard deviation $R\sqrt{E}$, where R is the resolution parameter under test. Next, the recoil energy spectrum is multiplied by the measured light yield L_y to obtain a spectrum in photoelectrons. The number of photoelectrons $N_{\rm pe}$ is allowed to fluctuate according to a Poisson distribution. The effect of the PMT gain fluctuations is incorporated by convolving the recoil energy spectrum in photoelectrons with a Gaussian single photoelectron resolution with standard deviation $R_{\rm spe}\sqrt{N_{\rm pe}}$, where $R_{\rm spe} = 0.6$ is the measured mean PMT single photoelectron resolution (Sec. 5.4.3). The measured trigger efficiency function discussed in Sec. 5.4.2 is then applied to the recoil energy spectrum. As mentioned earlier, the resulting recoil energy spectrum is divided by the simulation live time, computed from the neutron generator yield at the operating conditions (Sec. 5.3.2). Since R is left as a free parameter during the χ^2 minimization, any additional contribution to the resolution not accounted for will be absorbed in that parameter.

The last step involves multiplying the simulated recoil energy spectrum by an overall, energy independent efficiency ϵ, taken as the same for all scattering angle measurements. This efficiency loss is mostly due to the EJ301 energy threshold cut and to the uncertainty in the absolute neutron generator yield. Both are connected since a loss (gain) of efficiency in neutron detection with the EJ301 liquid scintillator is equivalent to a decrease (increase) in the true neutron yield. The efficiency ϵ is necessary because the detection efficiency of the EJ301 detectors has not been calibrated.

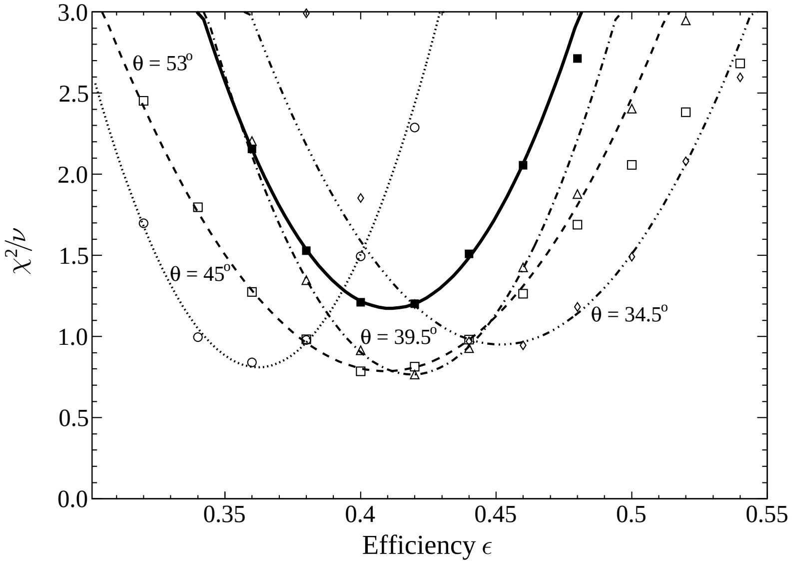

Figure 5.34: Reduced χ^2 values as a function of the efficiency ϵ for the individual fits of the simulated to measured recoil energy spectra for the 34.5° (diamonds), 39.5° (open circles), 45° (open squares), and 53° (open triangles) scattering angle measurements, and for the combined fit (solid squares). Parabola fits to the reduced χ^2 values near their minima are also shown for the 34.5° (dash triple dotted line), 39.5° (dash dotted line), 45° (dotted line), 53° (dashed line), and combined (solid line) measurements.

This efficiency is computed during the χ^2 minimization as an additional parameter for the measurement at the recoil energies of 6.5, 8.4, 10.7 and 14.8 keV. We used the measurements where the single elastic recoil peak is clearly visible. The combined best fit value for ϵ found was 0.41 whereas the individual values were 0.45, 0.42, 0.36, 0.41, respectively. Fig. 5.34 shows the χ^2 between the simulated and measured spectra as a function ϵ. The combined best fit value for the four measurements is taken as the efficiency for all measurements, while its uncertainty is taken as the maximum deviation in the measurements, thus $\epsilon = 0.41^{+0.04}_{-0.05}$. The 10% relative uncertainty on the efficiency reflects the fact that uncertainties in the neutron yield from the generator are at this level.

The fits of the simulated to the measured recoil spectra and associated χ^2 functions near their minima are shown in Figs. 5.35, 5.36, and 5.37 for all measured scattering angles. The $\mathcal{L}_{\mathrm{eff},j}$ and R_j parameters for each scattering angle are found by fitting a rotated paraboloid of the form

$$\chi^2(\mathcal{L}_{\mathrm{eff}}, R) = \chi^2_{\mathrm{min},j} + \left[\frac{(\mathcal{L}_{\mathrm{eff}} - \mathcal{L}_{\mathrm{eff},j})\cos\omega_j - (R - R_j)\sin\omega_j}{\mathcal{A}_j}\right]^2 + \left[\frac{(\mathcal{L}_{\mathrm{eff}} - \mathcal{L}_{\mathrm{eff},j})\sin\omega_j + (R - R_j)\cos\omega_j}{\mathcal{B}_j}\right]^2 \tag{5.21}$$

to the computed χ^2 values in the vicinity of its minimum. The additional parameters of the fit are the minimum χ^2, $\chi^2_{\mathrm{min},j}$, the paraboloid rotation angle ω_j, and the scaling parameters $\mathcal{A}_j$ and $\mathcal{B}_j$. The fitting procedure is used to average out the small variations in the χ^2 landscape. The 1-σ and 2-σ confidence contours for $\mathcal{L}_{\mathrm{eff},j}$ and R_j are obtained from the paraboloid fit by setting the left side of Eq. 5.21 to $\chi^2_{\mathrm{min},j} + \Delta\chi^2_{1\text{-}\sigma}$ and $\chi^2_{\mathrm{min},j} + \Delta\chi^2_{2\text{-}\sigma}$, respectively, where $\Delta\chi^2_{1\text{-}\sigma} = 2.30$ and $\Delta\chi^2_{2\text{-}\sigma} = 6.18$.

In Figs. 5.35, 5.36, and 5.37, the black histograms (left) are the measured nuclear recoil spectra while the dark blue histograms are the simulated spectra. The vertical green dashed lines show the range over which the χ^2 statistic is computed for each scattering angle and correspond to the values listed in Tab. 5.6. The light blue shaded region indicates the effect of 1-σ variations of $\mathcal{L}_{\mathrm{eff}}$ and R around the minimum. They are obtained by generating simulated nuclear recoil spectra with $\mathcal{L}_{\mathrm{eff}}$ and R values taken along the 1-σ ellipses shown in the χ^2 contour plots (right, solid black line) and recording the maximum and minimum rates in each bin. The χ^2 contour plots show the behavior of the χ^2 function around its minimum for each scattering angle. The minimum obtained from the paraboloid fit is indicated by a black dot while the 1-σ and 2-σ confidence contours for the $\mathcal{L}_{\mathrm{eff},j}$ and R_j parameters are shown as solid and dashed black lines respectively. The χ^2 value of each contour is also shown.

For energies below 6.5 keV there is an anti-correlation between $\mathcal{L}_{\mathrm{eff},j}$ and R_j. This can be understood by the fact that near the roll-off in the trigger efficiency, if $\mathcal{L}_{\mathrm{eff}}$ is lowered such that a larger fraction of the recoils produce scintillation signals unlikely to be observed then the resolution parameter R has to increase to match the rate measured, and vice-versa. In other words, since the nuclear recoil spectrum consists mostly of only one side of the

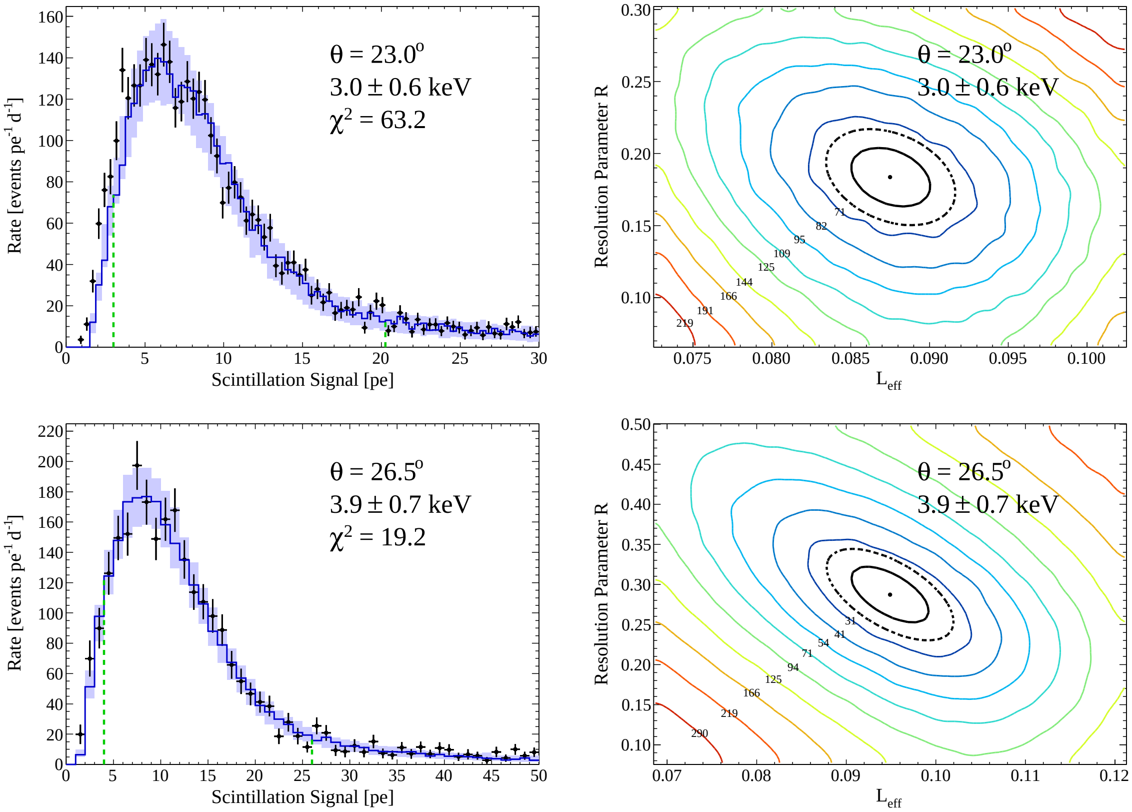

Figure 5.35: (left) Fits of Monte Carlo generated recoil spectra (solid lines) to the measured recoil spectra (data points) and contour plots of the χ^2 as a function of $\mathcal{L}_{\mathrm{eff}}$ and R (right), for the 23° and 26.5° scattering angles. The range used for each fit is indicated by the vertical green dashed lines while the light blue shaded region corresponds to 1-σ variations of $\mathcal{L}_{\mathrm{eff},j}$ and R_j around the minimum. The minimum is indicated by a black dot and the 1-σ and 2-σ contours by solid and dashed black lines, respectively. Figure (left) from Plante *et al.* (2011).

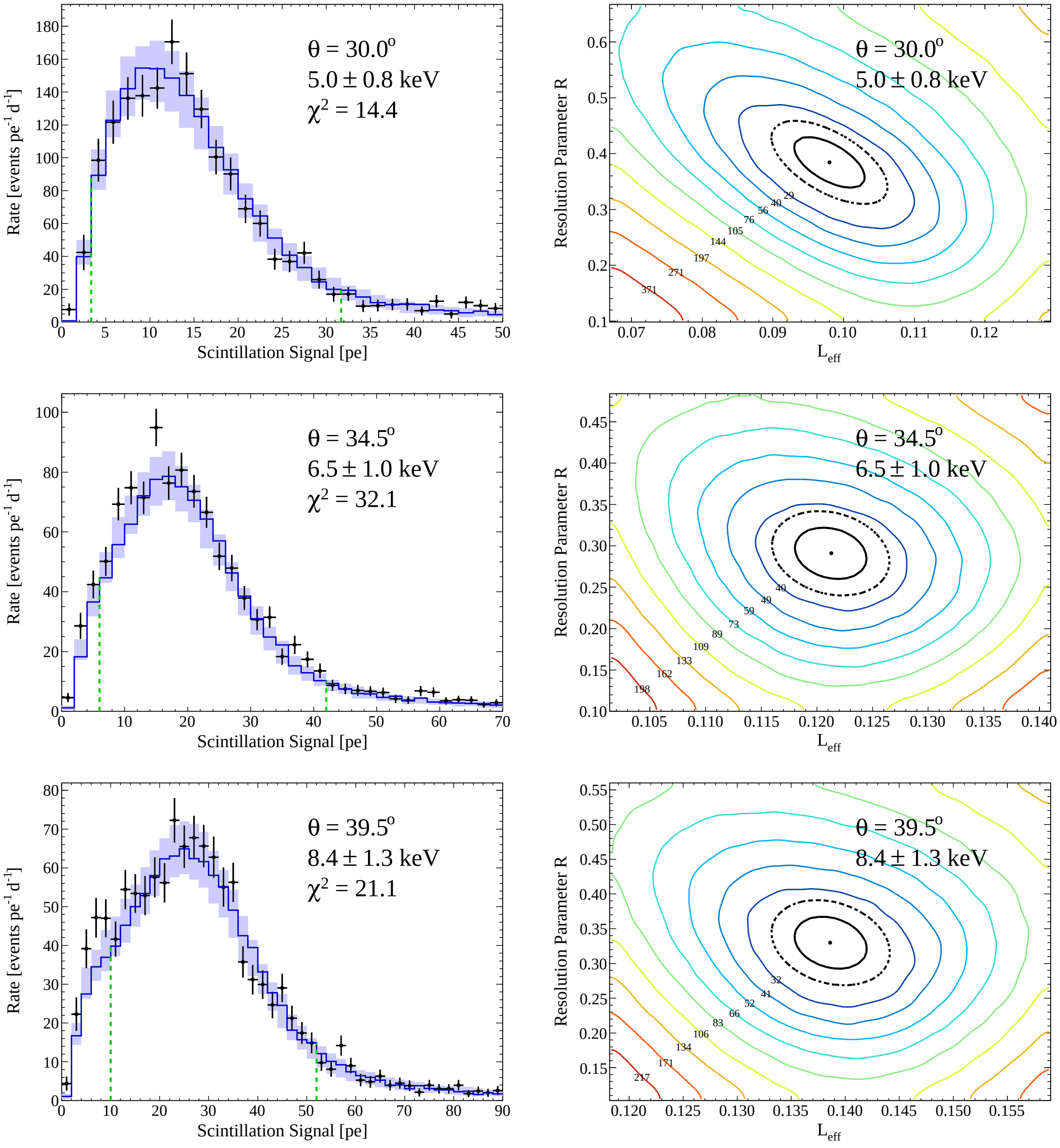

Figure 5.36: (left) Fits of Monte Carlo generated recoil spectra (solid lines) to the measured recoil spectra (data points) and contour plots of the χ^2 as a function of $\mathcal{L}_{\text{eff}}$ and R (right), for the 30°, 34.5°, and 39.5° scattering angles. Colors and lines as in Fig. 5.35. Figure (left) from Plante *et al.* (2011).

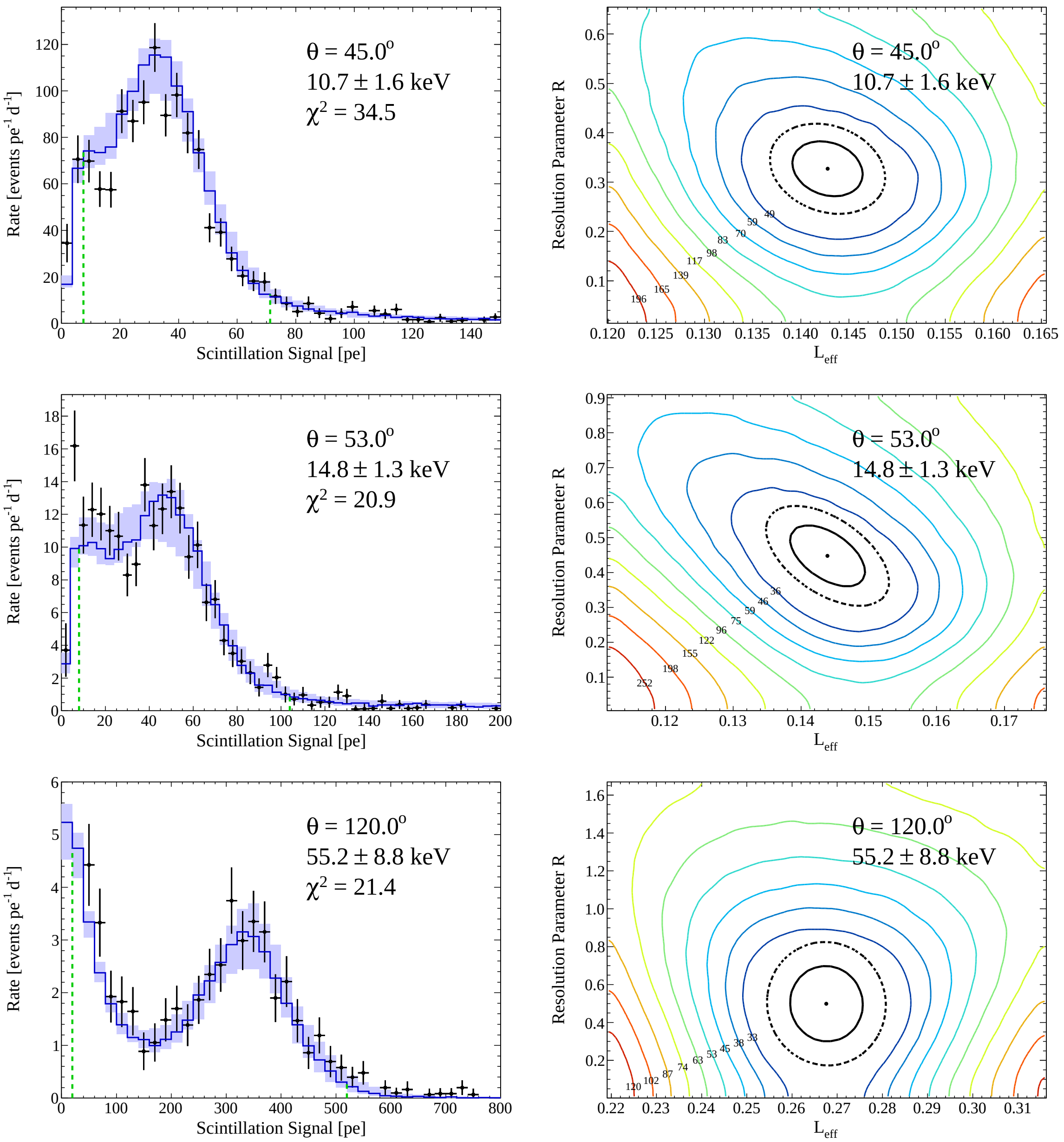

Figure 5.37: (left) Fits of Monte Carlo generated recoil spectra (solid lines) to the measured recoil spectra (data points) and contour plots of the χ^2 as a function of $\mathcal{L}_{\text{eff}}$ and R (right), for the 45°, 53°, and 120° scattering angles. Colors and lines as in Fig. 5.35. Figure (left) from Plante *et al.* (2011).

distribution, reducing the mean and broadening the simulated spectrum – or increasing the mean and reducing the spread – can still provide an adequate match. For energies of 6.5 keV and above, when the mean of the elastic recoil peak is clearly above the roll-off, then a lower $\mathcal{L}_{\rm eff}$ and larger R (or vice-versa) cannot provide a good spectral match and the anti-correlation gradually disappears. Still, the 53° scattering angle χ^2 contour plot shows an anti-correlation but this is probably due to the reduced statistics and the increased exponential background rate in the vicinity of the elastic recoil peak, the largest for all scattering angles.

5.13 Results

The procedure described in Sec. 5.12 was used to compute the energy dependence of $\mathcal{L}_{\rm eff}$ via the scattering angles measured. The $\mathcal{L}_{\rm eff}$ values obtained are listed in Tab. 5.7. Fig. 5.38 shows the results along with those of prior measurements at low energies (Aprile *et al.*, 2005, 2009; Chepel *et al.*, 2006; Horn *et al.*, 2011; Lebedenko *et al.*, 2009b; Manzur *et al.*, 2010; Sorensen *et al.*, 2009).

In Sec. 5.13.1 we describe the different terms included in the uncertainty on the measured $\mathcal{L}_{\rm eff}$ values, while in Secs. 5.13.2, 5.13.3, and 5.13.4 we discuss and assess possible additional systematic effects.

Table 5.7: Values of $\mathcal{L}_{\rm eff}$ obtained for each scattering angle measured, together with their errors as discussed in Sec. 5.13.1. Values obtained for the resolution parameter R are also given (including statistical error only).

θ	$E_{\rm nr}$ (keV)	$\mathcal{L}_{\rm eff}$	R
23°	3.0 ± 0.6	$0.088^{+0.014}_{-0.015}$	0.18 ± 0.02
26.5°	3.9 ± 0.7	$0.095^{+0.015}_{-0.016}$	0.29 ± 0.04
30°	5.0 ± 0.8	$0.098^{+0.014}_{-0.015}$	0.38 ± 0.05
34.5°	6.5 ± 1.0	0.121 ± 0.010	0.29 ± 0.03
39.5°	8.4 ± 1.3	0.139 ± 0.011	0.32 ± 0.04
45°	10.7 ± 1.6	0.143 ± 0.010	0.33 ± 0.06
53°	14.8 ± 1.3	0.144 ± 0.009	0.45 ± 0.09
120°	55.2 ± 8.8	0.268 ± 0.013	0.50 ± 0.20

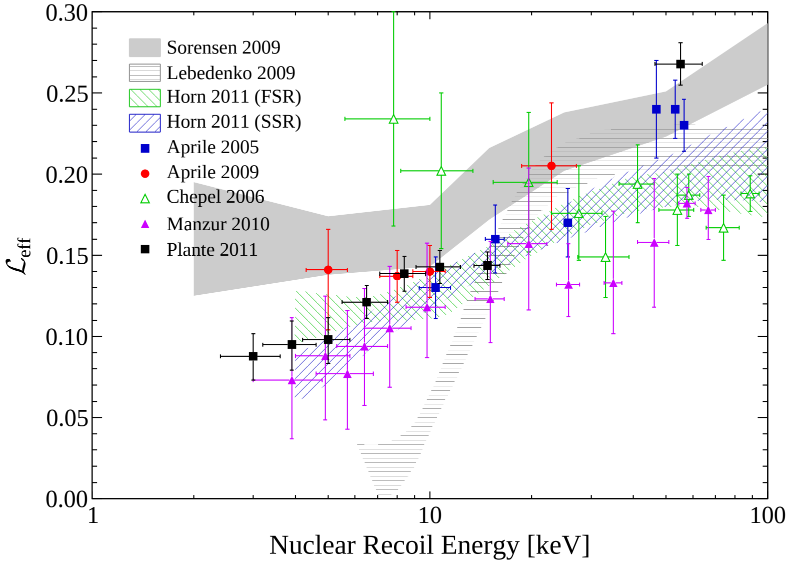

Figure 5.38: Measured $\mathcal{L}_{\mathrm{eff}}$ values as a function of nuclear recoil energy, together with measurements from other groups (Aprile *et al.*, 2005, 2009; Chepel *et al.*, 2006; Horn *et al.*, 2011; Lebedenko *et al.*, 2009b; Manzur *et al.*, 2010; Sorensen *et al.*, 2009). Figure from Plante *et al.* (2011).

5.13.1 Uncertainty

The total uncertainty on $\mathcal{L}_{\mathrm{eff}}$ is given by a combination of statistical and systematic factors with the statistical uncertainty taken from the fit to the data. The systematic uncertainties include contributions from the spread in nuclear recoil energies, $\sigma_{E_{\mathrm{nr}}}$, and uncertainties associated with the ^{57}Co light yield, σ_{L_y}, the efficiency of the EJ301 energy threshold cut, σ_{ϵ}, the positions of the neutron generator, σ_{r_g}, and of the EJ301 detectors, σ_{r_s}. Explicitly

$$\sigma^2_{\mathcal{L}_{\mathrm{eff}}} = \sigma^2_{\mathcal{L}_{\mathrm{eff}},\mathrm{fit}} + \left(\frac{\partial \mathcal{L}_{\mathrm{eff}}}{\partial L_y}\right)^2 \sigma^2_{L_y} + \left(\frac{\partial \mathcal{L}_{\mathrm{eff}}}{\partial E_{\mathrm{nr}}}\right)^2 \sigma^2_{E_{\mathrm{nr}}} + \left(\frac{\Delta \mathcal{L}_{\mathrm{eff}}}{\Delta \epsilon}\right)^2 \sigma^2_{\epsilon} + \left(\frac{\Delta \mathcal{L}_{\mathrm{eff}}}{\Delta r_g}\right)^2 \sigma^2_{r_g} + \left(\frac{\Delta \mathcal{L}_{\mathrm{eff}}}{\Delta r_s}\right)^2 \sigma^2_{r_s}. \quad (5.22)$$

The statistical uncertainty, $\sigma_{\mathcal{L}_{\mathrm{eff}},\mathrm{fit}}$, is obtained from the 1-σ contours of the paraboloid fits to the $\chi^2(\mathcal{L}_{\mathrm{eff},j}, R_j)$ functions, as described in Sec. 5.12. Since $\mathcal{L}_{\mathrm{eff}}$ depends linearly on the value of L_y its change with respect to L_y, $\partial\mathcal{L}_{\mathrm{eff}}/\partial L_y$, is computed straightforwardly. This is not the case for change in $\mathcal{L}_{\mathrm{eff}}$ with nuclear recoil energy, $\partial\mathcal{L}_{\mathrm{eff}}/\partial E_{\mathrm{nr}}$.

In theory, the systematic uncertainty on $\mathcal{L}_{\mathrm{eff}}$ due to uncertainties in nuclear recoil energies has two contributions, one from the uncertainty in the mean recoil energy E_{nr}, and one from the spread in nuclear recoil energies. However, in practice, the uncertainty on the mean recoil energy is much smaller than the spread in recoil energies. The systematic uncertainty from the spread in recoil energies comes about if $\mathcal{L}_{\text{eff}}$ varies substantially over the range of recoil energies of the single elastic recoil peak, that is, if the energies above or below the mean give rise to much different scintillation signals, then the scintillation spectrum will be stretched or compressed differently above and below, thus shifting its mean. In contrast, if $\mathcal{L}_{\text{eff}}$ did not vary with energy, the scintillation spectrum would be compressed by the same amount over the whole energy range and the systematic uncertainty due to the spread in recoil energies would be null. One would then include only the contribution from the uncertainty in the mean recoil energy. The change in $\mathcal{L}_{\text{eff}}$ with nuclear recoil energy, $\partial\mathcal{L}_{\text{eff}}/\partial E_{\text{nr}}$, is computed in closed form from a logarithmic fit to the measured $\mathcal{L}_{\text{eff}}$ values versus nuclear recoil energy. Explicitly the expression used is $\mathcal{L}_{\text{eff}}(E_{\text{nr}}) = \gamma \log(\kappa E_{\text{nr}})$, with $\gamma = 0.061 \pm 0.006$ and $\kappa = 1.1 \pm 0.3\,\text{keV}^{-1}$.

The systematic uncertainty introduced by the uncertainty in the neutron generator yield is taken into account via the EJ301 energy threshold cut efficiency uncertainty, σ_ϵ. That is, a loss (gain) of efficiency in neutron detection with the liquid scintillator is equivalent to a decrease (increase) in the true neutron yield. This assumes that there are no large spectral shape changes incurred by varying the liquid scintillator threshold cut. This is verified in Sec. 5.13.3 by examining the change in $\mathcal{L}_{\text{eff}}$ values obtained by varying the EJ301 energy threshold cut. The contribution to the systematic uncertainty on $\mathcal{L}_{\text{eff}}$ is calculated by repeating the χ^2 minimization at two different values of ϵ, $\epsilon_- = \epsilon - \sigma_\epsilon^- = 0.36$ and $\epsilon_+ = \epsilon + \sigma_\epsilon^+ = 0.45$, and computing the change in $\mathcal{L}_{\text{eff}}$ with respect to ϵ with

$$\frac{\Delta\mathcal{L}_{\text{eff}}}{\Delta\epsilon} = \frac{\mathcal{L}_{\text{eff}}|_{\epsilon=\epsilon_+} - \mathcal{L}_{\text{eff}}|_{\epsilon=\epsilon_-}}{\epsilon_+ - \epsilon_-}. \tag{5.23}$$

The change in the inferred $\mathcal{L}_{\text{eff}}$ values due to the uncertainties in the positions of the neutron generator and of the EJ301 detectors, $\Delta\mathcal{L}_{\text{eff}}/\Delta r_g$, and $\Delta\mathcal{L}_{\text{eff}}/\Delta r_s$, respectively, were calculated through a discrete approximation by performing additional GEANT4 simulations where each parameter is varied by small amounts. In the case of the uncertainty in the neutron generator position, two additional simulations were performed, one where the neutron production point was 1 cm higher and one where it was 1 cm lower than the position in the baseline simulation. The uncertainty in the neutron generator position was set to $\sigma_{r_g} = 5\,\text{mm}$, the same as the estimated uncertainty in the position of the EJ301 neutron detectors (Sec. 5.10). Similarly, in the case of the systematic uncertainty in $\mathcal{L}_{\text{eff}}$ due to the uncertainty in the EJ301 detector positions, two additional simulations were performed where neutron detectors are displaced by 1 cm in the positive and negative direction of maximum change in recoil energy, respectively. The systematic uncertainty contribution can also be computed analytically through the expression

$$\frac{\partial \mathcal{L}_{\text{eff}}}{\partial r_s} = \frac{\partial \mathcal{L}_{\text{eff}}}{\partial E_{\text{nr}}} \frac{\partial E_{\text{nr}}}{\partial \theta} \frac{\partial \theta}{\partial r_s} \tag{5.24}$$

where the change in position is also chosen along the direction of maximum change in recoil energy and yields similar results as the discrete approximation.

Table 5.8: Individual contributions to the uncertainty on $\mathcal{L}_{\text{eff}}$ for each scattering angle measured.

θ	E_{nr} (keV)	$\mathcal{L}_{\text{eff}}$	$\sigma_{\mathcal{L}_{\text{eff}}}$	$\sigma_{\mathcal{L}_{\text{eff}},\text{fit}}$	$\frac{\partial \mathcal{L}_{\text{eff}}}{\partial L_y}\sigma_{L_y}$	$\frac{\partial \mathcal{L}_{\text{eff}}}{\partial E_{\text{nr}}}\sigma_{E_{\text{nr}}}$	$\frac{\Delta \mathcal{L}_{\text{eff}}}{\Delta \epsilon}\sigma_{\epsilon}$	$\frac{\Delta \mathcal{L}_{\text{eff}}}{\Delta r_g}\sigma_{r_g}$	$\frac{\Delta \mathcal{L}_{\text{eff}}}{\Delta r_s}\sigma_{r_s}$
23°	3.0 ± 0.6	0.088	$^{+0.0140}_{-0.0147}$	0.0025	0.0016	0.0122	$^{+0.0060}_{-0.0076}$	0.0002	0.0015
26.5°	3.9 ± 0.7	0.095	$^{+0.0146}_{-0.0158}$	0.0045	0.0018	0.0109	$^{+0.0083}_{-0.0103}$	0.0008	0.0013
30°	5.0 ± 0.8	0.098	$^{+0.0135}_{-0.0146}$	0.0052	0.0018	0.0097	$^{+0.0074}_{-0.0093}$	0.0013	0.0011
34.5°	6.5 ± 1.0	0.121	0.0104	0.0033	0.0023	0.0094	$^{+0.0013}_{-0.0016}$	0.0011	0.0013
39.5°	8.4 ± 1.3	0.139	0.0108	0.0034	0.0026	0.0094	$^{+0.0011}_{-0.0013}$	0.0026	0.0012
45°	10.7 ± 1.6	0.143	0.0103	0.0037	0.0027	0.0091	$^{+0.0007}_{-0.0008}$	0.0011	0.0013
53°	14.8 ± 1.3	0.144	0.0086	0.0056	0.0053	0.0053	$^{+0.0021}_{-0.0026}$	0.0006	0.0006
120°	55.2 ± 8.8	0.268	0.0131	0.0073	0.0050	0.0097	$^{+0.0000}_{-0.0000}$	0.0005	0.0005

Tab. 5.8 lists the individual contributions to the uncertainty on $\mathcal{L}_{\text{eff}}$ for each scattering angle measured. The largest contribution to the total uncertainty in $\mathcal{L}_{\text{eff}}$ comes from the spread in recoil energy. At energies below 6.5 keV, this is followed by the uncertainty in the efficiency ϵ. This is expected as $\mathcal{L}_{\text{eff}}$ varies most with nuclear recoil energy in this region, and since the mean of the pure single elastic recoil peak is in the roll-off of the trigger efficiency curve. For energies of 6.5 keV and above, the statistical uncertainty from the fit is the next-to leading contribution to the total uncertainty. This is likely caused by the smaller statistics acquired for the higher recoil energy datasets.

5.13.2 Effect of the Trigger Efficiency

The systematic uncertainty in $\mathcal{L}_{\text{eff}}$ due to the uncertainty in the trigger efficiency roll-off has been investigated by varying the trigger efficiency function (Fig. 5.17). If, as in the $\mathcal{L}_{\text{eff}}$

analysis presented here, one assumes the measured trigger efficiency as the true efficiency, then its statistical uncertainty has a negligible effect on the inferred $\mathcal{L}_{\mathrm{eff}}$ values. However, if one assumes that a systematic effect is responsible for the discrepancy between the measured and simulated trigger efficiencies and takes the simulated efficiency as the true efficiency, then the effect on the $\mathcal{L}_{\mathrm{eff}}$ values below 6.5 keV is substantial. Tab. 5.9 list the $\mathcal{L}_{\mathrm{eff}}$ values obtained when multiplying the simulated recoil energy spectra by the simulated trigger efficiency instead of the measured efficiency. Fig. 5.39 shows the change in calculated $\mathcal{L}_{\mathrm{eff}}$ values in this case.

Table 5.9: Values of $\mathcal{L}_{\mathrm{eff}}$ obtained for each scattering angle measured in this study, assuming the simulated trigger efficiency of Fig. 5.17 as the true efficiency.

θ	E_{nr} (keV)	$\mathcal{L}_{\mathrm{eff,\,sim}}$
23°	3.0 ± 0.6	$0.102^{+0.013}_{-0.014}$
26.5°	3.9 ± 0.7	$0.110^{+0.014}_{-0.015}$
30°	5.0 ± 0.8	$0.111^{+0.013}_{-0.014}$
34.5°	6.5 ± 1.0	0.124 ± 0.010
39.5°	8.4 ± 1.3	0.140 ± 0.010
45°	10.7 ± 1.6	0.144 ± 0.010
53°	14.8 ± 1.3	0.147 ± 0.008
120°	55.2 ± 8.8	0.269 ± 0.012

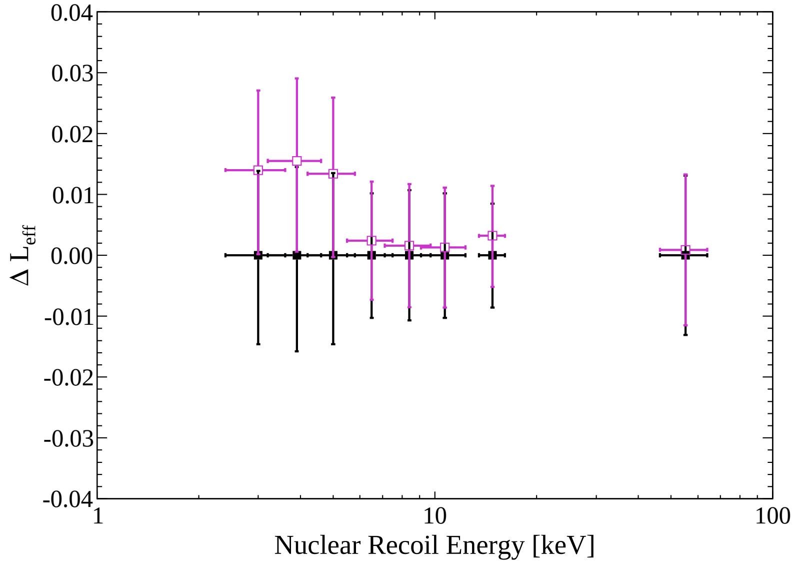

Figure 5.39: Change in $\mathcal{L}_{\mathrm{eff}}$ (magenta open squares) from taking the simulated trigger efficiency for the computation instead of the measured efficiency, with respect to the results of Tab. 5.7 (solid squares).

From Fig. 5.39, it is clear which energies are affected mostly by the trigger efficiency roll-off. For energies of 6.5 keV and above the effect is negligible. As mentioned in Sec. 5.4.3, we believe that hardware modeling inaccuracies are responsible for the discrepancy between the measured and simulated trigger efficiency and not a systematic effect in the efficiency measurement. That is, we expect the true trigger efficiency to be close to the measured efficiency but, in principle, it could be as good as the simulated efficiency although that is not very likely.

5.13.3 Effect of the EJ301 Energy Threshold Cut

The EJ301 energy threshold cut serves the purpose of reducing the background coming from neutrons that additionally scatter in other materials near the LXe detector and thus have a lower energy when reaching the EJ301 detector. In principle, if the nuclear recoil spectrum in the LXe detector varied drastically with the neutron energy deposited in the EJ301 detector the threshold chosen could have a systematic effect on $\mathcal{L}_{\mathrm{eff}}$. The effect is studied by repeating the analysis with two different EJ301 threshold energies, $30 \times 10^6\,\mathrm{e}^-$ and $45 \times 10^6\,\mathrm{e}^-$, below and above the cut chosen for the main analysis (Sec. 5.7). The resulting change in $\mathcal{L}_{\mathrm{eff}}$ values calculated is shown in Fig. 5.40. No significant bias in $\mathcal{L}_{\mathrm{eff}}$ results from the variation of this cut.

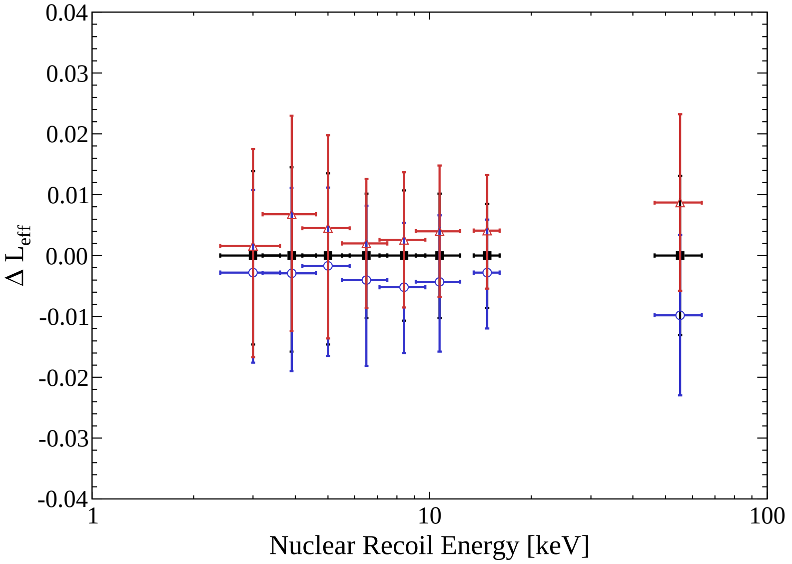

Figure 5.40: Change in $\mathcal{L}_{\mathrm{eff}}$ resulting from varying the EJ301 energy threshold cut from $30\times10^6\,\mathrm{e}^-$ (blue open circles) to $45\times10^6\,\mathrm{e}^-$ (red open triangle), with respect to the results of Tab. 5.7 (solid squares).

5.13.4 Effect of the Resolution Parameter R

The validity of the approach of extracting $\mathcal{L}_{\text{eff}}$ via the minimization of $\chi^2(\mathcal{L}_{\text{eff},j}, R_j)$ with the addition of a second parameter, the energy resolution parameter R, has been questioned (Collar, 2011). The question raised is not whether or not the simulated energy spectra should be convolved with an energy resolution function to infer the energy dependence of $\mathcal{L}_{\text{eff}}$ but rather that this function is predictable and that leaving it as a free parameter risks "substantially biasing $\mathcal{L}_{\text{eff}}$ towards artificially large values and reducing uncertainty". We disagree that adding the resolution parameter risks reducing uncertainty as adding a parameter that is correlated to another one will in general increase the uncertainty on the latter, not reduce it. Nonetheless, it is important to examine at which extent the values of $\mathcal{L}_{\text{eff}}$ are biased.

Among the previous low-energy direct measurements of $\mathcal{L}_{\text{eff}}$ (Aprile *et al.*, 2005, 2009; Chepel *et al.*, 2006; Manzur *et al.*, 2010) only the analysis of Manzur *et al.* considered the effects of the uncertainty in the energy resolution. In the analysis of Manzur *et al.*, the energy resolution function was determined from the measured recoil spectra at 56 keV and 66 keV and assumed to be of the form $\sigma = a\sqrt{N}$, where N is the number of photoelectrons. Energy spectra were convolved with this resolution function, with the geometrical energy spread subtracted in quadrature, and the systematic effect on $\mathcal{L}_{\text{eff}}$ was examined by varying the resolution within its uncertainty. There a few issues with this prescription. First, the number of energies used that enter the fit to extract the parameter a is very limited and at high energies compared to the energies at which the function extrapolated. Second, the recoil spectra used are at energies where the spread in nuclear recoil energies is dominated by multiple scattering in materials in the vicinity of the LXe detector (see Fig. 9 of Manzur *et al.* (2010)) and not by any processes inherent to the production of the scintillation signal in LXe or its detection by PMTs.

In order to verify if there is a systematic effect on the $\mathcal{L}_{\text{eff}}$ values calculated, and what is its size, when the resolution parameter R is left as a free parameter, the $\mathcal{L}_{\text{eff}}$ χ^2 analysis has been repeated by fixing the energy dependence of the resolution, using a fit to measured resolutions at higher energies, in a manner analogous to what was done in the analysis of Manzur *et al.*.

Scattering angles where the elastic single scatter peak is clearly above the trigger efficiency

ciency roll-off – energies of 6.5 keV and above – were fitted with Gaussian functions over an exponential background and the resolutions obtained are fitted to two different models for the energy dependence of the energy resolution, $a\sqrt{E}$ and $a\sqrt{E}+bE$. The energy spread due to the finite size of the detectors is subtracted in quadrature to remove its contribution. Fig. 5.41 shows the energy resolutions (σ/E) obtained via the Gaussian fits (open triangles) and the results of the fits to both models of the energy dependence. The values obtained in the $\chi^2(\mathcal{L}_{\mathrm{eff},j}, R_j)$ minimization described in Sec. 5.12 are also shown as a comparison (solid triangles). As both models describe the data properly, the model with fewer parameters, $a\sqrt{E}$, is used to obtain the energy resolution at a given recoil energy. Explicitly, the expression used is $\sigma(E) = \left(1.30 \pm 0.08\,\mathrm{keV}^{1/2}\right)\sqrt{E}$.

Fig. 5.42 shows the effect of fixing the energy resolution instead of leaving it as free parameter on the calculated $\mathcal{L}_{\mathrm{eff}}$ values. The change in $\mathcal{L}_{\mathrm{eff}}$ is well within the quoted error bars.

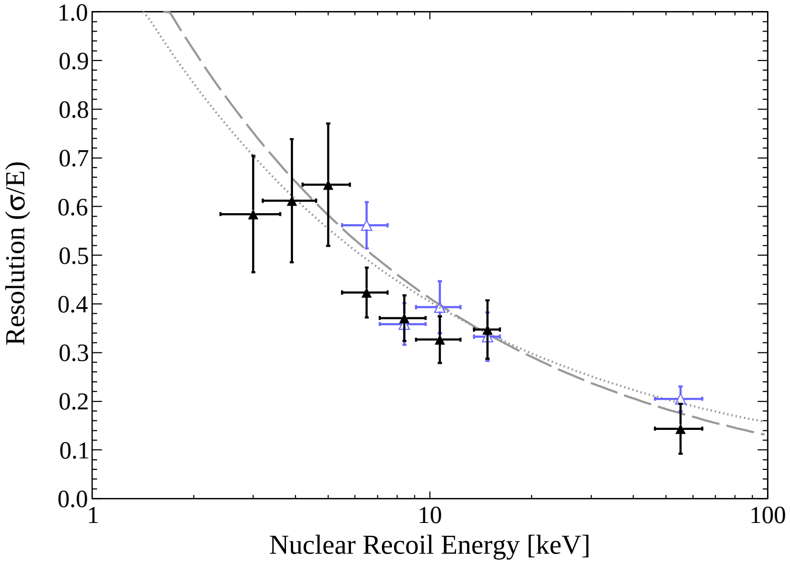

Figure 5.41: Measured nuclear recoil energy resolution (σ/E) from Gaussian fits over an exponential background, for energies of 6.5 keV and above (open triangles), and from the results of the χ^2 analysis described in Sec. 5.12, for all energies (solid triangles). In both cases the contribution from the spread in nuclear recoil energies due to the finite size of the detectors is subtracted in quadrature. Fits to two models for the energy dependence of the resolution, $a\sqrt{E}$ and $a\sqrt{E}+bE$, are also shown as dashed and dotted lines respectively. Both models are fitted only to the energy resolution values inferred from the Gaussian fits (open triangles).

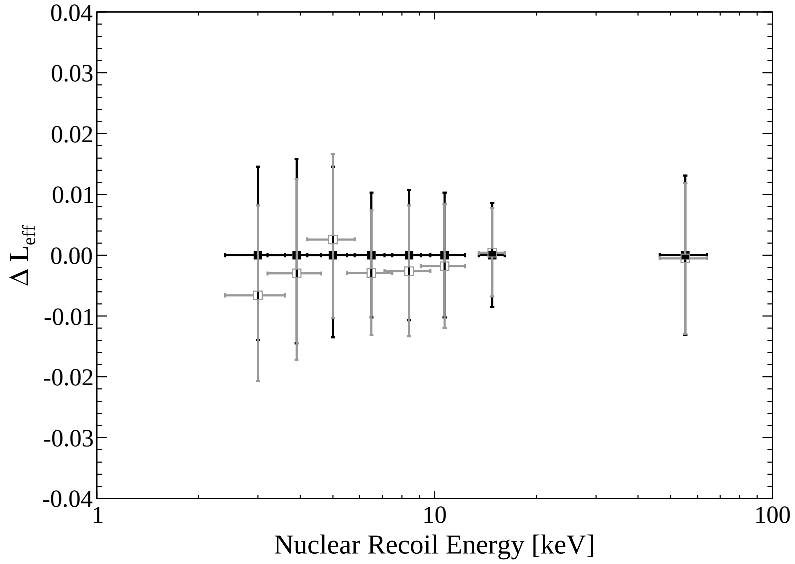

Figure 5.42: Change in $\mathcal{L}_{\mathrm{eff}}$ (open squares) as a result of fixing the energy resolution instead of leaving it as a free parameter, with respect to the results of Tab. 5.7 (solid squares).

5.14 Discussion

Our results are the most precise measurements of $\mathcal{L}_{\mathrm{eff}}$ at low energies so far, down to 3 keV. They suggest that $\mathcal{L}_{\mathrm{eff}}$ slowly decreases with decreasing energy, from 0.144 ± 0.009 at 15 keV to $0.088^{+0.014}_{-0.015}$ at 3 keV. The agreement at 8.4 and 10.7 keV with the points at 8 and 10 keV of Aprile *et al.* (2009) is excellent. Considering that the two measurements were performed with different LXe detectors, using different incident neutron energies, and at different neutron fluxes, reinforces the accuracy of the new measurement. The point at 5.1 keV is at the lower end of the error bar of the measurement of Aprile *et al.* (2009). The increased background due to neutron multiple scatters in materials surrounding the detector in that measurement could be responsible for this shift.

Our results below 10 keV are consistent with those of Manzur *et al.*, within errors. We point out, however, that the statistical errors quoted in Manzur *et al.* seem to be much larger than 1-σ errors, judging by the (reduced) χ^2 versus $\mathcal{L}_{\mathrm{eff}}$ plots of Fig. 11 of Manzur *et al.* (2010). In Tab. 1 of Manzur *et al.* (2010) the statistical and systematic errors are given separately and the caption of Fig. 11 states that "The points show the different $\mathcal{L}_{\mathrm{eff}}$ values tested while the curve is a fit to the points used to find the 1-σ errors on the $\mathcal{L}_{\mathrm{eff}}$ value". From Fig. 11 (a), we can extract that the χ^2 distribution for the 6 keV data point has 35 degrees of freedom, 37 bins minus 1 parameter, $\mathcal{L}_{\mathrm{eff}}$, minus 1 for the overall scaling left free. The confidence interval (statistical uncertainty only) for $\mathcal{L}_{\mathrm{eff}}$ quoted is $[0.077 - 0.022, 0.077 + 0.028]$, clearly the reduced χ^2 value at which the parabola reaches a width of $0.022 + 0.028 = 0.05$ is much higher than a reduced χ^2 of (35+1)/35, what would be expected for the 1-σ confidence interval of a 1 parameter fit.

The fact that our $\mathcal{L}_{\mathrm{eff}}$ values are systematically higher than those obtained by Manzur *et al.* could be explained by their use of the maximum neutron energy of 2.8 MeV instead of the mean energy in the calculation of $\mathcal{L}_{\mathrm{eff}}$ (Manalaysay, 2010). It could also be due to an underestimation of their true trigger efficiency, whose simulation was not validated with a measurement. As discussed in Sec. 5.13.2, since there is a discrepancy between our measurement of the trigger efficiency and the simulated efficiency, our results could also be systematically biased to lower $\mathcal{L}_{\mathrm{eff}}$ values. As mentioned earlier, because the trigger efficiency measurement was performed in a direct way, it can only be biased to lower trigger efficiency values. In other words, we cannot have less trigger signals than those that were measured. The size of the bias on $\mathcal{L}_{\mathrm{eff}}$, assuming that the simulated efficiency is the true efficiency, was shown in Tab. 5.9.

At low energies, our results are incompatible with the indirect $\mathcal{L}_{\mathrm{eff}}$ measurements of Sorensen *et al.* (2009) and Lebedenko *et al.* (2009b) or with considerably smaller $\mathcal{L}_{\mathrm{eff}}$ values such as those suggested in Collar (2010). However, they are compatible with the values of Horn *et al.* (2011). It is informative to note that the $\mathcal{L}_{\mathrm{eff}}$ derived from the first science run (FSR) of Horn *et al.*, higher at low energies than the one derived from the second science run (SSR), is also for the science run with the higher light detection efficiency (Fig. 2 of Horn *et al.*). The point at which both $\mathcal{L}_{\mathrm{eff}}$ curves start to diverge is also the point at which both light detection efficiency curves start to substantially differ.

We have not performed any measurement of $\mathcal{L}_{\mathrm{eff}}$ below 3 keV to avoid the low trigger efficiency region. If $\mathcal{L}_{\mathrm{eff}}$ were to decrease below 3 keV with the same logarithmic slope as observed between 3 and 10.7 keV, one would predict that at 2 keV, for example, $\mathcal{L}_{\mathrm{eff}}$ would be reduced to 0.0634. The single elastic recoil peak for such a measurement would lie at 3 pe, and thus at a trigger efficiency of 45%. In these trigger conditions, the fraction of the neutron scattering rate which produces measurable signals becomes comparable to the relative uncertainty on the neutron generator yield. The systematic uncertainty on $\mathcal{L}_{\mathrm{eff}}$ from the uncertainty in neutron generator yield would be considerably larger than for the 3 keV measurement. Fig. 5.43 shows a simulated recoil spectrum (black) that could be the result of a measurement at a scattering angle of 19.5°, corresponding to a recoil energy of 2.0 ± 0.5 keV. The green histogram shows the simulated recoil energy spectrum in mean number of photoelectrons, that is, without Poisson fluctuations in the number of photoelectrons. The gray dashed and solid histograms correspond to the expected recoil energy spectra in measured photoelectrons, with Poisson fluctuations and after the single photoelectron resolution have been taken into account. The gray solid histogram has an additional contribution to its spread in measured photoelectrons such that its resolution would be consistent with what could be expected at 2 keV from Fig. 5.41. Finally, the black histogram includes the effect of the trigger efficiency roll-off near threshold.

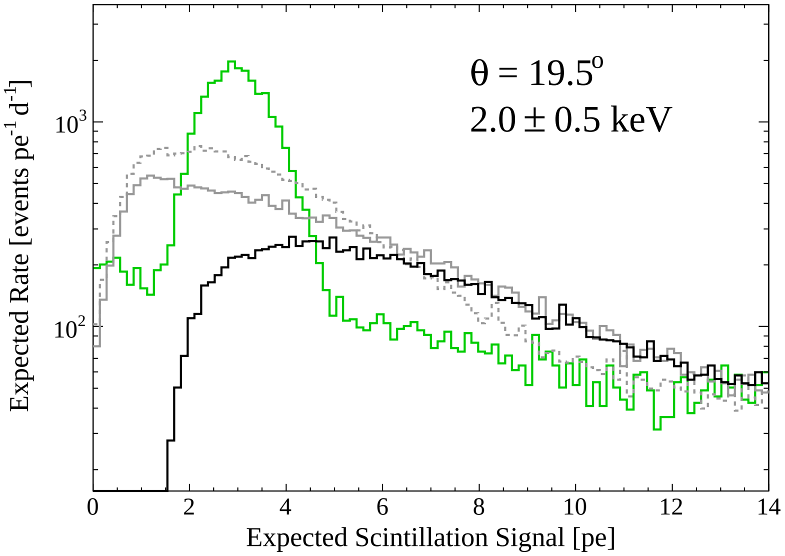

Figure 5.43: Expected recoil energy spectrum (black) for a scattering angle of 19.5°, assuming $\mathcal{L}_{\mathrm{eff}}(2\,\mathrm{keV}) = 0.0634$, along with the recoil energy spectrum without Poisson fluctuations (green), with Poisson fluctuations and finite single photoelectron resolution (dashed gray), with Poisson fluctuations, finite single photoelectron resolution and additional spread (gray solid, see text), and finally additionally including the effect of the trigger efficiency (black).

In the case where the effect of the trigger efficiency roll-off is neglected, the single elastic recoil peak is shifted to considerably lower values of the scintillation signal due to the low number of photoelectrons expected. In addition, once the effect of the trigger efficiency roll-off is taken into account, most of the rate at these low number of photoelectrons is lost. In contrast, the 3 keV measurement does not yet enter this regime where the position of the single elastic recoil peak is heavily biased by Poisson fluctuations in the number of detected photoelectrons.

5.15 Conclusions on Measurements of $\mathcal{L}_{\text{eff}}$

In this chapter we have described in detail the LXe detector, experimental setup, and analysis technique used to perform a new measurement of $\mathcal{L}_{\text{eff}}$ at low energies. The result is the most precise measurement of $\mathcal{L}_{\text{eff}}$ at low energies, to date. Several checks have been performed to demonstrate the robustness of the result. The measurement of $\mathcal{L}_{\text{eff}}$ at low energies is a surprisingly difficult measurement, where threshold effects and efficiencies can bias results. Bringing this project to fruition gave us some insights into which improvements could lead to a more precise measurement or to the elimination of certain systematic uncertainties. This section discusses these ideas.

At low energies, the largest contribution to the uncertainty on $\mathcal{L}_{\text{eff}}$, as mentioned earlier, comes from the uncertainty in recoil energies, through the variation of $\mathcal{L}_{\text{eff}}$ with energy. Obviously nothing can be done about the energy dependence of $\mathcal{L}_{\text{eff}}$ but the uncertainties in recoil energies can be reduced. Since most of the spread comes from the geometrical acceptance of the LXe detector and the liquid scintillators, one obvious solution is to place the neutron generator and the liquid scintillators further away from the LXe detector. Equivalently, one could reduce the size of the LXe detector instead of moving the generator away from it. The contributions to the spread from the neutron generator and liquid scintillator distances have to be taken into account simultaneously since the final elastic recoil energy distribution corresponds to the convolution of the allowed angular range from the generator to the LXe detector with the allowed angular range from the LXe detector to the liquid scintillator. Since the LXe detector and liquid scintillator coincidence rate will diminish rapidly as the neutron generator and the liquid scintillators are taken further away from the LXe detector the easiest solution is probably the use of an array of liquid scintillators. The only limitation in the number of liquid scintillators that could be used, besides the cost of the units, is the available space.

The next most important contribution to the uncertainty on $\mathcal{L}_{\text{eff}}$ is due to the uncertainty in the neutron generator flux. This could be improved by using an independent liquid scintillator detector, perhaps placed in the forward neutron production direction, which would be used to monitor the neutron flux. This would allow the verification of the constancy of the neutron flux over each measurement and reduce dramatically the uncertainty on the flux. A related improvement would be to perform a detection efficiency calibration of the liquid scintillator, probably only at the neutron energy used for the scattering experiment.

A more in-depth characterization of the energy-angle flux of the neutron generator would also benefit a future measurement. The angular straggling of deuterons in the target would be the next effect to incorporate into the neutron generator model. Additionally, by exploiting the correlation between the neutron emission angle and its energy it would also be possible to vary the neutron energy and the neutron flux within the same experimental setup. At deuteron energies of 80 keV, for example, one could vary the neutron energy from ~2.8 to ~2.2 MeV, in the forward and backward direction, respectively. Although the value of $\mathcal{L}_{\mathrm{eff}}$ at higher recoil energies is not as crucial for the interpretation of dark matter searches with LXe detectors, a measurement at energies above 20 keV would also be welcomed to clarify the behavior of the quantity. Such measurements should probably be performed with higher energy neutrons from the $^3\mathrm{H}(d,n)^4\mathrm{He}$ or $^3\mathrm{H}(p,n)^3\mathrm{He}$ reactions to avoid the region of low differential elastic scattering cross section of neutrons on Xe at angles larger than 60° (Fig. 5.33).

We find that our liquid scintillator positioning procedure with the aluminium rules and the laser tripod was adequate. The position uncertainty of the neutron generator is the smallest contribution to the systematic uncertainty on $\mathcal{L}_{\mathrm{eff}}$, followed by the contribution from the uncertainty in the EJ301 neutron detector positions. If the positioning accuracy can be maintained as the liquid scintillators are moved further away from the detector then its contribution to the systematic uncertainty on $\mathcal{L}_{\mathrm{eff}}$ would decrease as the inverse of the distance.

For measurements of $\mathcal{L}_{\mathrm{eff}}$ at low energies, where the efficiency roll-off near threshold cannot be avoided, a comprehensive analysis of the energy dependence of the trigger efficiency is required. In our case we have tried to improve the situation by measuring as directly as possible the efficiency but have faced a disagreement between the expected efficiency and the measured one. Needless to say that one area of improvement could be to try to resolve this discrepancy. More details on the PMT single photoelectron distributions could be used to refine the trigger efficiency simulation. Similarly, additional effects could be added to the modeling of the hardware components, the finite bandwidth of the discriminator for example. In parallel however, some investigation should go in the search for systematic effects in any trigger efficiency measurement performed. For example, in a measurement similar to ours one could think of collimating the ^{22}Na beam such that one would probe only portions of the active LXe volume.

The light detection efficiency will obviously remain one of the parameters with the most influence, almost directly determining the lowest recoil energy measurable. Considering that this LXe detector has the highest light detection efficiency achieved in a LXe detector, precise measurements of $\mathcal{L}_{\mathrm{eff}}$ in the near future at lower energies are probably impractical.

Chapter 6

Dark Matter Results from 100 Live Days of XENON100 Data

The response of the XENON100 detector to electronic recoils and to nuclear recoils was obtained during the during the commission run (`run_07`), which ended on January 12th, 2011. A very low background level of $< 6 \times 10^{-3}\,\mathrm{events\,keV^{-1}\,kg^{-1}\,d^{-1}}$ was also confirmed with data taken during the commissioning run, 11.2 days of which were used to obtain the first dark matter results of XENON100 (Sec. 4.6). All the elements were in place for the start of a science run. A dark matter search (`run_08`) was thus started on January 13th, 2010, 3 weeks after the neutron calibration, and ended on June 8th, 2010. After a neutron calibration one must wait a few weeks for the metastable Xe states produced during the calibration to decay (8.88 d and 11.84 d half-lives), although at 164 keV and 236 keV the γ rays produced do not have a large impact on the background in the energy range for a WIMP search. The summary of the data accumulated during this period (`run_08`) and the calibration and science data acquired in `run_07` is shown in Fig. 6.1.

The total data taking period of the dark matter search is 100.9 live days, after the removal of 18 days in April with the presence of increased electronic noise, and the rejection of ~2% of the exposure due to variations in the operating parameters of the detector. Events with their largest `S1` signal below 160 pe and below the 90% electronic recoil band quantile, in terms of $\log_{10}(\mathtt{S2}/\mathtt{S1})$, were blinded during the data taking. This left most of the electronic recoil events accessible to verify the quality of the data acquired. The calibration data acquired amounted to ~2.9 live days for ^{241}AmBe and 5.8 live days for

^{60}Co. The rate at low energies from a ^{60}Co calibration is such that one day is equivalent to approximately 200 days of background data in the fiducial volume chosen (Sec. 6.1.1).

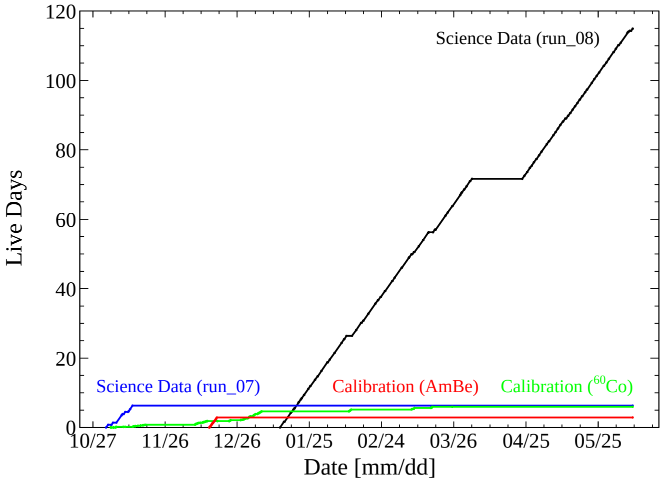

Figure 6.1: Summary of the accumulated science and calibration data from `run_07` and `run_08`. A period of data taking in April was rejected due to an increased electronic noise level. An additional ~2% of the exposure was rejected (not taken into account here) due to variations in detector operating conditions.

The electronic recoil background for this period is higher than the background inferred from the science data of the commissioning run (`run_07`). The value measured is $< 22 \times 10^{-3}\,\mathrm{events\,keV^{-1}\,kg^{-1}\,d^{-1}}$ compared to $< 6 \times 10^{-3}\,\mathrm{events\,keV^{-1}\,kg^{-1}\,d^{-1}}$ for the previous measurement. The additional background is due to ^{85}Kr, introduced into the detector via an air leak during the replacement of the Xe recirculation pump, which took place before the beginning of the dark matter search. The $^{\mathrm{nat}}$Kr concentration inferred was 700 ± 100 ppt compared to 143^{+130}_{-90} ppt previously. This implies an increased uniform background in the TPC from the β decays of ^{85}Kr.

6.1 Analysis

The different components of the analysis chain are very similar to those used for the results presented in Sec. 4.6. The raw data was processed with the event processing software described in Sec. 3.4.3. The neural network based position reconstruction algorithm was used while the positions calculated from the other algorithms were used for consistency checks. The event positions measured were transformed into physical event positions in the TPC with the position correction function described in Sec. 4.3.1, and the S1 and S2 signals were corrected for their spatial dependence (Secs. 4.3.2, 4.3.3, and 4.3.4). The $\mathsf{S2}\,(z)$ correction was smaller than for the previous results with the electron lifetime increasing from $230\,\mu$s to $380\,\mu$s during the data taking period. Lastly, the discrimination parameter was modified to the logarithm of the ratio of the $\mathsf{S2}$ signal from the bottom PMT array, $\mathsf{S2}_b$, to the $\mathsf{S1}$. The more uniform response of the signal of the bottom array as a function of position in the xy plane (Fig. 4.11), and hence smaller relative correction, was the motivation for this choice.

6.1.1 Data Selection

The energy window for the dark matter analysis was chosen between 4 and 30 pe which, from the $\mathcal{L}_{\text{eff}}$ parametrization used (Sec. 6.1.4), corresponds to $8.4 - 44.6\,\text{keV}_{\text{nr}}$. The lower threshold was set at 4 pe for the same reason as the previous dark matter analysis (Sec. 4.6), mostly because the acceptance of the $\mathsf{S1}$ twofold coincidence cut is high and because it allows to differentiate between true low energy $\mathsf{S1}$ signals from spurious electronic noise and other $\mathsf{S1}$-like features. The higher bound was chosen because most of the WIMP-induced nuclear recoils are expected below this energy.

The data selection cuts used can be separated in the same categories as described earlier, basic quality cuts, single scatter cuts, fiducial volume cuts, and consistency cuts. We detail the cuts used in each category.

Basic Quality Cuts

In the category of basic quality cuts, the cuts used are: a signal to noise cut, a $\mathsf{S1}$ coincidence cut, a $\mathsf{S2}$ lower threshold cut, and specific cuts designed to remove infrequent pathological events not compatible with true low energy interactions in the LXe volume. The signal to noise cut requires that the largest $\mathsf{S1}$ and $\mathsf{S2}$ signals comprise at least half of the total signal present in the waveform. The rest of the signal is often due to delayed single electron electron extraction $\mathsf{S2}$ signals (Sec. 4.2.4). The $\mathsf{S1}$ coincidence cut requires, as explained before, that at least two PMT register a signal above 0.35 pe within a $\pm 20\,\text{ns}$ window centered on the highest digitizer sample of the $\mathsf{S1}$ signal. Finally, the lower $\mathsf{S2}$ threshold cut requires events to have at least 300 pe in their largest $\mathsf{S2}$ signal. This is chosen in relation to the $> 99\%$ $\mathsf{S2}$ trigger efficiency above 300 pe.

Single Scatter Cuts

Since WIMPs are expected to scatter only once in the detector, cuts are applied to select events where only one interaction is present in the waveform, that is, in the best of circumstances, a single `S1` peak and a single `S2` peak. However there are several other factors that can produce additional `S1`-like or true `S1` features, as is the case for `S2` peaks. Specifically, additional `S1`-like features can be caused by PMT dark counts, very low yield single electron `S2` signals, or by accidental coincidences between two genuine interactions for example. Additional `S2`-like signals are most often the result of delayed extraction of single electrons.

There are three single scatter cuts applied: a single `S1` cut, a single `S2` cut, and a veto coincidence cut. The single `S1` cut requires that any other `S1` peak present in the waveform, besides the one with the largest PMT coincidence, either be consistent with electronic noise or PMT dark counts, that is, with a coincidence level below 2, or that it be unrelated to the `S2` signal, that is, with a drift time beyond the maximal value or with an uncharacteristically large `S2/S1` ratio. This cut is defined in this manner to keep a high acceptance on low energy events even in the presence of spurious electronic noise and large PMT dark count rates, which can artificially increase the coincidence level above threshold. The single `S2` cut requires that any other `S2` peaks present in the waveform be small enough to be consistent with delayed single electron emission. Finally, the veto coincidence cut, which is the same as the one used for the previous analysis (Sec. 4.6.1), rejects events with a `S1` signal in the veto volume larger than 0.35 pe which are in coincidence with the `S1` peak selected in the target volume.

Fiducial Volume Cut

The fiducial volume is increased to a 48 kg super-ellipsoidal volume, instead of the cylindrical 40 kg used in the previous dark matter results. In general, one would chose the optimal fiducial volume by maximizing the sensitivity given all known backgrounds. Specifically, one would construct the expected three dimensional position distribution of each source of background, statistical leakage from electronic recoils, anomalous leakage from electronic recoils or any other source, neutron-induced nuclear recoils, etc, add all the contributions, find three dimensional contours of equal background rate, and calculate the sensitivity for each contour.

Due to the uniform ^{85}Kr background present for this run, the fiducial volume was optimized on the expected statistical leakage from electronic recoils, from both detector materials and ^{85}Kr. The probability of an event leaking was considered to be independent of position, the event rate itself of course is not independent of position. The fiducial volume functional description chosen that could follow contours of equal rate is that of generalized super-ellipses in the r^2z plane, $\left|r^2/a\right|^m + \left|(z-z_0)/a\right|^n = 1$, with $m, n > 0$. The volume was chosen as large as possible but limited to regions of the TPC where the response of the detector is well understood, that is, away from surfaces since the volume itself is homogeneous. The final choice is shown in Fig. 6.6.

Consistency Cuts

The last category of cuts is consistency cuts, by which is meant cuts that require the S1 and S2 signals, and some of the derived parameters, to be consistent with single scatter interactions within the target. Three such cuts were applied in the analysis, a S2 width cut, a S1 pattern cut, and a position reconstruction cut.

The S2 width cut rejects events whose S2 signal width is inconsistent with that expected from the proportional scintillation signal of an electron cloud created at the z position calculated and drifted to the liquid surface. First, the width of a single electron S2 signal is on the order of $0.4\,\mu$s, which corresponds to the time an electron takes to travel across the 2.5 mm proportional amplification region with a drift velocity of $6.86\,\mathrm{mm}/\mu\mathrm{s}$ at $12\,\mathrm{kV\,cm^{-1}}$ and 2.25 atm. Since the electron cloud diffuses as it drifts from the interaction point to the surface, then we expect the width of the total S2 signal, the sum of all the amplified electron signals, to increase with the depth of the interaction. The S1 pattern cut rejects events whose S1 signal distribution on PMTs is inconsistent with the distribution expected for an event at the position reconstructed. The expected distribution of the S1 signal as a function of position within the TPC is obtained from ^{137}Cs calibration data taken at a low anode voltage to ensure no bias in the reconstructed positions. The expected distribution is simply the probability of a photon emitted at a position (x, y, z) to be detected by PMT i. This cut is designed to remove events with additional energy deposits in charge insensitive regions of the target volume, below the cathode for example. Finally, the position reconstruction cut has two requirements: that the S2 distribution on PMTs of the event be consistent with the expected distribution at the position calculated, and that the position calculated from all three position reconstruction algorithm be consistent. In practice the only true energy deposit events which do not satisfy the position reconstruction cut are events where two interactions occurred in the same z slice, within the double S2 peak resolution of the event processing software (~3 mm).

Cumulative Cut Acceptance

The acceptance was estimated for all cuts except the fiducial volume cut whose acceptance is taken into account by assigning an uncertainty on the fiducial mass. The cut acceptances are estimated using a variety of datasets: Monte Carlo simulations, ^{241}AmBe and ^{60}Co calibration data, and background data outside the blinded region of the dark matter search. Many of the cuts, such as the S2 width cut and the S1 pattern cut are constructed to have a high acceptance on single scatter nuclear recoil events by cutting at fixed quantiles (95% for example) in the distributions. Almost all cuts used have a mild energy dependence, with less than 5% variations over the energy range considered, and a high acceptance: signal to noise ~97%, S2 width ~90%, single S1 ~99%, single S2 ~95%, S1 pattern ~97%. The only exceptions are the S1 coincidence cut and the S2 threshold cut, the latter being responsible for most of the acceptance loss at low energies. The reason for this is easy to understand by looking at the nuclear recoil band calibration (Fig. 4.13). At low energies, the variance of the nuclear recoil band is large and the S2 threshold removes an increasing fraction of nuclear recoils with decreasing energy. To be accurate, those events are not actually all removed by the cut but rather that a trigger is not generated on their S2 signals with high efficiency. This is also exacerbated by the fact that events at longer drift times are more likely to fail to generate a trigger, due to electron attachment to impurities. The efficiency of the cut is thus estimated from a comparison of the measured S1 versus S2 distribution for nuclear recoils and a Monte Carlo simulation. The resulting cumulative cut acceptance for different WIMP masses is shown in Fig. 6.2.

The reason why the cumulative cut acceptance depends on the WIMP mass is not intuitive and deserves some explanation. The first element to the explanation is that for a detector with an energy threshold $Q_<$, and assuming a WIMP galactic escape velocity v_{esc}, there is a WIMP mass below which no recoils will have an energy higher than $Q_<$, given

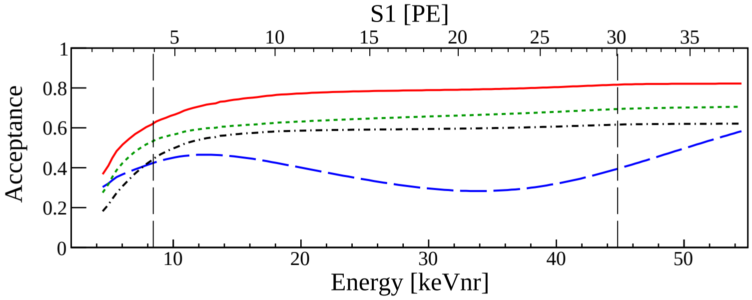

Figure 6.2: Cumulative cut acceptance for single scatter nuclear recoils within the fiducial volume for WIMP masses $m_\chi \geq 50\,\mathrm{GeV}/c^2$ (solid red line), $m_\chi = 10\,\mathrm{GeV}/c^2$ (dotted green line), $m_\chi = 7\,\mathrm{GeV}/c^2$ (dash-dotted black line). The cumulative cut acceptance for the optimum interval parallel analysis (see text), which uses a fixed $\log_{10}(\mathsf{S2}_b/\mathsf{S1})$ discrimination cut is also shown (dashed blue line). Figure from Aprile *et al.* (2011a).

by the condition (see Sec. 1.3.1)

$$Q_< \geq \frac{2m_r^2 v_{\mathrm{esc}}^2}{m_N} \tag{6.1}$$

$$m_\chi \leq \frac{m_N Q_< + \sqrt{2} m_N^{3/2} Q_<^{1/2} v_{\mathrm{esc}}}{2m_N v_{\mathrm{esc}}^2 - Q_<}. \tag{6.2}$$

For a Xe target and the $8.4\,\mathrm{keV_{nr}}$ threshold chosen, using $v_{\mathrm{esc}} = 544\,\mathrm{km/s}$, this corresponds to ~$14\,\mathrm{GeV}/c^2$. The sensitivity below this mass comes from the expectation that the measured scintillation signal of nuclear recoils can fluctuate above the S1 value that corresponds to the energy threshold, due to a finite energy resolution near threshold. Given the low scintillation light detection efficiency, ~0.035 pe/photon, fluctuations of the measured S1 signal near threshold are well approximated by Poisson statistics. However, even if the measured S1 signal can fluctuate above threshold, the S2 signal associated with the event in general does not fluctuate above the S2 trigger threshold. Consequently, the increase in sensitivity from upwards fluctuations of measured scintillation signals is also accompanied by an acceptance loss, via the S2 threshold cut. Even if the S1 signal of nuclear recoils induced by low mass WIMPs can fluctuate above threshold, the probability that the S2 signal be above the trigger threshold (and the S2 threshold cut) decreases for lower WIMP masses.

6.1.2 Profile Likelihood

Usually, the technique employed to calculate limits depends on the expected background in the signal region and on the uncertainty of the prediction. When no background is expected, one typically calculates the 90% confidence upper limit for the WIMP-nucleon cross section using a Poisson distribution with a mean of the observed number of events. In cases where the background is known beforehand and its rate predictable to reasonable accuracy, one normally uses the Feldman-Cousins approach (Feldman and Cousins, 1998) for the calculation of the 90% confidence upper limit for the cross section. Obviously, the resulting limit will be better if this background subtraction approach is used. However, this will result in a penalty if the prediction of the background is not accurate. For cases where there is a potential for the presence of an unexpected background, Yellin's optimum interval method (Yellin, 2002), or its two-dimensional generalization, is often employed. Both of these methods make use of the expected signal distribution in the energy range of the search. However, they are designed to result in upper limits only and do not have a natural extension to a detection claim, in contrast to the Feldman-Cousins method. All of these methods also do not allow to calculate a limit at a given confidence level including systematic uncertainties, which have to be treated separately (as was done for the results of Sec. 4.6.3 with $\mathcal{L}_{\text{eff}}$ for example).

The decision was made beforehand to use a new approach (Aprile *et al.*, 2011c) based on the profile likelihood ratio test to derive the results from the dark matter search. This approach allows the use of the full discrimination parameter space, and hence does not need the definition a priori of a signal region. The testing of both the background-only and the signal plus background hypotheses, regardless of the events observed, provides an objective criteria for a detection claim and does not result in undercoverage of the calculated limit from the so called "flip-flop" problem. It also allows the treatment of systematic uncertainties in a unified manner. A benchmark signal region was nevertheless defined to perform an optimal interval analysis in parallel and also because it allows a direct comparison of the expected background with the observed events.

6.1.3 Background Prediction

The upper bound of the benchmark signal region was defined at a fixed electronic recoil rejection of 99.75%, to provide maximum rejection of the uniform ^{85}Kr background. The lower bound was chosen as the 3-σ contour below the nuclear recoil band. The benchmark signal region is shown in Fig. 6.3, along with a subset of the nuclear recoil band calibration data (gray dots). The band and the signal region are shown on the discrimination axis with the electronic recoil band mean subtracted. The other boundaries are the energy range ($8.4 - 44.6\,\mathrm{keV_{nr}}$) and the $\mathsf{S2} = 300\,\mathrm{pe}$ software threshold.

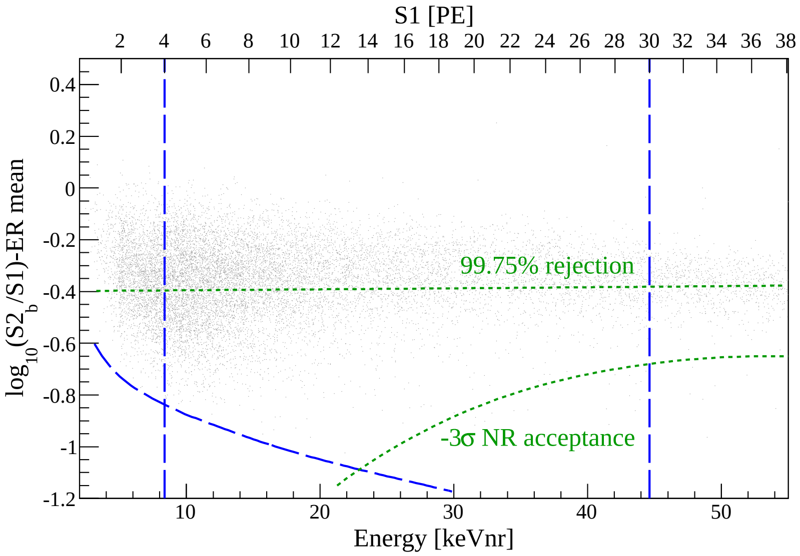

Figure 6.3: Benchmark signal region defined for the parallel optimum interval analysis bounded above at fixed electronic recoil rejection of 99.75% and below by the 3-σ contour of the nuclear recoil band.

The background in the signal region has a contribution from the statistical leakage from the electronic recoil background, anomalous leakage, and neutron-induced nuclear recoils. The statistical leakage, dominated by the ^{85}Kr background, was estimated from the non-blinded portion of the electronic recoil band. The total number of events expected from statistical leakage in the benchmark region for the 100.9 live days exposure is 1.14 ± 0.48. The anomalous leakage contribution to the background can in principle have many sources. As mentioned earlier, the electronic recoil band is empirically measured to be Gaussian distributed in $\log_{10}(\mathsf{S2}/\mathsf{S1})$ at the ~99.5% level, and this is also the case here in terms of $\log_{10}(\mathsf{S2}_b/\mathsf{S1})$ when only the bottom PMT array signal is used. Non-Gaussian events are observed however in electronic recoil calibration data. One event topology, initially identified in the XENON10 detector (Angle *et al.*, 2008a), and which can produce a non-Gaussian contribution is that of events with an additional scatter in a charge insensitive region of the target volume. The $\mathsf{S2}_b/\mathsf{S1}$ ratio is then artificially reduced due to the missing charge signal of the additional interaction. The expected rate of such event topologies and their spatial distribution was estimated via Monte Carlo simulations and is consistent with the rate observed in ^{60}Co calibration data when such events are selected by their $\mathsf{S1}$ PMT distribution. The observed anomalous leakage event rate in ^{60}Co calibration data appears higher than from that contribution alone however. The total anomalous leakage contribution is thus estimated by making the following assumptions. The first two assumptions are that this rate is uniformly distributed in energy and that ^{60}Co data is representative of the background in the energy range of the dark matter search. The last assumption is that the fraction of the electronic recoil background rate from ^{85}Kr do not contribute any anomalous leakage. Since ^{85}Kr undergoes β decay this is a reasonable assumption, at least for any contribution through a process similar as described earlier with additional interactions in a charge insensitive region. The total number of anomalous leakage events predicted in the fiducial volume and energy range for the 100.9 live days exposure is $0.56^{+0.21}_{-0.27}$.

The neutron-induced nuclear recoil background contribution is composed of muon-induced neutrons and neutrons produced by (α, n) and spontaneous fission reactions in the detector materials and the passive shield. The muon-induced neutron background dominates the nuclear recoil background with 70% of the expected rate, estimated from a simulation of the experimental site of the XENON100 experiment where muons are propagated according to the measured muon flux. The neutron energy spectrum and neutron yield from (α, n) and spontaneous fission reactions in detector materials are calculated from the measured radioactive contaminations (Aprile *et al.*, 2011d). These results are then used as input to a simulation that propagates the produced neutrons in the XENON100 detector geometry and determines the number of neutron-induced nuclear recoils in the fiducial volume and energy range that should be produced. The total number of single scatter nuclear recoils inside the fiducial volume and within the energy range chosen for the 100.9 live days of exposure is $0.31^{+0.22}_{-0.11}$. This corresponds to a number of single scatter nuclear recoil events in the benchmark signal region of $0.11^{+0.08}_{-0.04}$.

The total prediction in the benchmark signal region for the 48 kg fiducial volume and for the 100.9 days exposure is thus 1.8 ± 0.6 events.

6.1.4 Nuclear Recoil Equivalent Energy

The new measurement of $\mathcal{L}_{\text{eff}}$ at low energies discussed in Chap. 5 is the most precise measurement of this quantity at low energies, to date. The trend observed is of a slowly decreasing $\mathcal{L}_{\text{eff}}$ towards low energies. This new measurement has been taken into account for the parametrization of the energy dependence of $\mathcal{L}_{\text{eff}}$. As was the case for the parametrization used for the dark matter results described in Sec. 4.6, all published direct measurements of $\mathcal{L}_{\mathrm{eff}}$ are used in the procedure to derive the parametrization. The parametrization, together with its uncertainty, are obtained from a recoil energy dependent Gaussian fit to all measurements of $\mathcal{L}_{\mathrm{eff}}$. Below $3\,\mathrm{keV_{nr}}$, the $\mathcal{L}_{\mathrm{eff}}$ parametrization is logarithmically extrapolated to zero scintillation at $1\,\mathrm{keV_{nr}}$. The resulting parametrization and its uncertainty is shown in Fig. 6.4 along with the data from direct measurements of $\mathcal{L}_{\mathrm{eff}}$.

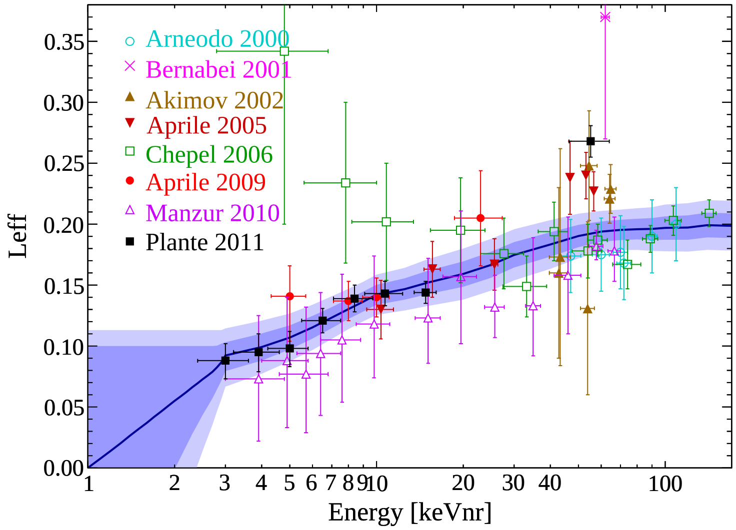

Figure 6.4: Parametrization used (blue line) for the energy dependence of $\mathcal{L}_{\mathrm{eff}}$. Below $3\,\mathrm{keV_{nr}}$, the parametrization is logarithmically extrapolated to zero scintillation at $1\,\mathrm{keV_{nr}}$. The dark blue and light blue shaded regions correspond to the 1-σ and 2-σ contours of the parametrization. The parametrization used is strongly supported by the recent $\mathcal{L}_{\mathrm{eff}}$ measurement described in Chap. 5. Figure from Aprile *et al.* (2011a).

6.2 Results

The data was unblinded on April 3rd 2011 and the analysis machinery was unleashed on the 100.9 days of exposure. After unblinding, a total of six events were observed in the predefined benchmark signal region. Inspection revealed, however, that three out of six events had a `S1` peak candidate clearly part of an electronic noise contamination in the waveform. One such event is shown in Fig. 6.7. The `S1` peak candidate is selected from part of a periodic structure present in the waveform. The `S1` coincidence is marginally fulfilled because the electronic noise is correlated on several PMT channels. The electronic noise structure even appears in channels where the associated PMT is not biased to high voltage. The events from the noise population mostly lie below the S1 analysis threshold of 4 pe but three of them leaked in the signal region. Events with their largest S1 peak candidate part of this noise population can be identified and rejected with a cut on the PMT coincidence level that considers the fact that the noise is correlated on other channels and by cutting on the S1 width. The combined acceptance of those post-unblinding cuts on single scatter nuclear recoils is essentially 100%.

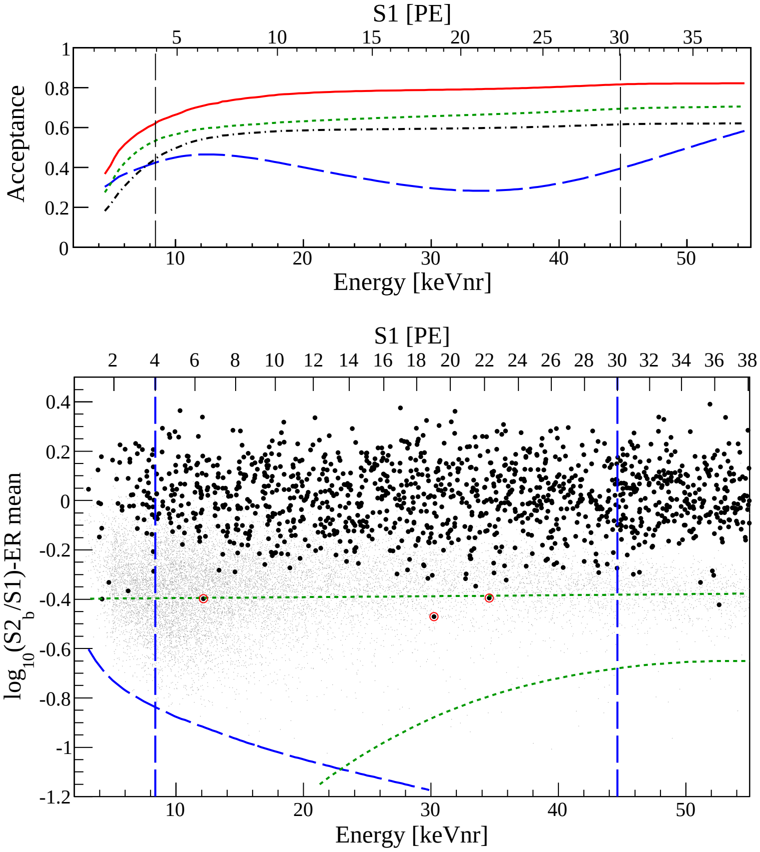

Figure 6.5: Cumulative cut acceptance (top, same as Fig. 6.2) and observed event distribution (bottom, black dots) in $\log_{10}(\mathsf{S2}_b/\mathsf{S1})$ as function of energy for the 100.9 live days exposure and passing all cuts (including post-unblinding cuts). Three candidate events remain (red circles) while 1.8 ± 0.6 events were expected as background. A subset of the ^{241}AmBe calibration data is also shown (gray dots). The dark matter search region was chosen between 4 and 30 pe ($8.4 - 44.6\,\mathrm{keV_{nr}}$) (vertical dashed blue lines) and above the S2 software threshold (curved dashed blue line). The optimum interval additionally uses a fixed 99.75% electronic recoil rejection cut (horizontal dashed green line) and the lower 3-σ contour of the nuclear recoil band (curved dashed green line). Figures from Aprile *et al.* (2011a).

After the application of the post-unblinding cuts to remove the noise population, three events are left in the benchmark signal region. Fig. 6.5 shows the observed event distribution (black dots) in $\log_{10}(\mathsf{S2}_b/\mathsf{S1})$ as function of energy for the 100.9 live days exposure (black dots) and the three candidate events (red circles). These events occurred on January 3rd, February 2nd, and June 3rd 2010, and have energies of $30.2\,\mathrm{keV_{nr}}$, $34.6\,\mathrm{keV_{nr}}$, and $12.1\,\mathrm{keV_{nr}}$, respectively. The waveforms of the three candidate events are shown in Figs. 6.8, 6.9, and 6.10.

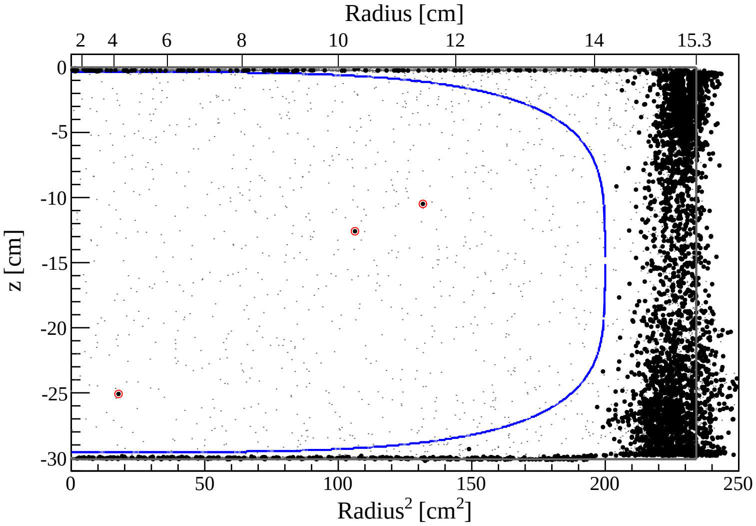

Figure 6.6: Spatial distribution of all events (small dots) within the energy range $8.4 - 44.6\,\mathrm{keV_{nr}}$ and passing all cuts (including post-unblinding cuts), not considering the fiducial volume cut, for the 100.9 live days, along with events below the 99.75% electronic recoil rejection line (large black dots). The three events remaining in the signal region are highlighted with red circles. The 48 kg fiducial volume cut chosen is also shown (dashed blue line). Only events within the fiducial volume shown here are in Fig. 6.5. Figure from Aprile *et al.* (2011a).

The spatial distribution of all events within the energy range $8.4-44.6\,\mathrm{keV_{nr}}$ and passing all cuts (including post-unblinding cuts), not considering the fiducial volume cut, are shown in Fig. 6.6. The three candidate events are not close to any of the boundaries of the fiducial volume hence the result would be the same under moderate variations of the fiducial volume cut. This figure is a beautiful and striking visual representation of the power of self-shielding as a background reduction technique. All events below the 99.75% electronic rejection line near the edges are efficiently removed by limiting the analysis to the homogeneous LXe volume. The origin of those low charge yield events (low $\mathsf{S2}_b/\mathsf{S1}$) is likely ionization electron losses near the walls of the chamber where the electric field lines bend near the field shaping wires and do not all lead to the liquid surface. An inhomogeneous detector response near its boundaries is practically impossible to avoid.

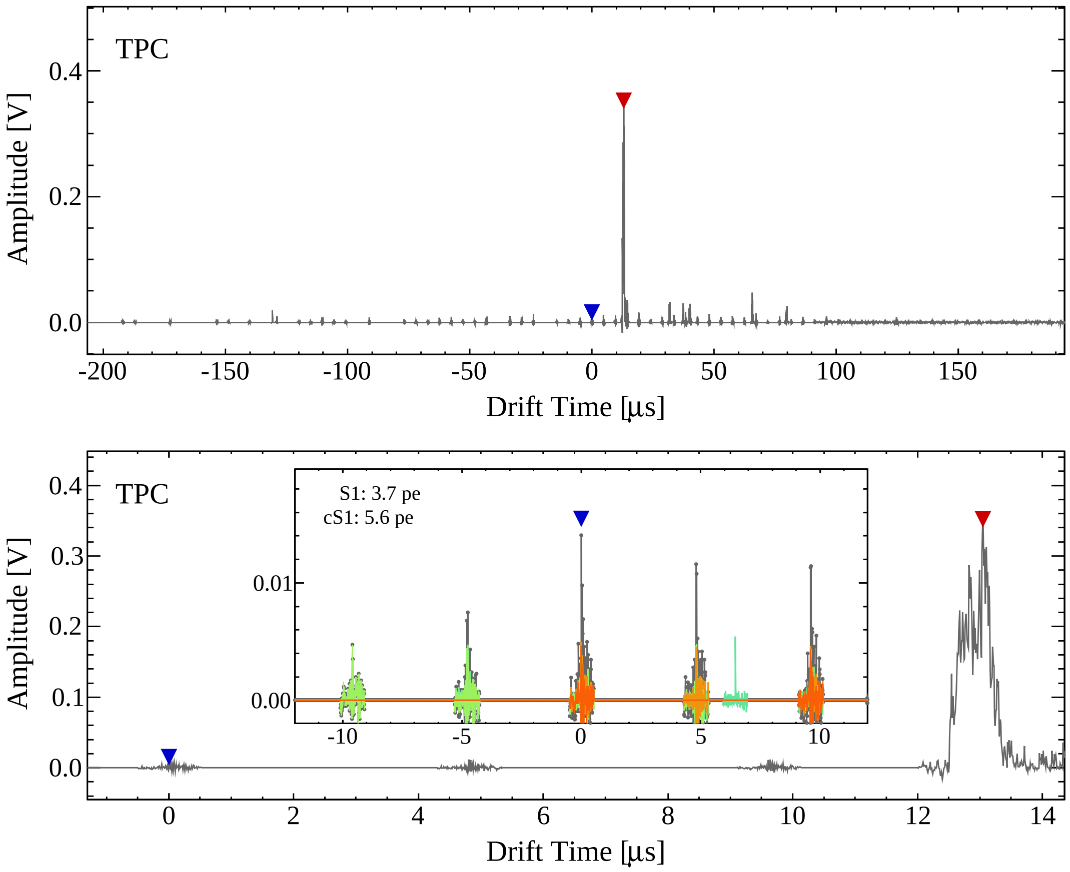

Figure 6.7: Summed waveform (gray line) and individual TPC PMT channel waveforms (color lines) of an event with an increased noise level where a S1 peak candidate (blue triangle) is selected from the periodic noise structure. The S2 peak candidate is indicated by a red triangle. No signal is registered in the veto (waveform not shown).

When considering the expectation from background of 1.8 ± 0.6 events, the observation of three events does not constitute evidence for the presence of a dark matter scattering signal in the data. In fact, the Poisson probability that a background process with an expectation of 1.8 ± 0.6 events yields an observation of 3 or more events is 28%. The p-value of the background-only hypothesis in the statistical analysis using the profile likelihood is 31%, not providing any evidence for a signal excess either. A limit on the WIMP-nucleon spin-independent elastic scattering cross section was calculated where it was assumed that WIMPs are distributed in an isothermal halo characterized by $v_0 = 220\,\mathrm{km/s}$, galactic escape velocity $v_{\mathrm{esc}} = 544^{+64}_{-46}\,\mathrm{km/s}$, and a density $\rho_0 = 0.3\,\mathrm{GeV}\,c^{-2}\,\mathrm{cm}^{-3}$. As was done in the previous dark matter analysis (Sec. 4.6.3), the S1 signal fluctuations near threshold are

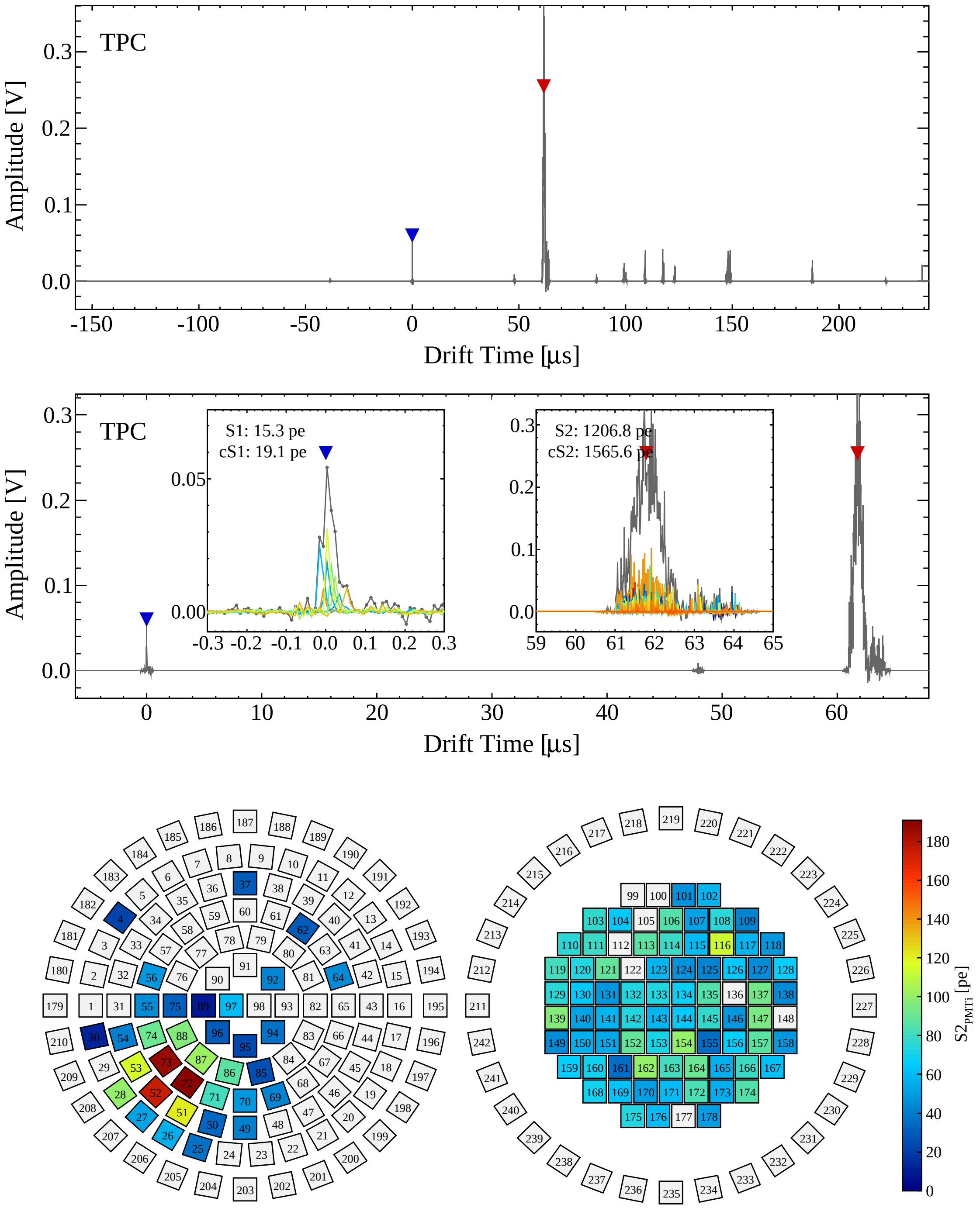

Figure 6.8: Summed waveform (gray line) and individual TPC PMT channel waveforms (color lines) of candidate event no. 1 (top). The position of the S1 (blue triangle) and S2 (red triangle) peak candidates is also indicated. No signal is registered in the veto (waveform not shown). The S2 signal PMT distribution is also shown (bottom).

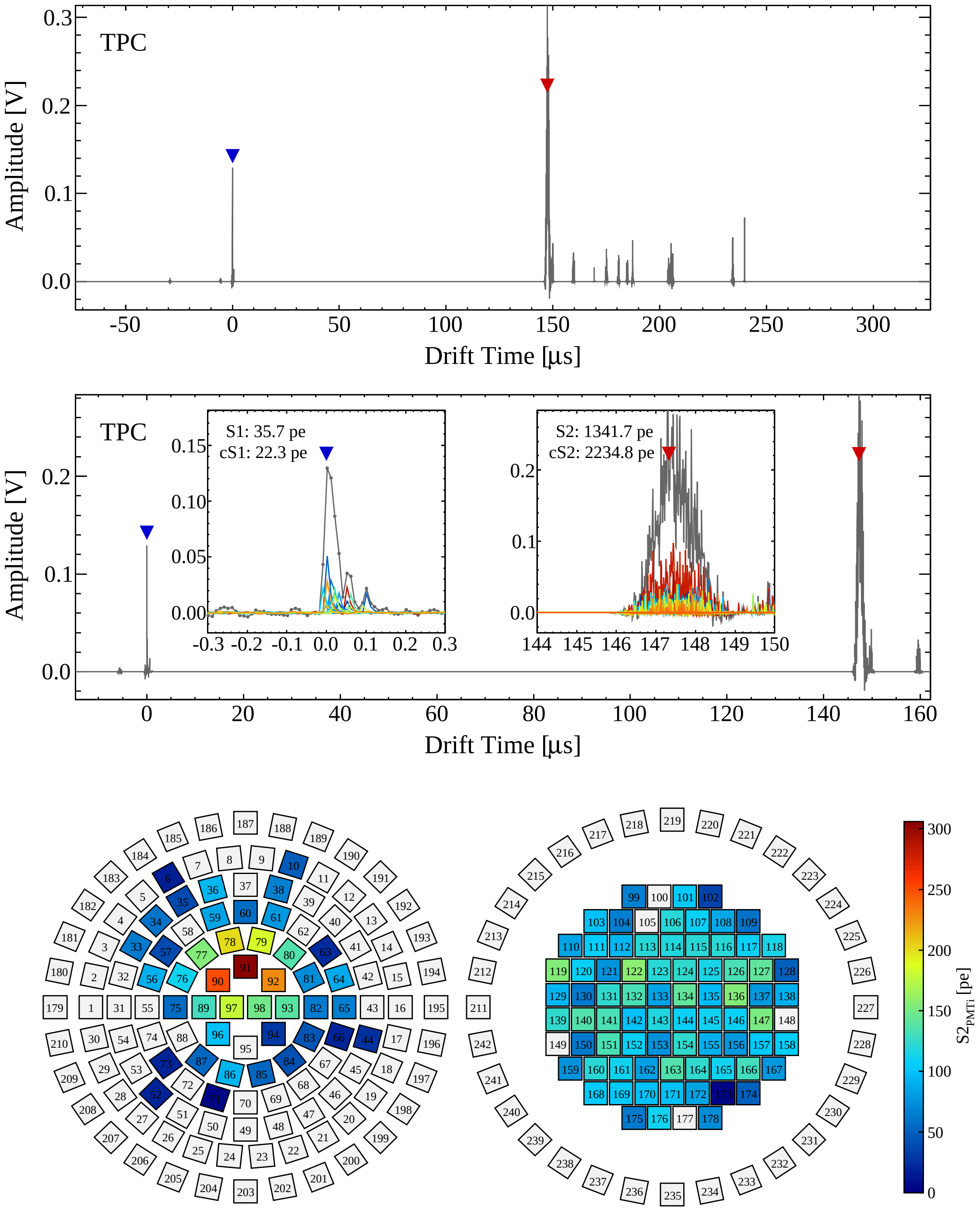

Figure 6.9: Summed waveform (gray line) and individual TPC PMT channel waveforms (color lines) of candidate event no. 2 (top). The position of the S1 (blue triangle) and S2 (red triangle) peak candidates is also indicated. No signal is registered in the veto (waveform not shown). The S2 signal PMT distribution is also shown (bottom).

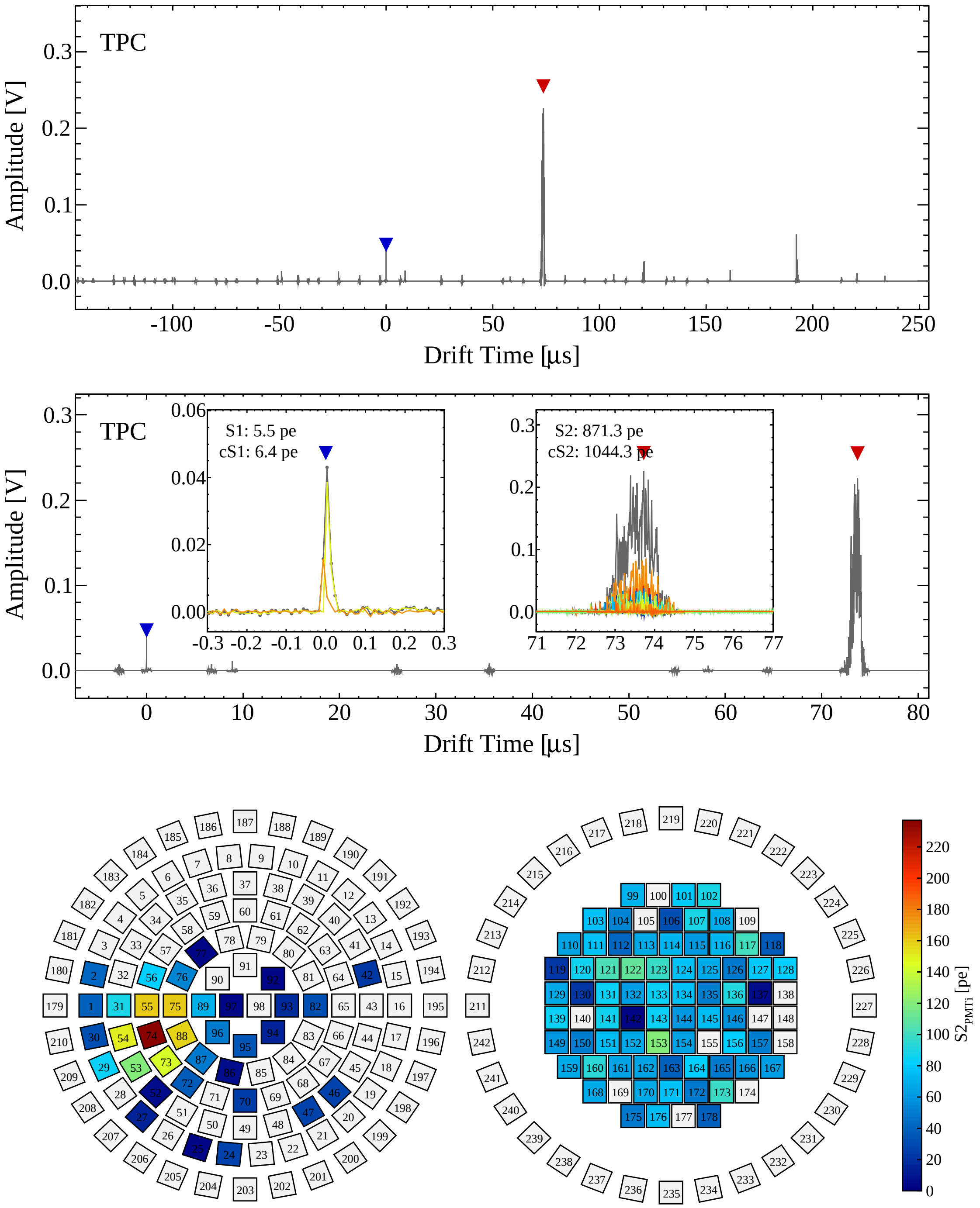

Figure 6.10: Summed waveform (gray line) and individual TPC PMT channel waveforms (color lines) of candidate event no. 3 (top). The position of the S1 (blue triangle) and S2 (red triangle) peak candidates is also indicated. No signal is registered in the veto (waveform not shown). The S2 signal PMT distribution is also shown (bottom).

assumed to be described by Poisson statistics, due to the small PMT S1 scintillation light detection probability. The uncertainties in the energy scale from the $\mathcal{L}_{\text{eff}}$ parameterization (Fig. 6.4) and in the galactic escape velocity are profiled out and incorporated into the limit. The resulting 90% confidence upper limit on the WIMP-nucleon spin-independent elastic scattering cross section is shown in Fig. 6.11 (blue line).

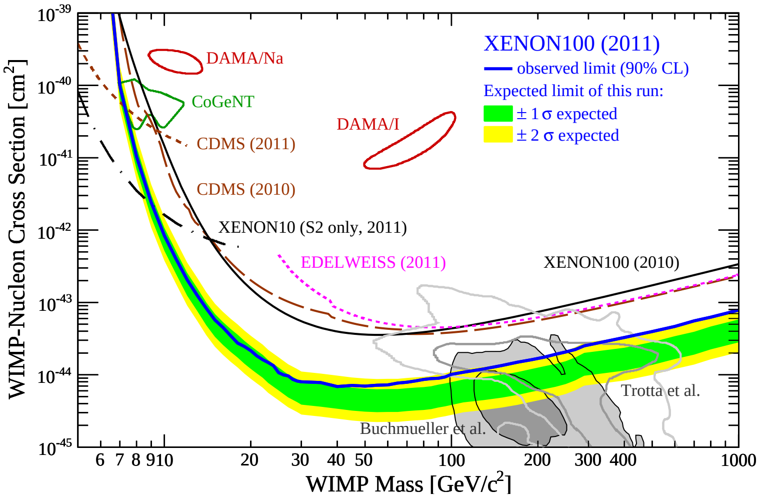

Figure 6.11: 90% confidence upper limit on the spin-independent WIMP-nucleon elastic scattering cross section as a function of WIMP mass from the 100.9 live days of XENON100 data acquired in 2010 (`run_08`) (blue line). The expected sensitivity (1-σ and 2-σ) of the 100.9 days exposure is also shown (green and yellow bands), along with the exclusion limit from the XENON100 first dark matter results (Aprile *et al.*, 2010), and from other direct detection experiments, EDELWEISS (Armengaud *et al.*, 2011), CDMS (2009) (Ahmed *et al.*, 2010), CDMS (2011) (Ahmed *et al.*, 2011), and XENON10 (2011) (Angle *et al.*, 2011). The expectations from theoretical models (Buchmueller *et al.*, 2011; Trotta *et al.*, 2008), and the 90% confidence areas favored by the CoGeNT (Aalseth *et al.*, 2011a) and DAMA (Savage *et al.*, 2009) are also shown. Figure from Aprile *et al.* (2011a).

The limit has a minimum of $7.0 \times 10^{-45}\,\text{cm}^2$ at a WIMP mass of $50\,\text{GeV}/c^2$. As mentioned before, the limit already includes the uncertainties associated with the energy dependence of $\mathcal{L}_{\text{eff}}$, as parametrized in Fig. 6.4, and the galactic escape velocity. The robustness was tested further by assuming no extrapolation of $\mathcal{L}_{\text{eff}}$ to energies below $3\,\text{keV}_{\text{nr}}$ and the impact is negligible at $m_\chi = 10\,\text{GeV}/c^2$. The sensitivity of the 100.9 days exposure (green and yellow bands) is computed by generating a large number of possible outcomes from hypothetical XENON100 dark matter searches with no signal with this exposure. The limit obtained is worst than the expected sensitivity at higher WIMP masses due to the presence of the two candidate events at higher recoil energy. This new limit excludes a large fraction of previously unexplored parameter space and constitutes an improvement of a factor ~4-5 over the previous XENON100 dark matter result. This new limit makes the interpretation of the CoGeNT (Aalseth *et al.*, 2011a) and DAMA (Savage *et al.*, 2009) signals as being due to light mass WIMPs even harder to reconcile with our results. In more general terms, the result shows the potential of low-background liquid noble gas detectors to detect WIMP dark matter in the near future.

6.3 Concluding Remarks

In this thesis we have described the research conducted in the context of the XENON100 dark matter search experiment: the initial simulation results and ideas that influenced the design, the construction and assembly steps, the detector and its subsystems (Chap. 3), a subset of the calibration results of the detector (Chap. 4), details on a new measurement of the scintillation efficiency of low-energy nuclear recoils in LXe (Chap. 5), and finally dark matter exclusion limits (Chap. 6).

The rapid scale up in target mass of liquid noble gas detectors (Alner *et al.*, 2007; Angle *et al.*, 2008a; Aprile *et al.*, 2010; Lebedenko *et al.*, 2009a; Minamino, 2010) and the simultaneous reduction in backgrounds show the potential of this technology to detect WIMP dark matter in the near future. Among the challenges that will need to be met as these detectors continue to increase in size, the purity of the detection medium, both impurities that attenuate the charge signal and radioactive impurities, the electronic recoil calibration, and the understanding of the response of the medium to low-energy nuclear recoils seem to require the most attention. Large purification speeds will certainly help in achieving the desired levels of electronegative impurities but measures will need to be taken to prevent the introduction of even extremely minute amounts of radioactive contaminants. As the electronic recoil background levels are reduced, so does the ability of the detection medium to be probed with external sources, especially since a simple increase of the source activity is not a viable solution due to the inherent dead time of large TPCs. The most promising approach is probably that of uniform calibration of the volume with isotopes that can be subsequently removed (through cryogenic distillation or the use of high temperature getters). In order to claim a discovery, it is clear that future experiments will need a robust understanding of the electronic and nuclear recoil background. The exponential dependence of the sensitivity to WIMPs with energy threshold also makes clear the need to continue to further our understanding of the low-energy response of the detector medium.

Whatever the outcome, the path surely is one that will be filled with interesting questions, rewarding challenges, and unexpected discoveries that ultimately broaden our understanding of the universe.

Bibliography

Aalseth, C. *et al.* (CoGeNT), *Experimental Constraints on a Dark Matter Origin for the DAMA Annual Modulation Effect*, Phys. Rev. Lett., **101** (2008), 251301.

Aalseth, C. E., *et al.* (CoGeNT), *Results from a Search for Light-Mass Dark Matter with a p-Type Point Contact Germanium Detector*, Phys. Rev. Lett., **106** (2011a), 131301.

Aalseth, C. E., *et al.* (CoGeNT), *Search for an Annual Modulation in a p-Type Point Contact Germanium Dark Matter Detector*, Phys. Rev. Lett., **107** (2011b), 141301.

Abe, K. *et al.* (XMASS), *The XMASS experiment*, J. Phys. Conf. Ser., **120** (2008), 042022.

Abe, K. *et al.* (XMASS), *Distillation of Liquid Xenon to Remove Krypton*, Astropart. Phys., **31** (2009), 290.

Ackerman, N. *et al.* (EXO), *Observation of Two-Neutrino Double-Beta Decay in* ^{136}Xe *with EXO-200*, (2011), `arXiv:1108.4193`.

Agostinelli, S. *et al.* (GEANT4), *GEANT4: A Simulation Toolkit*, Nucl. Instrum. Meth. Phys. Res., Sect. A, **506** (2003), 250.

Ahmed, Z. *et al.* (CDMS), *Search for Weakly Interacting Massive Particles with the First Five-Tower Data from the Cryogenic Dark Matter Search at the Soudan Underground Laboratory*, Phys. Rev. Lett., **102** (2009), 011301.

Ahmed, Z. *et al.* (CDMS-II), *Dark Matter Search Results from the CDMS II Experiment*, Science, **327** (2010), 1619.

Ahmed, Z. *et al.* (CDMS-II), *Results from a Low-Energy Analysis of the CDMS II Germanium Data*, Phys. Rev. Lett., **106** (2011), 131302.

Akerib, D. *et al.* (CDMS), *First Results from the Cryogenic Dark Matter Search in the Soudan Underground Lab*, Phys. Rev. Lett., **93** (2004), 211301.

Akerib, D. *et al.* (CDMS), *Limits on Spin-Independent Wimp-Nucleon Interactions from the Two-Tower Run of the Cryogenic Dark Matter Search*, Phys. Rev. Lett., **96** (2006a), 011302.

Akerib, D., *et al.*, *The SuperCDMS Proposal for Dark Matter Detection*, Nucl. Instrum. Meth. Phys. Res., Sect. A, **559** (2006b), 411.

Akimov, D. *et al.*, *Measurements of Scintillation Efficiency and Pulse-Shape for Low Energy Recoils in Liquid Xenon*, Phys. Lett. B, **524** (2002), 245.

Alner, G., *et al.*, *The DRIFT-II Dark Matter Detector: Design and Commissioning*, Nucl. Instrum. Meth. Phys. Res., Sect. A, **555** (2005), 173.

Alner, G. J. *et al.* (ZEPLIN-II), *First Limits on WIMP Nuclear Recoil Signals in ZEPLIN-II: A Two Phase Xenon Detector for Dark Matter Detection*, Astropart. Phys., **28** (2007), 287.

Alton, D. *et al.* (DarkSide), *DarkSide-50: A Direct Search for Dark Matter with New Techniques for Reducing Background*, 2011, `http://www.fnal.gov/directorate/program_planning/Nov2009PACPublic/DarkSideProposal.pdf`.

Angle, J. *et al.* (XENON10), *First Results from the XENON10 Dark Matter Experiment at the Gran Sasso National Laboratory*, Phys. Rev. Lett., **100** (2008a), 021303.

Angle, J. *et al.* (XENON10), *Limits on Spin-Dependent WIMP-Nucleon Cross-Sections From the XENON10 Experiment*, Phys. Rev. Lett., **101** (2008b), 091301.

Angle, J. *et al.* (XENON10), *A Search for Light Dark Matter in XENON10 Data*, Phys. Rev. Lett., **107** (2011), 051301.

Angloher, G. *et al.*, *Commissioning Run of the CRESST-II Dark Matter Search*, Astropart. Phys., **31** (2009), 270 .

Aprile, E., *et al.*, *Proportional Light in a Dual-Phase XENON Chamber*, IEEE Trans. Nucl. Sci., **51** (2004), 1986.

Aprile, E. *et al.*, *Scintillation Response of Liquid Xenon to Low Energy Nuclear Recoils*, Phys. Rev. D, **72** (2005), 072006.

Aprile, E., *et al.*, *Noble Gas Detectors*, Wiley, Weinheim, 2006a.

Aprile, E., *et al.*, *Simultaneous Measurement of Ionization and Scintillation from Nuclear Recoils in Liquid Xenon for a Dark Matter Experiment*, Phys. Rev. Lett., **97** (2006b), 081302.

Aprile, E., *et al.*, *Observation of Anticorrelation Between Scintillation and Ionization for MeV Gamma Rays in Liquid Xenon*, Phys. Rev. B, **76** (2007), 014115.

Aprile, E. *et al.*, *New Measurement of the Relative Scintillation Efficiency of Xenon Nuclear Recoils Below 10 keV*, Phys. Rev. C, **79** (2009), 045807.

Aprile, E. *et al.* (XENON100), *First Dark Matter Results from the XENON100 Experiment*, Phys. Rev. Lett., **105** (2010), 131302.

Aprile, E. *et al.* (XENON100), *Dark Matter Results from 100 Live Days of XENON100 Data*, Phys. Rev. Lett., **107** (2011a), 131302.

Aprile, E. *et al.* (XENON), *Design and Performance of the XENON10 Dark Matter Experiment*, Astropart. Phys., **34** (2011b), 679.

Aprile, E. *et al.* (XENON100), *Likelihood Approach to the First Dark Matter Results from XENON100*, Phys. Rev. D, **84** (2011c), 052003.

Aprile, E., *et al.* (XENON100), *Material Screening and Selection for XENON100*, Astropart. Phys., **35** (2011d), 43.

Aprile, E. *et al.* (XENON100), *Study of the Electromagnetic Background in the XENON100 Experiment*, Phys. Rev. D, **83** (2011e), 082001.

Aprile, E. *et al.* (XENON100), *The XENON100 Dark Matter Experiment*, (2011f), `arXiv:1107.2155`.

Archambault, S., *et al.*, *Dark Matter Spin-Dependent Limits for WIMP Interactions on F-19 by PICASSO*, Phys. Lett. B, **682** (2009), 185.

Armengaud, E. *et al.* (EDELWEISS), *Final Results of the EDELWEISS-II WIMP Search Using a 4-kg Array of Cryogenic Germanium Detectors with Interleaved Electrodes*, Phys. Lett. B, **702** (2011), 329.

Arneodo, F. *et al.*, *Scintillation Efficiency of Nuclear Recoil in Liquid Xenon*, Nucl. Instrum. Meth. Phys. Res., Sect. A, **449** (2000), 147.

Asztalos, S. *et al.* (ADMX), *A SQUID-Based Microwave Cavity Search for Dark-Matter Axions*, Phys. Rev. Lett., **104** (2010), 041301.

Asztalos, S. J., *et al.*, *Searches for Astrophysical and Cosmological Axions*, Ann. Rev. Nucl. Part. Sci., **56** (2006), 293.

Atrazhev, V., *et al.*, *Electron Transport Coefficients in Liquid Xenon*, in *Dielectric Liquids, 2005. ICDL 2005. 2005 IEEE International Conference on*, pp. 329–332, 2005.

Bakale, G., Sowada, U., and Schmidt, W. F., *Effect of an Electric Field on Electron Attachment to Sulfur Hexafluoride, Nitrous Oxide, and Molecular Oxygen in Liquid Argon and Xenon*, J. Phys. Chem., **80** (1976), 2556.

Barabanov, I. R., Gavrin, V. N., and Pshukov, A. M., *Liquid Xenon Scintillation Spectrometer*, Nucl. Instrum. Meth. Phys. Res., Sect. A, **254** (1987), 355.

Battat, J. B. R., *et al.*, *DMTPC: Dark Matter Detection with Directional Sensitivity*, (2010), `arXiv:1012.3912`.

Begeman, K., Broeils, A., and Sanders, R., *Extended Rotation Curves of Spiral Galaxies: Dark Haloes and Modified Dynamics*, Mon. Not. Roy. Astron. Soc., **249** (1991), 523.

Behnke, E. *et al.* (COUPP Collaboration), *Improved Spin-Dependent WIMP Limits from a Bubble Chamber*, Science, **319** (2008), 933.

Belogurov, S., *et al.*, *High Pressure Gas Scintillation Drift Chamber With Photomultipliers Inside of Working Medium*, in *Nuclear Science Symposium and Medical Imaging Conference Record, 1995., 1995 IEEE*, vol. 1, pp. 519–523, 1995.

Benetti, P. *et al.*, *First Results from a Dark Matter Search with Liquid Argon at 87K in the Gran Sasso Underground Laboratory*, Astropart. Phys., **28** (2008), 495 .

Berger, M., *et al.*, *ASTAR, Stopping Power and Range Tables for Helium Ions*, 2005a, `http://physics.nist.gov/PhysRefData/Star/Text/ASTAR.html`.

Berger, M., *et al.*, *ESTAR, Stopping Power and Range Tables for Electrons*, 2005b, `http://physics.nist.gov/PhysRefData/Star/Text/ESTAR.html`.

Berger, M., *et al.*, *PSTAR, Stopping Power and Range Tables for Protons*, 2005c, `http://physics.nist.gov/PhysRefData/Star/Text/PSTAR.html`.

Berger, M., *et al.*, *XCOM: Photon Cross Section Database*, 2010, `http://physics.nist.gov/xcom`.

Bernabei, R. *et al.*, *Light Response of a Pure Liquid Xenon Scintillator Irradiated with 2.5-MeV Neutrons*, Eur. Phys. J. direct C, **3** (2001), 11.

Bernabei, R. *et al.*, *First Results from DAMA/LIBRA and the Combined Results with DAMA/NaI*, Eur. Phys. J. C, **56** (2008), 333.

Boulay, M. and Hime, A., *Technique for Direct Detection of Weakly Interacting Massive Particles Using Scintillation Time Discrimination in Liquid Argon*, Astropart. Phys., **25** (2006), 179.

Bradač, M., *et al.*, *Revealing the Properties of Dark Matter in the Merging Cluster MACS J0025.4-1222*, Astrophys. J., **687** (2008), 959.

Bragg, W. H. and Kleeman, R., *On the α-Particles of Radium, and Their Loss of Range in Passing Through Various Atoms and Molecules*, Philos. Mag., **10** (1905), 318.

Bravin, M. *et al.*, *Simultaneous Measurement of Phonons and Scintillation Light for Active Background Rejection in the CRESST experiment*, Nucl. Instrum. Meth. Phys. Res., Sect. A, **444** (2000), 323.

Buchmueller, O., *et al.*, *Implications of Initial LHC Searches for Supersymmetry*, Eur. Phys. J. C, **71** (2011), 1634.

CAEN, *CAEN*, , `http://www.caen.it/`.

Cebrián, S. *et al.*, *First Results of the ROSEBUD Dark Matter Experiment*, Astroparticle Physics, **15** (2001), 79.

Chadwick, M., *et al.*, *ENDF/B-VII.0: Next Generation Evaluated Nuclear Data Library for Nuclear Science and Technology*, Nuclear Data Sheets, **107** (2006), 2931.

Chasman, C., *et al.*, *Band-Gap Effects in the Stopping of Ge-72* Atoms in Germanium*, Phys. Rev. Lett., **21** (1968), 1430.

Chepel, V. *et al.*, *Scintillation Efficiency of Liquid Xenon for Nuclear Recoils With the Energy Down to 5-keV*, Astropart. Phys., **26** (2006), 58.

Clowe, D., *et al.*, *A Direct Empirical Proof of the Existence of Dark Matter*, Astrophys. J. Lett., **648** (2006), L109.

Cohen, M. H. and Lekner, J., *Theory of Hot Electrons in Gases, Liquids, and Solids*, Phys. Rev., **158** (1967), 305.

Collar, J. I., *Light WIMP Searches: The Effect of the Uncertainty in Recoil Energy Scale and Quenching Factor*, (2010), `arXiv:1010.5187`.

Collar, J. I., *A Realistic Assessment of the Sensitivity of XENON10 and XENON100 to Light-Mass WIMPs*, (2011), `arXiv:1106.0653`.

Conti, E. *et al.*, *Correlated Fluctuations Between Luminescence and Ionization in Liquid Xenon*, Phys. Rev. B, **68** (2003), 054201.

Csikai, J., *Handbook of Fast Neutron Generators*, vol. 1, CRC Press, Boca Raton, Florida, 1987.

Dahl, C. E., *The Physics of Background Discrimination in Liquid Xenon, and First Results from Xenon10 in the Hunt for WIMP Dark Matter.*, Ph.D. thesis, Princeton University, 2009.

Dicke, R., *et al.*, *Cosmic Black-Body Radiation*, Astrophys. J., **142** (1965), 414.

Doke, T. *et al.*, *LET Dependence of Scintillation Yields in Liquid Argon*, Nucl. Instrum. Methods Phys. Res., Sect. A, **269** (1988), 291.

Doke, T., *et al.*, *Absolute Scintillation Yields in Liquid Argon and Xenon for Various Particles*, Jpn. J. Appl. Phys., **41** (2002), 1538.

Duffy, L. D., *et al.*, *A High Resolution Search for Dark-Matter Axions*, Phys. Rev. D, **74** (2006), 012006.

Dunkley, J. *et al.* (WMAP Collaboration), *Five-Year Wilkinson Microwave Anisotropy Probe (WMAP) Observations: Likelihoods and Parameters from the WMAP data*, Astrophys. J. Suppl., **180** (2009), 306.

Edwards, B. *et al.* (ZEPLIN-II), *Measurement of Single Electron Emission in Two-Phase Xenon*, Astropart. Phys., **30** (2008), 54.

Feldman, G. J. and Cousins, R. D., *A Unified Approach to the Classical Statistical Analysis of Small Signals*, Phys. Rev. D, **57** (1998), 3873.

Giboni, K. L. *et al.*, *Xenon Recirculation-Purification with a Heat Exchanger*, JINST, **6** (2011), P03002.

Girard, T., *et al.*, *Simple Dark Matter Search Results*, Phys. Lett. B, **621** (2005), 233.

Gordon, E., Khmelenko, V., and Rzhevsky, O., *Critical Phenomena in Electron Drift Through Condensed Rare Gases*, Chem. Phys. Lett., **217** (1994), 605.

Gushchin, E. M., Kruglov., A. A., and Obodovski, I. M., *Electron Dynamics in Condensed Argon and Xenon*, Sov. Phys. JETP, **55** (1982), 650.

Hamamatsu Photonics K.K., *Photomultiplier Tubes: Basics and Applications*, Hamamatsu Photonics K.K., 3rd ed., 2006, `http://sales.hamamatsu.com/assets/applications/ETD/pmt_handbook_complete.pdf`.

Hilt, O., Schmidt, W., and Khrapak, A., *Ionic Mobilities in Liquid Xenon*, IEEE Trans. on Diel. Elect. Insul., **1** (1994), 648 .

Hitachi, A., *Properties of Liquid Xenon Scintillation for Dark Matter Searches*, Astropart. Phys., **24** (2005), 247.

Hitachi, A. *et al.*, *Effect of Ionization Density on the Time Dependence of Luminescence from Liquid Argon and Xenon*, Phys. Rev. B, **27** (1983), 5279.

Horn, M. *et al.* (ZEPLIN-III), *Nuclear Recoil Scintillation And Ionisation Yields In Liquid Xenon From ZEPLIN-III Data*, (2011), `arXiv:1106.0694`.

Horowitz, C. J., Coakley, K., and McKinsey, D., *Supernova Observation via Neutrino - Nucleus Elastic Scattering in the CLEAN Detector*, Phys. Rev. D, **68** (2003), 023005.

Huang, S. S.-S. and Freeman, G. R., *Electron Mobilities in Gaseous, Critical, and Liquid Xenon: Density, Electric Field, and Temperature Effects: Quasilocalization*, J. Chem. Phys., **68** (1978), 1355.

ICRP, *Data for Use in Protection Against External Radiation, ICRP Publication 51*, Pergamon, Oxford, U.K., 1987.

Ishida, N., *et al.*, *Attenuation Length Measurements of Scintillation Light in Liquid Rare Gases and Their Mixtures Using an Improved Reflection Suppresser*, Nucl. Instrum. Meth. Phys. Res., Sect. A, **384** (1997), 380.

Jones, H. M. and Kunhardt, E. E., *Development of Pulsed Dielectric Breakdown in Liquids*, J. of Phys. D: Appl. Phys., **28** (1995), 178.

Jones, K. W. and Kraner, H. W., *Energy Lost to Ionization by 254-eV ^{73}Ge Atoms Stopping in Ge*, Phys. Rev. A, **11** (1975), 1347.

Jortner, J., *et al.*, *Localized Excitations in Condensed Ne, Ar, Kr, and Xe*, J. Chem. Phys., **42** (1965), 4250.

Jungman, G., Kamionkowski, M., and Griest, K., *Supersymmetric Dark Matter*, Phys. Rept., **267** (1996), 195.

Kish, A., *Dark Matter Search with the XENON100 Experiment*, Ph.D. thesis, University of Zurich, Switzerland, 2011.

Knoll, G. F., *Radiation Detection and Measurement; 3rd ed.*, Wiley, New York, NY, 2000.

Komatsu, E. *et al.* (WMAP Collaboration), *Seven-Year Wilkinson Microwave Anisotropy Probe (WMAP) Observations: Cosmological Interpretation*, Astrophys. J. Suppl., **192** (2011), 18.

Kubota, S., Hishida, M., and Raun, J., *Evidence for a Triplet State of the Self-Trapped Exciton States in Liquid Argon, Krypton and Xenon*, J. Phys. C, **11** (1978a), 2645.

Kubota, S. *et al.*, *Recombination Luminescence in Liquid Argon and in Liquid Xenon*, Phys. Rev. B, **17** (1978b), 2762.

Kuchnir, F. T. and Lynch, F. J., *Time-Dependence of Scintillations and the Effect on Pulse-Shape Discrimination*, IEEE Trans. Nucl. Sci., **15** (1968), 107.

Laffranchi, M. *et al.* (ArDM), *The ArDM project: a Liquid Argon TPC for Dark Matter Detection*, J. Phys. Conf. Ser., **65** (2007), 012014.

Larson, D., *et al.*, *Seven-Year Wilkinson Microwave Anisotropy Probe (WMAP) Observations: Power Spectra and WMAP-Derived Parameters*, Astrophys. J. Suppl., **192** (2011), 16.

Lebedenko, V. N. *et al.* (ZEPLIN-III), *Limits on the Spin-Dependent WIMP-Nucleon Cross-Sections from the First Science Run of the ZEPLIN-III Experiment*, Phys. Rev. Lett., **103** (2009a), 151302.

Lebedenko, V. N. *et al.* (ZEPLIN-III), *Result from the First Science Run of the ZEPLIN-III Dark Matter Search Experiment*, Phys. Rev. D, **80** (2009b), 052010.

Lee, H. *et al.* (KIMS Collaboration), *Limits on WIMP-Nucleon Cross Section with CsI(Tl) Crystal Detectors*, Phys. Rev. Lett., **99** (2007), 091301.

Lekner, J., *Motion of Electrons in Liquid Argon*, Phys. Rev., **158** (1967), 130.

Leo, W. R., *Techniques for Nuclear and Particle Physics Experiments: A How-To Approach*, Springer, Berlin, 2nd ed. ed., 1994.

Lewin, J. D. and Smith, P. F., *Review of Mathematics, Numerical Factors, and Corrections for Dark Matter Experiments Based on Elastic Nuclear Recoil*, Astropart. Phys., **6** (1996), 87.

Lindhard, J., *et al.*, *Integral Equations Governing Radiation Effects*, Mat. Fys. Medd. Dan. Vid. Selsk., **33** (1963), no. 10.

Lippincott, W., *et al.*, *Scintillation Time Dependence and Pulse Shape Discrimination in Liquid Argon*, Phys. Rev. C, **78** (2008), 035801.

Manalaysay, A., *Towards an Improved Understanding of the Relative Scintillation Efficiency of Nuclear Recoils in Liquid Xenon*, (2010), `arXiv:1007.3746`.

Manzur, A. *et al.*, *Scintillation Efficiency and Ionization Yield of Liquid Xenon for Mono-Energetic Nuclear Recoils Down to 4 keV*, Phys. Rev. C, **81** (2010), 025808.

McCabe, W. L. and Smith, J. C., *Unit Operations of Chemical Engineering*, McGraw-Hill, New York, NY, 3rd ed., 1976.

McKinsey, D. N. *et al.* (LUX), *The LUX Dark Matter Search*, J. Phys. Conf. Ser., **203** (2010), 012026.

Mei, D. M., *et al.*, *A Model of Nuclear Recoil Scintillation Efficiency in Noble Liquids*, Astropart. Phys., **30** (2008), 12.

Mei, Y., *Calibration and Dark Matter Search with the XENON100 Experiment*, Ph.D. thesis, Rice University, TX, 2011.

Messous, Y. *et al.*, *Calibration of a Ge Crystal with Nuclear Recoils for the Development of a Dark Matter Detector*, Astropart. Phys., **3** (1995), 361 .

Minamino, A. (XMASS), *XMASS Experiment, Dark Matter Search with Liquid Xenon Detector*, Nucl. Instrum. Meth. Phys. Res., Sect. A, **623** (2010), 448.

Moulin, E., Mayet, F., and Santos, D., *Supersymmetric Dark Matter Search via Spin-Dependent Interaction with He-3*, Phys. Lett. B, **614** (2005), 143.

Nishimura, H., *et al.*, *Tracking Performance of the NEWAGE-0.3a Direction-Sensitive Dark Matter Detector*, Astropart. Phys., **31** (2009), 185.

Pack, J. L., *et al.*, *Longitudinal Electron Diffusion Coefficients in Gases: Noble Gases*, J. Appl. Phys., **71** (1992), 5363.

Peccei, R. and Quinn, H. R., *CP Conservation in the Presence of Instantons*, Phys. Rev. Lett., **38** (1977), 1440.

Penzias, A. A. and Wilson, R. W., *A Measurement of Excess Antenna Temperature at 4080-Mc/s*, Astrophys. J., **142** (1965), 419.

Plante, G., *et al.*, *New Measurement of the Scintillation Efficiency of Low-Energy Nuclear Recoils in Liquid Xenon*, Phys. Rev. C, **84** (2011), 045805.

Savage, C., *et al.*, *Compatibility of DAMA/LIBRA Dark Matter Detection with Other Searches*, JCAP, **0904** (2009), 010.

Schmidt, W. F., *The Basic Properties of Liquid Xenon as Related to its Application in Radiation Detectors*, in *Technique and Application of Xenon Detectors. Proceedings of the International Workshop, Kashiwa, Japan, December 3-4, 2001*, edited by Y. Suzuki, M. Nakahata, Y. Koshio, and S. Moriyama, pp. 1–16, World Scientific, 2002.

Schwenter, N., Kock, E.-E., and Jortner, J., *Electronic Excitations in Condensed Rare Gases*, Springer Tracts in Modern Physics, Springer-Verlag/Elsevier, New York, 1985.

Seguinot, J., *et al.*, *Liquid Xenon Ionization and Scintillation: Studies for a Totally Active Vector Electromagnetic Calorimeter*, Nucl. Instrum. Meth. Phys. Res., Sect. A, **323** (1992), 583.

Silva, C., *et al.*, *Reflectance of Polytetrafluoroethylene for Xenon Scintillation Light*, J. Appl. Phys., **107** (2010), 064902.

Sofue, Y. and Rubin, V., *Rotation Curves of Spiral Galaxies*, Ann. Rev. Astron. Astrophys., **39** (2001), 137.

Solovov, V., *et al.*, *Measurement of the Refractive Index and Attenuation Length of Liquid Xenon for its Scintillation Light*, Nucl. Instrum. Meth. Phys. Res., Sect. A, **516** (2004), 462.

Sorensen, P. and Dahl, C. E., *Nuclear Recoil Energy Scale in Liquid Xenon with Application to the Direct Detection of Dark Matter*, Phys. Rev. D, **83** (2011), 063501.

Sorensen, P. *et al.* (XENON), *The Scintillation and Ionization Yield of Liquid Xenon for Nuclear Recoils*, Nucl. Instrum. Meth. Phys. Res., Sect. A, **601** (2009), 339.

Sorensen, P. F., *A Position-Sensitive Liquid Xenon Time-Projection Chamber for Direct Detection of Dark Matter: The XENON10 Experiment*, Ph.D. thesis, Brown University, RI, 2008.

Spergel, D. N., *The Motion of the Earth and the Detection of WIMPs*, Phys. Rev. D, **37** (1988), 1353.

Steinberger, I. T. and Asaf, U., *Band-Structure Parameters of Solid and Liquid Xenon*, Phys. Rev. B, **8** (1973), 914.

Taiyo Nippon Sanso, *Taiyo Nippon Sanso*, , `http://www.tn-sanso.co.jp/en/`.

Takahashi, T., *et al.*, *Average Energy Expended per Ion Pair in Liquid Xenon*, Phys. Rev. A, **12** (1975), 1771.

Trotta, R., *et al.*, *The Impact of Priors and Observables on Parameter Inferences in the Constrained MSSM*, J. High Energy Phys., **12** (2008), 024.

Tuli, J. K., *Evaluated Nuclear Structure Data File. A Manual for Preparation of Data Sets*, Brookhaven Nat. Lab., Upton, NY, 2001, submitted on 1 Feb 2001.

Wagner, E. B., Davis, F. J., and Hurst, G. S., *Time of Flight Investigations of Electron Transport in Some Atomic and Molecular Gases*, J. Chem. Phys., **47** (1967), 3138.

Weinberg, S., *A New Light Boson?*, Phys. Rev. Lett., **40** (1978), 223.

Wilczek, F., *Problem of Strong p and t Invariance in the Presence of Instantons*, Phys. Rev. Lett., **40** (1978), 279.

Yamashita, M. *et al.*, *Scintillation Response of Liquid Xe Surrounded by PTFE Reflector for Gamma Rays*, Nucl. Instrum. Meth. Phys. Res., Sect. A, **535** (2004), 692 .

Yellin, S., *Finding an upper limit in the presence of unknown background*, Phys. Rev. D, **66** (2002), 032005.

Ziegler, J., *SRIM, The Stopping and Range of Ions in Matter*, 2011, `http://www.srim.org/`.

Zwicky, F., *Spectral Displacement of Extra Galactic Nebulae*, Helv. Phys. Acta, **6** (1933), 110.